

Submitted to Cardiff University for the degree of doctor of philosophy,



Simulation of Irradiated Graphite

Alex Theodosiou

September 2010

UMI Number: U564738

All rights reserved

INFORMATION TO ALL USERS

The quality of this reproduction is dependent upon the quality of the copy submitted.

In the unlikely event that the author did not send a complete manuscript and there are missing pages, these will be noted. Also, if material had to be removed, a note will indicate the deletion.



UMI U564738

Published by ProQuest LLC 2013. Copyright in the Dissertation held by the Author.
Microform Edition © ProQuest LLC.


All rights reserved. This work is protected against
unauthorized copying under Title 17, United States Code.



ProQuest LLC
789 East Eisenhower Parkway
P.O. Box 1346
Ann Arbor, MI 48106-1346

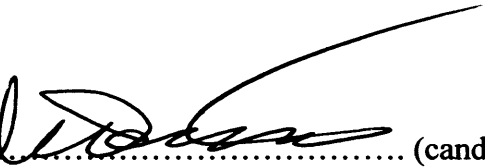
Declaration

This work has not previously been accepted for any degree and is not concurrently submitted in candidature for any degree.

Signed..... (candidate) Date ...12-04-11.....

Statement 1

This thesis is being submitted in partial fulfilment of the requirements for the degree of PhD

Signed..... (candidate) Date ...12-04-11.....


Statement 2

This thesis is the result of my own independent work/investigation, except where otherwise stated. Other sources are acknowledged by explicit reference.

Signed..... (candidate) Date ...12-04-11.....

Statement 3

I hereby give consent for my thesis, if accepted, to be available for the photocopying and for inter-library loan, and for the title and summary to be made available to outside organisations.

Signed..... (candidate) Date ...12-04-11.....

Abstract

A detailed scientific investigation is carried out into the effects of ion irradiation on graphite systems. The results obtained have been compared with analogous radiation induced effects seen in neutron irradiated material. Results indicate that ion irradiation causes structural damage of the graphite lattice, as expected, in a very similar way to neutron irradiation. Such damage is also largely recoverable through thermal annealing. However, certain differences are observed and it seems likely that these are due to differences in the nature of the damage caused, and the recovery of such damage, on the fundamental level.

Ultra-high vacuum (UHV) equipment was used to irradiate samples of nuclear grade graphite and highly-orientated pyrolytic graphite (HOPG) with inert gas ions and external facilities were also used to irradiate with carbon ions at higher energies. After irradiation a variety of scientific techniques were used to analyse the damage caused as a result of the irradiation.

Raman spectroscopy was used extensively to study the samples after irradiation and results indicated the presence of significant ion-induced damage through analysis of the I_D/I_G ratio. The results were shown to be analogous to neutron induced damage and the amount of damage present was seen to be dependant on ion mass, ion energy and of course the total ion dose. A broad Raman feature was observed at 1500 cm^{-1} , after a critical ion dose and such a feature has been rarely observed in neutron irradiated material, this feature perhaps suggests a fundamental difference between the damage occurring and a difference in the type and extent of defects produced. Raman was also used to effectively monitor damage recovery processes occurring as a result of thermal annealing and such recovery was seen to be analogous to the recovery seen in neutron damages materials.

Differential scanning calorimetry (DSC) was used to detect any exothermic release, when heating the sample after irradiation, occurring as a result of a build-up of Wigner-like energy, a phenomenon commonly seen in neutron irradiated graphite. In

one case of high energy He⁺ ion irradiation such an exotherm was observed at 226 °C, the expected temperature range for Wigner-like release, however this result was very difficult to reproduce thus suggesting a fragile balance of ion irradiation parameters resulting in the necessary defects required to observe any Wigner release. Transmission electron microscopy (TEM) showed clearly that the atomic structure of nuclear grade graphite material was markedly altered as a result of ion irradiation, leading to an amorphous-like structure. These results are in agreement with published TEM work on neutron irradiated material and again highlight a similarity between the two forms of radiation.

X-ray diffraction (XRD) was also utilised and samples were analysed before and after irradiation. Contrary to XRD patterns of neutron irradiated graphite, there seemed to be little change in the XRD patterns after irradiation and the expected broadening and peak shift of the <002> peak was not seen, suggesting a difference in the damage caused to the system. Further work is required here to understand why this is the case and again a deeper understanding of the underlying damage mechanisms would be beneficial.

Acknowledgements

I would like to express my thanks firstly to my supervisors Dr Albert Carley and Dr Stuart Taylor for their support and guidance throughout the PhD. Particular thanks to Dr David Morgan for help with day-to-day problem solving and helping to keep the working environment somewhat entertaining. Also I would like to thank Prof. Gary Attard for allowing me to use his Raman microscope and Dr Rob Taylor for training.

I would like to thank Prof. Barry Marsden and the members of the Nuclear Graphite Research Group in Manchester, particularly Dr Abbie Jones for helpful advice throughout with thanks also to Lewis, Will, Michael and Lorraine for always making feel welcome up in Manchester. This goes for Lisa and Louise too who provided me with a place to stay and many enjoyable nights.

I am extremely grateful to the people I worked with at various institutions for helping with certain experiments that could not be carried out at Cardiff. These include Dr Mike Ward from Leeds University, Dr Jonathan Hinks from the University of Salford, Dr Gareth Hughes and Dr Lisa Karlsson from Oxford, Dr Nianhua Peng and Dr Chris Jeynes from Surrey Ion Beam Centre and Dr Nelly Toulhoat and Prof. Nathalie Moncoffre from the University of Lyon.

Also thanks to the Support Staff at Cardiff University for helping out on many occasions throughout my PhD, these include Terrie, Alison, Sarah and Matt and also Jamie and Gaz. A special thanks is reserved for Alun and Jon from the workshop who, amongst other things, had to machine the graphite for me on many occasions.

Finally, I would like to thank my friends at Cardiff for making my PhD an enjoyable experience, these include Adrian, Rhys, Egg, Doley, Bish, Jon, Kareem, Lee and many others. Last, but not least, a big thanks to my parents, Jan and Theo, for their continuous support, love and encouragement throughout even if they didn't really understand what I was doing!

Glossary

Abbreviations Used:

AGR	Advanced Gas-cooled Reactor
ASTRA	Adaptierter Schwimmbecken-Typ-Reaktor Austria
BEPO	British Experimental Pile Grade Zero
CP-1	Chicago Pile-1
CTE	Co-efficient of Thermal Expansion
DSC	Differential Scanning Calorimetry
EBR-1	Experimental Breeder Reactor-1
EPSRC	Engineering and Physical Sciences Research Council
ESCA	Electron Spectroscopy for Chemical Analysis
FIB	Focussed Ion Beam
GLEEP	Graphite Low-Energy Experimental Pile
IAEA	International Atomic Energy Agency
ILW	Intermediate Level Waste
KNOO	Keeping the Nuclear Option Open
MAGNOX	Magnesium Non-Oxidising
NDA	Nuclear Decommissioning Authority
NGRG	Nuclear Graphite Research Group
PGA	Pile Grade-A (Graphite)
PKA	Primary Knock-on Atom
PWR	Pressurised Water Reactor
TEM	Transmission Electron Microscopy
TRISO	Tristructural-isotropic
UHV	Ultra High Vacuum
USAEC	Unites States Atomic Energy Commission
VHTR	Very High Temperature Reactor
XPS	X-ray Photoelectron Spectroscopy
XRD	X-ray Diffraction

Contents

Chapter 1 – Introduction

1.1. Project Overview	1
1.2. Nuclear Power	2
1.2.1. Overview	
1.2.2. Historical	
1.2.3. Reactor Design and Engineering	
1.2.3.1. Nuclear Power in the UK	
1.2.3.2. Advanced Gas-Cooled Reactors	
1.2.4. Neutron Moderators	
1.2.4.1. Graphite as a Moderator	
1.3. Manufacture of Nuclear Graphite	8
1.4. Different Graphite Grades	11
1.4.1. Pile Grade-A Graphite	
1.4.2. Gilsocarbon	
1.4.3. Graphite in Generation IV Reactors	
1.5. Disadvantages of Graphite	14
1.5.1. Wigner Effect	
1.5.2. Wigner Energy	
1.5.3. Graphite Waste	
1.6. Scientific Proposal	18
1.7. Summary	18
1.8. References	19

Chapter 2 - Experimental

2.1. Introduction	23
2.2. Ultra-High Vacuum	24
2.2.1. The Ion Bombadment Vacuum Chamber	
2.2.2. Vacuum Theory	
2.2.3. Achieving UHV Conditions	
2.2.3.1. Diffusion Pump	
2.2.4. Monitoring System Pressure	
2.2.5. Operating the Vacuum System	
2.2.5.1. Baking the System	
2.2.5.2. Loading a Sample	

2.2.6. Methods of Irradiation	
2.2.6.1. Cold-Cathode Ion Gun	
2.2.6.2. Higher Energy Facilities	
2.2.6.2.1. Surrey Ion Beam Centre	
2.2.6.2.2. Universitié de Lyon	
2.3. Characterisation Techniques Employed	31
2.3.1. Raman Spectroscopy	
2.3.1.1. Background / Theory	
2.3.1.1.1. Molecular Vibrations	
2.3.1.2. Application	
2.3.1.3. Instrumentation	
2.3.2. Differential Scanning Calorimetry (DSC)	
2.3.2.1. Background / Theory	
2.3.2.2. Application	
2.3.2.3. Instrumentation	
2.3.3. X-Ray Photoelectron Spectroscopy (XPS)	
2.3.3.1. Background / Theory	
2.3.3.2. Application	
2.3.3.3. Instrumentation	
2.3.4. X-Ray Diffraction (XRD)	
2.3.4.1. Background / Theory	
2.3.4.2. Application	
2.3.4.3. Instrumentation	
2.3.5. Transmission Electron Microscopy (TEM)	
2.3.5.1. Background / Theory	
2.3.5.2. Sample Preparation	
2.3.5.3. Application	
2.3.5.4. Instrumentation	
2.4. References	49

Chapter 3 – Atomic Displacement Processes

3.1. Introduction	51
3.2. Theory	51
3.2.1. Collision Cascade Theory	
3.2.2. Atomic Displacement Energy	
3.2.3. Replacement Collisions	
3.2.4. Cascade Overlap	
3.3. Stopping and Range of Ions in Matter (SRIM)	57
3.3.1. Energy Loss Mechanisms	
3.3.2. Nuclear Stopping	
3.3.3. Electronic Stopping	
3.3.3.1. Light Ions	
3.3.3.2. Heavy Ions	
3.3.4. The Range of Ions in Matter	

3.3.5. Channelling	
3.3.6. SRIM Computer Package	
3.4. Neutrons	68
3.4.1. Fast Neutrons	
3.4.2. Neutron Interaction with Matter	
3.4.3. Using Ions to Simulate Neutrons	
3.5. Conclusion	71
3.6. References	71

Chapter 4 – Raman Analysis of Ion Irradiated Graphite ($E < 10$ keV)

4.1. Introduction	75
4.2. Experimental Apparatus	76
4.3. Raman Investigation	76
4.3.1. Raman Analysis of Virgin Graphites	
4.3.2. Origin of the Raman Bands	
4.3.3. Symmetry Elements of Graphite	
4.3.4. Raman Activation	
4.3.5. Disorder Induced Raman Bands	
4.3.6. The TK relation	
4.4. Results	83
4.4.1. Time-Resolved Raman Analysis	
4.4.1.1. Ion Implantation Profiles	
4.4.2. Effect of Ion Mass	
4.4.3. Effect of Ion Energy	
4.4.4. Second Order Raman Spectra	
4.4.4.1. Disorder Induced Changes	
4.4.4.2. Effect of Ion Energy	
4.5. Conclusion	105
4.6. References	106

Chapter 5 – Temperature Annealing of Ion Irradiated Graphite

5.1. Introduction	110
5.2. Experimental	110
5.3. Overview / Background	111
5.3.1. Stored (Wigner) Energy	
5.3.2. Energy Storage and Thermal Annealing	

5.3.3. The Intimate Frenkel Pair

5.4. Results and Discussion	117
5.4.1. Room Temperature Irradiations	
5.4.1.1. DSC Analysis	
5.4.1.2. Raman Study	
5.4.1.3. Ion Implantation	
5.4.1.4. XPS	
5.4.1.5. Effect of Ion Dose	
5.4.1.6. Effect of Holding Time	
5.4.2. Low Temperature Irradiations	
5.4.2.1. DSC Analysis	
5.4.2.2. Raman Analysis	
5.4.2.3. Highly Amorphised Graphite	
5.4.3. High Temperature Irradiations	
5.4.4. TEM Analysis	
5.5. Conclusion	143
5.6. References	144

Chapter 6 - High Energy (≥ 100 keV) Ion Irradiation

6.1. Introduction	148
6.2. Experimental	148
6.3. Results	150
6.3.1. Carbon Ion Irradiations	
6.3.1.1. Ion Implantation	
6.3.1.2. Raman Analysis	
6.3.1.3. XRD	
6.3.1.4. DSC	
6.3.2. Irradiations at Higher Energies (> 1.0 MeV)	
6.3.2.1. Ion Implantation	
6.3.2.2. Raman Analysis	
6.3.2.3. XRD	
6.3.2.4. DSC	
6.4. Conclusion	172
6.5. References	173

Chapter 7 - Conclusions

7.1. Overview	175
---------------	-----

7.2. Summary of Results	175
7.2.1. Raman	
7.2.2. XPS	
7.2.3. XRD	
7.2.4. Annealing	
7.2.5. DSC	
7.2.6. TEM	
7.3. Summary	179
7.4. Future Work	180

*“If we knew what we were doing then it
wouldn't be called research”*

Albert Einstein

Chapter 1

Introduction

1.1. Project Overview

This project aims to help the nuclear industry, particularly in the UK, by attempting to provide a comprehensive understanding of the behaviour of nuclear graphite throughout its operational lifetime. An in-depth scientific study is employed which helps to understand the affect of radiation on graphite, particularly at the microscopic level. Such work will also benefit those involved in decommissioning, where the appropriate treatment and disposal of large amounts of irradiated nuclear grade graphite is an important issue, especially in the UK, where graphite has been used extensively as moderator material in many nuclear reactors and as such accounts for approximately 33% by volume of all the UK nuclear intermediate level waste (ILW) waste resulting from the civil and military nuclear program [1].

This work has been part of a four-year government funded initiative entitled Keeping the Nuclear Option Open (EPSRC KNOO Grant number: EP/C549465/1), which is part of the UK's research councils energy programme. KNOO was setup to maintain and develop skills important to the nuclear power generation and is the largest commitment to fission reactor research in the UK in the last thirty years [2]. The initiative involved extensive collaboration between universities and had a large input from the industrial sector.

Graphite research was only one aspect of the KNOO program. The work in this project was carried out alongside the Nuclear Graphite Research Group (NGRG),

Manchester, headed by Professor Barry Marsden. Researchers in the NGRG have studied extensively the irradiation-induced behaviour of a variety of nuclear grade graphites and this work, carried out predominately at Cardiff University, compliments well with the work at the NGRG.

1.2. Nuclear Power

1.2.1 Overview

Less than one hundred years ago, the word 'nuclear' did not exist. Today it is a word that evokes an opinion in almost everyone. For a lot of people this opinion tends to be a negative one, instantly bringing to the minds memories and images relating only to warfare. The Second World War, the Cold War era and also present day politics all invoke a sense of fear and distrust in what, for many people, is the unknown. In spite of all the negative connotations, 'nuclear' science can be used to good effect. Many countries have realised this and as a result nuclear power has been utilised across the world, with many countries keen to utilise this relatively new science to improve energy production.

The controversy surrounding nuclear power is well publicised, with the topic seeming to divide many people. Various advantages and disadvantages are being drafted up by both sides, with protestors focussing on safety issues, cost and the problem of long term nuclear waste; whilst the general scientific community are insisting on safety, efficiency and the environmental benefits arising from the lack of greenhouse gasses.

Unfortunately there is no hiding from the fact that accidents can happen and have happened. Incidents such as the Windscale fire (Cumbria, 1957), Three Mile Island (Pennsylvania, 1979) and Chernobyl in 1986 have done little to convince the general public about the safety of such facilities.

However, the effectiveness of nuclear power and its ability to produce vast amounts of energy using a relatively small amount of fuel is undeniable. It has a low carbon footprint and does not contribute directly to global warming due to its minimal impact on the ozone layer.

1.2.2. Historical

"It is conceivable that when heavy nuclei are bombarded with neutrons these nuclei could break down into several fairly large fragments, which are certainly isotopes of known elements, but not neighbours of the irradiated elements."

Ida Noddack, "Angewandte Chemie", No. 47, 1934.

This statement, although not taken seriously at the time, was the start of a paradigm shift in the thinking of the scientific community. Ida Noddack is seen as the first person to speculate about the realism of nuclear fission. The rest of the scientific community however, disregarded this proposal and considered the 'splitting of the atom' to be an absurd idea, impossible to prove experimentally. At this time it was thought that neutron bombardment simply added one atomic unit to the mass each time and thus produced the transuranic elements [3].

Initial nuclear research was carried out by Enrico Fermi and colleagues in 1934 when they started using neutrons as projectiles and began looking at the effects of neutron bombardment on an atoms nucleus [4]. Building on this work, Otto Hahn, Lise Meitner and Fritz Strassmann performed the first successful nuclear fission experiment in 1938, and discovered that an isotope of barium was produced from neutron bombardment of uranium [5]. This experiment proved Noddack's hypothesis to be correct; it was a breakthrough and essentially marked the discovery of nuclear fission, arguably one of the most important scientific discoveries of all time. The findings to this study were published in the famous journal *Die Naturwissenschaften*; and, for this work, Otto Hahn received the Nobel Prize for chemistry in 1944 [6].

Extensive work into this field began shortly after Hahn's discovery largely due to the start of the Manhattan Project and the quest to build the world's first fission (atomic) bomb. In 1942 Enrico Fermi supervised the assembly of the world's first artificial nuclear reactor, known as Chicago Pile-1 (CP-1), which initiated the world's first self-sustaining nuclear reaction. The reactor achieved criticality before being shut down 33 minutes later by Fermi [7]. The neutron moderator used in CP-1 was graphite,

although the purity of the graphite used was not comparable to nuclear graphites which are commercially available today. CP-1 used approximately 385.5 tonnes of graphite, produced from a variety of different sources all with differing properties [8].

The success of CP-1 led to further work in the area; however it was almost a decade until the energy from a nuclear reactor was harnessed for the generation of electricity. In 1951, the Experimental Breeder reactor (EBR-1) reached criticality, in the Idaho desert and generated enough electricity to power four 200 W light bulbs [9]. The power output increased and EBR-1 was used for experimental purposes until it was decommissioned in 1964 [10].

1.2.3. Reactor Design and Engineering

The International Atomic Energy Agency (IAEA) reported that in December 2009 there were 436 reactors worldwide across 31 different countries [11]. Figures have shown that despite a small decline since 2007, the amount of energy generated through nuclear power is estimated to be currently around 2558 TWh annually, supplying approximately 14% of the worlds electricity demand [12].

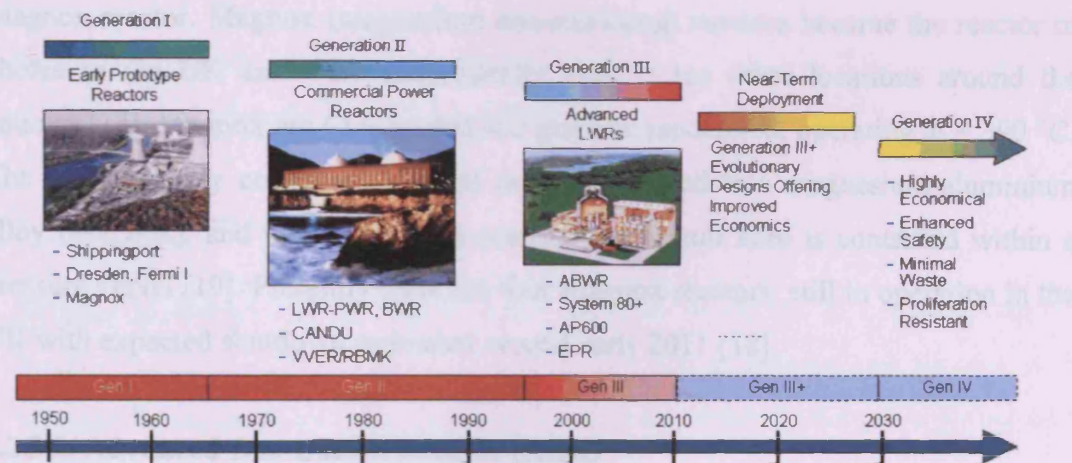


Fig. 1.1: A timeline of nuclear reactor design [13].

Today there are many types of nuclear reactor in operation around the world, with a variety of different coolants and moderators available to choose from. Reactors are divided into categories based on their design e.g. Generation I reactors are the earliest type of design whereas Generation III reactors are considered the most modern and advanced type of reactor (Fig. 1.1)

Generation IV are proposed 'ultra-modern' reactors that are currently being researched offering superior safety and reliability with advancements in sustainability and economics [14]. Currently the UK has only Generation I and II type reactors in operation [15].

1.2.3.1. Nuclear Power in the United Kingdom

The British nuclear program started in 1946 with the development of GLEEP (Graphite Low Energy Experimental Pile) which was a low powered (0.05 MW) air cooled, graphite moderated reactor [16]. It began operating in 1947 and was the first working reactor in Western Europe.

Following this, two new reactors were built at Windscale in 1950 with the intention of providing plutonium for the UK weapons program [17]. Shortly after an electricity generating reactor was built nearby at Calder Hall and was a Generation I type Magnox reactor. Magnox (magnesium non-oxidising) reactors became the reactor of choice in the UK and were subsequently built at ten other locations around the country [18]. Magnox are CO₂ cooled and graphite moderated, operating at ~ 390 °C. The fuel assembly consists of natural uranium encased in a magnesium-aluminium alloy (Magnox), and unlike previous reactors the reactor core is contained within a pressure vessel [19]. Presently there are four Magnox reactors still in operation in the UK with expected shutdown estimated around early 2011 [18].

1.2.3.2. Advanced Gas-Cooled Reactor (AGR)

The next generation of reactor was first built in 1962 and the design was an improvement on its Magnox predecessor. The Generation II reactor was the advanced gas-cooled reactor (AGR) which is also CO₂ cooled and graphite moderated. The initial prototype AGR produced 110 MWh of power however by the late 1970s such

designs could produce over 1 GWh per reactor [19]. AGR reactors operate at higher temperatures to the Magnox design, $\sim 650\text{ }^{\circ}\text{C}$, thus improving the thermal efficiency. Other advancements include improved safety measures, and the use of enriched uranium means refuelling is required less often, though power can still be produced whilst refuelling is taking place in these AGR designs [20].

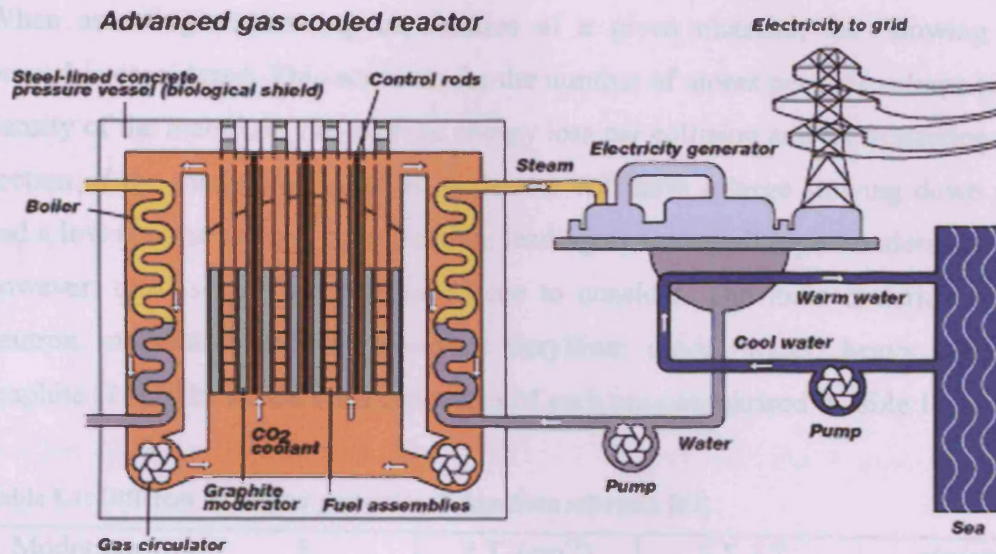


Fig. 1.3: Schematic of a typical AGR reactor [21].

There are currently 14 AGR's in operation in the UK [22] over six nuclear sites, four of which are planned to be closed by 2015 [15].

1.2.4. Neutron Moderators

Neutron moderator are needed in order to slow down the fast moving neutrons (emitted as fission products) to a velocity of a few kilometres per second; at this velocity the neutrons are much more likely to cause further fission, thus giving rise to a self-sustaining chain reaction.

Essential to a good neutron moderator is the ability of the substance to essentially reflect neutrons, while absorbing some of their energy via elastic collisions. Materials consisting of lighter atoms are better at this since more energy is transferred per

collision the lighter the target nucleus is. After multiple collisions with the moderator the neutrons become sufficiently de-energised, such that their velocity becomes comparable to the thermal velocities of the nuclei; these neutrons are then called thermal neutrons. A thermal neutron typically has an energy of around 0.025 eV, corresponding to a velocity of $2.2 \times 10^5 \text{ cm.s}^{-1}$. A fast neutron has energies typically in the order of 2.0 MeV [23].

When assessing moderating capabilities of a given material, the ‘slowing down power’ is considered. This accounts for the number of atoms per unit volume (i.e. the density of the material), the average energy loss per collision and the scattering cross-section of the moderator. A good moderator will have a large slowing down power and a low neutron capture cross section, leading to an overall high ‘moderating ratio’, however; cost is also an important issue to consider. The main materials used as neutron moderators are beryllium or beryllium oxide, water, heavy water and graphite [24]. The moderating properties of each are summarised in table 1.1.

Table 1.1: Different moderator properties. Taken from reference [24].

Moderator	ξ	$\xi \Sigma_s (\text{cm}^{-1})$	$\xi \Sigma_s / \Sigma_a$	$\rho (\text{g/cm}^3)$
Graphite	0.158	0.063	200	1.65
Be	0.206	0.16	150	1.84
BeO	0.17	0.11	180	2.80
H ₂ O	0.93	1.5	70	1.00
D ₂ O	0.51	0.18	21000	1.10

Where, ξ is the average logarithmic energy decrement for each neutron collision, $\xi \Sigma_s$ is the slowing down power (Σ_s refers to the level of scattering and Σ_a to absorption) and $\xi \Sigma_s / \Sigma_a$ is the moderating ratio.

Beryllium is a good moderator however it is relatively difficult to machine, is expensive and also poses a toxicity threat. Water is also a very good moderator and is very cheap and easy to handle, however hydrogen readily absorbs neutrons and as a result, in early reactors, enriched uranium was required which used to be a costly process. Heavy water has a very high moderating ratio however the cost of generating

the deuterated water is very high [25]. Overall, many scientists and engineers see graphite as the moderator of choice. It is cheap and easily machined, non-toxic and offers acceptable moderating capabilities [24] as well as being able to maintain its strength even at very high temperatures; it is also desirable as it can be manufactured at extremely pure levels, on an industrial scale [26]. However a major concern is that upon irradiation the properties of graphite are markedly altered. It should be mentioned though that despite the many advantages of using graphite as a moderator, technological advancements have meant that light water moderators are no longer as expensive to use as they used to be and as a result it is the most commonly used moderator in use today.

1.2.4.1. Graphite as a moderator

As mentioned, in 1942, Enrico Fermi suggested the use of graphite as a neutron moderator in the first attempt to create a self-sustaining nuclear reaction (CP-1). Studies carried out around this time in the USSR also showed that graphite moderated nuclear reactors were desirable for many reasons [27].

Parallel to Enrico Fermi's work, studies carried out by Eugene. P. Wigner in December 1942 showed that the graphite lattice would be distorted by fast neutrons emitted from the fission reactions [28]. These neutrons could strike the carbon atoms thus displacing from their lattice sites by momentum transfer therefore having a considerable effect on many of the properties of graphite (Wigner effect). Accompanying this is a build up of potential energy (Wigner energy) since the removed carbon atoms (interstitials) are now in non-ideal locations. If this energy is allowed to accumulate it could escape in a powerful rush of heat.

1.3. Manufacture of Nuclear Graphite

Naturally occurring graphite is mined in Sri Lanka, Madagascar, USA, Russia, South Korea, Mexico, Austria, the Czech Republic and Italy with the biggest producers of natural graphite being South Korea and Austria [29].

The manufacture of artificial polycrystalline nuclear graphite focuses largely on purity. Purity levels exceeding 99.999% carbon are desirable and to achieve this the conventional manufacturing process is modified with care being taken to remove neutron absorbing impurities, such as boron [30].

The process is summarised below:

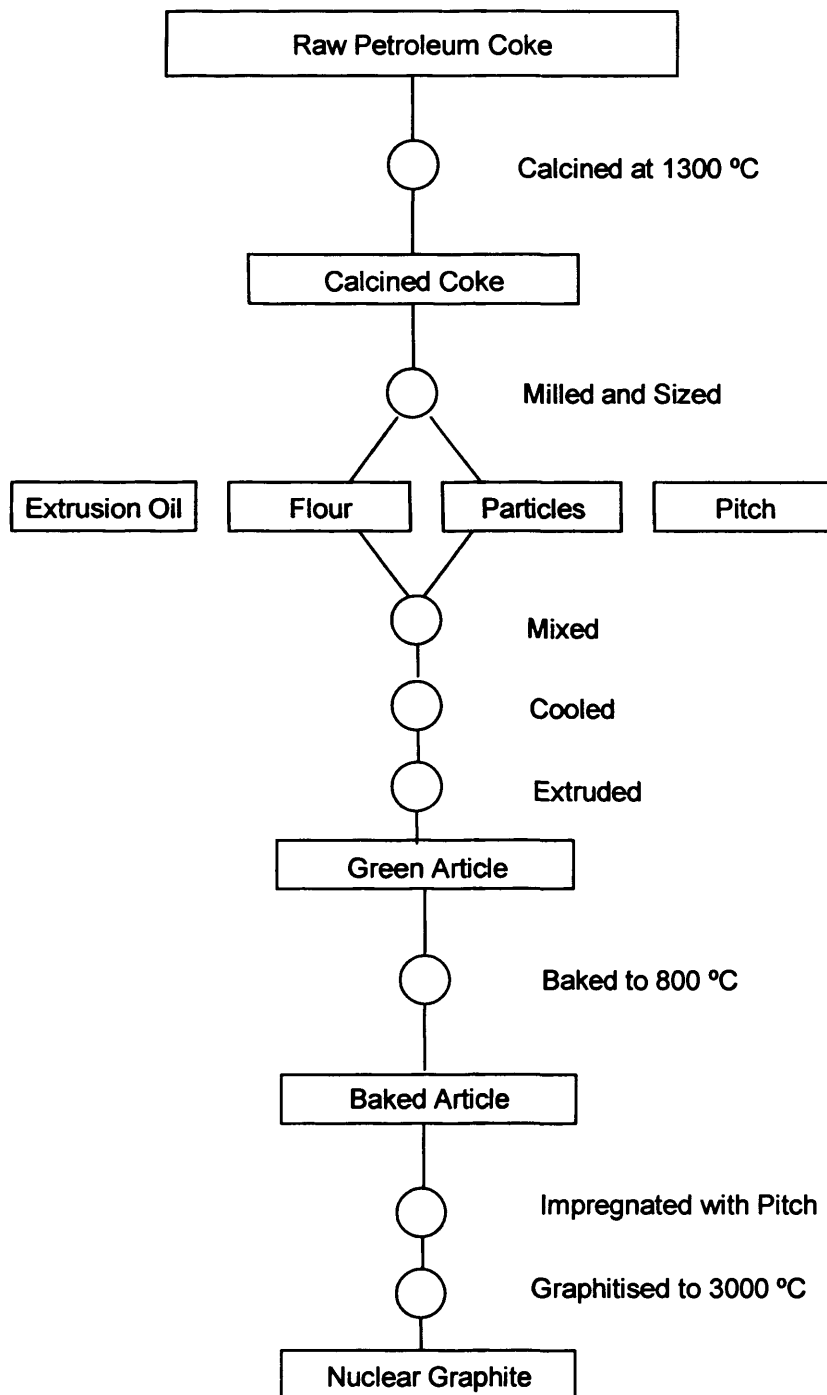


Fig. 1.4: The major processing steps in the manufacture of a typical nuclear grade graphite [30].

There are two phases that make up polygranular graphite, the filler material and the binder phase. In the USA the most common filler material used is petroleum coke whilst in Europe a coke derived from coal-tar pitch was preferred [30]. In the UK, naturally occurring bitumen found in Utah, USA, known as Gilsonite, was used in the AGRs [31].

The binder phase used is typically a coal-tar pitch, derived from the distillation of coal tar. It is an inexpensive material that could be produced in massive quantities. The pitch has the property of being solid at room temperature but fluid at higher temperatures, thus allowing thorough mixing of the filler and binder.

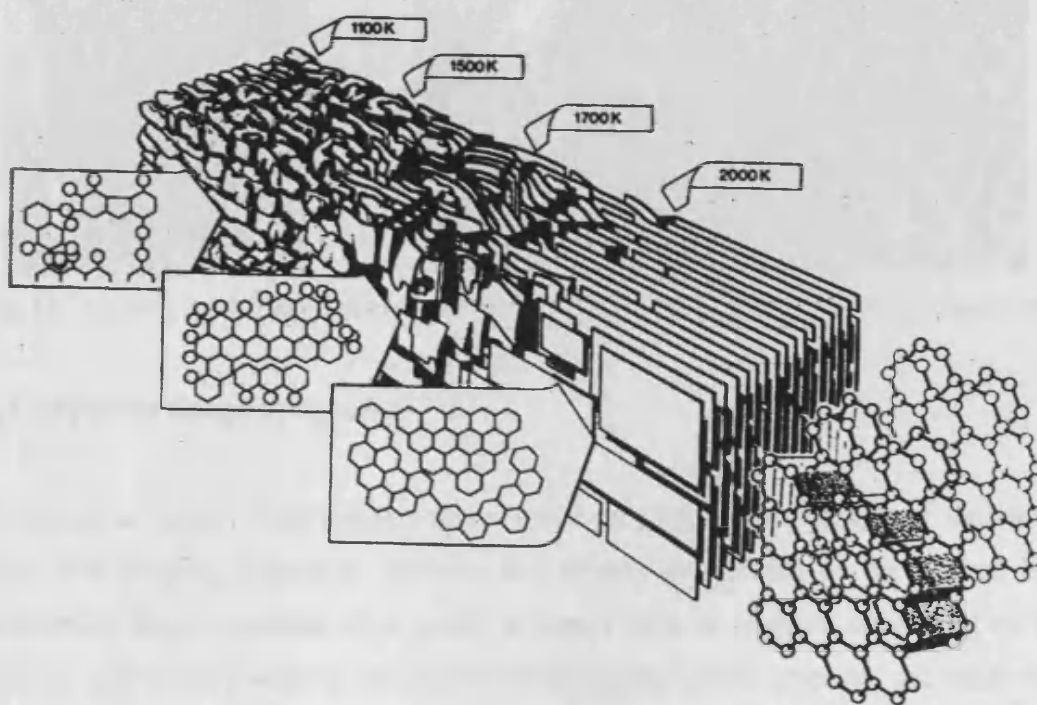


Fig. 1.5: Marsh-Griffiths model of the graphitisation process [33], defined as a solid state transformation of thermodynamically unstable non-graphitic carbon into graphite by thermal activation [34]. It is important to note that after graphitisation the crystal structure is still not 'perfect' and there is approximately one stacking fault in every six layer planes of the ABAB structure.

After graphitisation the graphite is finally purified and then ready to be machined into the desired shape. A typical graphite brick used in a reactor core is shown below [31].

Once mixed the coke particles are now said to be plasticised and therefore can be easily formed through extrusion, moulding and isostatic pressing. Further baking carbonises the binder phase before pitch impregnation is used to increase density and strength. Finally intense heating over several weeks (2800-3000 °C) allows migration of the carbon atoms to a more thermodynamically stable state, e.g. into a graphite lattice and the removal of any volatile impurities. This final step is known as graphitisation and is commonly completed in a Acheson or longitudinal furnace [32].

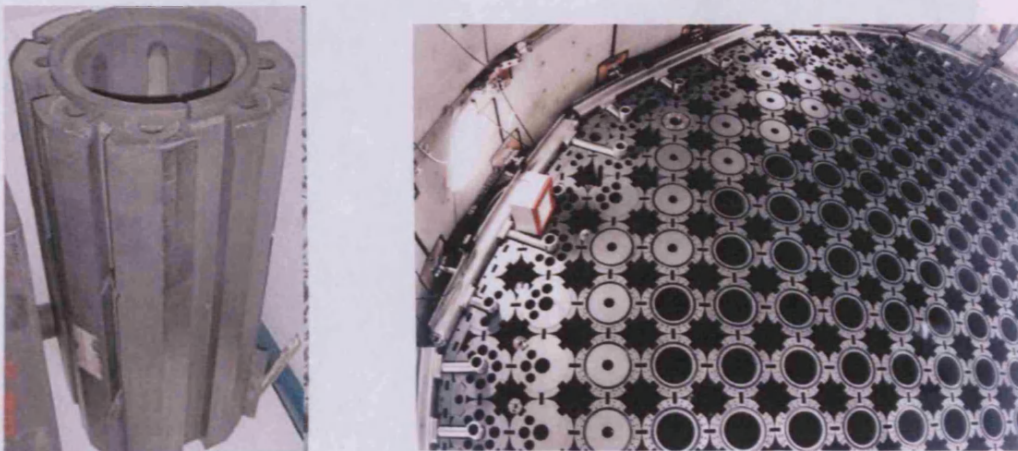


Fig. 1.6: A typical AGR graphite sleeve (left) and an AGR core under construction in Torness (right).

1.4. Different Graphites grades

There are a variety of different nuclear grade graphites used throughout the world, each with varying properties, porosity and density determined by the desired bulk properties. Some countries may prefer a certain type of graphite depending on the type of reactor they wish to use, however all nuclear grade graphites are made in a similar process to that described above. Some of the larger international graphite producing companies in the world today include SGL Carbon (Germany), Graftech International Ltd (USA) and Toyo Tanso (Japan):

1. GrafTech (Previously: British Acheson Electrodes Ltd (BAEL), which then became United Carbide Corporation (UCAR)).

2. SGL (Previously Anglo Great Lakes (AGL) later amalgamated with Pechiney in France)

BAEL was based in Sheffield and AGL in Newcastle-on-Tyne, both factories no longer manufacture graphite in the UK and the factories no longer exist.

1.4.1. Pile Grade-A (PGA) Graphite.

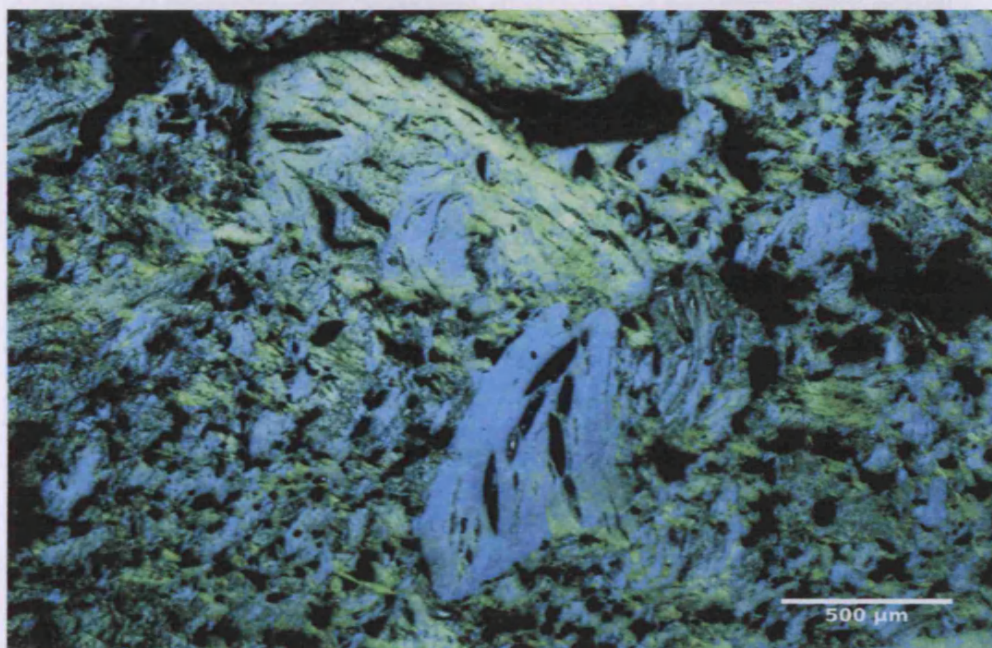


Fig. 1.7: A polarised optical micrograph of PGA showing aligned needle like filler material and the inherent porosity (courtesy of Dr A. Jones).

PGA is derived from a petroleum coke which is a by-product of the oil refining process. The coke filler particles are shown in Fig. 1.7 and are large needle shaped, these are generally aligned due to the extrusion process with the layer planes in PGA tending to lie parallel to the extrusion axis. PGA is an highly anisotropic graphite with very high levels of open porosity ($\sim 11\%$) [35].

1.4.2. Gilsocarbon

Gilsocarbon is made using Gilsonite coke particles. This coke is manufactured from a naturally occurring asphalt coke discovered in Utah, USA by Samuel Gilson in 1884 [31]. The asphalt is refined and the bi-product is the Gilsonite coke required.

The Gilsonite gives rise to large, spherical onion-like filler particles (Fig. 1.8) and is also characterised by areas of longitudinal porosity and gas evolution pores in the binder phase. Gilsocarbon is an isotropic graphite, and has a higher density and strength than PGA with less open porosity. The molding process means the coke particles are randomly orientated.

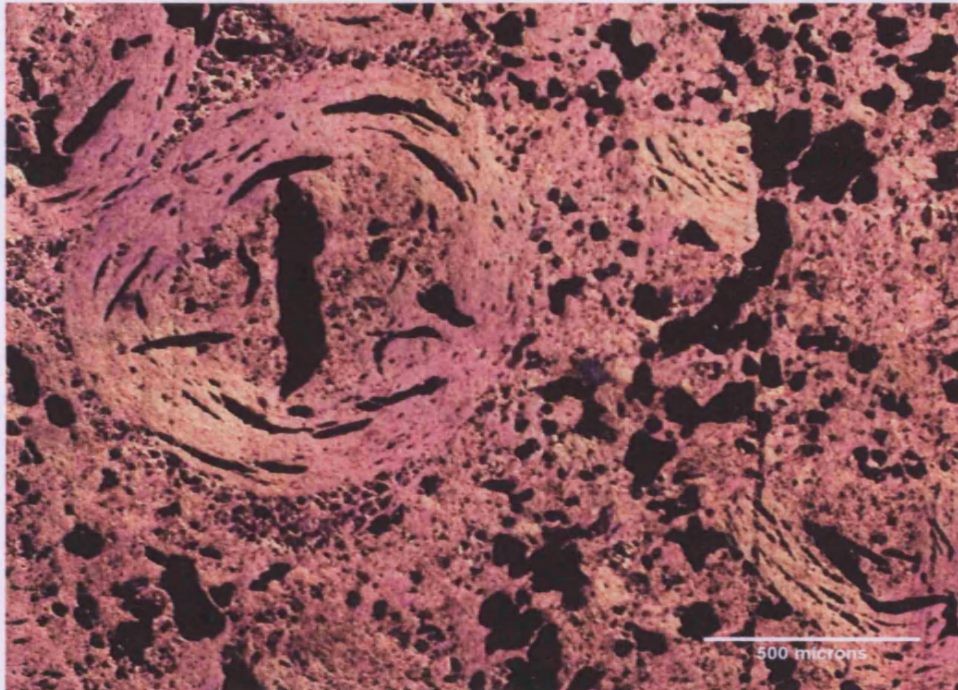


Fig. 1.8: A polarised optical micrograph of Gilsocarbon showing large onion-like spherical filler particle and many gas evolution pores (courtesy of Dr A. Jones).

1.4.3. Graphite in Generation IV Reactors

Graphite has been highlighted as a major component in the design for the future build of the Gen IV type very high temperature reactor (VHTR). The VHTR design is helium cooled and graphite moderated as well as using graphite in the fuel assembly [14]. Operating temperatures are predicted to be in the range of 1000 °C allowing the production of heat which can be used to produce hydrogen from water using various techniques as well as obviously generating electricity. Test reactors for the VHTR design are currently being built in China [36].

The fuel for these reactors involves the use of TRISO particles. These are multi-layered micro fuel particles consisting of a uranium dioxide core (0.5 mm) surrounded by a porous carbon buffer, a layer of silicon carbide and another layer of pyrolytic carbon. This TRISO particle is encased in a graphite matrix, giving a final spherical fuel sphere of approximately 60 mm diameter [37].

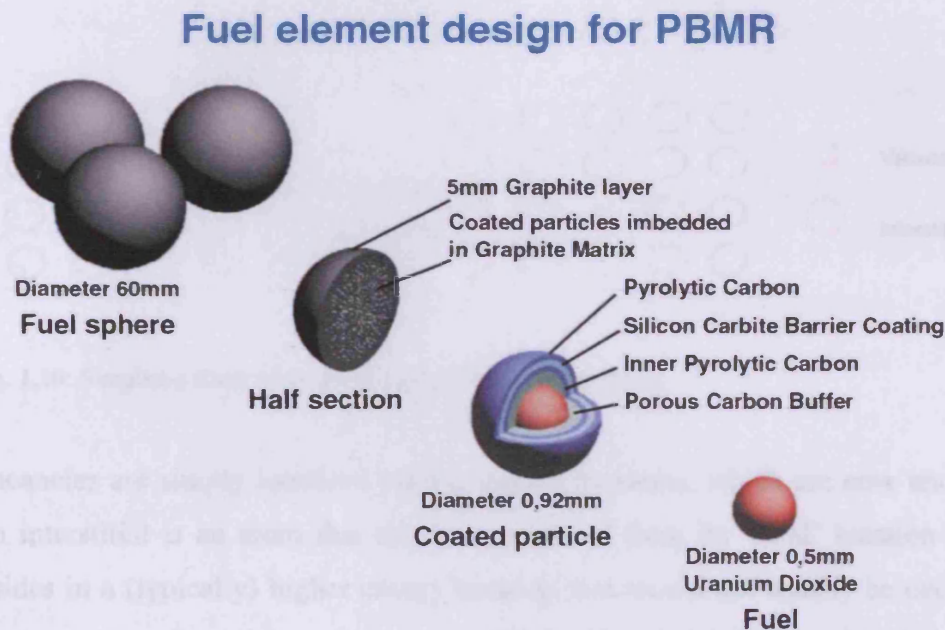


Fig. 1.9: Make-up of a TRISO fuel particle to be used in VHT reactors [38].

The use of graphite in this design means that it is important to understand its behaviour under high dose and high temperature and to understand the associated property changes [14].

1.5. Disadvantages of Graphite

1.5.1. Wigner Effect

Parallel to Enrico Fermi's pioneering work with CP-1, Eugene. P. Wigner and his team were busy working on constructing a large plutonium-producing pile. This work led Wigner to postulate that high energy neutrons would act as projectiles and would displace the carbon atoms within the graphite crystals from their equilibrium lattice

sites thus changing the properties and behaviour of the graphite in such a way as to adversely affect the operation of the reactor [39].

Early research carried out in metals showed that property changes in metals were due to the generation of point defects caused by irradiation. It wasn't long before this idea was applied to graphite. The two main types of defect associated with graphite irradiation are vacancies and interstitials shown simplistically in the diagram below.

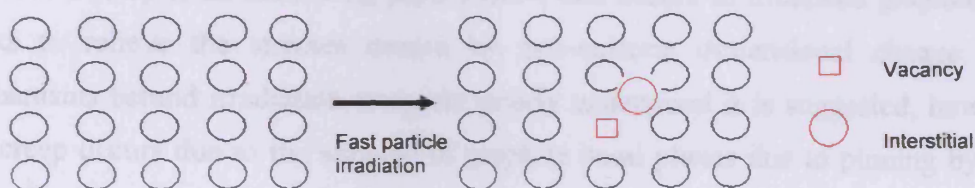


Fig. 1.10: Simplistic illustration of the formation of a Frenkel pair.

Vacancies are simply locations once occupied by atoms, which are now unoccupied. An interstitial is an atom that has been removed from its 'ideal' location and now resides in a (typically) higher energy location that would not usually be occupied by an atom. A nearby pairing of vacancy and interstitial is known as a Frenkel defect or Frenkel pair. It is the accumulation of Frenkel pairs and associated irradiation-induced defects that are believed to lead to the observed changes to the physical properties of graphite throughout the reactor lifetime [40].

Such defects lead to significant dimensional changes throughout the bulk of the graphite crystal and as a result properties such as thermal conductivity, electrical conductivity, elasticity and strength are affected [41-45].

Other interesting and important property changes include dimensional change, a change in the coefficient of thermal expansion (CTE) and irradiation creep. Dimensional change is an important aspect since it has a macroscopic effect on the graphite bricks, potentially challenging the integrity of the core structure. Radiation damage causes an expansion in the c-axis, due to the generation of interstitials, and a corresponding contraction in the a-axis, due to the collapse of vacancy defects and a

graphitisation process meaning that in order to reduce the affect of dimensional change a highly graphitised material should be chosen with larger crystallites. Direct measurements of the CTE of HOPG shows that it is an order of magnitude higher in the c-axis than in the a-axis [40]. CTE is temperature dependant and also dependant on the graphite crystallite size due to accommodating porosity. At temperatures below 300 °C the CTE in the c-axis decreases with dose, until it reaches a constant value whereas the CTE in the a-axis increases with dose [49]. The relationship between initial dimensional change rate and CTE has been found to be linear at low doses [50]. Irradiation creep is an interesting phenomenon that occurs in irradiated graphite and works to relieve the stresses caused by non-uniform dimensional change. The mechanisms behind irradiation creep are poorly understood it is suggested, however that creep occurs due to the slipping of graphite basal planes due to pinning by fast neutron irradiation and unpinning under load [51]. The general consensus is that the creep behaviour of graphite is closely related to the dimensional change [52], the CTE [53], Poisson's ratio [54] and Young's modulus [55].

1.5.2. Wigner Energy

An important consequence of neutron irradiation of graphite is the build up of internal, stored energy known as Wigner energy. As mentioned, this is a form of potential energy associated to the displaced atoms residing in non-ideal locations as a result of the neutron-atom interactions. When enough Wigner energy is stored in a graphite system then it becomes a possible hazard since there is the potential for the energy to suddenly release itself in the form of heat. This can occur when the interstitial atoms overcome their thermodynamic barrier to recombination, resulting in Frenkel pair annihilation and the subsequent release of energy.

Wigner energy release has been linked to the Windscale disaster of 1957, where the temperature of the graphite core rose considerably and rapidly, damaging the fuel cladding and consequently oxidising the uranium, resulting in a fire [17]. Since then the dangers surrounding Wigner energy release have been of concern to those in the nuclear community and the processes involved in its build up and release have been of general scientific interest. The accumulation of Wigner energy can be controlled by carefully heating the graphite components so as to release any built up Wigner energy

in a controlled and safe manner, this process known as annealing was commonly used in industry to overcome the risks involved; however in the case of the Windscale disaster erroneous temperature readings meant that this could not be done effectively [17], leading to rapid damage to the fuel cladding and subsequent oxidising of the uranium fuel.

The annealing of graphite means that Wigner energy is only really of concern in reactors operating below ~ 130 °C, since above this temperature Wigner energy would not accumulate as it would be instantly annealed out [56] and therefore graphite components of the Magnox (PGA) and AGR fleets (Gilsocarbon) can be disposed of without considering the effect of Wigner energy, however the earlier test and plutonium production reactors, employed particularly in the UK, operated at much lower temperatures; meaning that the graphite used is susceptible to Wigner energy accumulation. Other low temperature reactors include Oak Ridge X-10 and the French G-1 reactors [57]. A build-up of Wigner energy becomes a problem for those concerned with the decommissioning of these graphite cores since if some external event or some internal chemical reaction causes the temperature of the graphite to increase then a significant release of Wigner energy can occur [58]. Under certain conditions the temperature can rise above the specific heat capacity of the graphite resulting in a self-sustaining release of Wigner energy [56], posing a danger to those involved with its handling. Samples of graphite have been found to contain as much as ~ 2700 Jg⁻¹ of stored, Wigner energy, which if all released at once could theoretically lead to a temperature rise of ~ 1500 °C assuming adiabatic conditions. For these reasons some authors have deemed it unacceptable to store or dispose of graphite containing significant releasable stored energy, such graphite should be annealed to remove the energy which could cause self-heating [59]. The release of stored energy in the repository may damage the repository leading to the possibility of water easily leaching into the waste.

1.5.3. Graphite Waste

The UK has the largest inventory of irradiated graphite, with approximately 94,000 tonnes, 81,000 of which is intermediate level waste assumed to require deep geological disposal. Graphite waste is problematic due to the significant amounts of

long-lived radionuclides such as ^{14}C and ^{36}Cl , and in some cases the potential risk of releasing stored Wigner energy. These issues must be considered if an effective long-term waste management program is to be established [60] Presently there is no internationally accepted solution for dealing with graphite waste. Because of the safety issues raised by potential Wigner energy release, UK Nirex Ltd, responsible for managing the waste from Windscale Pile 1, has assessed in detail the significance of Wigner energy and have developed models and appropriate disposal concepts to deal with any safety concerns [61]. Some authors deem it possible to store and dispose of graphite waste containing stored energy by using non-grouted packages since it is the overheating of the packaging caused through the release of stored energy as the grout exothermic reaction takes place that is the issue; potentially causing the packaging to become damaged.

1.6. Scientific Proposal

This project will involve ion irradiating samples of nuclear grade graphite, predominately Magnox PGA, with a reference material of highly-orientated pyrolytic graphite (HOPG) in an attempt to simulate the affects of neutron irradiation. Using ions to induce damage into materials is a proven concept which has the advantage, in this case, of not producing any radioactive isotopes within the graphite thus eliminating the need for expensive laboratory equipment to handle and prepare the samples. Ion irradiation is also relatively simple and can be carried out with standard vacuum equipment at relatively low cost. Ion irradiation will induce damage into the graphite system allowing for a thorough investigation into its effects, particularly on the microscopic level, focussing on the breakdown of lattice structure and the possible generation and release of stored, Wigner energy.

1.7. Summary

The behaviour of graphite under irradiation is well documented, however despite this further knowledge is required in order to understand the fundamental processes occurring on the atomic scale. Wigner energy, its accumulation and release, is still really poorly understood and even though the majority of graphite moderated nuclear reactors used have operated at high enough temperatures so as to reduce its impact

significantly, there are still a few thousand tonnes of graphite worldwide which may require treatment and disposal in order to remove the high levels of Wigner energy. The IAEA and the National Decommissioning Authority (NDA) highlight that Wigner energy is a potential safety risk and as a result a scientific study into its build-up and release can be of great importance not to mention of scientific interest generally. Other aspects of irradiation-induced damage will also be studied extensively in order to understand the loss of crystallinity and the tendency towards amorphisation. The recovery of such damage will be monitored through systematic annealing of the samples, thus allowing recovery mechanisms to be analysed.

1.8. References

- [1] National Decommissioning Authority, 'Final Waste Issues Group Report' (2007).
- [2] www.knoo.org (last accessed 21-09-2010).
- [3] W.E. Stephens, 'Nuclear Fission and Atomic Energy', Inman Press (2007).
- [4] <http://history1900s.about.com/cs/people/p/fermi.htm> (last accessed 21-09-2010).
- [5] O. Hahn, F. Strassmann, *Naturwissenschaften*, **27** (1939) 11.
- [6] www.nobelprize.org (last accessed 21-09-2010).
- [7] E. Fermi, 'Possibility of a Chain Reaction, USAEC Report CP-383', University of Chicago, (1942).
- [8] E. Fermi, *Am. J. Phys.*, **20** (1952) 536.
- [9] R. Michal, 'Fifty years ago in december: Atomic reactor EBR-1 first produced electricity', (www.ans.org) (2001) (last accessed 24-02-2011).
- [10] Idaho National Laboratory, 'EBR-1 Factsheet', www.inl.gov (last accessed 21-09-2010)
- [11] T. Findlay, 'The future of Nuclear Energy to 2030 and its Implications for Safety, Security and Non-Proliferation', The Centre for International Governance Innovation (CIGI), Ontario, (2010).
- [12] A. Theodosiou, A.F. Carley, S.H. Taylor, *J. Nucl. Mat.*, **403** (2010) 108.
- [13] www.ne.anl.gov/images/activ/programs/geniv/picture1.jp (last accessed 21-09-2010)
- [14] T. Abram, S. Ion, *Energy Policy*, **36** (2008) 4323.
- [15] <http://www.iaea.org/cgi-bin/db.page.pl/pris.powrea.htm?country=GB>, (last accessed 12-09-2010)

- [16] www.ukaea.co.uk (last accessed 15-09-2010)
- [17] L. Arnold, 'Windscale 1957: Anatomy of a Nuclear Accident', Palgrave Macmillan, London, (1992).
- [18] www.world-nuclear.org (last accessed 21--09-2010).
- [19] Springfields Fuels Limited, 'The Magnox Story' (www.nuclearsites.co.uk) (2008) (last accessed 21-09-2010).
- [20] P. Breeze, 'Power Generation Technologies', Elsevier, Oxford, (2005).
- [21] www.nucleartourist.com (last accessed 20-09-2010).
- [22] G. Holt, 'Radioactive graphite management at UK Magnox nuclear power stations', British Nuclear Fuels Ltd., Berkeley, UK (undated).
- [23] T.D. Burchell, Nuclear Graphite and Radiation Effects, 'Encyclopedia of Materials: Science and Technology', Elsevier Science Limited (2001).
- [24] P.F. Nichols, E.M. Woodruff, 'Nuclear Properties', in: R.E. Nightingale (Ed.) 'Nuclear Graphite', Academic Press, New York and London, (1962).
- [25] W.M. Stacey, 'Nuclear Reactor Physics', Wiley-VCH, (2007).
- [26] C.A. Switzer Jr, L.H. Juel, Machining Practice, in: R.E. Nightingale (Ed.) 'Nuclear Graphite', Academic Press, New York and London, (1962).
- [27] R.E. Nightingale, 'Graphite in the Nuclear Industry', in: 'Nuclear Graphite', Academic Press, New York and London, (1962).
- [28] E. Fermi, 'Report for Month Ending December 15, 1942', Physics Division, USAEC Report CP-387, University of Chicago, (1942).
- [29] J. Emsley, 'Nature's Building Blocks', Oxford University Press, (2001).
- [30] W.P. Eatherly, E.L. Piper, 'Manufacture', in: R.E. Nightingale (Ed.) 'Nuclear Graphite', Academic Press, New York and London, (1962).
- [31] A. Jones, B. Marsden, Nuclear Graphite Manufacture, Microstructure and Unirradiated Properties, (2009).
- [32] G. Hall, B. Marsden, A. Fok, *The Nuclear Engineer*, **45** (undated) 128.
- [33] H. Marsh, J. Griffiths, 'Ext. Abstracts International Conference on Carbon', Toyohashi, Japan, (1982).
- [34] H. Marsh, 'Introduction to Carbon Science', Butterworth-Heinemann, (1989).
- [35] J.H.W. Simmons, 'Radiation Damage in Graphite', Pergamon Press, Oxford, (1965).
- [36] Z. Zhang et al. '2nd International Topical Meeting on High Temperature Reactor Technology', Beijing (2004).

- [37] M. L. Pritchard, 'Analysis of the pebble-bed VHTR spectrum shifting capabilities of advanced fuel cycles', PhD Thesis, Texas A&M University(2006).
- [38] <http://blogs.princeton.edu/chm333/f2006/nuclear/trisoball.jp> (last accessed 20-09-2010).
- [39] E.P. Wigner, USAEC Report CP-387, University of Chicago (1942).
- [40] B.T. Kelly, 'Physics of Graphite', Applied Science Publishers, London, (1981).
- [41] R.E. Nightingale, H.H. Yoshikawa, E.M. Woodruff, 'Radiation-induced Structural and Dimensional Changes', in: R.E. Nightingale (Ed.) 'Nuclear Graphite', Academic Press, New York and London, (1962).
- [42] H.H.W. Losty, 'Radiation Effects on Mechanical Properties', in: R.E. Nightingale (Ed.) 'Nuclear Graphite', Academic Press, New York and London, (1962).
- [43] R.E. Nightingale, 'Radiation Effects on Electrical and Thermal Properties', in: R.E. Nightingale (Ed.) 'Nuclear Graphite', Academic Press, New York and London, (1962).
- [44] R.E. Nightingale, H.H. Yoshikawa, H.H.W. Losty, 'Physical Properties', in: R.E. Nightingale (Ed.) 'Nuclear Graphite', Academic Press, New York and London, (1962).
- [45] T. Maruyama, T. Kaito, S. Onose, I. Shibahara, J. Nucl. Mater., 225 (1995) 267.
- [46] B.T. Kelly, Carbon, 20 (1982) 3.
- [47] B.T. Kelly, W.H. Martin, P.T. Nettley, Phil. Trans. Roy. Soc. Lond. A, 260 (1966) 37.
- [48] J.E. Brocklehurst, B.T. Kelly, Carbon, 31 (1993) 155.
- [49] H. Bridge, Carbon, 2 (1964) 83.
- [50] J.H.W. Simmons, 'The effects of irradiation on the mechanical properties of graphite in third conference on Carbon', 1959, Buffalo, Pergamon Press, New York, (1959).
- [51] B.T. Kelly, J.E. Brocklehurst, J. Nucl. Mat., 65 (1977) 79.
- [52] B.T. Kelly, T.D. Burchell, Carbon, 32 (1994) 119.
- [53] B.T. Kelly, Carbon, 30 (1992) 379.
- [54] R.J. Price, 'Review of irradiation induced creep in graphite under HTGR conditions', General Atomic Report, GA-A16402 (1981).
- [55] T. Oku, K. Fujisaki, M. Eto, J. Nucl. Mat., 152 (1988) 225.
- [56] B.T. Kelly, B.J. Marsden, K. Hall, D.G. Martin, A. Harper, A. Blanchard, 'Irradiation damage in graphite due to fast neutrons in fission and fusion systems', IAEA-TECDOC-1154, (2000).

[57] R.E. Nightingale, 'Stored Energy', in: R.E. Nightingale (Ed.) 'Nuclear Graphite', Academic Press, New York and London, (1962).

[58] Environmental Agency, 'Wigner Energy in Irradiated Graphite and Post-Closure Safety', R&D Technical Report P3-80/TR (2002).

[59] B.J. Marsden, A.J. Wickham et al., 'Characterization, Treatment and Conditioning of Radioactive Graphite from Decommissioning of Nuclear Reactors', IAEA-TECDOC-1521 (2006).

[60] Large & Associates, Report ref: R3069-A5 (2008).

[61] R.M. Guppy, J. McCarthy, S.J. Wisbey, 'Technical Assesment of the Significance of Wigner Energy for Disposal of Graphite Wastes from the Windscale Piles', in. Proceedings of the Technical Committee Meeting 'Nuclear Graphite Waste Management', IAEA, Manchester, (1999).

Chapter 2

Experimental

2.1. Introduction

The irradiation of solids by charged particles has been an area of scientific interest for some time; with early experiments involving only low energy radiation. However, these early experiments led to such discoveries as the phenomenon of sputtering, the process by which solid atoms are ejected into the gas phase following the impact of highly energetic ions [1]. Such observations were made as early as 1852 by Sir William Grove who created the worlds first sputter deposited metal film, describing the process as “cathodic disintegration” [2].

Since the discovery of radioactivity in 1896 by Henri Becquerel [3], and therefore the availability of higher sources of energy, many bulk affects have also been observed. Insights into bulk irradiation damage were achieved early on, with early work carried out by Joly [4] relating the pleochoric holes in minerals such as mica to bombardment damage due to radioactive elements. Shortly after the building of the first of nuclear reactor in 1942 much work was done both experimentally and theoretically on the effects of radiation on solids in general [5-6]. However, with the role of graphite in the nuclear field becoming prominent, the affects of radiation of graphite became a focal point of scientific research.

The invention of the mercury vapour diffusion pump by Wolfgang Gaede in 1913 [7] (subsequently improved by Irving Langmuir) allowed much lower pressures than those previously used experimentally by Thompson and others working in the mass spectroscopy field. Further modifications by Cecil Burch in 1928 used low-vapour pressure oils to achieve even lower pressures [8]. After the second world war, Kai Siegbahn and others [9] employed this technology and built the first ESCA (electron spectroscopy for chemical analysis) high vacuum spectrometer capable of carrying out what is now known as X-ray Photoelectron Spectroscopy (XPS) [10]. Modified versions of this original instrument are still used today, with UHV technology being widely used in many scientific fields, particularly in physical chemistry and surface science.

2.2. Ultra High Vacuum (UHV)

2.2.1. The Ion Bombardment Vacuum Chamber

In order to carry out the ion irradiation of graphite effectively, it is necessary to achieve high vacuum conditions in order to minimise contamination and allow for effective ion bombardment of the graphite samples. In order to do this a custom designed UHV chamber was built at Cardiff University, specifically to irradiate small samples with inert gas ions. The system used (Fig. 2.1) was constructed from UHV compatible stainless steel and used an oil diffusion pump to achieve the low pressures required. Although theoretically UHV is not essential for successful ion impact, the acquisition of even lower pressures can only provide a cleaner system, and hence improve the experimental environment.

The system is equipped with an ion sputtering gun, fast entry lock for rapid sample turn around and a sample probe (with a custom sample holder constructed in-house) with the facility to cool and heat the sample between 80 K and 700 K. A gas line has also been set up to facilitate the transfer of the irradiating gas from the gas cylinder, straight into the ionization chamber within the ion gun.

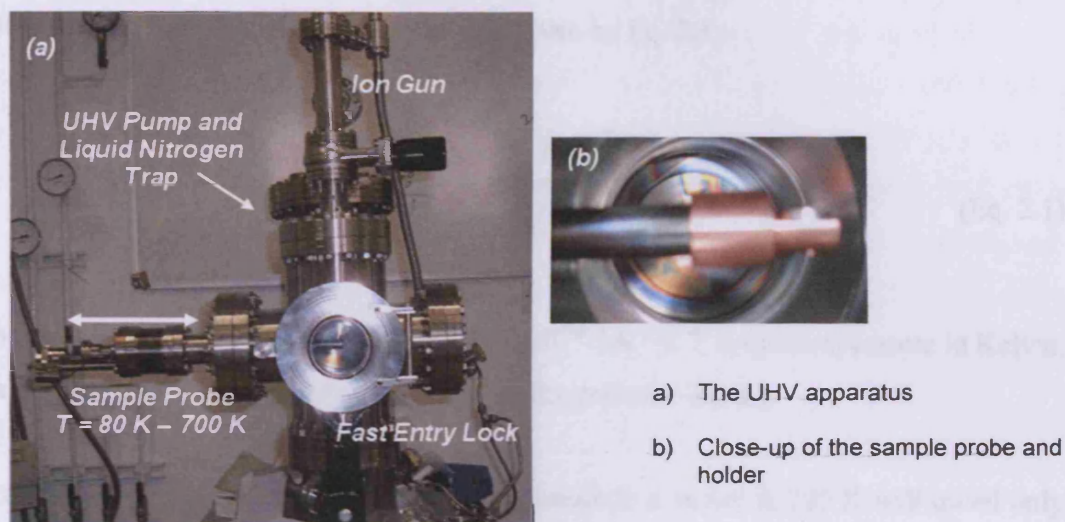


Fig. 2.1: Custom built UHV chamber used for ion irradiation.

2.2.2. Vacuum Theory

A vacuum environment is considered to be at UHV when the pressures are lower than 10^{-8} mbar ($\sim 10^{-6}$ Pa). Table 2.1 summarises the different degrees of vacuum [11]:

Table 2.1: Definition of vacuum regimes [11].

Definition	Pressure (mbar)
Low Vacuum	$10^3 - 1$
Medium Vacuum	$1 - 10^{-3}$
High Vacuum (HV)	$10^{-3} - 10^{-8}$
Ultra High Vacuum (UHV)	$10^{-8} - 10^{-12}$
Extreme High Vacuum (XHV)	$< 10^{-12}$

At UHV pressures the behaviour of molecules is significantly different from that at 'normal' atmospheric pressures (1000 mbar), especially in relation to the molecules' mean free path.

The mean free path of a molecule is the average (mean) distance traveled by a molecule before it collides with other particles, and is given by Eq. 2.1:

$$\ell = \frac{k_B T}{\sqrt{2} \pi d^2 p} \quad (\text{Eq. 2.1})$$

Where k_B is the Boltzmann Constant ($1.381 \times 10^{-23} \text{ J.K}^{-1}$), T is the temperature in Kelvin, d is the diameter of the molecule (m) and P is the pressure (mbar).

At atmospheric pressure (10^3 mbar) a N_2 molecule in a vessel at 295 K will travel only 6.6×10^{-6} cm before colliding with another molecule; however at UHV (10^{-10} mbar) the same molecule could travel, on average, 660 km before colliding with another molecule. That is, as the pressure decreases the mean free path increases in a linearly proportional manner [12].

The most important effect on the level of vacuum within a system is the behaviour of the gas molecules inside. The Knudsen number (K_n), named after Danish physicist Martin Knudsen, is a measure of the ratio between the mean free path of a molecules and a representative length scale. It is written as follows [12]:

$$k_n = \frac{\lambda}{L} = \frac{k_B T}{\sqrt{2} \pi d^2 P L} \quad (\text{Eq. 2.2})$$

λ is the mean free path of the molecule in meters and L is the representative length scale of the system in meters.

When $\lambda \gg L$, that is $K_n \gg 1$, the molecules within the system will have a mean free path comparable to the length scale of the system. This means that the molecules predominately collide with the walls of the chamber and do not follow a uniform trajectory, instead the molecules move around from wall to wall in a random fashion and

are therefore pumped away differently; that is, they are not physically pulled in towards the pump (as in a vacuum cleaner for example) but instead are pumped away when the molecules collide with the pump and get trapped in it. From this, it follows that the diameter of the various pipes, flanges etc. must be taken into consideration, since the diameter of the inlet flange to the pump will have a direct effect on the pumping speed. It can be calculated that for pressures below 2×10^{-3} mbar the mean free path becomes such that, in the smallest diameter flanges and pipes typically used in UHV (34 mm nominal), collisions with the system walls predominate and we can say that the gas has entered free molecular flow [12].

2.2.3. Achieving UHV Conditions

In order to achieve such low pressure conditions specialised equipment must be used, with different options available for different applications. Tightening of the steel bolts must be done with care, making sure that even pressure is applied to the gasket all the way around so as to create a strong metal-metal seal. When handling the internal equipment in the chamber gloves should be used to avoid any grease contaminating the internal surfaces. A variety of pumps can be used to achieve UHV conditions, each of them operating in a different way; this project used only one custom-built vacuum system (Fig. 2.1) which used a diffusion pump to achieve the low pressures.

2.2.3.1. Diffusion Pump

The diffusion pump used in this system was an Edwards EO4 oil diffusion pump and the oil used in this pump was Santovac 5[®] which is a polyphenyl ether with a boiling point of 476.1 °C at atmospheric pressure [13] and a vapour pressure at 25 °C equal to $\sim 4.0 \times 10^{-10}$ torr ($\sim 5.33 \times 10^{-10}$ mbar) [13].

The basis of a diffusion pump is described in detail elsewhere [12], but put briefly, oil is heated from the bottom, causing the molecules to evaporate and rise. They then get deflected downwards at high speeds where they interact with the gas molecules nearby

dragging them down towards the exhaust where they are pumped away by the backing pump. That is, for a diffusion pump to work effectively it must be 'backed' by another pump which works to carry away the gaseous molecules. Typically, a standard rotary vane pump is used for this. Oil is not lost since the perimeter of the diffusion pump is water cooled, causing condensation of the molecules as they reach the sides. Before a diffusion pump can be used the system must be brought down from atmospheric pressure to a pressure of $10^{-2} - 10^{-3}$ mbar; this is achieved through a simple rotary vane pump.

2.2.4. Monitoring the System Pressure

To monitor the pressure in a vacuum system, two types of gauge are commonly used: pirani gauges and ionization gauges (based on the Bayard-Alpert design). Firstly, a pirani gauge is used to measure relatively higher pressures in the region of $0.5 - 10^{-3}$ mbar. They are typically connected to the backing / rotary pumps and are used to measure the roughing pressure generated by these. Ionisation gauges measure pressures in the range 10^{-3} mbar - $<10^{-10}$ mbar. More information on the operation of pirani gauges and ionization gauges can be found elsewhere [12]. The ion bombardment chamber at Cardiff was equipped with a VG ZVIG-22 hot-cathode ionisation gauge, which is of a Bayerd-Alpert design and fitted with tungsten filaments.

2.2.5. Operating the Vacuum System

2.2.5.1. Baking the System

In order for the system to pump down to UHV effectively it is first necessary to bake the system. Baking involves heating the entire system, whereby at elevated temperatures it is far easier for surface adsorbed molecules to desorb and get pumped away. Also any gas molecules and contaminants present within the bulk of the stainless steel can diffuse more rapidly to the surface, where they too can desorb and get pumped away. The baking temperature used can vary from system to system but between $100\text{ }^{\circ}\text{C}$ and $200\text{ }^{\circ}\text{C}$ for a period of approximately 24 hours is typical. Temperatures exceeding $100\text{ }^{\circ}\text{C}$ are required

in order to remove the water vapour that is inevitably present. However, care is taken not to reach too high temperatures as damage to the seals, joints etc becomes a possibility. There are also safety issues involved with leaving such a large system at such high temperatures, unattended overnight.

Bakeout is required in order to tackle the problem of outgassing. Stainless steel is permeable to many molecules with others easily adsorbing onto the surface. It is the desorption of these molecules that can lead to pressures staying relatively high. An appropriate bakeout can reduce outgassing rates by more than three orders of magnitude, resulting in pressures of 10^{-10} mbar and below. Typical gasses that tend to outgas from the steel chamber are H_2 , O_2 , CH_4 , CO and H_2O (water vapour) [12]. Another obstacle to even lower pressures is the diffusion of hydrogen, from the atmosphere, through the stainless steel and into the vacuum environment. Hydrogen from the air can easily permeate through the system walls, more so as the pressure decreases. This can become significant at UHV and stops the pressures from getting even lower.

In order to bake the ion bombardment chamber at Cardiff, the system is covered in heating tape which can be heated through electrical resistance up to approx 160 °C. Care is taken to ensure that the tape is distributed around the system in equal quantities all over to produce the same level of heating to all parts of the system. This is important as a cooler area, known as a cold-spot, may act to re-adsorb some of the desorbed molecules, thus counteracting the effect of the pump. These molecules will then re-distribute themselves around the system when the system cools back down, thus leading to a slightly elevated pressure. Aluminium foil is used to cover the heating tape, acting as a heat insulator. The heating tape is switched on and a thermostat is used to monitor the temperature; the system is then left for approximately 24 hours whilst being continually pumped.

2.2.5.2. Loading a Sample

To load a new sample the system is isolated from the diffusion pump and vented with inert gas, typically N₂. The sample is placed inside the sample holder (Fig. 2.2) and loaded into the system, so that it is sitting directly underneath the ion gun. As always, gloves are used to minimize contamination. Once in place the front door is closed and the system is roughed down to 10⁻² mbar, before being opened up again to the diffusion pump where it is pumped down to UHV conditions.

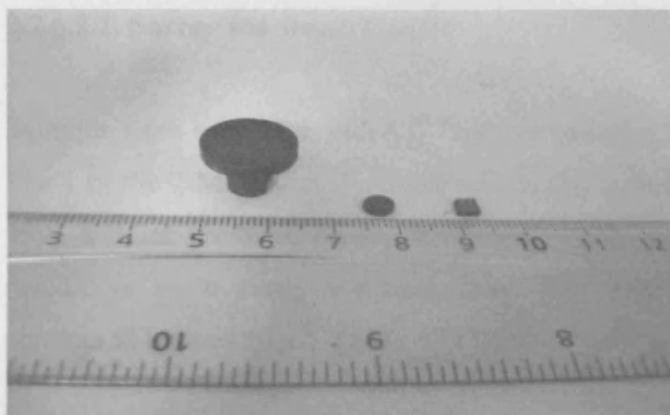


Fig. 2.2: From left to right: custom made graphite sample holder, typical PGA disc used, and a piece of HOPG.

2.2.6. Methods of Sample Irradiation

The effective ion irradiation of graphite forms the basis of this project and thus it follows that the method of ion irradiation and the various parameters such as ion energy, sample current and total fluence play a very important part of this study. A variety of different techniques were utilised in order to irradiate the graphite samples, the majority of the work being carried out in Cardiff, whilst the higher energy work was carried out at the Ion Beam Centre in Surrey and at the Institute of Nuclear Physics, at the Université de Lyon, France. A brief description of the different methods of sample irradiation, and the equipment used is outlined below.

2.2.6.1. Cold-Cathode Ion Gun

A VG AG2 ion gun was used extensively to irradiate the samples in the custom built vacuum chamber at ion energies between 1- 5 keV. The gun is specifically designed to be UHV compatible and is placed at the top of the system, directly above the sample, such that the ion beams strike the sample normal to the surface.

2.2.6.2. Higher Energy Facilities (See Chapter 6)

2.2.6.2.1. Surrey Ion Beam Centre

Samples were irradiated with C^{+++} ions of energies 200 keV, 400 keV and 800 keV on line 1 of the 2 MeV Van de Graaff accelerator at Surrey. The implanter was installed in 1991 and has produced beams of many types of ion up to 4 MeV with excellent mass resolution, beam purity and uniformity. The machine is capable of achieving beam currents as high as $50 \mu A$ [14].



Fig. 2.3: Photograph of the high-energy ion implanter at the Surrey Ion Beam Centre.

2.2.6.2.2. Université de Lyon, France

Some samples were irradiated in France at the Institute of Nuclear Physics, Université de Lyon. Samples were irradiated on the Van De Graaff facility with high energy He^{++} and Ar^{+++} ions, the multiple charging is required in order to achieve the high energies of 7.5 and 8.0 MeV respectively. The system produces highly pure ion beams able to uniformly irradiate a surface of 1.0 cm^2 . The Van De Graaff generator is housed upstairs and the ions are projected downwards before being deflected 90° and focused towards the sample.

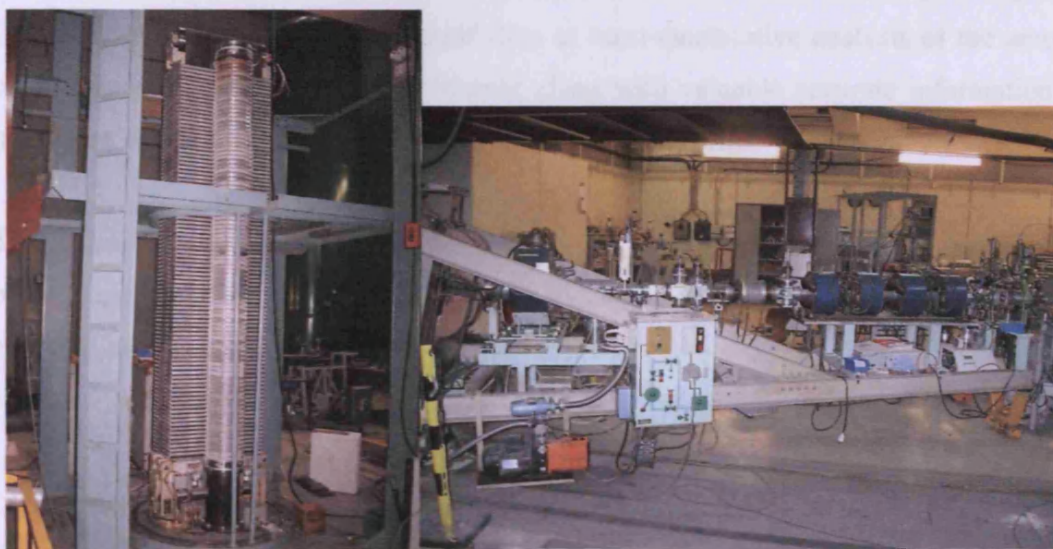


Fig. 2.4: (left) Van De Graaff generator housed upstairs and (right) the beam line at 90° to the generator. The samples are held to the far right of the picture at the end of the beam line.

2.3. Characterisation Techniques Employed – Spectroscopic and Analytical

Within this project a variety of different spectroscopic and analytical techniques were utilised in order to gain valuable information on the effect of sample irradiation. Raman spectroscopy was used extensively to gain information on the irradiation induced damage to the graphite, whilst other techniques included differential scanning calorimetry which was used to detect any heat release in the samples after irradiation, due to irradiation induced stored energy build-up. X-ray diffraction and x-ray photoelectron spectroscopy

were used to probe for bulk and surface information respectively and microscopy was utilised to try and achieve a visualisation of the any ion damage at the atomic scale.

2.3.1. Raman Spectroscopy

2.3.1.1. Background/Theory

Raman spectroscopy is a spectroscopic technique that uses the interaction of monochromatic light (typically from a laser) with a molecule, to analyse the vibrational, rotational and other low-frequency modes of that system. A characteristic spectral pattern (“fingerprint”) is generated and quantitative or semi-quantitative analysis of the amount of substance in a sample can be obtained along with valuable accurate information on molecular bonding i.e. chemical structures and physical forms.

The technique is based upon the principle of the inelastic scattering of light; a phenomenon that has been known about since the 1920's. Smekal [15] was the first to hypothesise the idea in 1923 and five years later the theory was experimentally proven by Raman and Krishnan [16] using sunlight focused by a telescope.

Light (photons) can either be absorbed by matter, scattered by it or can just pass straight through. For adsorption to occur the wavelength, and therefore the energy, of an incoming photon must correspond to the energy gap between the ground state and the excited state of a particular molecule within the sample; it is this change that is typically measured in adsorption spectroscopy. However, for scattering to occur this is not the case. The incident photon can interact with the target system, such that it is either scattered elastically or inelastically. During this event, the photon polarizes the electron cloud thus creating a short-lived higher energy state which is inherently unstable. This state quickly decomposes back down to lower energy, re-emitting the photon.

Elastic scattering involves the interaction with the electron cloud only, causing a very small change in the photons frequency; this tends to be the dominant process in scattering

events and is known as Rayleigh scattering, the process responsible for the blue colour of the sky. However, sometimes (one in every $10^6 - 10^8$ events) the incoming photon can interact with the nuclei so as to induce nuclear motion; due to the larger mass of the nuclei a significant energy change is involved and the process is therefore inelastic, and it is this process that defines Raman scattering [17].

Upon Raman scattering the subsequent energy change can either be higher or lower, depending on the initial vibrational state of the molecule. If the molecule initially existed in the ground state, then Stokes scattering occurs, but if the molecule initially existed in a vibrationally excited state then anti-Stokes scattering occurs. The processes of Rayleigh and Raman (both Stokes, and anti-Stokes) scattering are illustrated below (Fig. 2.5).

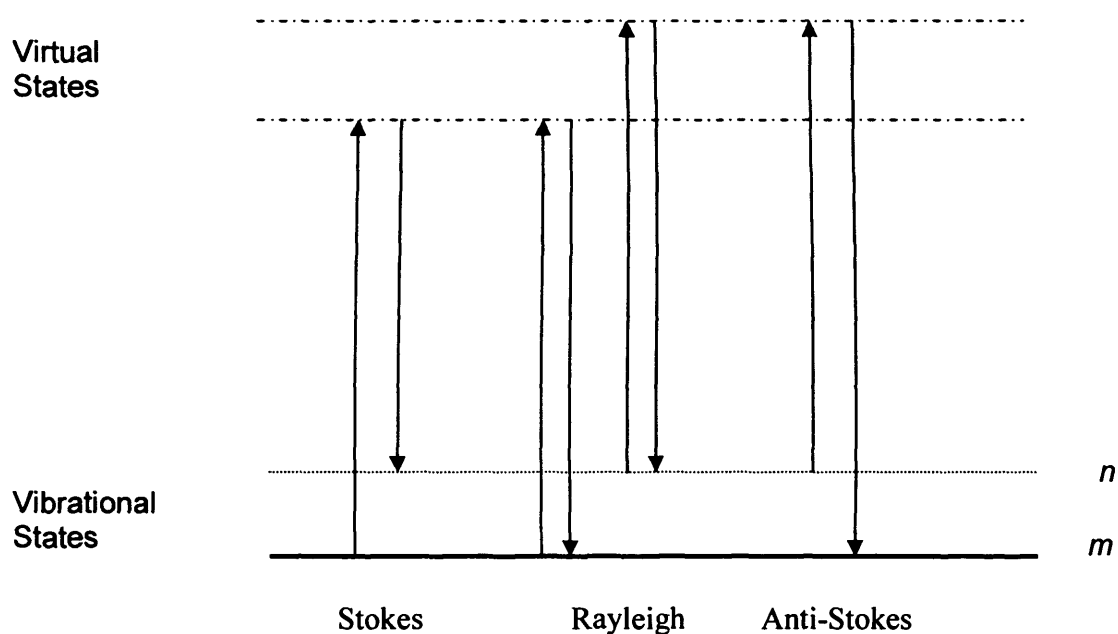


Fig. 2.5: A diagram of the energy changes involved in the various photon scattering processes.

In either case, as stated previously, the energy of the virtual state is defined by the energy of the incoming laser. It is also essential to note that the majority of Raman scattering will consist of Stokes Raman scattering. This can be simply explained by the fact that most molecules at rest, and at room temperature, prior to interaction with the laser, are more likely to exist in the ground vibrational state.

2.3.1.1.1. Molecular Vibrations

With molecular vibrations being the main focal point of Raman spectroscopy, Hooke's law (Eq. 2.3) is both very important and practical for interpreting Raman spectra. It gives the relationship between frequency, the mass of the atoms involved in a particular vibration, and the bond strength for a particular diatomic molecule:

$$\nu = \frac{1}{2\pi c} \sqrt{\frac{K}{\mu}} \quad (\text{Eq. 2.3})$$

ν is the frequency of the vibration, c is the velocity of light, k is the force constant between two masses (A and B) and μ is the reduced mass ($[m_1 \times m_2 / (m_1 + m_2)]$) of those two masses (A and B).

Hooke's law allows us to understand why the lighter the involved atoms are, the higher the frequency of the vibration will be (*i.e.* C-H vibrations are located around 3000 cm^{-1} , whilst C-I vibrations occur around 500 cm^{-1}). Also, as the force constant is a direct measure of bond strength, the stronger the bond, the higher the frequency will be [17]. Overtone vibrational modes can also be observed at higher frequencies, these will be discussed in more detail later.

2.3.1.2. Applications

The applications for Raman spectroscopy are not as extensive as those for Infra-Red spectroscopy. However Raman can be more effective for studying organic compounds, particularly those with double bonds which tend to be relatively weak in Infra-Red. With regards to this project, only graphite is being studied and Raman spectroscopy has been shown to be very effective for this, as illustrated by the large body of work in the literature. Raman is employed in this project as an effective means of measuring the C-C

vibrations in the graphite lattice, and how they change with ion irradiation. Analysing and interpreting these changes provides useful information on the nature of the ion effects on the system.

2.3.1.3. Instrumentation

Raman measurements were carried out using a LabRam HR confocal microscope from Horiba Jobin Yvon Ltd. Incident illumination of 514.5 nm was provided by a 10 mW cw-Ar laser and any annealing effects were considered negligible due to the relatively low power used [18]. The microscope was equipped with a $\times 50$ long working distance objective lens with a numerical aperture of 0.55 and a working distance of 8.1 mm producing a spot size of 1.4 μm . A $\times 10$ condenser lens with a focal length of 300 mm was used to focus the laser onto the objective lens. A 1024 pixel CCD peltier cooled detector was used to detect the scattered radiation. The resultant Raman spectra was analysed via the Labspec 5.0 software program. A Lorentzian lineshape was assumed for all peaks and accurate peak intensities were obtained through numerical decomposition by fitting a polynomial curve to the data set and subtracting such that the baseline was zero.

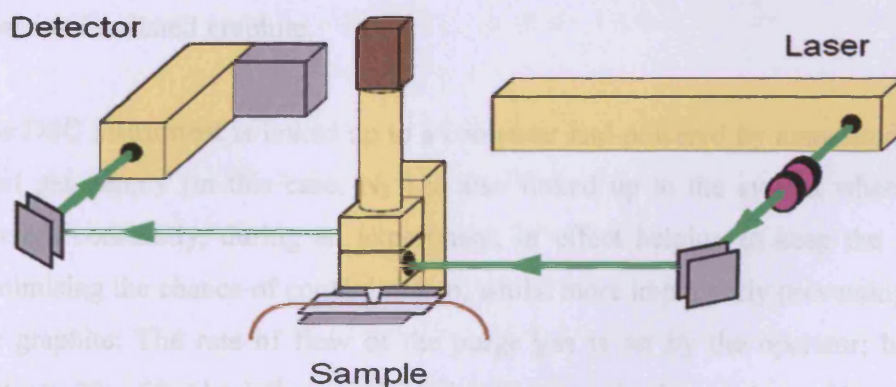


Fig. 2.6: Simplistic schematic of a typical Raman setup [20].

When conducting the Raman analysis the irradiated samples used are HOPG (5.0 mm x 5.0 mm x 3.0 mm), unless stated otherwise. This is because polycrystalline graphites tend to be inhomogeneous causing difficulties when trying to obtain consistent Raman data at various positions on the surface [19].

2.3.2. Differential Scanning Calorimetry (DSC)

2.3.2.1. Background/Theory

DSC is a thermoanalytical technique which investigates the flow of heat throughout a sample. That is, DSC can provide information about heat loss or heat gain during physical transformations such as phase transitions. DSC requires a reference to be used alongside the sample being studied. The technique works by increasing the temperature of both the reference and the sample at the same rate, generally in a linear fashion with respect to time. At some point during heating the sample may undergo a phase transition; this will either require a greater, or lesser, amount of heat flow into the sample with respect to the reference; depending on whether the process involved is endothermic or exothermic respectively [21]. DSC has a vast variety of applications; however, in the context of this work it is used solely as a means of detecting any exothermic heat releases from ion irradiated graphite.

The DSC instrument is linked up to a computer and powered by associated software. An inert gas supply (in this case, N₂) is also linked up to the system where it is purged through constantly, during an experiment, in effect helping to keep the system clean, minimising the chance of contamination, whilst more importantly preventing oxidation of the graphite. The rate of flow of the purge gas is set by the operator; however, rates between 20 – 50 ml min⁻¹ are typical. A refrigerator is also used to achieve rapid cooling rates if necessary.

There are two main types of differential scanning calorimeter: heat flux DSC and power-compensated DSC. Both instruments consist of a sample pan and a reference pan (which

is basically an empty sample pan) made of aluminium, which acts as a radiation shield. Aluminium also has a high thermal conductivity making it a suitable material. Both pans are then heated uniformly and the difference in heat flow between them is measured and displayed on screen in real time, in a plot against temperature. The temperature ramp can be accurately programmed to rise at a constant rate; this is known as 'temperature scanning'. This project will utilise only the power-compensated instrument, a schematic of which is shown below (Fig. 2.7). This setup was pioneered by Perkin-Elmer, who have since manufactured many different types and models of power compensated DSC instruments.

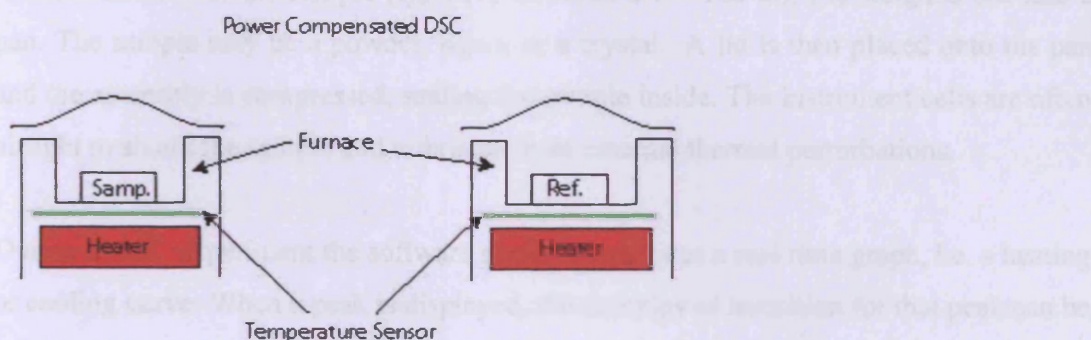


Fig. 2.7: A schematic of a power-compensated DSC system as used in this study.

In power compensated calorimeters, separate heaters are used for the sample and reference. Both are heated identically whilst monitoring the electrical power used by the heaters. Temperature is recorded electronically by sensors situated directly underneath the samples. The high temperatures reached require platinum resistance thermometers to be used since platinum has a very high melting point.

The system consists of two temperature control circuits. One monitors the progress of the temperature control program thus assuring that the heat ramp set by the operator is the average temperature of the sample and the reference pan. The other circuit is a differential temperature control circuit and is used to measure the temperatures of both the sample and reference pans, relative to each other. The circuit can detect any differences in temperature and can adjust the heaters automatically in such a way as to

maintain the same temperature in both. Essentially the system is maintained in a “temperature null” state at all times. It is the output of the differential temperature control circuit that is used to generate the DSC curve, which is the visual representation of the data obtained from the instrument *via* software on a computer. The amount of power required to maintain system equilibrium is directly proportional to the energy changes occurring within the sample. No complex heat flux Eq.s are necessary when using the power-compensated method since the system directly measures energy flow to and from the sample [22].

A small amount of the sample (typically between 0.1 – 100 mg) is weighed out into a pan. The sample may be a powder, liquid or a crystal. A lid is then placed onto the pan and the assembly is compressed, sealing the sample inside. The instrument cells are often airtight to shield the sample and reference from external thermal perturbations.

During a DSC experiment the software package generates a real time graph, i.e. a heating or cooling curve. When a peak is displayed, the enthalpy of transition for that peak can be calculated by the following Eq.:

$$\Delta H = KA \quad (\text{Eq 2.4})$$

Where ΔH is the enthalpy of transition, K is the calorimetric constant, and A is the area under the curve. The calorimetric constant will vary from instrument to instrument and can be determined by analyzing a well-characterised sample with known enthalpies of transition [21]. The value of A is determined by integrating the peaks; this may be easily done using the computer software.

2.3.2.2. Application

DSC is important to this work since it is a very effective way of monitoring small energy releases from a sample. In the study of neutron irradiated graphite much work has been

published using DSC to monitor stored energy release, occurring as a result of neutron bombardment; hence it is hoped that the same methods may be applied to monitor any analogous stored energy release occurring as a result of ion-bombardment.

2.3.2.3. Instrumentation Used

The DSC used was a Perkin-Elmer Diamond DSC. This instrument works on the power compensation temperature null principle, measuring temperature and energy directly. The machine has a temperature range of -170 – 730 °C within an accuracy of ± 0.1 °C. The calorimetry has an accuracy of $< \pm 1\%$ and a sensitivity of 0.2 μW [22].

2.3.3. X-Ray Photoelectron Spectroscopy (XPS)

2.3.3.1. Background/Theory

XPS is a surface sensitive technique, providing both qualitative and quantitative information. XPS can provide us with elemental identity of a surface and also the chemical state (oxidation state) in which the element is present.

The technique is based on the principle of the photoelectric effect. Initially discovered by Heinrich Rudolph Hertz [23] and subsequently explained mathematically by Albert Einstein [24] (Nobel prize 1921), the photoelectric effect is regarded widely as a huge leap forward in scientific thinking at the time, and led to important developments in quantum mechanics.

The theory involved states that when a material is irradiated with photons (typically X-rays) of energy $h\nu$ then there is a certain probability that an electron (photoelectron) would be emitted from the target atom

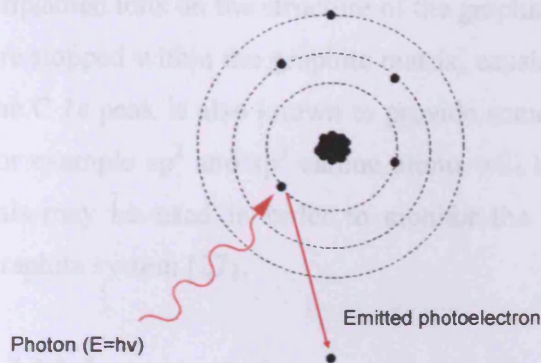


Fig. 2.8: Schematic representation of photoemission

This process is known as photoemission, and the energy of the photoelectron can be calculated and will relate back to the binding energy of the atom from which it came, hence providing elemental information.

$$E_{binding} = E_{photon} - E_{kinetic} - \Phi \quad (\text{Eq. 2.5})$$

Where Φ is the work function of the instrument; in this particular case $\Phi = 4.2$ eV [25].

The surface sensitivity arises from the fact that only the photoelectrons close to the surface will be able to 'escape' and reach the detector. That is, 99.9% of the photoelectrons detected have come from a distance no greater than 3λ , where λ is the mean free path; this distance is usually in the region of a few nanometers. Photoelectrons coming from any deeper than this are highly likely to be scattered by other atoms, through inelastic collisions and other interactions and hence are unlikely to reach the detector [26].

2.3.3.2. Application

XPS is utilized in this project as an effective means of identifying the presence of any implanted species within the surface of the sample. We can use XPS to determine if

implantation has occurred and if so come to some conclusions on the affect of the implanted ions on the structure of the graphite lattice. In ion bombarded graphite the ions are stopped within the graphite matrix, causing disruption to the ideal lattice. Analysis of the C 1s peak is also known to provide some information on the type of carbon present; for example sp^2 and sp^3 carbon atoms will have slightly different binding energies, and this may be used in order to monitor the breakdown of structure in the sp^2 bonded graphite system [27].

2.3.3.3. Instrumentation

The XPS instrument used was a Kratos Axis Ultra – DLD, combining the next generation of photoelectron detector, incorporating quantitative, real time parallel imaging with highest resolution spectroscopy. X-rays are provided by a monochromatic Al $K\alpha$ source, with an associated photon energy of 1486.6 eV.

2.3.4. X-Ray Diffraction (XRD)

2.3.4.1. Background/Theory

XRD is a broad term that encompasses a family of non-destructive analytical techniques that use X-Rays to obtain information from a target material. It can be a relatively quick and easy way of obtaining information on the crystallographic nature of a compound *i.e.* whether or not there is any long-range order, the arrangements of the atoms within that material, chemical composition and physical properties. It is a very effective bulk technique which relies on the elastic scattering of incoming X-Rays by the electrons present in the target material, to provide information on the structure of the target; the X-Rays are effective in doing this as their wavelength (1-100 Angstroms) is in the same region as the typical distance between planes within a crystal lattice.

Developing on earlier work by Max von Laue, William Henry Bragg and William Lawrence Bragg came up with Bragg's Law in 1913 which describes the conditions

required for constructive interference of scattered X-Rays from successive crystallographic planes of the lattice [28]. Bragg's law is given by Eq. 2.6:

$$n\lambda = 2d \sin \theta \quad (\text{Eq. 2.6})$$

Where λ is the wavelength of the X-rays, θ is the incident angle and d is the interlayer distance.

An illustration of this is shown below:

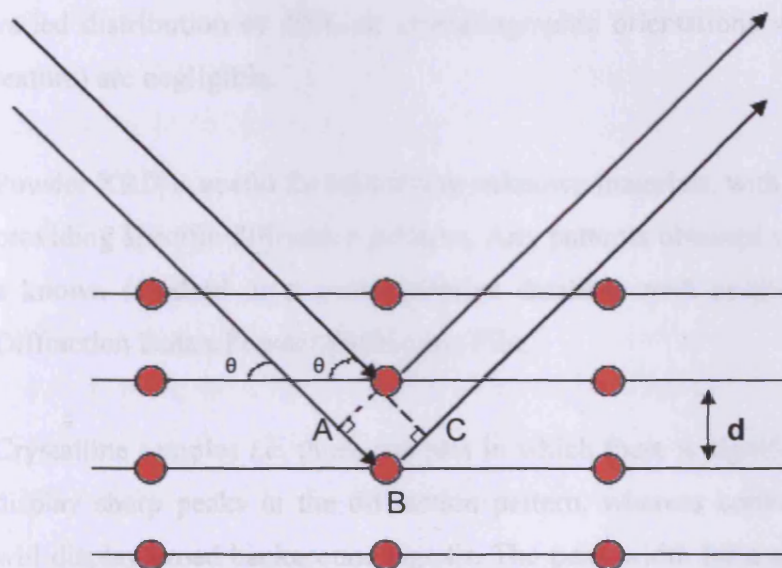


Fig. 2.9: Illustration highlighting the diffraction phenomenon which is the basis of XRD.

When the X-ray strikes an atom it is scattered by the electrons orbiting that atom. As a result a portion of the X-ray energy is re-radiated as a spherical wave. The large majority of the scattering events will cancel each other out in a phenomenon known as destructive interference, however if each scatterer (host atom) is arranged symmetrically and separated at a distance, d , then the spherical waves will be synchronized and hence add together constructively only when their path length difference i.e. $AB + BC$ (or $2d \sin \theta$) equals an integer of the wavelength, λ . Only these scattered X-Rays will reach the detector and so, from the θ value of the observed reflection, the interlayer spacing, d , can be calculated from the Bragg Eq. (Eq. 2.6).

The work carried out in this project focused solely on powder-XRD which uses the same principles to gather information also on crystallite size (grain size) and preferred orientation in polycrystalline or powdered solid samples. Powder XRD differs from single crystal XRD in that, with powders, every single possible crystalline orientation is represented equally. This averaging causes the three-dimensional reciprocal space to be projected into one dimension, a process which results in a loss of a lot of the information available. It should be noted that in practice true randomness is obtained by rotating the sample at a constant rate throughout the experiment to ensure that the effects of the varied distribution of different crystallographic orientations within the sample (*i.e.* the texture) are negligible.

Powder XRD is useful for identifying unknown materials, with different crystalline solids providing specific diffraction patterns, Any patterns obtained can then be compared with a known standard or a comprehensive database such as the International Centre for Diffraction Data's Powder Diffraction File.

Crystalline samples *i.e.* those samples in which there is significant long-range order will display sharp peaks in the diffraction pattern, whereas conversely amorphous samples will display broad background signals. The peak width for a specific phase of a material can be related to the mean crystallite size of that material through the Scherrer Eq. [29-30]. Now modern software packages are able to calculate this very easily for the user.

Glancing-angle (or Grazing-incidence) XRD is a form of XRD which allows analysis of only the surface of the specimen. This is possible by placing the sample at an acute angle with respect to the X-Ray source, which remains static throughout the run. The detector then moves across the desired 2θ range. The more acute the angle the more surface sensitive the technique since the X-Rays literally glance off the surface into the detector (Fig. 2.10). However, when the angle is too small the signal to noise ratio becomes such that the quality of the data is compromised.

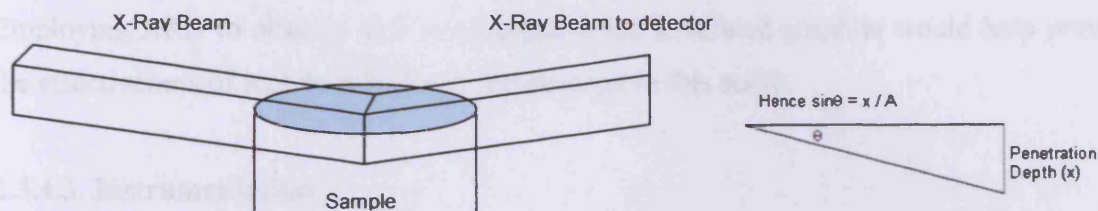


Fig. 2.10: A representation of Glancing-Angle XRD and the means by which to calculate the penetration depth.

The energy of the X-rays, the incident angle, the thickness of the sample and the density all have an effect on the penetration depth of the X-rays, and hence the area from which the data are being retrieved. Simple trigonometry may be used to calculate the penetration depth or alternatively modern software packages will do this easily once the various parameters are input.

2.3.4.2. Application

XRD has previously illustrated the effects of neutron irradiation on graphite [31]. Clear peak broadenings can be observed, with an eventual merging and even loss of peaks at particularly high neutron doses. The $\langle 002 \rangle$ peak can be affected considerably, becoming very broad and shifting considerably upon irradiation.

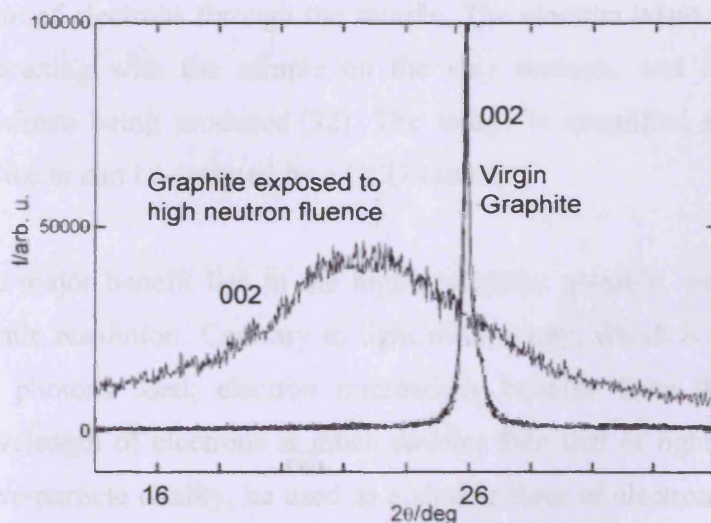


Fig. 2.11: XRD comparison of virgin graphite and graphite exposed to a high dose of neutron irradiation. Adapted from reference [28].

Employing XRD to observe similar changes in ion irradiated graphite would help prove the effectiveness of ions to mimic neutron damage in this sense.

2.3.4.3. Instrumentation

The diffractometer used was a Phillips PANalytical X'Pert diffractometer fitted with a hemispherical analyser. The X-rays were Cu K α radiation ($\lambda = 1.541 \text{ \AA}$) and were run at a voltage of 40 kV and an emission current of 30 mA. The spectrometer was calibrated periodically using silicon which has well known, well-defined, strong diffraction peaks. Data analysis was carried out using the Hi-Score software package. Glancing-angle XRD was carried out at Manchester University using an analogous Phillips diffractometer, under the same settings, equipped with a low angle detector. For this work an incident angle of 2 degrees was chosen through the 2θ range of 20-90 $^\circ$.

2.3.5. Transmission Electron Microscopy (TEM)

2.3.5.1. Background/Theory

TEM is a technique whereby a very thin sample ($\sim 100 \text{ nm}$) may be imaged by passing a beam of electrons through the sample. The electron beam will pass through the sample, interacting with the sample on the way through, and resulting in an image of the specimen being produced [32]. The image is magnified and focused onto an imaging device or can be detected by a CCD camera.

The major benefit lies in the high resolution possible, which in some cases may give atomic resolution. Contrary to light microscopy, which is limited by the wavelength of the photons used; electron microscopy benefits from the fact that the De Broglie wavelength of electrons is much smaller than that of light; and can, due to the idea of wave-particle duality, be used as a shorter form of electromagnetic radiation with which to study the sample [33].

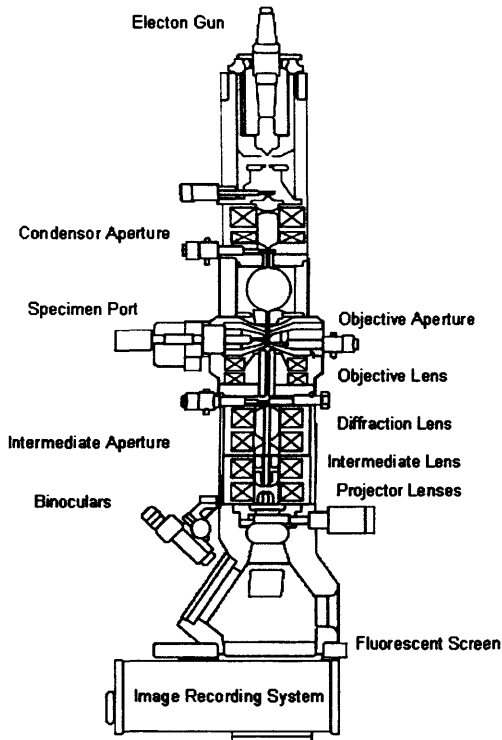


Fig. 2.12: A diagram of a typical TEM.

2.3.5.2. Sample Preparation

For TEM analysis the samples must be transparent to electrons, and thus typically < 100 nm thick. There are a variety of methods for doing this; the method employed to prepare the graphite samples in this project was using a Focused Ion Beam (FIB) [34-35], which has the advantage of site-specificity. FIB involves using an ion beam to etch out a small section from the specimen using a beam of ions to remove bulk material and leave behind a desired specimen. Firstly, once a region of interest is found, a protective layer of Pt is deposited onto the surface of the sample in order to protect the top surface from damage during thinning.

To etch out the sample, Typically Ga^+ ions are used at energies ranging from 5 – 50 keV. The Ga^+ ions strike the specimen in a controlled manner, typically at low current. This

causes sputtering to take place, and the atoms at the surface of the sample are ejected into the gas phase. Eventually the focused ion beam will create a wedge like crater into the specimen (Fig. 2.13 left), where the host atoms have been gradually removed. Through careful manipulation by the operator the desired section can be 'lifted out' (Fig. 2.13 centre) and transferred to a TEM grid [36] using a micro-manipulator which is welded to the sample by another layer of Pt, essentially a Pt weld (Fig. 2.13 right).

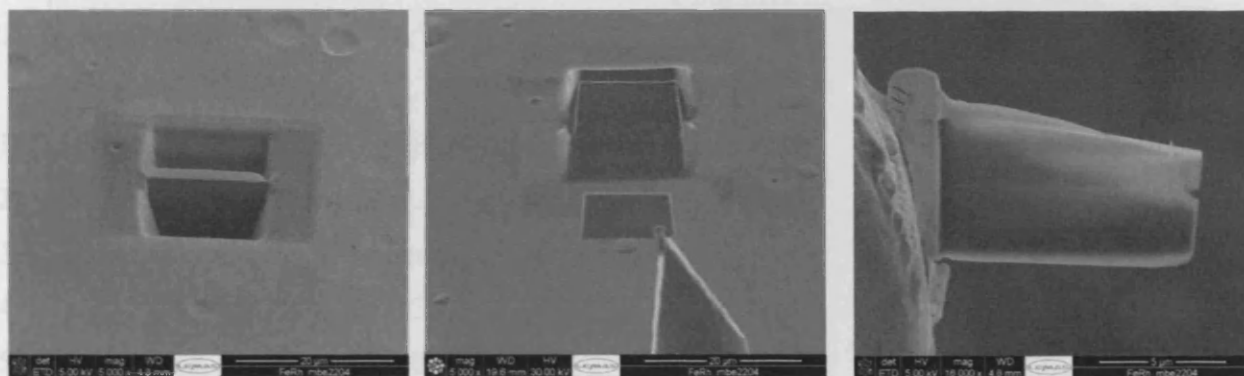


Fig. 2.13: Wedge-like crater milled into HOPG surface (left), Sample lifted out by manipulator (centre) and sample attached to Cu grid ready for further thinning (right).

If further thinning is required then the sample can be thinned again using a controlled ion beam, until the sample becomes thin enough for TEM analysis.

2.3.5.3. Application

TEM is useful to this project as it will help to gain information on the ion induced damage, at the atomic scale. Ideally the breakdown of long-range order can be observed in ion-irradiated samples, with a clear damage layer that is not present within virgin material. TEM has the potential to shed light on the damage processes occurring and the types of defects forming, due to ion irradiation, at a fundamental level.

2.3.5.4. Instrumentation

TEM analysis was carried out on a Philips CM200 Super-Twin FEGTEM operated at 197 keV, fitted with a Gatan GIF200 imaging filter. The microscope is capable of a point resolution of 0.24 nm. The FIB sample preparation was carried out using an FEI Nova200 Nanolab Dual Beam system.

2.4. References:

- [1] G.H. Kinchin, R.S. Pease, *Rep. Prog. Phys.*, **18** (1955) 1.
- [2] W.R. Grove, *Phil. Trans. Roy. Soc.*, **142** (1852) 87.
- [3] A.H. Becquerel, *Comptes Rendus*, **122** (1896) 420.
- [4] J. Joly, *Phil. Mag.*, **13** (1907) 381.
- [5] F. Seitz, *Disc. Faraday. Soc.*, **5** (1949) 271.
- [6] J.C. Slater, *J. Appl. Phys.*, **22** (1951) 237.
- [7] W. Gaede, *Annalen de Physik*, **46** (1915) 357.
- [8] C.R. Burch, *Nature*, **122** (1928) 729.
- [9] K. Siegbahn, C. B. Nordling, A. Fahlman, 'ESCA - Atomic, Molecular and Solid State Structure Studied by Means of Electron Spectroscopy', *Nova, Acta Regiae Soc. Sci. Upsaliensis, Ser. IV, Vol 20* (1967).
- [10] D. Briggs, 'Surface analysis of polymers by XPS and static SIMS', Cambridge University Press, (1997).
- [11] D.J. Pacey, 'Measurement of Vacuum', Butterworth-Heinemann, Boston, (2003).
- [12] A. Chambers, R.K. Fitch, B.S. Halliday, Basic Vacuum Technology 2nd Edition, Institute of Physics, Bristol, (1998).
- [13] <http://www.2spi.com/catalog/vac/santovac-5.shtml> (last accessed 25-02-2011)
- [14] www.ee.surrey.ac.uk/ibc (last accessed 25-02-2011)
- [15] A. Smekal, *Naturwissenschaften*, **11** (1923) 873.
- [16] C.V. Raman, K.S. Krishnan, *Nature*, **121** (1928) 501.
- [17] E. Smith, G. Dent, 'Modern Raman Spectroscopy - A Practical Approach', Wiley, Cirencester, (2005).

-
- [18] M. Bowden, D.J. Gardiner, J.M. Southall, *J. Appl. Phys*, **71** (1992) 521.
- [19] M.R. Ammar, J.-N. Rouzaud, C.-E. Vaudey, N. Toulhoat, N. Moncoffre, 'Structural Characterisation of Ion Implanted Nuclear Graphite', Lyon, France, (2009).
- [20] M.P. House, *The Selective Oxidation of Methanol over Iron Molybdate Catalysts*, PhD Thesis, Cardiff University, Cardiff, (2008).
- [21] P.J. Haines, 'Principles of Thermal Analysis and Calorimetry', RSC Paperbacks, Cambridge, (2002).
- [22] Perkin-Elmer, 'Diamond DSC User Manual' (undated).
- [23] H. Hertz, *Ann. Physik*, **31** (1887) 983.
- [24] A. Einstein, *Ann. Physik*, **17** (1905) 132.
- [25] D.J. Morgan, XPS Access Manager, Cardiff University, *Personal Communication*, (2009).
- [26] G. Attard, C. Barnes, 'Surfaces', Oxford Science Publications, (1998).
- [27] L.A. Dollard, 'Chemistry of Carbon and Modified Carbon Surfaces', PhD Thesis, Cardiff University, Cardiff, (1996).
- [28] H.P. Myers, 'Introductory Solid State Physics', Taylor & Francis, (2002).
- [29] B.D. Cullity, S.R. Stock, 'Elements of X-Ray Diffraction 3rd Edition', Prentice-Hall Inc., (2001).
- [30] R. Jenkins, R.L. Snyder, 'Introduction to X-Ray Powder Diffractometry', Wiley, (1996).
- [31] D. Lexa, A.J. Kropf, *J. Nucl. Mat*, **348** (2006) 122.
- [32] D. Williams, C.B. Carter, 'Transmission Electron Microscopy', Plenum Press, (1996).
- [33] R. Egerton, 'Physical Principles of Electron Microscopy', Springer, (2005).
- [34] J. Orloff, M. Utlaut, L. Swanson, 'High Resolution Focussed Ion Beams: FIB and its Applications', Springer Press, (2003).
- [35] L.A. Gianuzzi, F.A. Stevens, 'An Introduction to Focussed Ion Beams: Instrumentation, Theory, Techniques and Practice', Springer Press, (2004).
- [36] J. Mayer, L.A. Gianuzzi, T. Kamino, J. Michael, *MRS Bulletin*, **32** (2007) 400.

Chapter 3

Atomic Displacement Processes

3.1 Introduction

The result of neutron irradiation on graphite is to induce atomic displacements through a series of collisions. Such consequences can have a negative effect on the graphite with respect to its application in the nuclear industry and the associated build-up of potential energy can pose a threat. However, particle irradiation is able to displace atoms, as it does in graphite, just as easily in other materials too, with the processes involved being complex and difficult to predict. Atomic displacements can occur regardless of the incident species and much work has been published on the processes behind particle-solid interactions, throughout the twentieth century. This chapter will aim to provide some background to this work and also review the processes that are involved in ion-solid interactions and relate them to neutron interactions that occur within a reactor core.

3.2. Theory

3.2.1 Collision Cascade Theory

When an incident particle, with sufficient energy, collides with the first target atom a collision cascade may begin with the first step being the generation of a primary knock-on atom (PKA). The PKA is essentially the struck atom that has now gained energy from the projectile and is moving through the material itself. At this point the PKA can dissipate its initial kinetic energy either through electron excitation of the

medium or of itself, sometimes leading to ionisation, or it can collide with other atoms in an almost elastic collision. The PKA can, with enough energy, create another knock-on event causing another atom to be dislocated, thus generating a secondary knock-on atom, which goes on to do the same. Consequently, a branching effect of successive collisions (see Fig. 3.1) can be envisaged, producing more and more atoms travelling at near-thermal velocities.

These atoms are also accompanied by some degree of electron excitation, and eventually through energy loss mechanisms the collision cascade comes to an end; typically taking, in total, less than a picosecond [1]. The PKA comes to rest in a non-ideal location, which is energetically higher than its usual position; this stationary atom is referred to as an interstitial. In graphite the interstitial atoms generally assumed to reside in between the graphene layers.

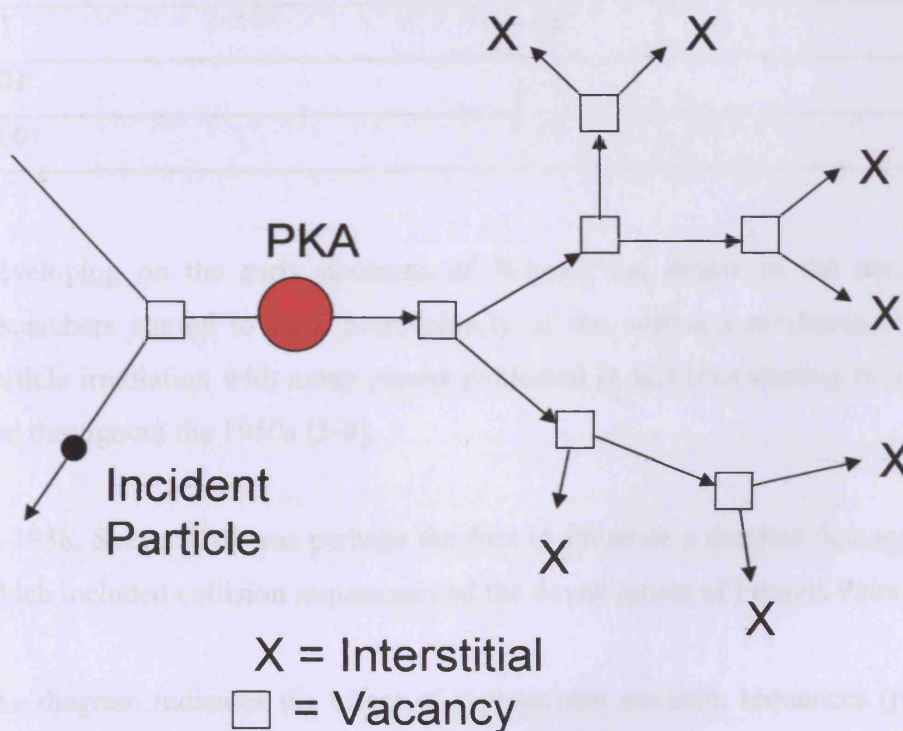


Fig. 3.1: Schematic of a collision cascade caused through the production of a primary knock-on. (After M.W Thompson, 1969 [2]).

In fast neutron irradiation, in particular, it is the behaviour of the primary knock-on atoms that has considerable effect, since it is during the period that the PKA is coming to rest that the majority of the atomic displacements occur [3].

It follows that the more PKA atoms that are produced the greater the radiation damage. The total number of PKAs produced is obviously dependant on the number of collisions a neutron makes in slowing down to rest, and hence is proportional to the initial neutron energy. In reactor grade graphite the number of PKA atoms created can be calculated as a function of the initial neutron energy (c.f. Table 3.1):

Table 3.1: Number of displaced carbon atoms depending on initial neutron energy [4].

Initial Neutron Energy (MeV)	Number of PKAs Created
10	73
2	58
1	55
0.1	40
0.01	26
0.001	11

Developing on the early concerns of Wigner and others in the nuclear industry researchers started to look more closely at the collision mechanisms involved in particle irradiation with many papers published in this area starting in the late 1940s and throughout the 1950s [5-9].

In 1958, Seeger [10] was perhaps the first to illustrate a detailed damage mechanism which included collision sequences and the development of Frenkel Pairs (Fig. 3.2).

The diagram indicates the effect of replacement collision sequences (referred to as crowdions [11]) and the existence of exchange collisions. The depleted zone is a concept originally proposed by Brinkman [12] and arises from the ejection of atoms concentrated within the cascade core, a direct result of the thermalisation of the PKA.

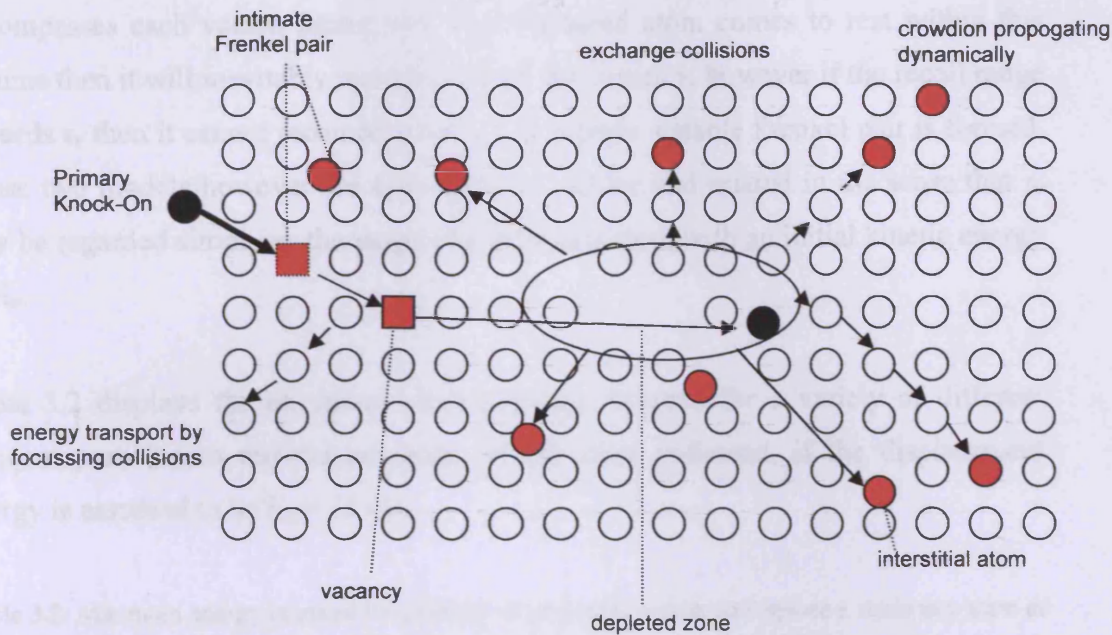


Fig. 3.2: An illustration of a damage mechanism induced by a primary knock-on atom (after Seeger [10]).

3.2.2 Atom Displacement Energy

A significant factor that determines the number of displacements that are produced upon irradiation is something called the 'unit displacement energy', E_d , the energy required to remove an atom from its preferred lattice position. It is known from thermodynamic data that atoms are bound in solids with energies of typically 5 eV [13]. Thus, it follows that more energy would be required to remove the atom from its lattice position. Much work was carried out in the 1950s to obtain this value for various materials [14-17] with Werner studying 23 different metals [18], providing a range of values from 20 eV for Pb up to 180 eV for Hf. Because of the measured differences from material to material a general isotropic value, estimated by Seitz [6], of 25 eV is typically used for graphite.

Two different models are used to describe the limits placed by the unit displacement energy. Firstly the Kinchin and Pease model [13,19] which is a relatively simple approach: that is, if the incident kinetic energy, $E \geq E_d$ then the atom is 'permanently' displaced. However, if $E < E_d$ then the atom may be temporarily displaced, shortly returning, resulting in no displacement. The other model, developed slightly earlier by Fletcher and Brown [20] suggests that there is an instability volume of radius ' r_v ' that

encompasses each vacant lattice site. If a displaced atom comes to rest within this volume then it will inevitably recombine with the vacancy, however if the recoil range exceeds r_v then it cannot recombine and consequently a stable Frenkel pair is formed. These two models however are actually quite similar and related in the sense that r_v may be regarded simply as the range of a recoiling atom with an initial kinetic energy of E_d .

Table 3.2 displays the minimum kinetic energy required for a variety of different incident particles to remove an atom, of the mass indicated, if the displacement energy is assumed to be $E_d = 25$ eV.

Table 3.2: Minimum energy required by a variety of projectile species to displace a stationary atom of varying mass, assuming $E_d = 25$ eV [13]. Highlighted in red is mass 12 amu for graphite [4].

Weight of Stationary Atoms (amu)	10	12	50	100	200
Neutrons, Protons (ev)	76	88	325	638	1263
Electrons, γ -rays (MeV)	0.1	0.12	0.41	0.68	1.1
α -particles (ev)	31	33	91	169	325
Fission fragments (mass = 100 a.m.u) (ev)	85	65	30	25	27

The data follows from the fact that the maximum energy, E_{\max} , than can be transferred to a moving particle of mass M_1 and energy E to a stationary atom of M_2 is:

$$E_{\max} = \Lambda E \quad (\text{Eq. 3.1})$$

where from the early paper by J.J Thompson [21] it is known that:

$$\Lambda = 4M_1M_2/(M_1+M_2)^2 \quad (\text{Eq. 3.2})$$

For electrons, relativistic effects must be considered resulting in the expression used:

$$E_{\max} = 2E(E-2mc^2)/M_2c^2 \quad (\text{Eq. 3.3})$$

where m = electron mass and c is the velocity of light.

If E_d is known for a target, then it is possible to estimate the average number of displacements produced through irradiation by a particle of a known energy. E_0 .

To do this the simplified Kinchin-Pease Hard-Sphere model is used:

$$N_d(E_0) = 0.43v(E_0)/E_d \quad (\text{Eq. 3.4})$$

where $v(E_0)$ is the amount of energy available in nuclear collisions, which is the initial energy minus the energy lost through electronic excitations.

3.2.3 Replacement Collisions

Another aspect of defect production is the possibility of replacement collisions. This is when an atom is displaced by the incident particle but the energy of that particle is insufficient to escape the vacancy. This results in the incident particle taking the place of the original atom, and although the elemental identity may be different, the overall number of atoms in the lattice is unchanged and hence there is no defect production. Replacement collisions are more likely to occur when the initial kinetic energies are relatively low and the mass of the two atoms is not too dissimilar, they are of particular importance in crystals of high symmetry.

3.2.4 Cascade Overlap

After a sufficient dose the movement of implanted particles and recoil atoms becomes random and difficult to predict [22]. An important product of this randomisation is that it is possible for atomic replacement to occur as a result of a collision cascade engulfing an already damaged area. Such atomic replacements will occur when an atom from a collision cascade collides with an interstitial produced by a previous cascade, resulting in an interstitial/vacancy annihilation. Such processes can lead to a decrease in overall damage production. The likelihood of such events occurring is given by a Poisson distribution [23].

Experiments have been carried out proving the existence of such a phenomenon. English et al [24] noted that a 1 keV cascade in a perfect Cu crystal led to the average production of 5.3 Frenkel defects, which after a repeated cascade dropped to 4.3. It should be noted that this process is more dominant in neutron and ion irradiation and less so for electron irradiation; also, the effects seem more significant at low temperatures as one would expect [25].

3.3 Stopping and Range of Ions in Matter (SRIM)

3.3.1 Energy Loss Mechanisms

The mechanisms discussed in this section are fundamental to the study of radiation damage, since it is when the particles are slowing down to rest, due to the forces acted upon them, that the majority of atomic displacements *i.e.* damage occurs. There is a significant history involved in the study of the stopping and range of ions into matter, which is both interesting and complex. A comprehensive account can be found in the book by Ziegler, Biersack and Ziegler [26]. Here, a brief account of the history will be given along with the up to date theory of energy loss by matter.

In 1913 Neils Bohr published his first paper “on the theory of the decrease of velocity of electrified particles on passing through matter” [27] in which he concluded that the energy loss could be divided into two components: nuclear stopping (energy loss to the hosts’ nucleus) and electronic stopping (energy loss to the hosts’ electrons).

Twenty years later, following on from this work, Bethe and Bloch revised the problems from a quantum mechanical viewpoint and derived, in the Born approximation, the fundamental equations for the slowing down and stopping of very fast particles through a quantized medium [28-29].

The 1940s saw the discovery of nuclear fission and consequently a sudden interest in the analysis of the transport of fission fragments through matter. The main problem caused by such projectiles was the partially stripped ion, known as the ‘effective charge’ problem. Many scientists such as Fermi [30], Lamb [31], Knipp [32] and Bohr [33-34] were working on this problem, with Bohr suggesting that the ion should

be considered to be stripped of all its electrons with velocities lower than the ion velocity. It was shown that:

$$Z_1^* = Z_1^{1/3} V/V_0 \quad (\text{Eq. 3.5})$$

Where Z_1 is the atomic number of the ion, Z_1^* is the effective charge in energy lost to the target electrons, V is the ion velocity and V_0 is the Bohr velocity (2×10^8 cm/sec).

In 1963, almost a decade of work by Lindhard and co-workers [35-36] led to the first unified approach to stopping and range theory, known as the Lindhard, Scharff and Schiott (LSS) theory [37]. The LSS theory was the last of the comprehensive theories based on statistical models of atom-atom collisions and was able to predict the range of ions in solids within a factor or two. Current theory and models allow for stopping powers to be calculated with an average accuracy of better than 10% for low energy heavy ions, and better than 2% for high velocity light ions. Range distributions for amorphous elemental targets have about the same accuracy [26]. The impact of this unified theory should not be under-estimated, with many modern widely used computer programs based on the LSS principles (*e.g.* SRIM).

3.3.2 Nuclear Stopping

Nuclear stopping involves the loss of energy of a projectile to its target nucleus *via* an elastic collision. This process is predominant for the slowing of neutrons in matter and is also significant for ions. In a two atom scattering model the transfer of energy depends on the mass and charge of the two particles involved and also the initial velocity and direction of the projectile species. As a charged particles moves through matter it can interact with the stationary atoms, causing them to recoil by giving away a portion of its energy, whilst it itself is deflected away. The final velocities and trajectories of the two particles after this interaction can be calculated through classical means and applying the principles of the conversation of energy and momentum.

The amount of energy loss is determined through the screened Coulomb interactions, and is usually a significant amount leading to ion deflections and atomic

displacements. Such screening means that in reality ion-atom collisions are not 'hard-sphere' and that the two central cores never 'touch'. Instead the interactions are electrostatic, with the distance of closest approach becoming smaller as the projectile energy increases.

The distance of closest approach, r_{\min} , is determined by the initial energy, E_0 , the interaction potential $V(r)$ and the impact parameter, b :

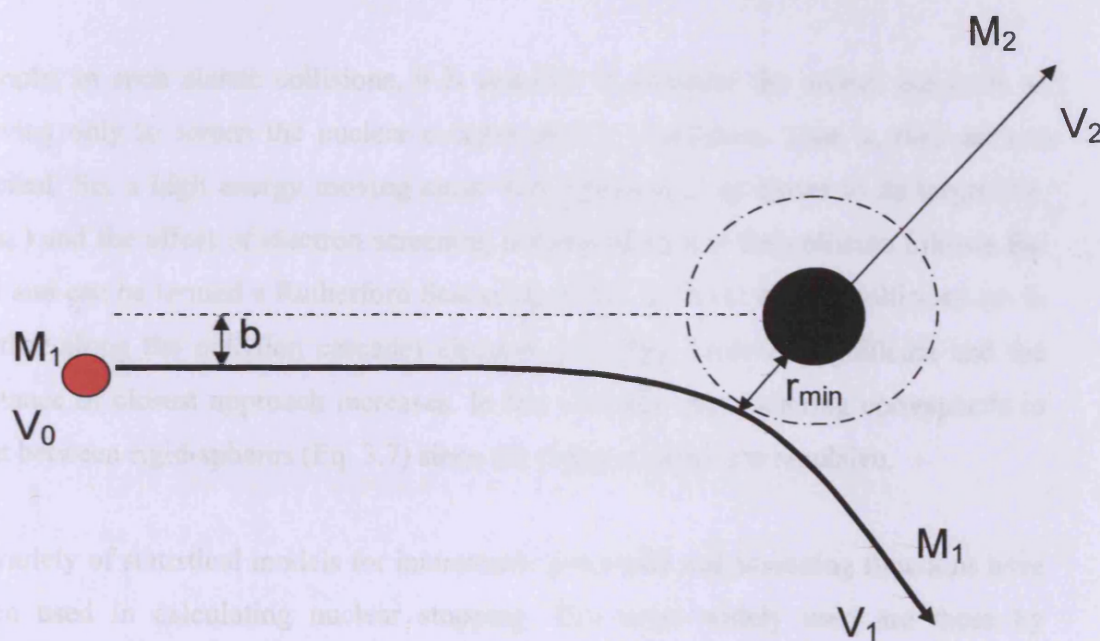


Fig. 3.3: The two nuclei never actually 'touch' and are separated by a energy dependent distance r_{\min} .

With typical collisions taking place: $a_0 < r < r_0$, where r_0 is the equilibrium position of the next atom ($\sim 2.5 \text{ \AA}$) and a_0 is the Bohr radius (size of atomic shell) = 0.53 \AA .

When $r \gg r_0$ interactions are weak compared to the velocity of the moving particle. When $r < a_0$ nuclear collisions and the Columbic potential dominate and hence the repulsive potential, $V(r)$ is simply the Columbic repulsion:

$$V(r) = Z_1 Z_2 e^2 / r \quad (\text{Eq. 3.6})$$

In the majority of instances, $a_0 < r < r_0$ in which case the Columbic potential is reduced and the screening effect of the electrons must be considered, hence:

$$V(r) = Z_1 Z_2 e^2 / r \cdot (\chi(r/a)) \quad (\text{Eq. 3.7})$$

Where $\chi(r)$ is the screening function, Z_1 and Z_2 are the charges of the interacting nuclei, r the distance between them and a is the so called screening parameter (2.06×10^{-9} cm for carbon).

Simply, in such elastic collisions, it is possible to consider the atoms' electrons as serving only to screen the nuclear charges during a collision. That is, they are not excited. So, a high energy moving atom will approach a lot closer to its target (*i.e.* $r < a_0$) and the effect of electron screening is diminished and the collision follows Eq. 3.6 and can be termed a Rutherford Scattering event. In lower energy collisions (as in further along the collision cascade) electron screening becomes significant and the distance of closest approach increases. In this scenario the scattering corresponds to that between rigid-spheres (Eq. 3.7) since the electron fields are repulsive.

A variety of statistical models for interatomic potentials and screening functions have been used in calculating nuclear stopping. The most widely used are those by Sommerfield [38], Moliere [39], Lenz-Jensen [40-41] and Bohr [42]. Each of which may be seen as a Columbic term ($1/r$) multiplied by a "screening" function, defined as the ratio of the actual atomic potential at some radius to the potential caused by an unscreened nucleus:

$$\Phi = V(r)/(Ze/r) \quad (\text{Eq. 3.8})$$

Where Φ is the screening function, $V(r)$ is the potential at radius r , Z is the atomic number and e is the electronic charge.

As the ion approaches the stationary atom the electron containing atomic orbitals will begin to merge and in this case the number of actual electrons in that specific volume element may change. The overlap volume will contain electrons from both atoms and the electrons within that overlap volume can be treated as a free electron gas. Such

overlap volumes absorb energy due to the Pauli principle which states that there must be promotion of electrons into higher energy levels upon increased electron density. This consequently decreases the attractive potential.

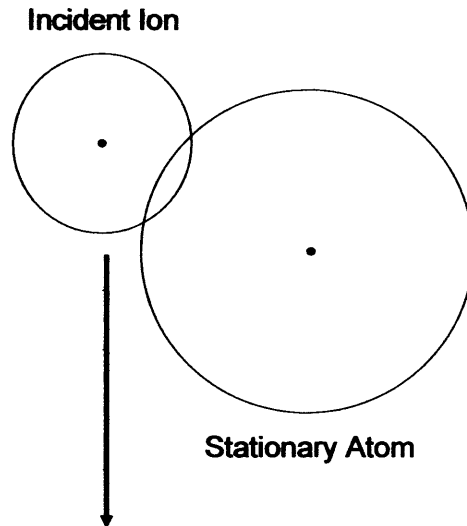


Fig. 3.4: Overlapping electron orbitals during the interaction between a moving ion and a stationary atom. Electrons in this overlap will experience Pauli promotion to higher energy levels.

To calculate interatomic potentials each atom must be considered as a spherically symmetric charge distribution with a central point charge. The total interaction potential, V , can be expressed as:

$$V = V_{nn} + V_{en} + V_{ee} + V_k + V_a \quad (\text{Eq. 3.9})$$

Where V_{nn} is the electrostatic potential energy between the nuclei, V_{ee} is the pure electrostatic interaction energy between the two electron clouds, V_{en} is the interaction energy between each nucleus and the other electron cloud, V_k is the Pauli induced increase in electron kinetic energy in the overlap region and V_a is the increase in exchange energy of these electrons.

Each parameter will not be discussed further here but for more details and derivation the reader is referred to reference [23].

3.3.3. Electronic Stopping

This concerns the loss of energy of a projectile through the transfer of energy from itself to the electrons surrounding a target nucleus. This is an inelastic process resulting in a small energy loss per collision and negligible deflection. Electronic energy losses are predominant in ions travelling with low mass and high energy, which explains why the trajectories are initially close to a straight line through the material. It is only when sufficient energy is lost that nuclear stopping predominates and vacancy production can occur. In general, electronic stopping is not of great significance when considering radiation damage, particularly through the production of Frenkel defects, since it does not directly result in atomic displacement. For this reason a relatively brief account is given here where more detail may be found by referring to the corresponding references stated.

Electronic stopping is made complicated due to the fact that both the ion and the target are changing continuously during the passage of the ion. The charge state of the ion changes depending on its velocity and of the electron density within the target at a particular region. The charge density on the ion will also polarise and change shape in accordance to the target electrons which will also polarise in front of and around the incoming ion. As the ion penetrates the electron cloud and their orbitals overlap, electrons will be promoted to high energy excited states through Pauli promotion.

When considering electronic stopping there are different regimes (rules) which apply depending on the ion energy. For energies less than 10 MeV, which is the regime we are concerned with, the Lindhard-Ziegler approach is used. This method states that when the velocity of the ion, V_i , is less than the Bohr velocity of atomic electrons, V_0 ($V_0 = 2.188 \times 10^6 \text{ ms}^{-1}$) then the ions' electrons remain bound to the ion and tend to neutralise through electron capture. However, when $c/10 > V_i > V_0$ then the opposite occurs, where the ions' electrons are lost to the target material until the ion becomes fully stripped and the charge state is maximised. This occurs when $V_i \approx V_0 Z^{2/3}$

A 2.0 MeV He^+ ion has a velocity of $9.8 \times 10^6 \text{ ms}^{-1}$ and so will become fully stripped before undergoing nuclear stopping and eventually coming to rest.

3.3.3.1. Light Ions (Protons and He⁺)

Much of the early work in this area focussed on the proton since it was believed that if a proton was always stripped of its electron whilst in the solid then it could be considered the purest test of any stopping power theory of particles penetrating an electron plasma. Many researchers worked on this when eventually Brandt and Kitagawa [43] suggested that it was possible to assume that a proton in a solid always had a charge of +1. This can be justified since the diameter of the orbit of a 1s electron around a proton is larger than the interatomic spacing found in most solids. Hence a neutral H atom, could not survive in a solid for a appreciable amount of time. Once values were obtained for protons, He⁺ values could be obtained from ‘scaling’ the results [32]. So, for He⁺ ions one can simply multiply the stopping for protons at the same velocity by the He⁺ effective charge at that velocity [26].

3.3.3.2. Heavy Ions (Z>2)

The study of the electronic stopping of heavy ions is split into three velocity regimes: low velocity (< 25 keV), high velocity (>200 keV) and medium velocity (25-200 keV). Low velocity ions have velocities lower than the solids’ Fermi velocity (typically 0.7-1.3 V₀) and thus are moving much more slowly than the majority of the target electrons, leading to mostly adiabatic collisions with the ion without direct energy loss. In this case the electronic stopping cross sections are proportional to velocity [44-46].

For high velocity ions it was found that it was effective to scale proton stopping powers to equivalent heavy ion stopping powers through Thomas-Fermi scaling values. A fairly simple expression for the electronic stopping can be given as:

$$S_{HI} = S_H (Z_{HI}^*)^2 = S_H Z_{HI}^2 \gamma^2, \quad \gamma = 1 - \exp[-V_I / (V_0 Z_I^{2/3})] \quad (\text{Eq. 3.10})$$

Medium velocity heavy ions are studied through the models constructed by Brandt and Kitagawa [43] and Kreussler, Varelas and Brandt [47]. These will not be discussed here since the work carried out in this project was done at energies ≤ 5 keV (on the

irradiation system at Cardiff) or ≥ 200 keV (on external particle generators) and hence fall into either the low velocity or high velocity regimes, briefly discussed above.

3.3.4. The Range of Ions in Matter

Due to the stopping processes outlined above it is inevitable that the incident ion will eventually come to rest, perhaps within the target. The path of an ion through a target is a stochastic (random) process; two ions of the same energy going into the same target will not stop at the same place, thus the implantation of the ion results in a statistical distribution.

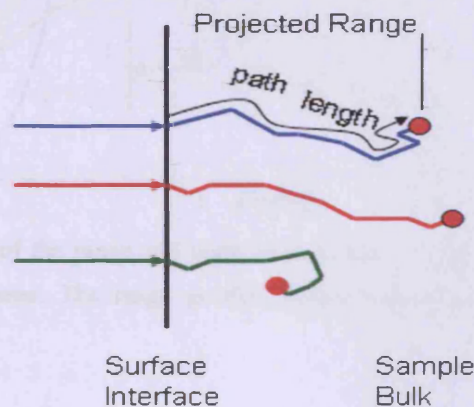


Fig. 3.5: An illustration of the path of an ion as it enters a solid target. The behaviour of the ion and the range is essentially random [48].

The range distribution of an ion can be determined by four main factors: the ion mass, its energy (*i.e.* momentum), the mass of the target atoms and the target density. The distribution of the ions in the target material throughout the irradiation will depend on these parameters.

Another four different parameters are then used to describe the distribution obtained, these are the mean range which is the average stopping position of the ions, the standard deviation, which is the width of the distribution, the skewness, which is the asymmetry of the distribution and finally the kurtosis, which is the 'flatness' of the distribution.

In order to reconstruct the distribution from these parameters a general shape must be assumed. The most successful used to describe such ion implantation is defined by the Pearson family of curves, which are essentially 'bell-shaped' profiles.

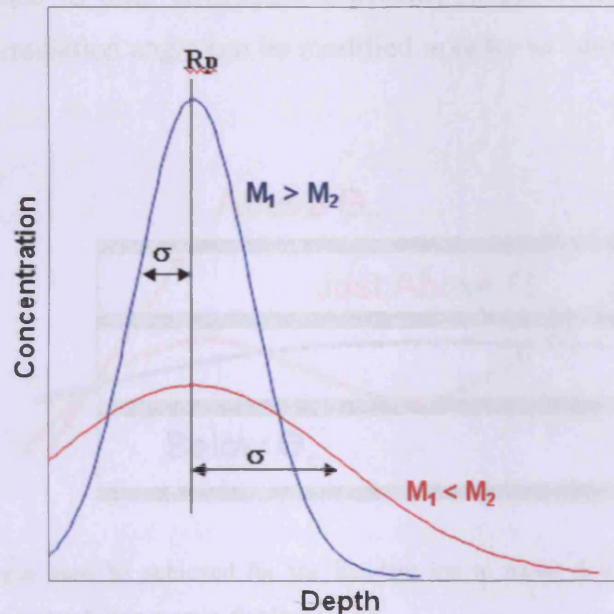


Fig. 3.6: A representation of the range and standard deviation of ions in matter depending, and the effect of the ratio of masses. The range profiles follow reasonably closely that of a Gaussian distribution.

The mathematics will not be discussed here and to make things easier the well-known Gaussian distribution can often be used to describe the distribution of ion implantation very well giving good agreement with the Pearson curves. The Gaussian function is symmetric and also bell-shaped. It only considers the mean range and the standard deviation (Fig. 3.6) (skewness and kurtosis are not considered).

3.3.5. Channelling

A dramatic effect on ion range can be seen when the ions travel directly down the main crystallographic directions of the lattice in a process referred to as channelling. Well channelled ions experience less nuclear and electronic stopping and thus are able to travel much further distances (between a factor of 2 -50 times further) and cause fewer atomic displacements [48].

Channelling was first identified by Robinson and Oen [49] and was subsequently confirmed experimentally by several groups [50-52].

It can be manipulated to one's advantage, especially in industries interested in Si doping, where the irradiation angle can be modified in order to 'steer' the ion down a particular channel.

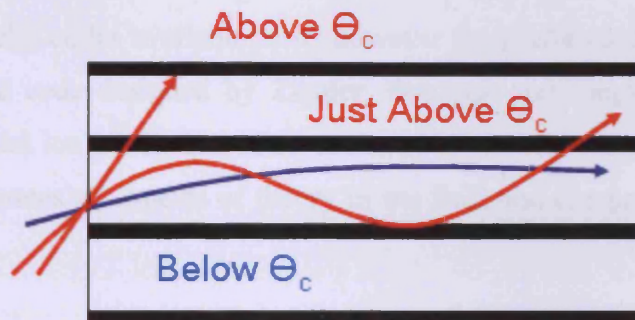


Fig. 3.7: A critical angle must be achieved for the incident ion to travel down the atomic planes, resulting in a greater range but fewer atomic displacements.

It is known that for Si the critical angle, Θ_c , is between $3^\circ - 5^\circ$ for the $\langle 110 \rangle$ and $\langle 111 \rangle$ directions [53-54]. Such an angle may be determined by:

$$\Theta_c = [(a_{T-F}/d)\Theta_1]^{1/2} \quad (\text{Eq. 3.11})$$

Where $\Theta_1 = (Z_1 Z_2 e^2 / E_d)^{1/2}$, Θ_c is the critical angle, d is the distance between planes and a_{T-F} (Thomas-Fermi screening length) = $0.8853 a_0 \sqrt{(Z_1^2/3 + Z_2^2/3)}$ where a_0 is the Bohr radius (0.53 \AA).

Gradually a channelled ion will come to rest through a series of glancing collisions with the target atoms, which will eventually steer the ion out from the "free space" and into the atoms. Usually such glancing collisions will have energies less than E_d and atomic displacements will not occur until the governed motion results in more direct impacts.

3.3.6. Stopping and Range of Ions in Matter (SRIM) computer package (www.srim.org)

The development in computer power since the 1950s has seen a variety of useful computer codes being developed, which are able to utilise the theory discussed above and adapt it to be able to predict and model the interaction of radiation with matter to a good degree of accuracy. Codes such as SPECTER [55-56] and MARLOWE [57] were the first popular codes available; now however the preferred choice is SRIM, a Monte-Carlo based code designed by Ziegler, Biersack and Ziegler [26], and used specifically to model ion irradiation of a vast array of different target materials. The latest code incorporates all aspects of theory in the field and can provide a wealth of useful information.

Monte Carlo simulation may be described as a computation technique that relies on the generation of random numbers to compute the solution to a problem. [58] It is used effectively in many areas of physics and has been used to model the thermalisation of neutrons in matter Monte Carlo Neutron Program (MCNP) developed by Oak Ridge National Laboratory. The MCNP package is extremely powerful but is also expensive to obtain. For this project the freely obtainable SRIM program is utilised, which uses similar Monte Carlo methods to provide a very accurate model of the behaviour of ions in matter, which forms the basis of this project.

The SRIM code is very easy to use and the screens are self-explanatory. Below is an example of a calculation carried out by SRIM (Fig. 3.8).

This calculation is for irradiation of graphite with 5.0 keV He⁺ ions. The central animation is a good visual guide and can help to envisage the path of the ions as they penetrate the graphite surface. On the right of the screenshot there is information regarding the ion, the energy loss and the sputtering yield (the rate at which carbon atoms are ejected away from the substrate). In the top right is an important estimation, indicating the number of vacancies per ion. The 'distributions' section in the bottom left allows the user to gain other important information from the calculation.

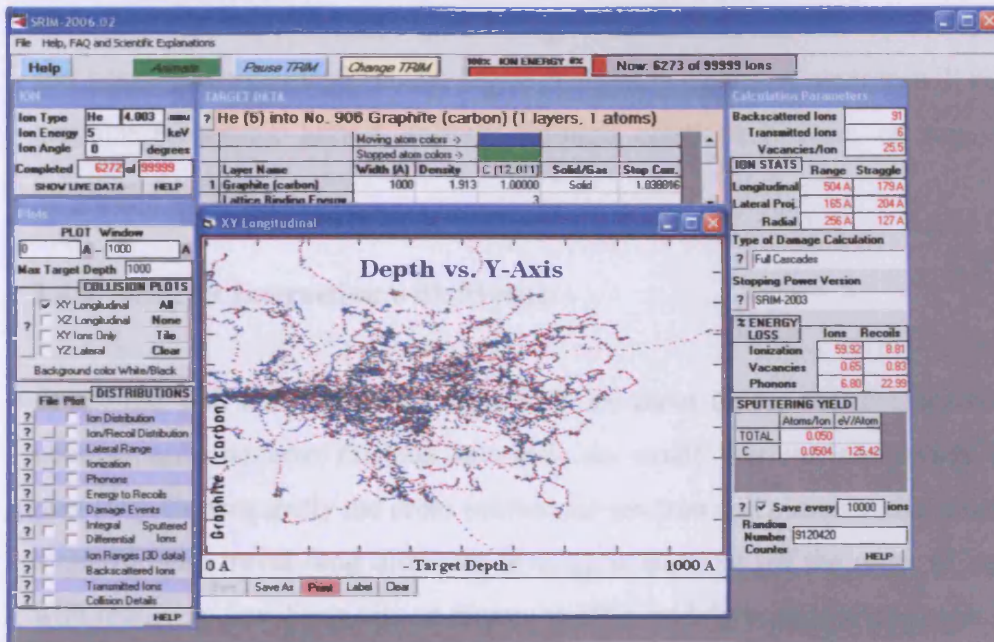


Fig. 3.8: Screenshot from a typical SRIM calculation.

3.4. Neutrons

3.4.1. Fast Neutrons

Within a reactor core it is the radiation damage induced in the moderator (graphite) from fission neutrons that is of interest to those in the nuclear industry. These neutrons, generated from the fission of ^{235}U (or ^{239}Pu), have a wide range of energies, from thermal neutrons (~ 30 meV) up to high energies of ~ 10 MeV [1]; the mean energy, however, is taken to be 2.0 MeV [59].

The interaction of neutrons with matter is somewhat different to that of ion irradiation since there is no effective charge and no electron cloud. The collisions of neutrons can therefore be seen as the simple hard-sphere type and can be effective in atomic displacement, even at relatively low energies. Primarily, neutrons interact with matter via elastic collisions (i.e. the billiard ball model), and are the most important events when addressing radiation damage. However, it should be mentioned that neutrons can also interact through inelastic scattering (where the target nucleus is left in an excited state) and neutron capture. Neutron capture can then lead to gamma emission or fission and radioactive decay. However, these are not of concern here, since

moderator material is chosen specifically to have a low neutron capture cross-section and hence promote elastic scattering of the fast neutrons. A neutron will react with a graphite moderator almost entirely through elastic collisions, causing significant radiation damage.

3.4.2. Neutron Interaction with Matter

A neutron will not interact strongly with an atom unless the distance between the neutron and the host nucleus becomes so small that nuclear forces come into play [60]. Consequently the cross section for neutron collision is rather small and thus a neutron can travel long distances through a material (of the order of centimetres) with relatively few direct hits on atoms, at often widely separated positions.

However, when a collision does occur, the particles obey the rules of classical mechanics and the conservation of energy. The first atom the neutron hits will receive a considerable fraction of its energy, with the precise amount increasing the more similar the masses of the two species. The PKA may then go on to displace atoms of its own, thus creating secondary recoil atoms, as discussed previously, whilst simultaneously the rebounding neutron will travel to its next collision (likely to be a relatively large distance) where it again gives up a similar fraction of its energy (less in absolute terms) and the process continues, until the cascade comes to an halt.

The recoil energy spectrum, $N(E)dE$, of the struck atoms is given by:

$$N(E)dE = dE/E_{\max}(0 \leq E \leq E_{\max}) \quad (\text{Eq. 3.12})$$

where E_{\max} is given by Eq. 3.3.

Only a small proportion of struck atoms (E_d/E_{\max}) are not displaced, hence the cross-section for producing a primary knock on, σ_p , is essentially equal to the neutron cross section. For heavy target elements E_{\max} rarely exceeds the ionisation limit, L_c , and so the average number of displaced atoms per neutron collision can be given by:

$$N_d = E_{\max}/4E_d \quad (\text{Eq. 3.13})$$

The majority of displacements occur in targets of moderate atomic mass. This can be explained since very heavy elements will take up only a small amount of recoil energy, whereas very light elements will take more energy but lose it more quickly through ionisation.

Graphite is of moderate mass ($C = 12$ amu) and is known to be very susceptible to atomic displacement. The measured E_d in graphite is approx 28 eV [61] and it has been estimated that for every fast neutron (mean energy 2 MeV) that hits the graphite lattice, approximately 22,000 atoms are displaced from their lattice sites (Table 3.3)

Table 3.3: Estimate of the number of displaced carbon atoms as a function of initial neutron energy [62].

Neutron Energy (MeV)	Approx Total Number of Displacements
10	50000
2	22000
1	18000
0.1	2500

The majority of these are caused by the primary knock-ons and the associated secondary and tertiary knock-ons, which have less and less energy, becoming so low that they are unable to ionise but can dissipate the energy through nuclear collisions [63]. This means that neutron irradiation can be characterised by many isolated regions of damage, with a major fraction of the total neutron energy going directly to defect production *via* the recoil atoms.

3.4.3. Using ions to simulate neutrons

The primary differences between irradiation by neutrons and irradiation by ions is that ion irradiation is very inhomogeneous and the penetration depths are much smaller. Neutrons are relatively homogeneous and bounce around the target material causing displacement cascades, often relatively large distances apart, thus creating pockets of damaged areas spread around the target. Ion irradiation may cause analogous

displacement cascades, but they will not be as spread out and the damage will be localised to the surface. The reason for this is that the collision cross-section for an ion and an atom is much larger than for a neutron and the same atom. This is because the ion can act on the atom through electrostatic forces and ordinary inter-atomic repulsions, which have a much greater range of action than the nuclear forces responsible for neutron collisions. Obviously the mass of the ion plays a major role and if the mass of the ion is considerably larger than that of the target then damage will be severe, but in a very localised manner.

The stopping force differs in that ions succumb to electronic stopping whilst neutrons do not. The effect of this varies, again depending on ion mass and velocity. A proton, for example travelling at high energy will stop almost only through electronic processes causing very few atomic displacements whilst a heavy ion at equivalent energy will possess more nuclear stopping and cause far more displacements, as discussed in section 3.3.2.

3.5. Conclusion

In summary, simulating neutron damage with ions may be somewhat difficult, but tuning the irradiation parameters, such as ion mass and ion energy, can lead to improved similarities between the two. Note that it is worth emphasising again that the damage caused through neutron irradiation, and the primary cause of Frenkel defects, is the damage caused by the primary knock-on atoms slowing down to rest and not by the neutrons themselves and so, provided ions can create equivalent PKA induced cascades then, in theory, the damage accumulation should be very similar. The SRIM program is a powerful tool that can provide insight into the damage caused through detailed calculations and importantly can give an accurate measurement of ion penetration depth, which is of great importance to the work carried out in this project.

3.6. References:

[1] M.T. Robinson, *J. Nucl. Mat.*, **216** (1994) 1.

- [2] M.W. Thompson, 'Defects and Radiation Damage in Metals', Cambridge University Press, (1969).
- [3] G.J. Dienes, *Annu. Rev. Nucl. Sci.*, **2** (1953) 1194.
- [4] D.R. De Halas, 'Theory of Radiation Effects in Graphite', in: R.E. Nightingale (Ed.) 'Nuclear Graphite', Academic Press: New York and London, (1962).
- [5] M. Burton, *J. Phys. Chem.*, **51** (1947) 611.
- [6] F. Seitz, *Disc. Faraday. Soc.*, **5** (1949) 271.
- [7] F. Seitz, *Phys. To-day*, **5** (1952) 6.
- [8] J.S. Koehler, F. Seitz, *Z. Phys*, **138** (1954) 238.
- [9] T. Broom, *Phil. Mag. Suppl.*, **3** (1954) 26.
- [10] A. Seeger, 'Conference on the Peaceful Uses of Atomic Energy', in: 2nd UN International Conference on the Peaceful Uses of Atomic Energy, United Nations, New York (1958), pp. 250.
- [11] J.B. Gibson, A.N. Goland, et al., *Phys. Rev.*, **120** (1960) 1229.
- [12] J.A. Brinkman, *J. Appl. Phys.*, **25** (1954) 951.
- [13] G.H. Kinchin, R.S. Pease, *Rep. Prog. Phys*, **18** (1955) 1.
- [14] E.E. Klontz, K. Lark-Horovitz, *Phys. Rev.*, **82** (1951) 763.
- [15] D.T. Eggen, M.J. Laubenstein, *Phys. Rev.*, **91** (1953) 238.
- [16] R.A. Dugdale, 'Report of Bristol Conference on Defects in Crystalline Solids' (London: Physical Society), (1955).
- [17] J. Denney, *Phys. Rev.*, **92** (1953) 531.
- [18] G.K. Werner, *Phys. Rev.*, **93** (1954) 633.
- [19] G.H. Kinchin, R.S. Pease, *J. Nucl. Energy*, **1** (1955) 200.
- [20] R.C. Fletcher, W.L. Brown, *Phys. Rev.*, **92** (1953) 585.
- [21] Thompson, J.J, *Phil. Mag.*, **6-23** (1912) 449.
- [22] P. Sigmund, A. Gras Marti, *Nuclear Instruments & Methods*, **182/183** (1982) 25.
- [23] K. Dettmann, G. Leibfried, K. Schroeder, *Phys. Status. Solidi.*, **22** (1967) 433.
- [24] C.A. English, W.J. Phythian, A.J.E. Foreman, *J. Nucl. Mat.*, **174** (1989) 135.
- [25] C. Abromeit, *J. Nucl. Mat.*, **216** (1994) 78.
- [26] J.F. Ziegler, J.P. Biersack, M.D. Ziegler, 'The Stopping and Range of Ions in Matter', Srim Co., USA (2008).
- [27] N. Bohr, *Phil. Mag.*, **25** (1913) 10.
- [28] F. Bloch, *Z. f. Physik*, **81** (1933) 363.
- [29] H.A. Bethe, *Z. f. Physik*, **76** (1933) 293.

- [30] E. Fermi, *Phys. Rev.*, **57** (1940) 485.
- [31] W.E. Lamb, *Phys. Rev.*, **58** (1940) 696.
- [32] J. Knipp, E. Teller, *Phys. Rev.*, **59** (1941) 659.
- [33] N. Bohr, *Phys. Rev.*, **59** (1941) 270.
- [34] N. Bohr, *Phys. Rev.*, **58** (1940) 654.
- [35] J. Lindhard, *Mat. Fys. Medd. Kgl. Dan. Vid. Selsk*, **28** (1954) 8.
- [36] J. Lindhard, M. Scharff, *Mat. Fys. Medd. Kgl. Dan. Vid. Selsk*, **27** (1953) 15.
- [37] J. Lindhard, M. Scharff, H.E. Schiott, *Mat. Fys. Medd. Kgl. Dan. Vid. Selsk*, **33** (1963) 14.
- [38] A. Sommerfield, *Z. f. Physik*, **78** (1932) 283.
- [39] G. Moliere, *Z. f. Naturforschung*, **A2** (1947) 133.
- [40] W. Lenz, *Z. f. Physik*, **71** (1932) 713.
- [41] W. Lenz, W. Jensen, *Z. f. Physik*, **77** (1932) 722.
- [42] N. Bohr, *Mat. Fys. Medd. Kgl. Dan. Vid. Selsk*, **18** (1948) 8.
- [43] W. Brandt, M. Kitagawa, *Phys. Rev.*, **25B** (1982) 5631.
- [44] O.B. Firsov, *Sov. Phys.*, **9** (1959) 1076.
- [45] C.D. Moak, M.D. Brown, *Phys. Rev.*, **149** (1966) 244.
- [46] M.D. Brown, C.D. Moak, *Phys. Rev.*, **B6** (1972) 90.
- [47] S. Kreussler, C. Varelas, W. Brandt, *Phys. Rev.*, **23B** (1981) 82.
- [48] R. Webb, 'Introduction to Ion-Solid Interactions', Surrey Ion Beam Centre, Ion Beam Training Course (2009).
- [49] M.T. Robinson, O.S. Oen, *Phys. Rev.*, **132** (1963) 2385.
- [50] G.R. Piercy, F. Brown, et al., *Phys. Rev. Lett.*, **10** (1963) 399.
- [51] H. Lutz, S. Sizmann, *Phys. Lett.*, **5** (1963) 113.
- [52] R.S. Nelson, M.W. Thompson, *Philos. Mag.*, **8** (1963) 1677.
- [53] L.C. Feldman, J.W. Mayer, 'Fundamentals of Surface and Thin Film Analysis', North-Holland, New York, (1986).
- [54] W.-K. Chu, J.W. Mayer, M.A. Nicolet, 'Backscattering Spectrometry', Academic Press: New York, (1978).
- [55] L.R. Greenwood, R.K. Smither, 'SPECTER: Neutron Damage Calculations for Materials Irradiations', Technical Report, Argonne National Lab. USA (1985).
- [56] G.R. Odette, D.R. Dorian, *Nucl. Technol.*, **29** (1976) 346.
- [57] M.T. Robinson, *Nucl. Instr. and Meth.*, **B67** (1992) 396.
- [58] L. Peralta, *Eur. J. Phys.*, **23** (2002).

[59] B.E. Watt, *Phys. Rev*, **31** (1952).

[60] J.C. Slater, *J. Appl. Phys.*, **22** (1951) 237.

[61] B.T. Kelly, 'Physics of Graphite', Applied Science Publishers, London, (1981).

[62] G.J. Dienes, *J. Appl. Phys.*, **23** (1952) 1194.

[63] J.H.W. Simmons, 'Radiation Damage in Graphite', Pergamon Press, Oxford, (1965).

Chapter 4

Raman Analysis of Graphite After Inert-Gas Ion-Irradiation ($E < 10 \text{ keV}$)

4.1. Introduction

Raman spectroscopy of black materials such as carbon black and graphite was not possible until the advent of the laser as a Raman source [1]. Since then much work has been carried out on the Raman spectra of such materials due to a renewed interest in their structural properties as a result of their many valuable applications, particularly in the semiconductor [2-4] and nuclear industries [5-9].

Raman scattering is extremely sensitive to structural disorder due to radiation damage, and therefore is an excellent tool for determining the effects of radiation damage upon the graphite lattice. The instrument is used to detect returning photons which have been inelastically scattered due to the change of polarization caused by the phonon mode [10] (c.f. Chapter 2).

Early work in the field by Tuinstra and Koenig [11] used Raman spectroscopy to study the structure of various types of graphite, ranging from highly crystalline graphite and more polycrystalline and disordered carbon black and natural carbon flakes. The authors identified the presence of an intense single band at $\sim 1580 \text{ cm}^{-1}$ for the highly crystalline samples, whereas the more disordered graphite displayed another band at $\sim 1350 \text{ cm}^{-1}$. This band was

observed to increase in intensity, with respect to the 1580 cm^{-1} band, the more polycrystalline the material was. Subsequently the two bands were referred to as the G (graphite) band, at 1580 cm^{-1} , and the D (disorder) band at $\sim 1350\text{ cm}^{-1}$.

Smith et al [12] used Raman spectroscopy in an early analysis of argon ion irradiated graphite and found that the same band at 1350 cm^{-1} started to appear as a result of the Ar^+ radiation. Therefore it was concluded that the ion irradiation induced a structural decomposition, changing originally crystalline carbon material to more disordered amorphous-like carbon; from this work it became clear that ions could indeed damage the graphite lattice and Raman could be effectively used to monitor that damage, which may be related to similar processes that occur through neutron bombardment within a reactor core.

4.2. Experimental Apparatus

Ion irradiations were carried out in the UHV system described previously (Chapter 2) and the experimental parameters used are as stated. After each irradiation the system was vented with nitrogen and the irradiated samples were removed and analysed through Raman spectroscopy. Samples of HOPG were used, unless otherwise stated, to avoid the difficulties involved in obtaining consistent Raman data from polycrystalline graphites [13]. When required, a fresh HOPG surface was obtained through cleavage of a layer using adhesive tape.

4.3. Raman Investigation

4.3.1. Raman Analysis of Virgin Graphites.

To appreciate the ion-induced effects on the Raman spectra of graphite it is important to first know the nature of the virgin material from which we can compare and contrast. Fig. 4.1 is the Raman spectra obtained for virgin samples of HOPG, Gilsocarbon and PGA.

As previously mentioned, the HOPG spectra contains a single intense G band at 1580 cm^{-1} in the lower energy regime (first order spectrum) and three more peaks in the higher energy regime (second order spectrum), including a small peak at $\sim 2450\text{ cm}^{-1}$, a more intense doublet peak at $\sim 2710\text{ cm}^{-1}$ (D* band) and a further smaller peak at $\sim 3250\text{ cm}^{-1}$ (G* band). Gilsocarbon and PGA exhibit the D band at 1350 cm^{-1} which is not present in HOPG, and also

an additional band is present in the second order spectra at $\sim 2950 \text{ cm}^{-1}$. In the case of Gilsocarbon and PGA the peak at $\sim 2710 \text{ cm}^{-1}$ is observed to be considerably less defined. An additional disorder-related band at $\sim 1620 \text{ cm}^{-1}$ is also present in the nuclear grade material but not observed in the more ordered HOPG.

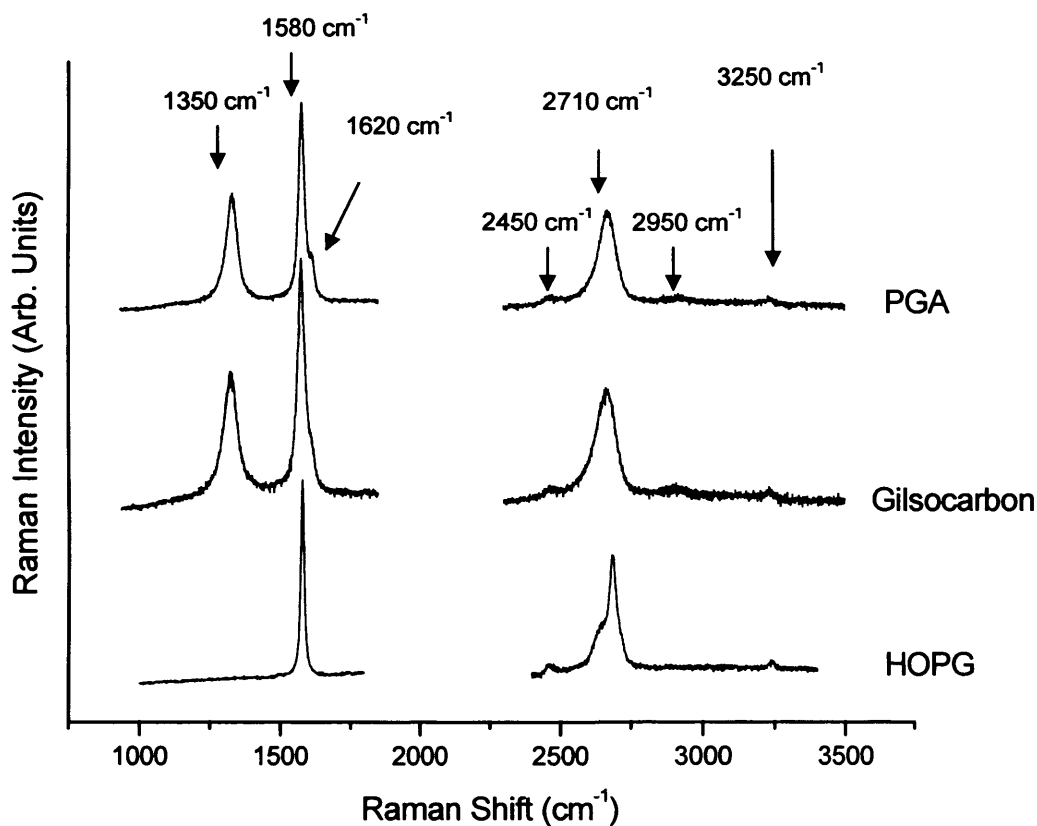


Fig. 4.1: Raman spectrum of three different virgin graphitic materials. Peak positions are not exact, but within $\pm 5 \text{ cm}^{-1}$.

4.3.2. Origin of the Raman Bands

In order to understand the significance of each of these bands and the various changes induced through ion-irradiation it is important to know their origins, an area which has been studied intensely, with many publications throughout the 1970's involving Raman [14-15] and infra-red [16-17] studies of graphite. From this work researchers were able to accurately establish the zone-centre optic modes for graphite, assigning the phonon energies and symmetries to all the high-symmetry points in the Brillouin zone [18]; despite this intense interest it should be noted that, even now, the full underlying mechanisms involved in the Raman analysis of graphitic materials is still not perfectly understood.

4.3.3. Symmetry Elements of Graphite.

Since the atomic layers in graphite are held together only by very weak Van der Waals forces then it is often sufficient to study only a single two-dimensional atomic layer (graphene). This, at first, makes things a lot easier as the effect of stacking the planes is not considered. However in Raman spectroscopy even the weak Van der Waals forces can have an effect on the selection rules and hence for this reason the symmetries for the three-dimensional graphite must be subsequently calculated as they will be different from two-dimensional graphene.

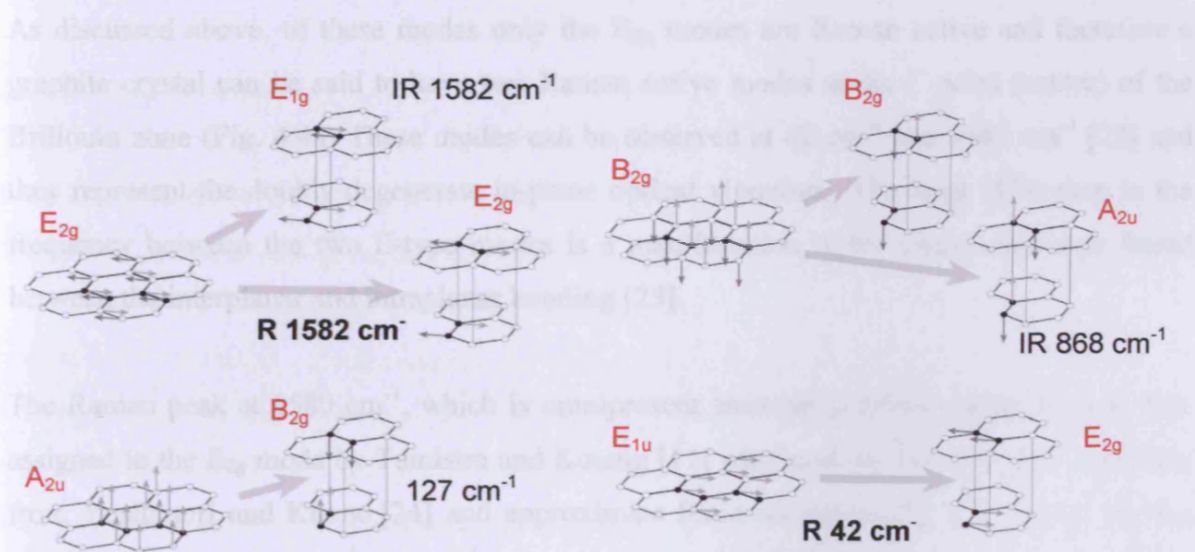


Fig. 4.2: Phonon eigenvectors for graphene and graphite, taken from Reich and Thomsen [19].

The six normal vibrational modes of graphene (at $q=0$) (where q is the wave vector of the scattered phonon) have been found by standard methods [10,20-21] and can be described by the following irreducible representations:

$$\Gamma_{\text{vib}, 2D} = A_{2u} + B_{2g} + E_{1u} + E_{2g}.$$

Where A_{2u} and E_{1u} are translations of the plane and the B_{2g} mode is an optical phonon arising from carbon atoms moving perpendicular to the graphene plane. Of these only the doubly degenerate optical E_{2g} vibrational mode is Raman active (Fig. 4.2).

From the optic modes derived for graphene, the phonon modes of three-dimensional graphite can be found by combining the above two-dimensional modes either in phase i.e. $\Gamma_{\text{vib}, 2\text{D}} \times A_{1g}$ or out of phase, $\Gamma_{\text{vib}, 2\text{D}} \times B_{1u}$.

From Fig. 4.2 we can see how the graphene modes are able to split into higher frequency out-of-phase and lower frequency in-phase vibrations and thus the phonon symmetries of graphite are found to be:

$$\Gamma_{\text{vib}, 3\text{D}} = 2A_{2u} + 2B_{2g} + 2E_{1u} + 2E_{2g}$$

As discussed above, of these modes only the E_{2g} modes are Raman active and therefore a graphite crystal can be said to have two Raman active modes at the Γ point (centre) of the Brillouin zone (Fig. 4.4a) These modes can be observed at 42 cm^{-1} and 1582 cm^{-1} [22] and they represent the doubly degenerate in-plane optical vibration. The large difference in the frequency between the two E-type modes is a manifestation of the large anisotropy found between the interplanar and intraplanar bonding [23].

The Raman peak at 1580 cm^{-1} , which is omnipresent amongst graphitic materials, was first assigned to the E_{2g} mode by Tuinistra and Koenig [11] who used secular equations, formulas from Yoshimori and Kitano [24] and approximate force constants [25] to calculate the E_{2g} frequency to be 1688 cm^{-1} . Despite being $>100 \text{ cm}^{-1}$ in error, this was deemed within experimental error (due to the approximate force constants used) and hence these calculations were seen as evidence for the assignment of the Raman band at 1582 cm^{-1} to the E_{2g} mode (Fig. 4.3).

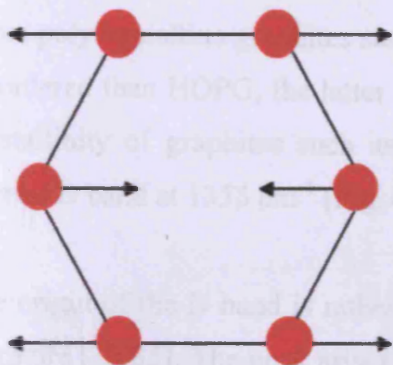


Fig. 4.3: The breathing mode of E_{2g} symmetry responsible for the G band observed.

It should be noted that the other E-symmetry mode at 42 cm^{-1} is the result of interplanar “rigid-layer shear” whereby the graphene planes slide over each other [19] and can only be seen through special techniques [26].

The A_{2u} and E_{1u} modes are IR active and have been observed at 867 and 1588 cm^{-1} respectively [16]. The B_{2g} modes are optically inactive, however, neutron scattering experiments have been carried out whereby one of the modes has been observed at 127 cm^{-1} whereas the other appears at a frequency similar to that of the A_{2u} mode at approximately 867 cm^{-1} [27-28]. Contrary to the E-symmetry modes, the A and B symmetry modes represent the out-of-plane atomic displacements [22].

4.3.4. Raman Activation

When the photon energy is above the band gap, electrons of all wave vectors can be excited. In graphite, the band gap lies in the visible range only in a small region of k space around the K point (Fig. 4.4). Disordered carbon materials consist of both sp^3 and sp^2 sites. sp^3 sites involve only σ -bonding orbitals whereas sp^2 sites also possess π -bonding character. Unlike σ -bonding, π -bonding can be long range, and can interact with many π states close by, forming conjugated bonds as is the case in benzene. Due to this interaction with neighbouring π states longer range polarisability is enhanced. This enhancement increases as the amount of π – bonding increases, which is maximised when pairs of aligned π states, six-fold aromatic rings, or graphitic clusters are formed [29].

4.3.5. Disorder Induced Raman Bands

More polycrystalline graphites such as Gilsocarbon and PGA are inherently more structurally disordered than HOPG, the latter is much more of an ‘ideal’ graphite structure. The reduced crystallinity of graphites such as Gilsocarbon and PGA gives rise to the aforementioned Raman D band at 1355 cm^{-1} (Fig. 4.1).

The origin of the D band is rather complex and has been debated thoroughly throughout the literature [30-35]. The peak arises from phonons near the K zone boundary, which undergo a breathing movement of A_{1g} symmetry (Fig. 4.5). The A_{1g} mode is forbidden in ‘ideal’ graphite as the changes in polarisability cancel over the infinite crystal; in the presence of

structural disorder however, this no longer holds true and subsequently the D band can be observed.

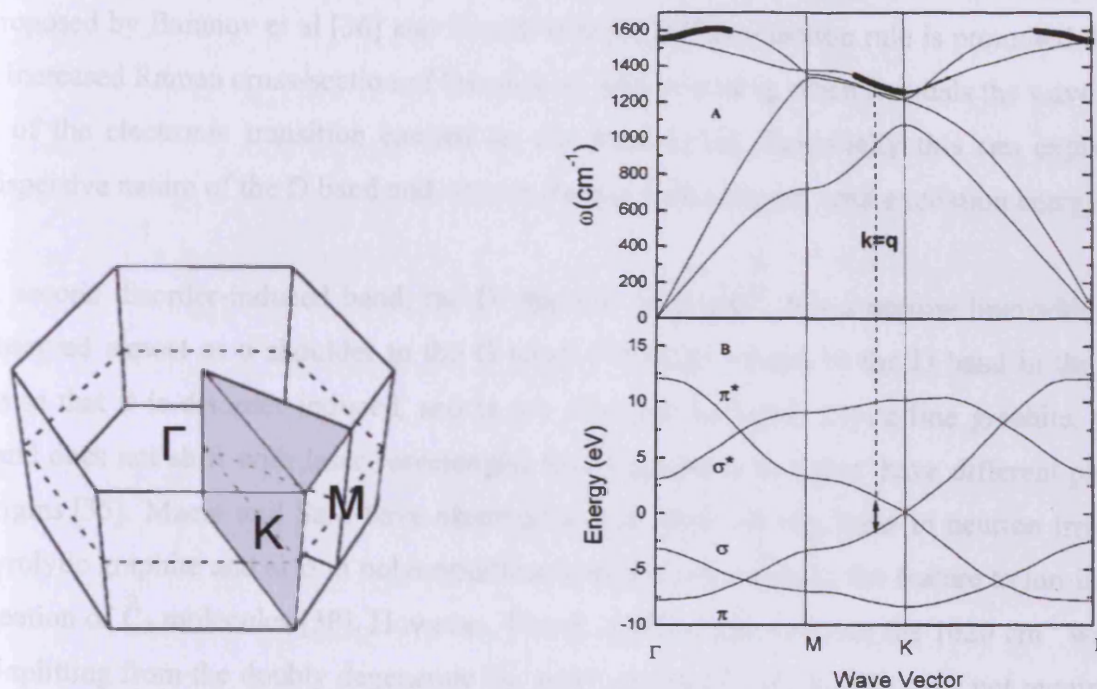


Fig. 4.4: a) (left) the first Brillouin Zone[†] of graphite. The irreducible domain is spanned by the triangle linking the critical point of high symmetry, Γ -M-K- Γ . b) (right) The phonon dispersion curve (top) and electronic band structure (bottom) of a single layer of graphite, taken from references [18] and [25] respectively. The σ states lie far from the Fermi level (double arrow). The π and empty π^* states overlap and touch at the K boundary. The bold line from K to M corresponds to phonons selected by the $k = q$ 'quasi' selection rule, indicated by the vertical dashed line. The bold line from Γ marks the mapping of the E_{2g} eigenvector.

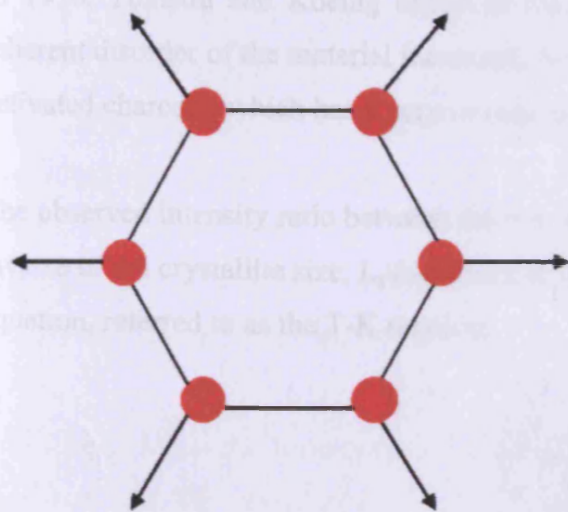


Fig. 4.5: Breathing mode of A_{1g} symmetry, responsible for the disorder (D) band.

[†] The Brillouin Zone is a defined primitive cell within the reciprocal lattice of a system within which the behaviour of waves is representative of the behaviour throughout the entire system [1].

The fundamental Raman selection rule of $q \approx 0$ is relaxed through disorder and the A_{1g} breathing mode is activated through the enhancement of the $k = q$ ‘quasi’ selection rule as proposed by Baranov et al [36] and Pocsik et al [37]. This selection rule is promoted through an increased Raman cross-section of the phonon wave vector q , when it equals the wave vector k of the electronic transition excited by the photon [32]. Essentially this can explain the dispersive nature of the D band and why its Raman shift changes with excitation energy [35].

A second disorder-induced band, the D’ band at 1620 cm^{-1} , has a narrow linewidth and is observed almost as a shoulder to the G band. Although related to the D band in the broad sense that it is disorder induced, and is not observed in highly crystalline graphite, the D’ band does not shift with laser wavelength, thus suggesting that they have different physical origins [35]. Maeto and Sato have observed the presence of this band in neutron irradiated pyrolytic graphite and also in polycrystalline material and assigned the feature to ion-induced creation of C_2 molecules [38]. However, Tsu et al [39] suggested that the 1620 cm^{-1} was due to splitting from the doubly degenerate E_{2g} band and that C_2 molecules were not required for its presence. Modern Raman theory has led to the identification of a double resonance Raman mechanism which is now seen as responsible for the 1620 cm^{-1} feature along with the other disorder induced bands (c.f. 4.4.4.).

4.3.6. The TK Relation

In 1970, Tuinstra and Koenig observed that the intensity of the D band increased as the inherent disorder of the material increased, from commercial grade polycrystalline graphite to activated charcoal, which has a very intense D band signal [11].

The observed intensity ratio between the two bands, I_D/I_G , was found to be proportional to the inverse of the crystallite size, L_a (determined through x-ray diffraction), through the following equation, referred to as the T-K relation.

$$\frac{I_D}{I_G} = \frac{C}{L_a} \quad (\text{Eq. 4.1})$$

Where $C = 4.4 \text{ nm}$ when $\lambda = 514.5 \text{ nm}$.

The relation has been verified many times using XRD to determine the crystallite size independently [30,40-42] and has been explained theoretically by Lespade et al who explained Eq. 4.1 with respect to the finite size of the crystallites [43]. Consequently Raman has been widely used in the field to monitor the accumulation of damage in graphite.

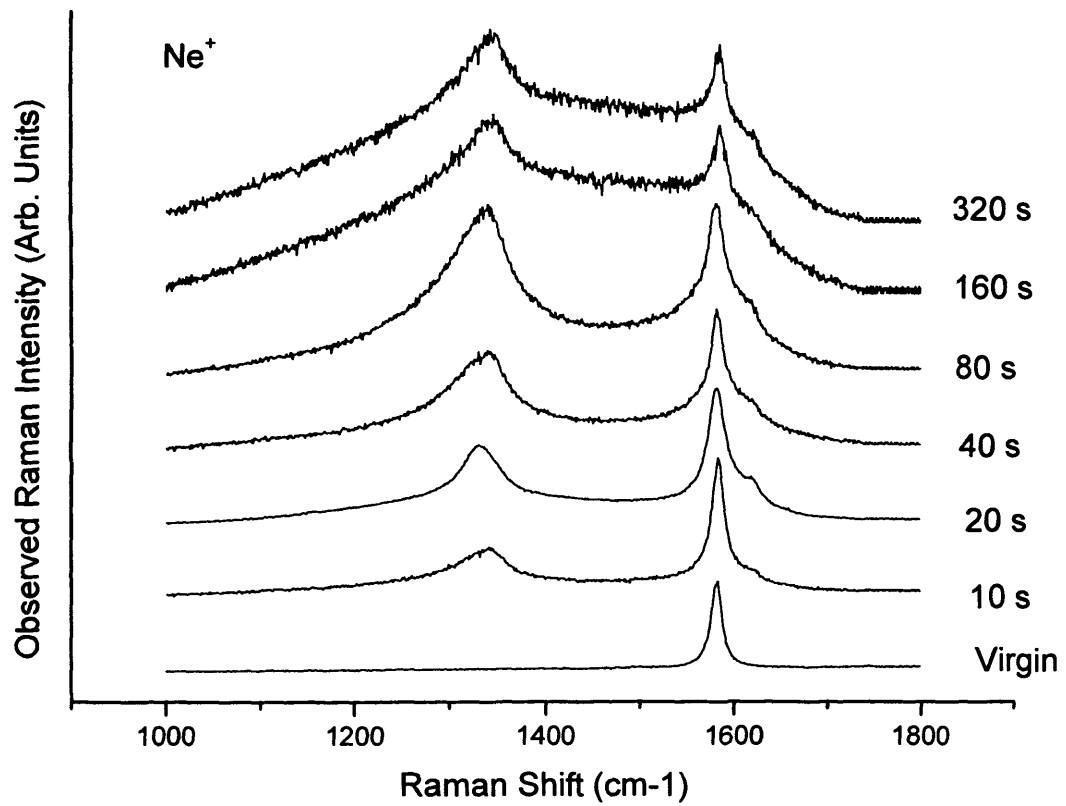
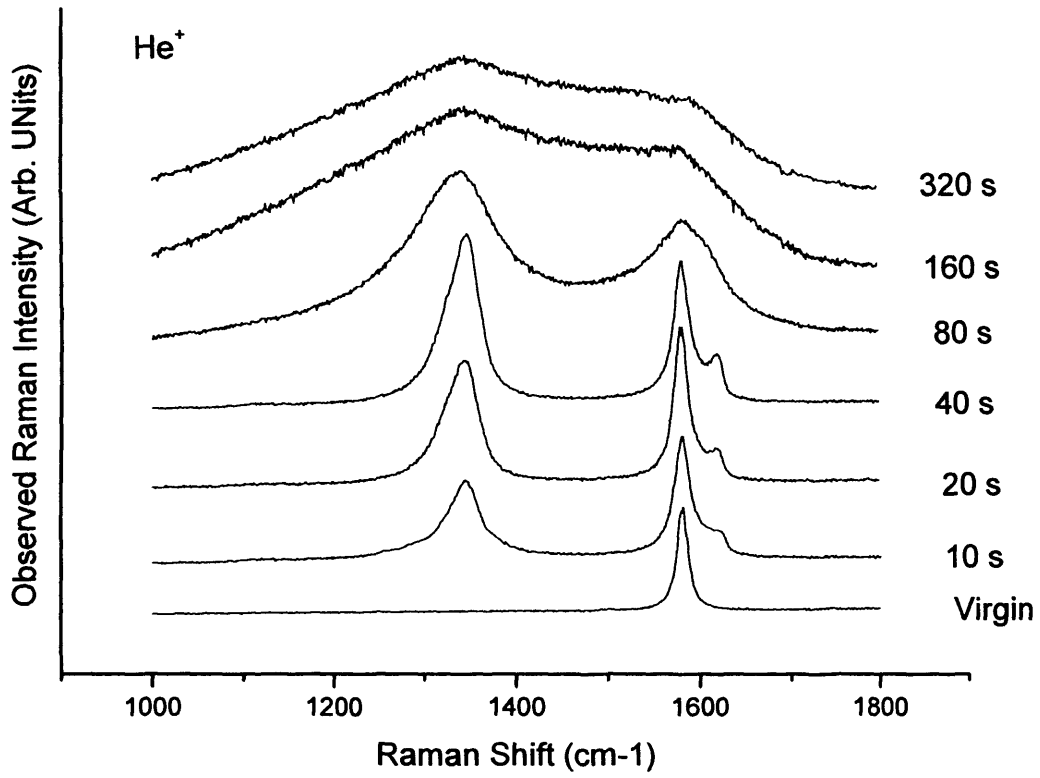
The T-K relation links the D peak intensity to phonon confinement caused through the production of structural defects. It works through relating the intensity of the essentially forbidden phonon to the “amount of breaking” of the $q \approx 0$ selection rule. The relation works very well and was fundamental to many Raman investigations into ion-irradiated graphite particularly through the 1990s [44-48]. However at higher doses the T-K relation has been shown to break down and should not be used exclusively when the crystallites become very small, e.g. < 2 nm [49-50]. At such high levels of damage the I_D/I_G ratio may become saturated and no longer follow linearly the rate of damage accumulation. Such results have been published by Theodosiou et al [51] and are discussed in Chapter 5. However, the theory of phonon confinement does not explain on its own certain features of the Raman spectrum, such as the relatively high peak intensities of the disorder bands, and as a result the activation of the D peak is now accepted to be due to a double resonance effect [29] (c.f. 4.4.4).

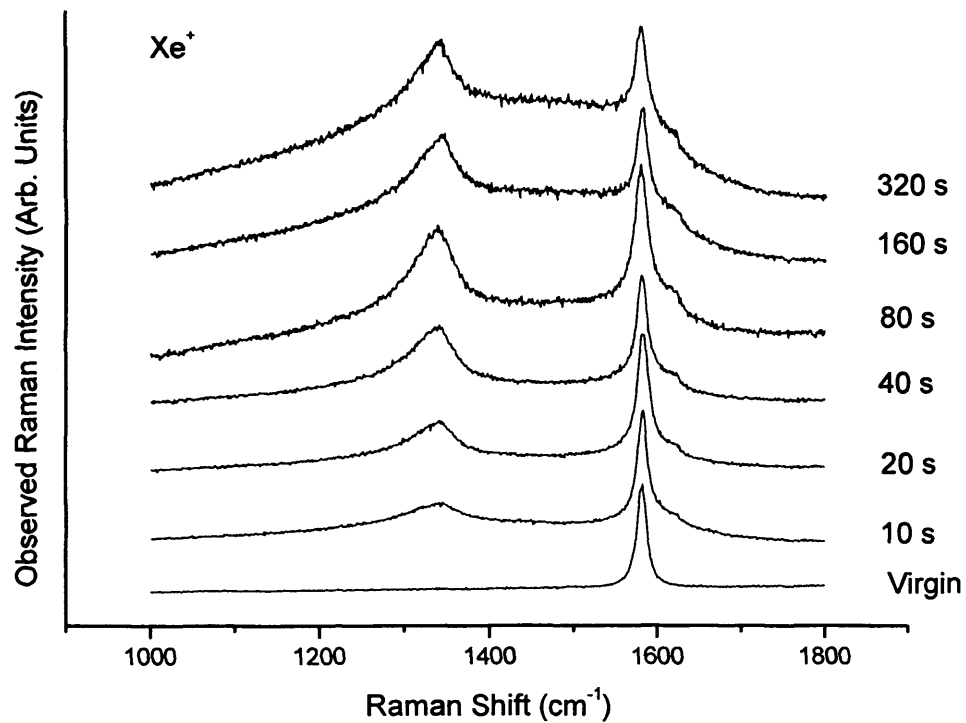
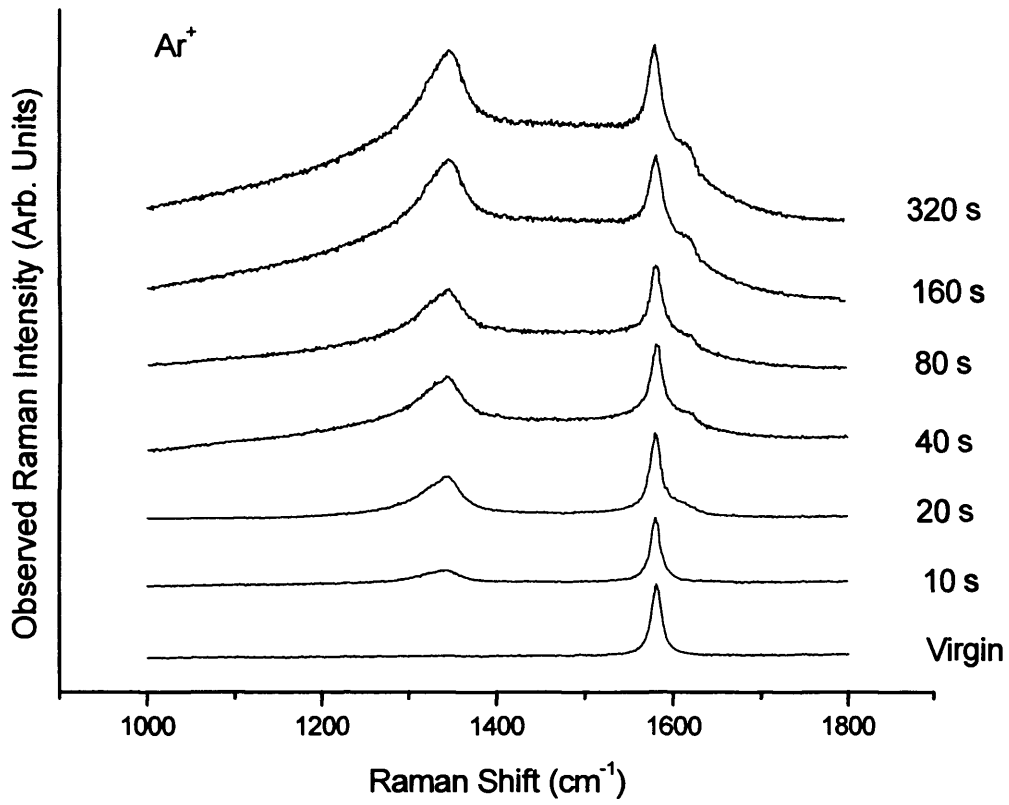
4.4. Results

4.4.1. A Time-Resolved Raman analysis

Samples of HOPG (5.0 x 5.0 x 2.0 mm) were irradiated with 5 keV He⁺, Ne⁺, Ar⁺ and Xe⁺ ions in the custom-built UHV ion irradiation chamber described previously (See 2.2.1). A constant gas pressure of 2.0×10^{-5} mbar was used throughout and all irradiations were carried out at room temperature. Four samples were irradiated, one for each ion, with total doses not exceeding 5.0×10^{19} ions.m⁻². Sample currents were measured through a multimeter connected to the target through an electronically isolated probe. The ion flux was approximately 5.0×10^{12} ions.cm⁻²s⁻¹ and Raman measurements were taken after an irradiation time of 10, 20, 40, 80, 160 and 320 s.

Figs. 4.6_{A-D} show the time-resolved Raman spectra obtained for ion irradiation using He⁺, Ne⁺, Ar⁺ and Xe⁺ respectively. Each spectrum was taken at twice the total irradiation time of the previous spectrum, up to a time of 320 s. N.B. only one sample was used for each ion irradiation and hence the time is cumulative





Figs. 4.6A-D: A time-resolved analysis of the Raman spectra obtained for 5 keV ion irradiation of HOPG, using He⁺, Ne⁺, Ar⁺ and Xe⁺ respectively at a constant ion flux of 5.0×10^{12} ions.cm⁻².s⁻¹.

Consistent features were observed for each of the ions studied, with trends agreeing with previously published work in the field [44-45,52]. That is, the I_D/I_G ratio increases with increasing fluence, and hence the crystallite size is decreasing. Importantly these trends are the same as those observed in neutron irradiated graphite, which is as expected due to comparable damage mechanisms (as discussed in the previous chapter). Niwase et al [53] conducted Raman analysis on ISO-880U nuclear grade graphite taken from the core of the Japan Materials Testing Reactor which was irradiated at fluences up to 7.0×10^{20} n.cm⁻² and at energies not below 1.0 MeV. The results they obtained are very similar to those seen in Figs. 4.6A-D, particularly to those obtained for He⁺.

The emergence of the disorder induced D band at approx 1350 cm⁻¹ is the prominent feature, which steadily increases in intensity with increasing fluence; simultaneously the intensity of the G band slowly decreases resulting in an increased I_D/I_G ratio and reflecting a decrease in the crystallite size. Other notable features include an increase in the linewidth of the D band and a stark increase in the intensity of the spectral region between the D and G bands, in the range 1400 cm⁻¹ – 1580 cm⁻¹ which is particularly prominent at higher doses. The extent of the broadening seems to be more significant for the He⁺ irradiated samples, and is likely to be mass related. The D' peak centred at 1620 cm⁻¹ becomes apparent after 10 seconds irradiation, increasing in intensity before becoming a shoulder to the G band. In the case of He⁺ bombardment the D' peak seems to be more prominent and separated from the G band, up to an irradiation time of 80 seconds, where again it merges with the G band and becomes indistinguishable from it. This happens only at an I_D/I_G ratio of approximately 1.4, corresponding to a crystallite size of around 3.2 nm (Eq. 4.1).

Using the Raman software, the I_D/I_G ratio from the Raman spectra can be calculated whereby, via the TK relation, it can be used to provide information on the crystallite size, that is, the amount of damage caused through ion bombardment (Fig. 4.7).

The graph shows two main trends. The rate of increase of R_{obs} (observed I_D/I_G ratio) i.e. the rate of increase of damage, is initially rapid before reaching a particular dose, which in this case is 4.0×10^{18} ions.m⁻² (80 s irradiation time) after which there is relatively little increase and the shape of the graph begins to plateau. The other significant trend is that the R_{obs} values

obtained are higher at each particular time interval, the lighter/smaller the incident ion species.

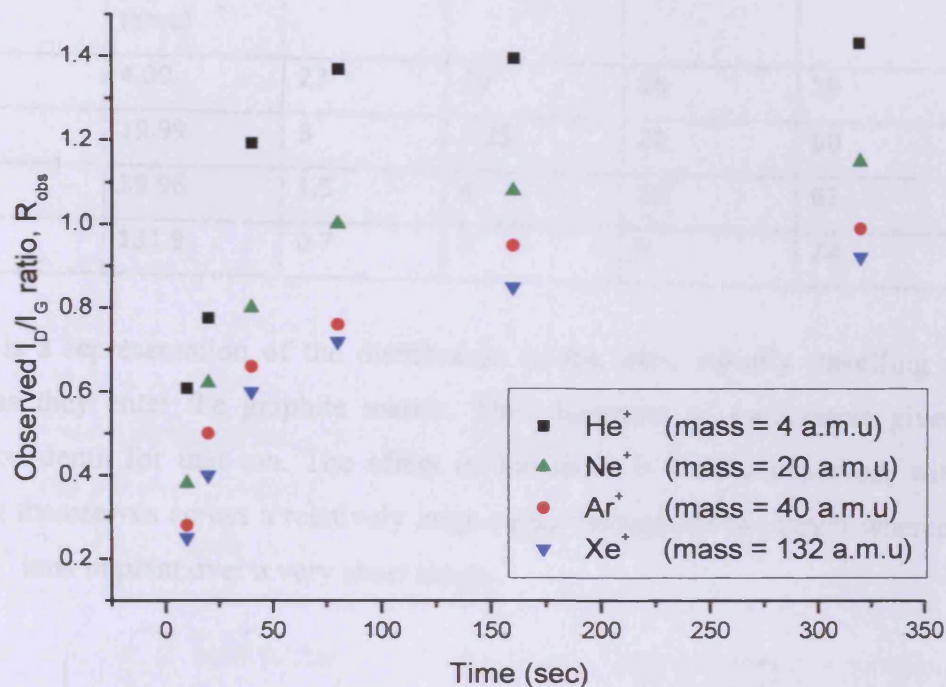


Fig. 4.7: Time-dependence of the observed I_D/I_G ratio for 5 keV ion irradiation.

This seems to be counterintuitive, since smaller ions will have less probability of colliding with a carbon atom and initiating a collision cascade. Conversely, larger ions such as Xe^+ will have a larger destructive area and may interact with more than one carbon atom at a time. However, the differences observed are related directly to the penetration depth of the ions into the graphite material, which itself is dependant on the ion mass. To calculate the penetration depths of the ions into the graphite and their behaviour as they penetrate the surface, a Monte-Carlo code, The Stopping and Range of Ions in Matter (SRIM 2008) [54], can be used. The theory behind this has been discussed in detail in Chapter 3.

4.4.1.1. Ion Implantation Profiles – SRIM 2008

The damage profile within a target caused by ion bombardment is known to be approximated by a Gaussian function [46]. The SRIM 2008 code can calculate this for many ion-solid interactions and for the irradiation of graphite by 5 keV He^+ , Ne^+ , Ar^+ and Xe^+ ions the results are presented in Table 1:

Table 4.1: Parameters of the damage profile approximated by a Gaussian function for the irradiation of graphite by 5 keV ions. χ_0 is the mean implantation depth, σ is the standard deviation and ρ is the whole range of energy distribution, which is the range over which the ions deposit all their kinetic energy.

Ion	Ion Mass (amu)	χ_0 (nm)	σ (nm)	ρ (nm)	Vacancies/ion
He ⁺	4.00	23	29	88	29
Ne ⁺	19.99	3	6.25	22	60
Ar ⁺	39.96	1.5	4	12	63
Xe ⁺	131.9	0.7	3	9	74

Fig. 4.8 is a representation of the distribution of the ions, initially travelling with 5 keV energy, as they enter the graphite matrix. The maximum of each curve gives the mean penetration depth for that ion. The effect of ion mass is clearly observed, with He⁺ ions spreading themselves across a relatively large range throughout the target whereas the much larger Xe⁺ ions implant over a very short range.

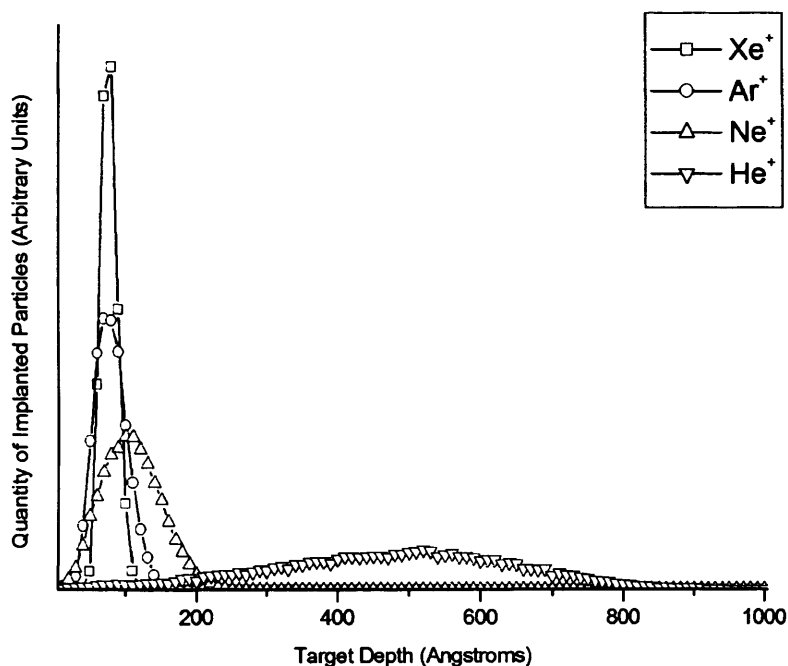


Fig. 4.8: The implantation profiles of 5 keV He⁺, Ne⁺, Ar⁺ and Xe⁺ ions in graphite modelled by SRIM 2008.

From Fig. 4.8 we can envisage a scenario by which a heavier, larger ion may not penetrate as deeply as a lighter ion, for the same energy; the heavier atoms may cause significantly more damage by producing many more carbon atom displacements. On the other hand a lighter ion may cause much less damage in that same particular region but may cause more damage at

greater depths to which the larger ions could not reach. This is emphasised by the increase in vacancies per ion as ion mass increases, with a Xe^+ ion causing approximately 74 vacancies/ion whilst a He^+ ion produces only 29 (Table 4.1).

To get accurate information on the damaged caused by the various ions, and hence understand more effectively the influence of ion mass, it is important to analyse the Raman data coming from the damaged region only. This is because the optical skin depth, that is the depth at which the Raman laser can penetrate into the graphite, is 40 nm for light of wavelength 514.5 nm [47-48]. Therefore, the data in Figs. 4.6_{B-D} consists of a superposition of both damaged and undamaged regions, which for Xe^+ particularly is largely the latter, and can perhaps give a misleading representation of the true ion effects. If for example Raman information was obtained from only the first 5 nm then the signal for the disorder induced band would be far stronger for Xe^+ irradiation, even stronger than for He^+ irradiation. This has been proved by Ishida et al [55] who studied HOPG irradiated by 2 keV argon ions through surface enhanced Raman scattering (SERS); their results agreed with their predictions and the D band intensity was far higher than an identical sample carried out through traditional Raman analysis.

To obtain the actual intensity I_D/I_G ratio, from the damaged region only, the observed intensity ratio, R_{obs} must be converted to the actual intensity ratio, R_0 , through the following equation:

$$R_{\text{obs}} = \frac{8R_0 P \pi m}{\lambda} \int_0^{\rho} F(x) \exp(-8\pi m x / \lambda) dx \quad (\text{Eq. 4.2})$$

Where ρ is the whole range of energy deposition (see Table 4.1), m is the optical parameter (0.9 for carbon material), λ is the wavelength of the exciting light, x is the depth and $F(x)$ is the depth profile of the damaged layer, normalised to unity).

To solve Eq. 4.2 it is first necessary to run the SRIM calculation for a period of time under the correct parameters: ion energy, incident angle, target identity (graphite) and density. A simulation of the ion-graphite interaction including the resulting cascades is run and after an appropriate amount of ions, in this case 5000, the simulation is then stopped and the data exported and fitted to a Gaussian distribution.

Fig. 4.9 is a screenshot taken from SRIM 2008 run for the parameters outlined in Table 1. The different damage profiles can be easily seen for the different ions studied.

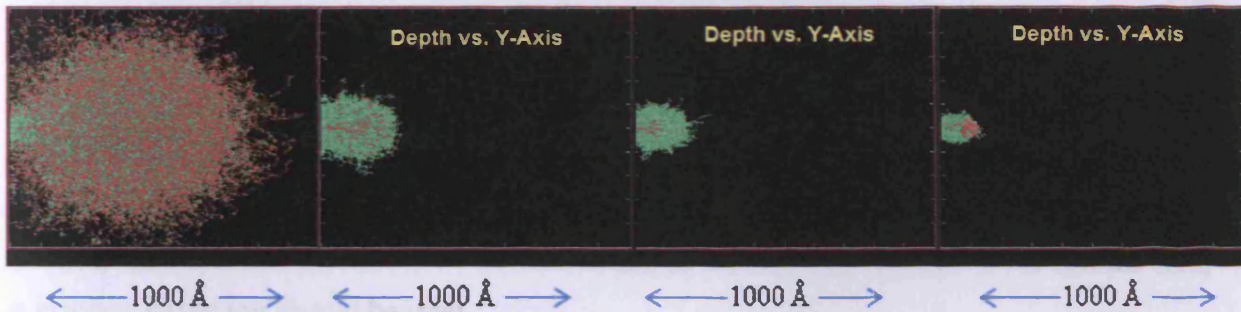


Fig. 4.9: A visual representation of the distribution of 5 keV He^+ , Ne^+ , Ar^+ and Xe^+ ions (left to right) as they penetrate a graphite surface. Green represents displaced carbon atoms and red represents the ion path.

For each of these ion irradiation simulations SRIM can output files providing information on the energy distribution of the ion before coming to rest. The data can be plotted and a Gaussian curve can be fitted.

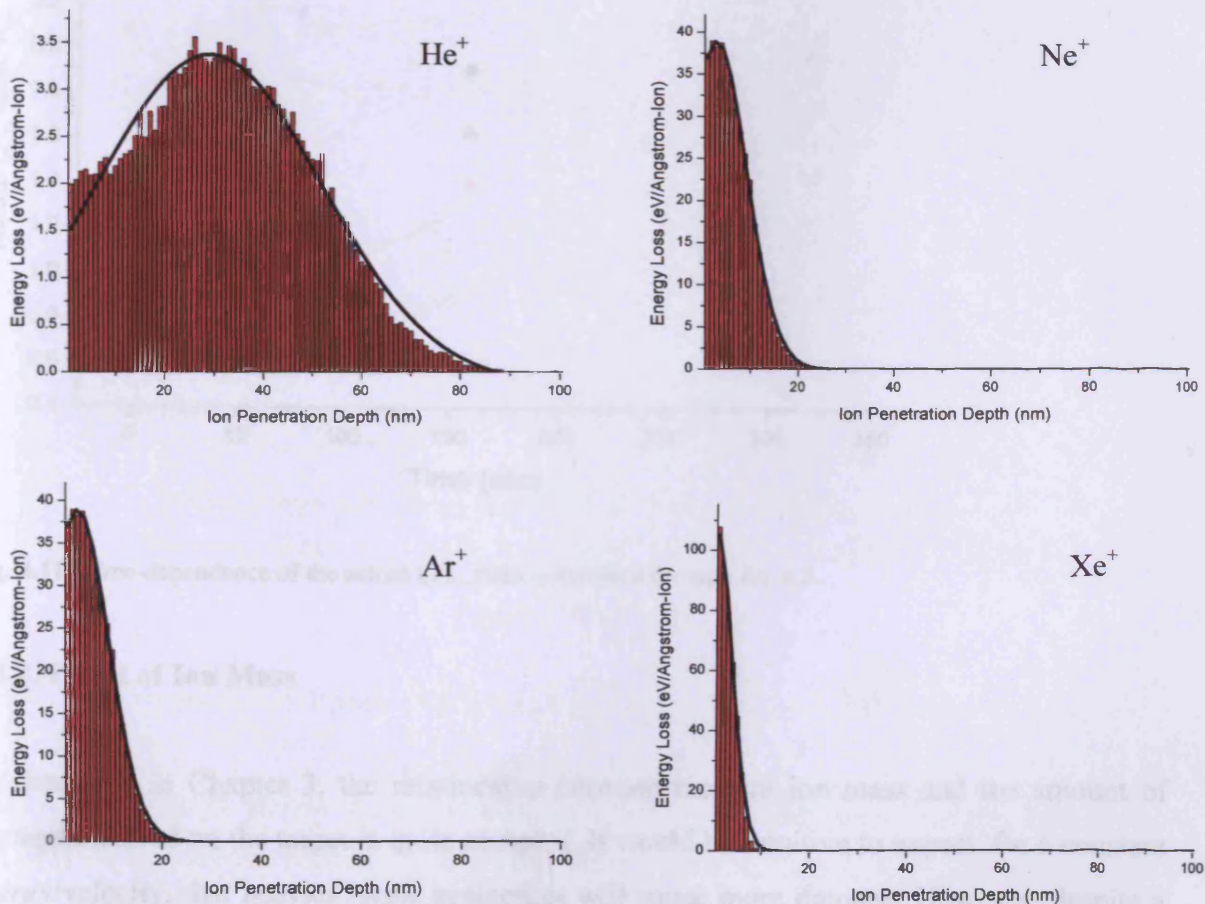


Fig. 4.10: Plot of ion energy distribution as calculated through SRIM 2008 for 5 keV He^+ , Ne^+ , Ar^+ and Xe^+ passing through graphite. The black line is the result of a Gaussian fit.

The Gaussian is fitted such that the integral of the area under the curve is normalised to unity. This then allows for Eq. 4.2 to be solved giving values of $R_0 \approx 1, 1.5, 2$ and $3 \times R_{\text{obs}}$ for He^+ , Ne^+ , Ar^+ and Xe^+ respectively and thus a plot analogous to Fig. 4.7 can be made with actual intensity ratios for each of the ions (Fig. 4.11).

The results now show that the ions of heavier mass actually lead to a higher I_D/I_G ratio i.e. lead to increased damage albeit throughout a smaller depth. Therefore for breaking bonds and causing significant loss of structure i.e. a tendency towards amorphisation in the surface area, a heavier, larger ion should be used.

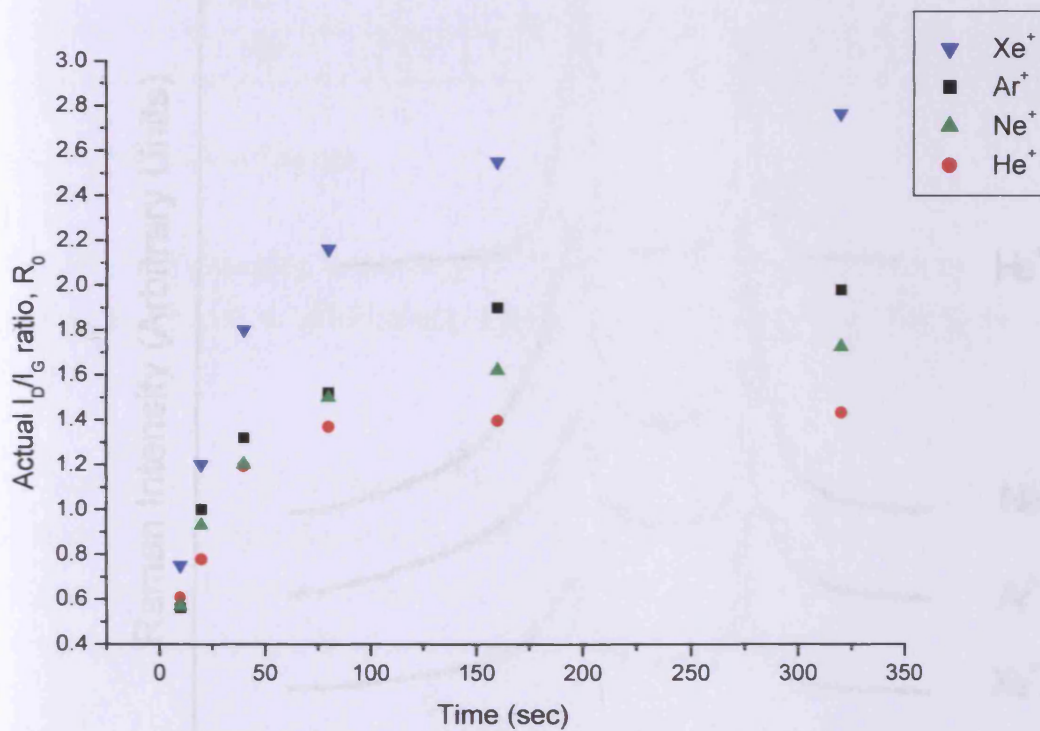


Fig. 4.11: Time-dependence of the actual I_D/I_G ratio, calculated through Eq. 4.2.

4.4.2. Effect of Ion Mass

As described in Chapter 3, the relationship between incident ion mass and the amount of damage incurred on the target is quite complex. It would be intuitive to expect, for a constant energy/velocity, that heavier larger projectiles will cause more damage. However, despite a greater momentum ($P=mv$), heavier ions are slowed more effectively by the bulk substrate,

leading to a relatively low penetration depth. On the other hand, lighter ions of lesser momentum will travel further into the target material because the amount of collisions with the host atoms are significantly less.

From Fig. 4.7 it can be seen that the observed I_D/I_G ratios are higher for light He^+ ions than for heavier ions this can be attributed to the reasons discussed previously. Table 4.2 contains the actual Raman intensity values which show an increased I_D/I_G ratio, in the damaged region, for the heavier ions.

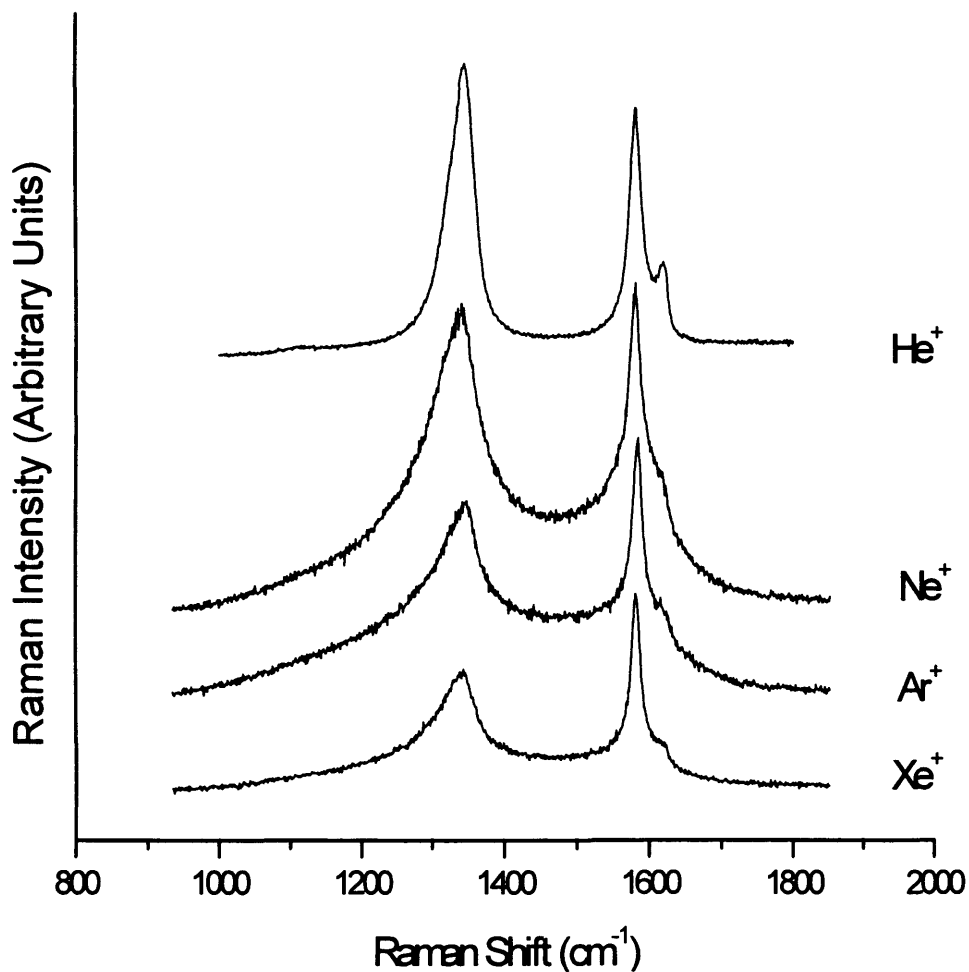


Fig. 4.12: Raman spectra of HOPG irradiated with ions of varying mass at an equal dose of 5.0×10^{14} ions.cm⁻²

Other notable features include a difference in linewidth as the ion mass changes; however, the change is non-linear. Nakamura et al [56] have shown an increase in linewidth to be inversely proportional to crystallite size, in the same way as the I_D/I_G ratio is, and consequently an increased linewidth can be taken as a loss of crystallinity. Linewidth is

expected to increase with increasing dose [44], and indeed this is observed in the present study, however it has also been found previously to increase at a faster rate for larger ions which, for the data obtained in this study, is not the case.

Table 4.2: Results of Raman analysis of HOPG irradiated with ions of varying mass at an equal dose of 5.0×10^{14} ions.cm⁻².

Ion	Ion Mass (amu)	Projected Range at 5 keV (nm)	D band linewidth (cm ⁻¹)	Observed I _D /I _G ratio (Robs)	Actual I _D /I _G ratio, R0
He ⁺	4.003	42.6	42.2	1.21	1.21
Ne ⁺	19.992	9.8	78.6	0.95	1.425
Ar ⁺	39.962	7.1	58.3	0.74	1.48
Xe ⁺	131.904	7.1	63.2	0.57	1.71

4.4.3. Effect of Ion Energy

The effect of changing ion energy is to increase the overall momentum of the incident particle and hence to subsequently increase its mean penetration depth into the graphite target.

An increase in the initial kinetic energy of the ion will result in an increase in the maximum amount of energy transferred to the first carbon atom that is hit, and hence will result in that primary knock-on atom having more energy with which to complete its collision cascade, resulting in more atomic displacements and structural disorder [57].

The SRIM simulations, Fig. 4.13 show that as expected He⁺ irradiation causes far more widespread damage than Xe⁺ for an equivalent energy, with carbon atoms being displaced beyond 100 nm for 8 keV irradiation (Table 4.2). The Xe⁺ irradiation is much more localised to the surface region, however one can presume, due to the far greater size, that the damage within this area is considerably higher. Energy distributions follow a Gaussian profile, with the mean penetration depth increasing with energy, considerably more for He⁺ than for Xe⁺ since more energy is required to implant Xe⁺ further due to its higher mass (Figs. 4.14 and 4.15).

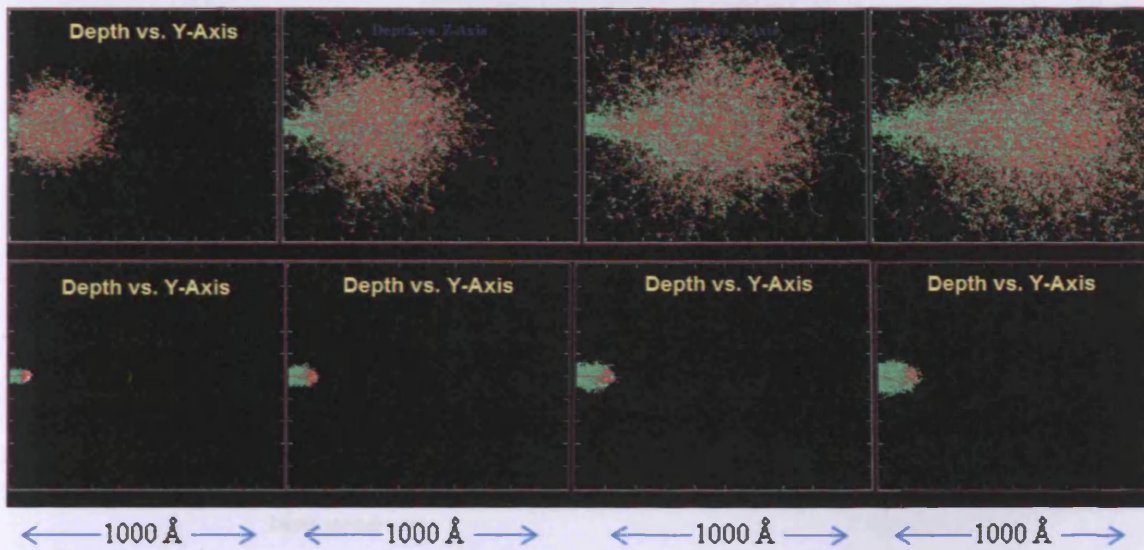


Fig. 4.13: A visual representation of the collision cascades generated from He⁺ (top row) and Xe⁺ (bottom row) irradiation of graphite at ion energies of 2 keV, 4 keV, 6 keV and 8 keV (from left to right respectively) as simulated by SRIM 2008. Green represents displaced carbon atoms and red represents the ion path.

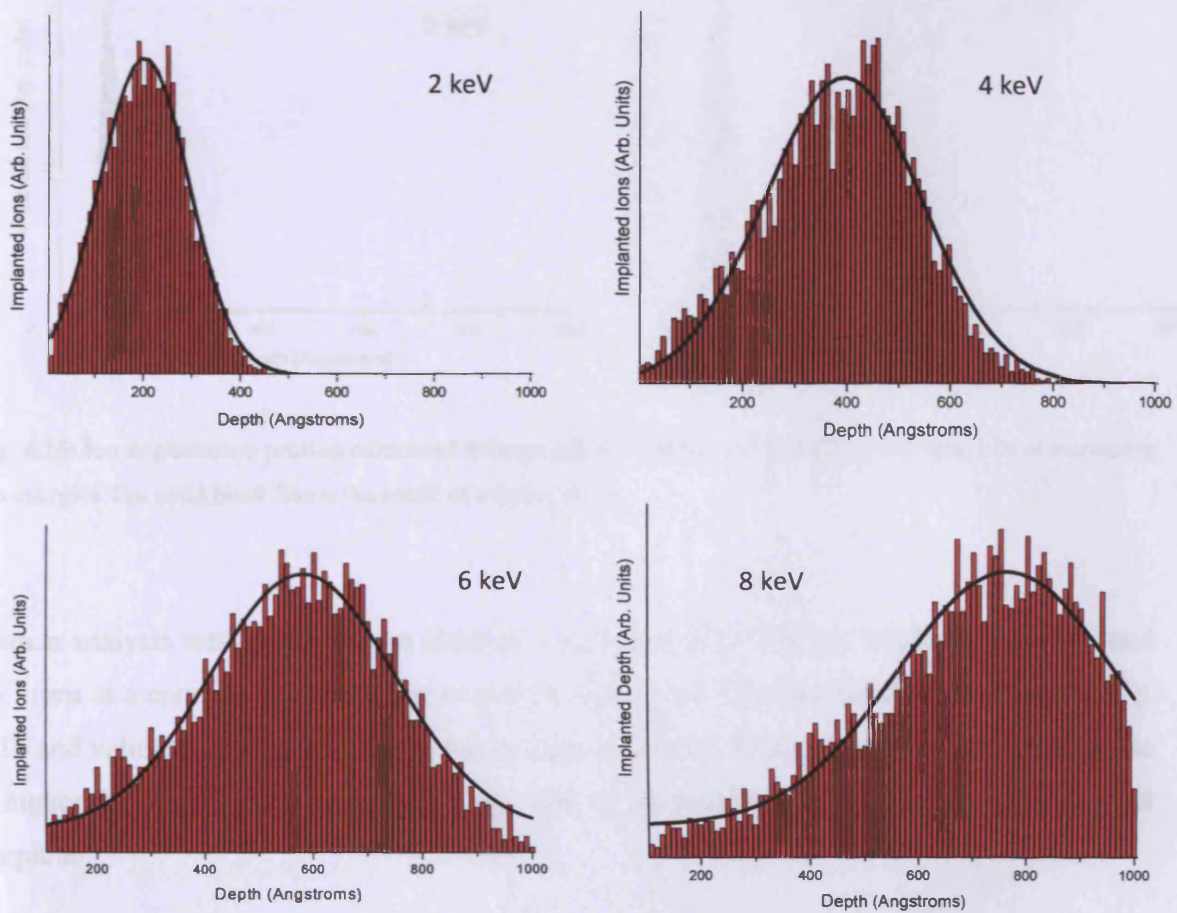


Fig. 4.14: Ion implantation profiles calculated through SRIM 2008 for He⁺ irradiation into graphite at increasing ion energies. The solid black line is the result of a Gaussian fit.

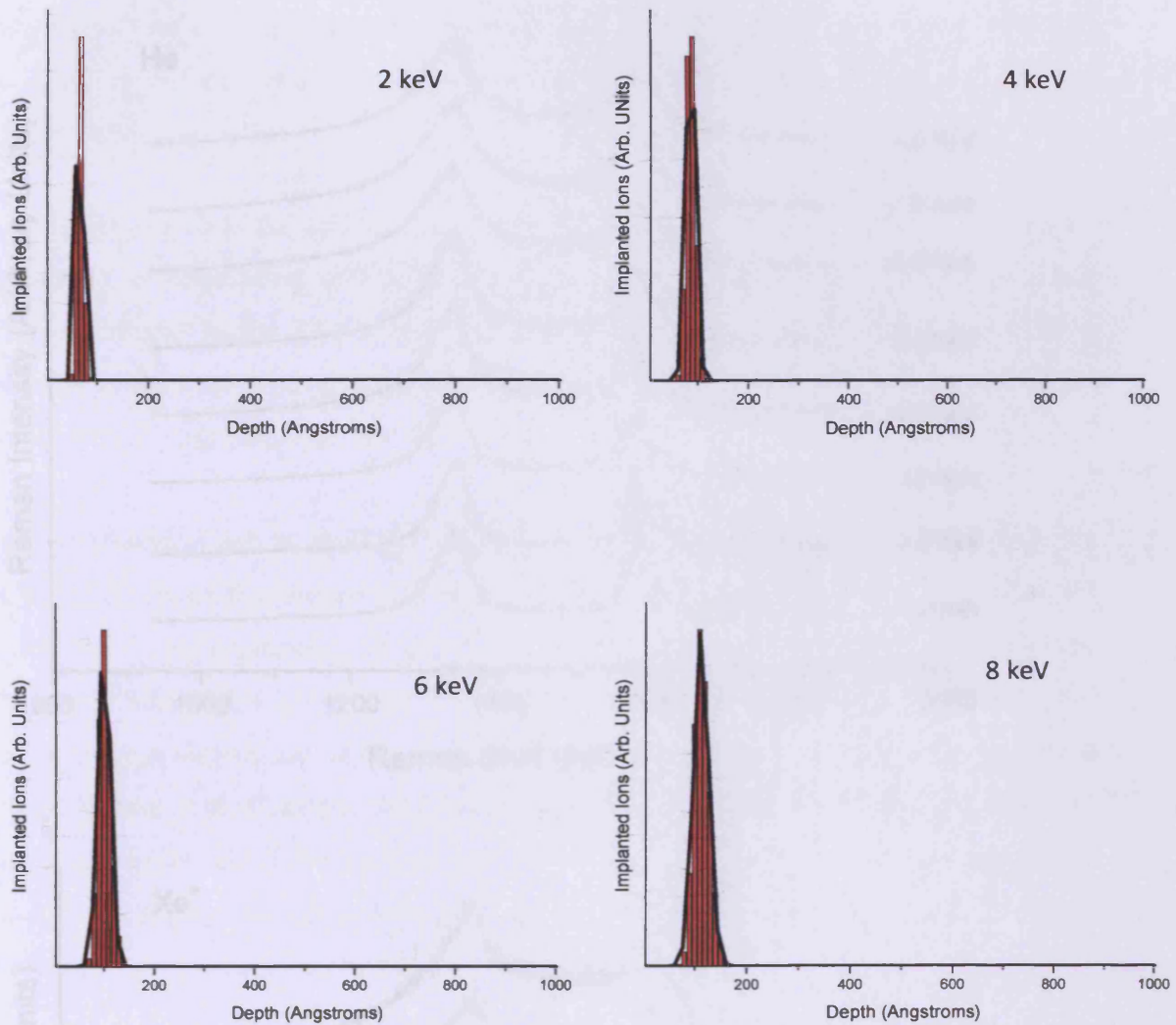


Fig. 4.15: Ion implantation profiles calculated through SRIM 2008 for Xe⁺ irradiation into graphite at increasing ion energies. The solid black line is the result of a Gaussian fit.

Raman analysis was carried out on identical virgin samples of HOPG irradiated with He⁺ and Xe⁺ ions at a constant fluence but at varying ion energies. The data obtained is shown in Fig. 4.16 and validates the SRIM data shown in Figs. 4.13-4.15, that is the lighter He⁺ ion exhibits a higher I_D/I_G ratio, for a given energy, due to its increased penetration depth into the graphite.

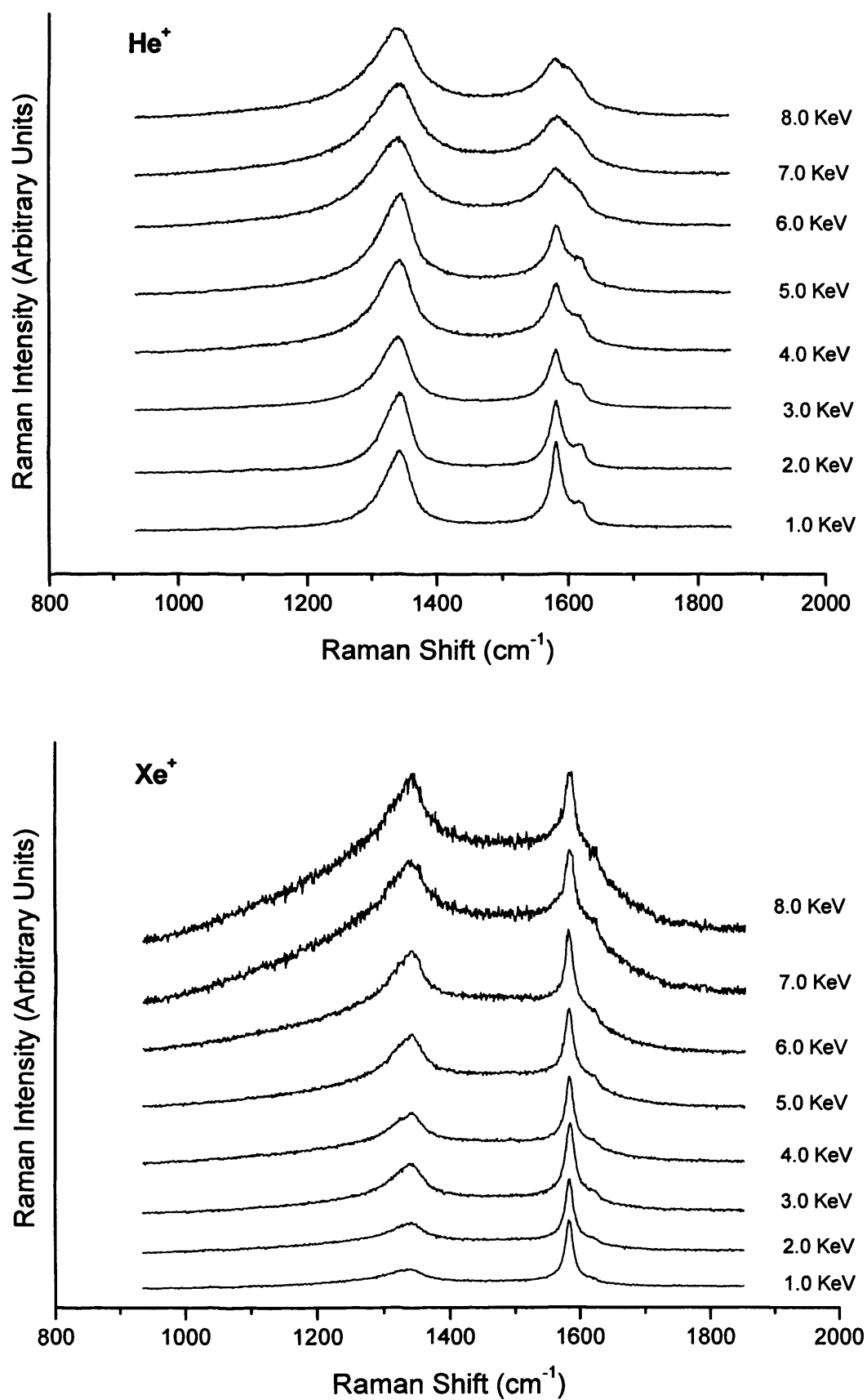


Fig. 4.16: A Raman study into the effect of changing initial ion energy for He⁺ (top) and Xe⁺ (bottom).

Fig. 4.17 exhibits a clear correlation between ion energy and R_{obs} . For He^+ an almost linear increase is observed up to an energy of approximately 6 keV before a slight decline begins at 8 keV. These results can be explained by the linear relationship between ion energy and ion penetration depth (Fig. 4.18).

Since it is known that the optical skin depth is approximately 40 nm then at energies corresponding to penetration depths less than that, some non-affected, essentially virgin material, contributes to the Raman spectrum. However, the percentage of this contribution decreases as penetration depth (i.e. ion energy) increases, up until 40 nm is reached where the contribution from virgin material becomes essentially zero.

Due to the effects of ion straggling, and the inherent approximations associated with the SRIM software, its predictions are not expected to be exact. For 6 keV ions the penetration depth for He^+ is approximately 58 nm, which will result in no contribution from virgin material, and from Fig. 4.13 (above) it can be seen that for 6 keV the region around the optical skin depth experiences a lot of ion induced damage. For this reason we can expect R_{obs} to be highest at this energy. As the energy is increased further, the mean penetration depth becomes quite significantly higher than the 40 nm target and as a result the majority of the ion-induced damage occurs beyond this and therefore is not observed through the Raman analysis, thus most probably explaining the slight decrease in R_{obs} .

This affect is more prominent for lighter particles such as protons and helium ions since they have smaller collision cross-sections and are stopped through electronic processes rather than nuclear collisions. This means that such particles will not typically interact with the host lattice until it starts to slow down and reach the end of its trajectory path. Therefore high energy irradiation with light particles is expected to show no considerable signs of damage through Raman analysis since the mean penetration depth will far exceed the optical skin depth and for the reasons explained, there will be very little damage caused within the 40 nm threshold.

SRIM 2008 can estimate the amount of energy transferred to the first carbon atom and the results are displayed in Table 4.3. A much larger percentage of the initial energy is transferred to the carbon atom for the heavier Xe^+ ion than for He^+ . This trend is expected from the theory of the interaction of ions with matter, discussed in Chapter 3.

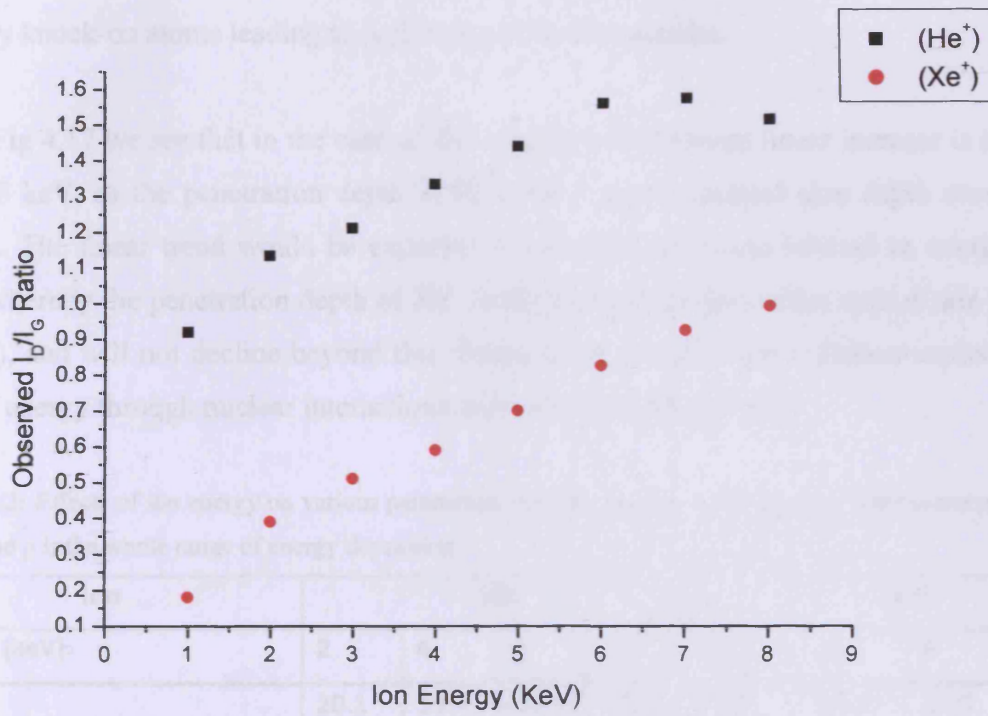


Fig. 4.17: Energy dependence of observed I_D/I_G ratio for He^+ and Xe^+ at a constant dose of 8.0×10^{14} ions. cm^{-2} .

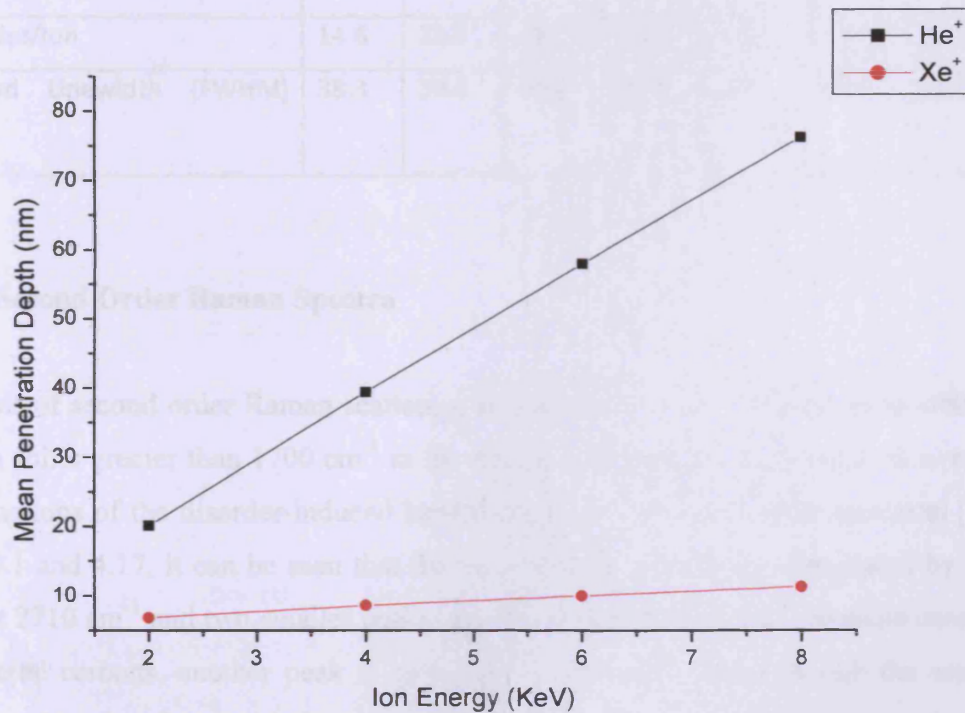


Fig. 4.18: Linear dependence of ion penetration depth on ion energy for He^+ and Xe^+ , as calculated using SRIM 2008.

Consequently more vacancies are produced from each ion due to higher energies of the primary knock-on atoms leading to prolonged collision cascades.

From Fig 4.17 we see that in the case of Xe^+ irradiation an almost linear increase is observed up to 8 keV, as the penetration depth is far lower than the optical skin depth even at this energy. The linear trend would be expected to continue up to and beyond an energy of 90 keV (whereby the penetration depth of Xe^+ at this energy is equal to the optical skin depth of 40 nm), and will not decline beyond this threshold due to its larger collision-section and its loss of energy through nuclear interactions and atomic displacements.

Table 4.3: Effects of ion energy on various parameters, for He^+ and Xe^+ irradiation. χ_0 is the mean penetration depth and ρ is the whole range of energy deposition.

Ion	He^+				Xe^+			
	2	4	6	8	2	4	6	8
Energy (keV)								
χ_0 (nm)	20.1	39.4	57.9	76.2	6.8	8.6	10.0	11.3
ρ (nm)	41	71	98	122	5	7.6	10.0	12.5
Energy transferred to first C atom (keV)	0.76	1.28	1.82	1.95	1.60	3.36	5.12	6.87
Vacancies/Ion	14.6	23.0	30.0	33.5	31.0	58.5	84.5	108.8
D band Linewidth (FWHM) (cm^{-1})	38.3	39.4	49.1	58.4	40.9	44.9	48.3	48.7

4.4.4. Second Order Raman Spectra

Analysis of second order Raman scattering in graphite is related to any peaks obtained with Raman shifts greater than 1700 cm^{-1} in the Raman spectra and corresponds to overtones and combinations of the disorder-induced bands observed in the first-order spectrum [19]. From Figs. 4.1 and 4.17, it can be seen that the second order spectra are dominated by an intense peak at 2710 cm^{-1} and two smaller peaks at 2450 cm^{-1} and 3250 cm^{-1} . In some cases, in more disordered carbons, another peak is observed at 2950 cm^{-1} . Even though the second order spectrum is somewhat less informative on the level of structural disorder present, previous work has shown the second order spectrum to be even more sensitive than the first order spectrum to the formation of heavy lattice damage within the optical skin depth, and therefore

it is important to study the origin and nature of these peaks [58] along with their behaviour under ion irradiation.

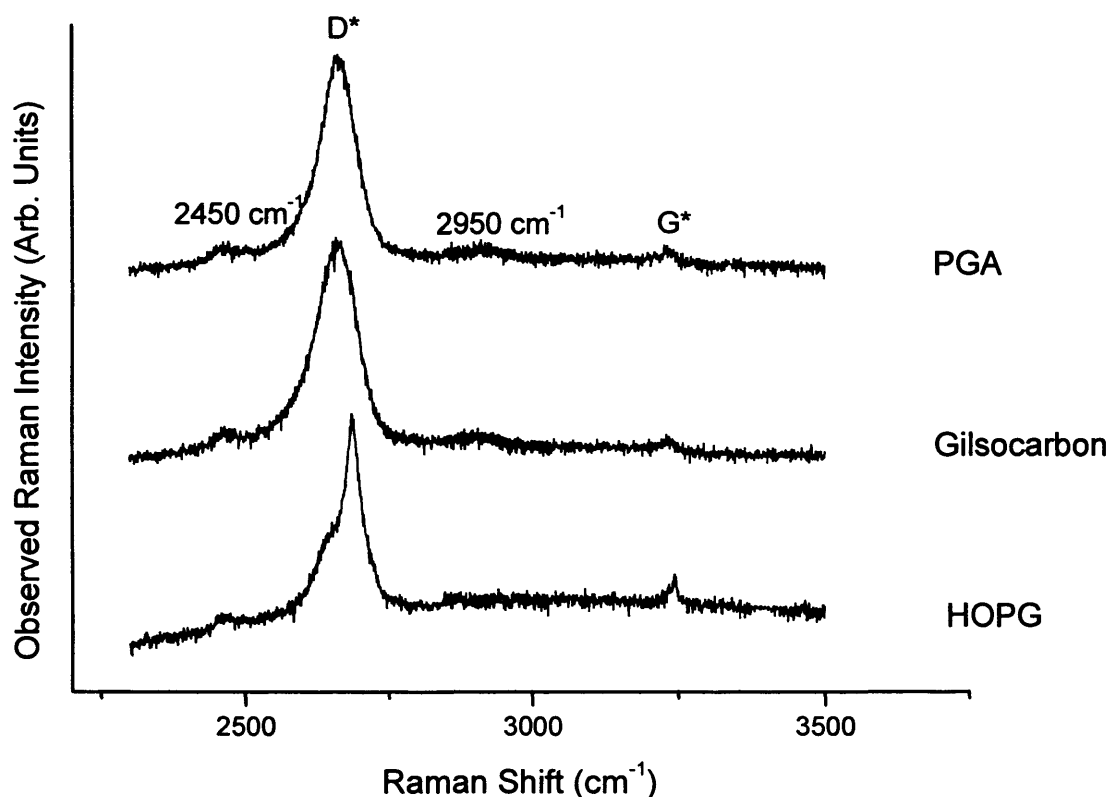


Fig. 4.19: The second order Raman spectra obtained for virgin HOPG, Gilsocarbon and PGA.

The most prominent peak is observed at twice the energy of the D band, at 2710 cm^{-1} ($2 \times 1355\text{ cm}^{-1}$) and hence is ascribed the D^* mode [26]. Ferrari noted that the position of this peak shifts with excitation energy and as a result can be attributed to a double-resonant Raman scattering event, in the same way as its first-order counterpart [59]. Such a process links the phonon wavevectors to the electronic overtone of the D mode where the electron is backscattered by a second phonon instead of a defect [19] and probably arises from the flatness of several branches between K and M in the band structure [60], occurring through the selective enhancement at a particular phonon frequency. The details of double-resonant Raman processes in graphite is a complex field and will not be discussed in detail here, however a good description can be found in the review by Reich and Thomsen [19]. In virgin graphite the D^* band is clearly a doublet, consisting of two peaks centred at approximately 2695 and 2735 cm^{-1} [35] and has been shown to be a good indication of c axis ordering and consequently of turbostraticity [61].

The lowest frequency band in the second order spectrum is a step rise feature occurring at 2450 cm^{-1} and is found to be present in both virgin and disordered samples. The origin of this band was investigated by Shimada et al [62] and Maultzsch et al [63] who found that, unlike the D^* band, the position of the peak does not change with changing laser excitation energy and as a result was attributed to $q = k$ phonons through a combination of transverse optical (TO) and longitudinal acoustic (LA) phonon modes [64-65]. The energy of the peak is approximately twice the peak at 1225 cm^{-1} and is therefore associated with the peak observed in the density of states in the Nicklow, Wakabayashi and Smith (NWS) model [28] and is seen as an overtone of longitudinal optical (LO) phonons near the k -points observed experimentally by Elman et al [58]. Additionally this feature is thought to arise from phonons in the same k -space region as that of the D^* band and represents the intersection of the low-frequency and high-frequency “in-plane” modes [66].

The highest frequency band in the second order spectrum occurs at 3250 cm^{-1} and thus can be attributed to scattering from the highest frequency portions of the Σ and T branches [23]. The energy is almost twice that of the observed D' band ($2 \times 1620\text{ cm}^{-1}$) and hence Nemanich and Solin [15] propose this occurs due to overtone scattering of the highest frequency feature in the first order spectrum

4.4.4.1. Disorder Induced Changes in the Second Order Spectrum

As structural disorder increases e.g. from HOPG to nuclear grade polycrystalline graphites, or as a result of ion bombardment, the second order spectrum becomes affected in a variety of ways. The prominent area to be affected, even at relatively small doses is the appearance of the D^* band at 2710 cm^{-1} . The clear doublet structure starts to become distorted and a broader peak is observed. Such a result is indicative of structural disturbance and is consistent with poorly organised stacking of the graphite layers [66].

Fig. 4.20 shows the change of the second order spectrum with increasing amounts of 5 keV He^+ and Xe^+ ion bombardment. Ne^+ and Ar^+ are omitted for the sake of brevity but follow the expected trend, as observed in the first order analysis (Figs. 4.6A-D)

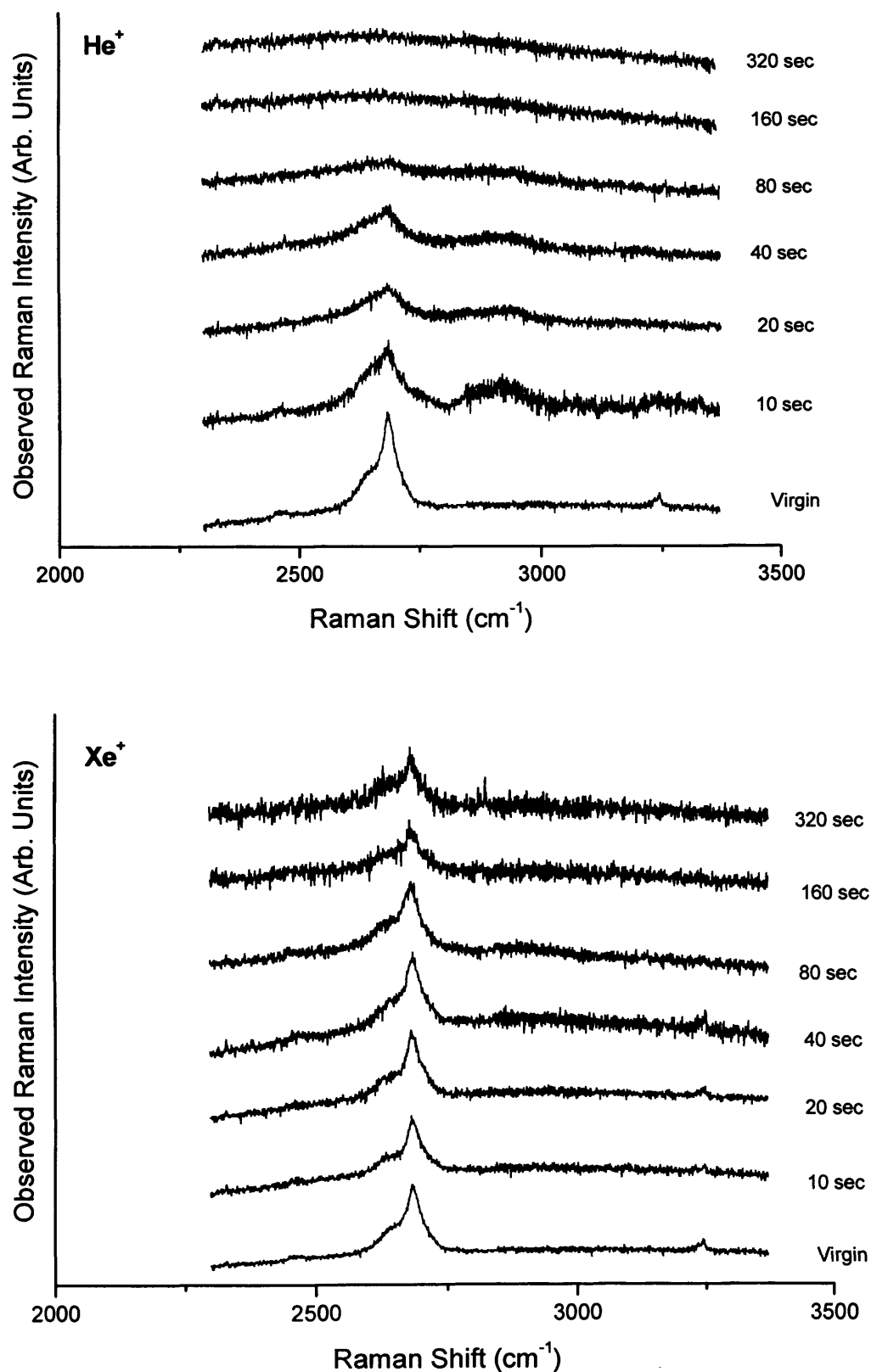


Fig. 4.20 A time resolved analysis of the second order Raman spectra obtained for 5 keV ion irradiation of HOPG, for He^+ (top) and Xe^+ (bottom) at a constant ion flux of 5.0×10^{12} ions. cm^{-2} .s. Each spectrum was taken at twice the total irradiation time of the previous spectrum, up to a time of 320 s.

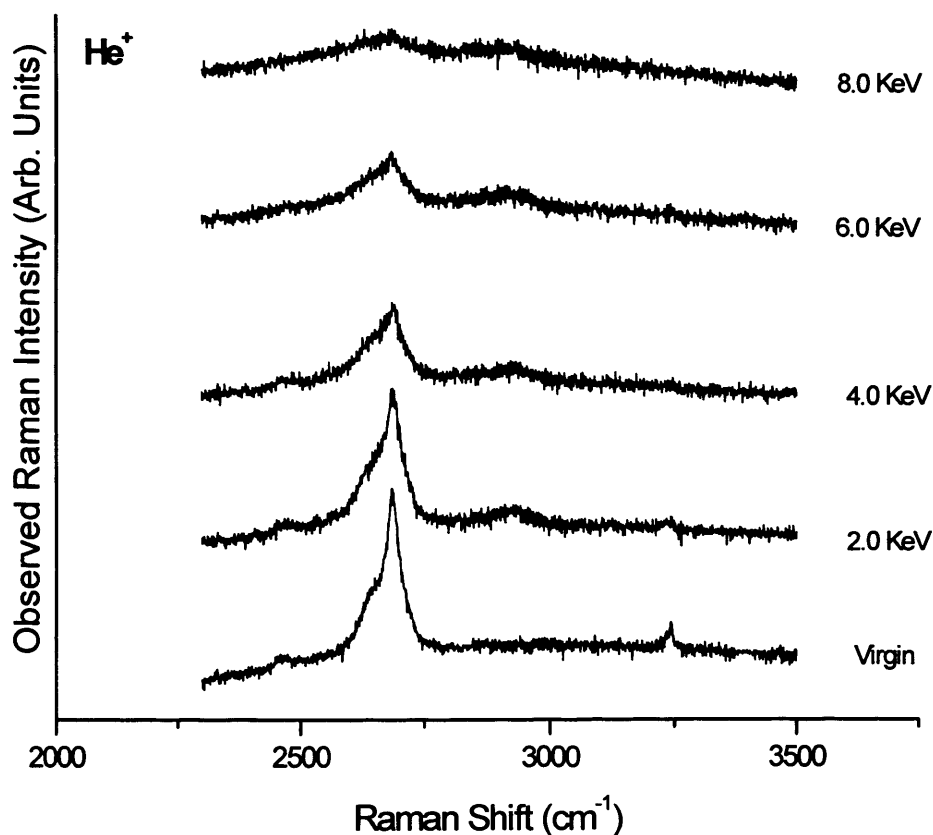
The intensity of the D* band decreases with increased ion fluence and starts to broaden and lose its clear doublet structure. Barros et al [66] have suggested that the broadening occurring towards lower energy is due to a contribution from graphene-like material (2-dimensional graphite), which consists of a single narrow component, centred at approximately 2670 cm^{-1} . Other observations include the overlap of the 2450 cm^{-1} band with the D* band, also contributing to the broadening and structure of the D* band. It is also observed that upon increasing dose the signal to noise level is reduced and subsequently the band at 3250 cm^{-1} is not seen at higher doses. As is the case in the first order spectra, the disorder induced changes are more prominent for He^+ irradiation and again this is due to the effect of ion mass on the penetration depth.

The final point of interest is the appearance of another broader band at 2950 cm^{-1} , which appears as the samples become more disordered, that is as the crystallite size gets smaller. Tsu et al suggested that the 2950 cm^{-1} band is due to hydrogen impurities; [39] however, Nemanich and Solin [26] carried out polishing experiments and found that this band appears reasonably strongly as a result of the polishing process and thus is likely to be related to 'damage' not impurities. Wright et al [67] ascribe the 2950 cm^{-1} band to a combination of scattering associated with the D and G bands ($1355 + 1580 \approx 2950$). However, it can be seen that the sum of the frequencies of the 1355 and 1620 cm^{-1} first-order modes is even closer to the 2950 cm^{-1} feature and hence it can be argued that this feature is caused from a combination of the mentioned strong density of states in the first-order spectrum. Analysis by Nemanich and Solin [23] of the linewidth of this mode also provides evidence consistent with this explanation, since the width is very similar to that of the overtone mode at 2710 cm^{-1} . This would be expected as this mode is an overtone of the 1355 cm^{-1} feature and the feature at 1620 cm^{-1} would make up the small difference as this band is very narrow.

Unlike the first order spectra there is no real method of quantitatively relating the second order Raman spectrum directly to the damage caused i.e. there is no applicable analogue to the TK relation for the second order peaks. Therefore one must analyse the spectrum carefully, using the decrease in the D* intensity, the increased broadening and the appearance and prominence of the disorder induced 2950 cm^{-1} peak as a visual representation of the level of damage.

4.4.4.2. Effect of Ion Energy on the Second Order Raman Spectrum

In an analogous manner to the first order spectra, the second order Raman spectrum depends on the ion energy and its affect on the penetration depth of the ion. Again, He^+ shows the most significant change in the second order spectra, being remarkably different from the virgin material, the more so as the ion penetration depth reaches the optical skin depth. Xe^+ does not penetrate as far and as a result, even at 8 keV irradiation, the second order spectrum is relatively similar to the virgin material, though some marked ion induced effects are clear. The results obtained from Fig. 4.21 confirm that the second order spectra behave as expected like the first order spectra in terms of changing towards a more amorphous-like spectrum as ion energy increases.



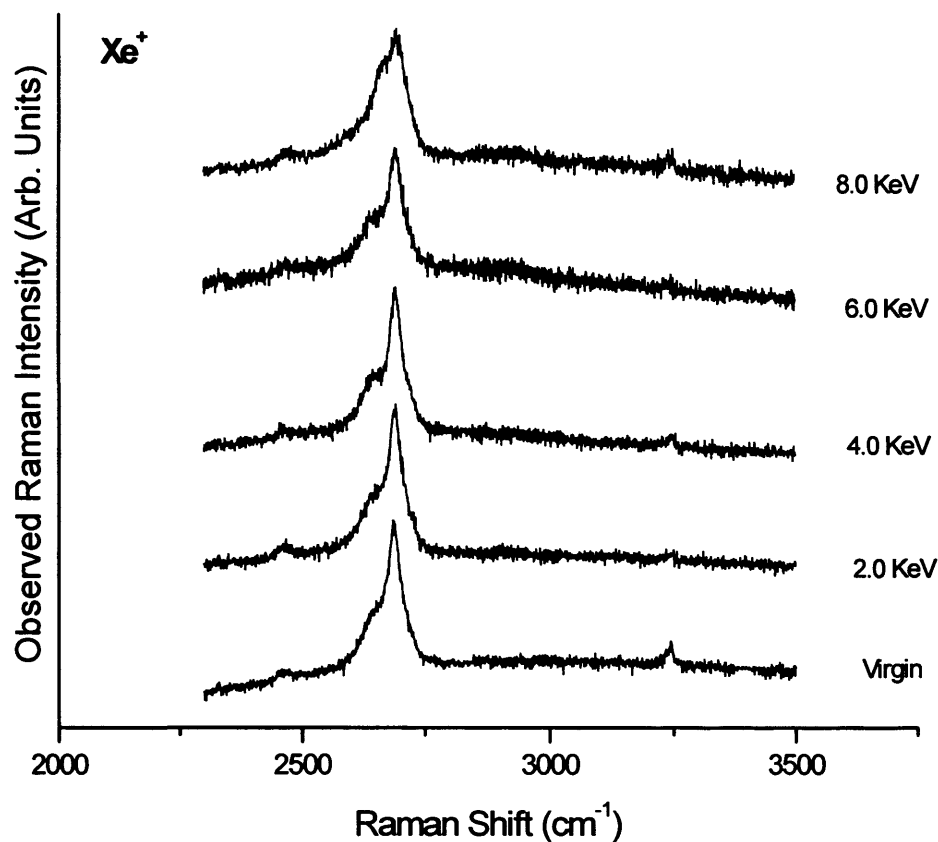


Fig. 4.21: A 2nd order Raman study of the effect of changing initial ion energy for He⁺ (top) and Xe⁺ (bottom). All samples were irradiated to a constant dose.

4.5. Conclusion

The Raman spectra of graphitic materials are extremely complex and still not fully understood at the fundamental level. However, despite this, the results are interesting and can provide information on the structure of the material at the atomic scale. The Raman spectrum is highly sensitive to structural deformation and is therefore affected greatly through ion irradiation as well as neutron bombardment. The T-K relation can be used to assess the structural disorder present within the system and is a useful means of assessing the total damage caused through ion irradiation.

However, at higher doses, when the crystallites become very small and long-range order is reduced significantly, the T-K relation breaks down and cannot be used on its own to assess the structural damage. At this point other factors may be used such as the extent of broadening, the increase in linewidth, particularly for the D band, and also the emergence of a third band at 1500 cm⁻¹, only present in highly disordered systems. The second order spectra

may also be used to study the effects of ion irradiation, particularly through the emergence of the 2950 cm^{-1} peak and the decrease in intensity of the D* peak.

SRIM 2008 has been shown to be a useful tool in predicting the extent of damage caused by a particular ion at a particular energy in a particular material. Using the program, accurate ion penetration depths can be deduced, allowing for meaningful analysis of the Raman spectra obtained.

In summary, increasing the ion mass leads to more pronounced structural damage through more atomic displacements, although the actual extent of the damaged region is reduced. Generally, for analysis through Raman spectroscopy the penetration depth of the ion must be comparable to the optical skin depth of the laser, which is approximately 40 nm in this instance. When this is the case the observed Raman spectrum gives a reasonable description of the damage to the system; however when the penetration depth is less than 40 nm, is often the case for ions of higher mass, the Raman spectra obtained consisted largely of signal from essentially virgin material. When corrected for, the results indicate a significant increase in damage for heavier ions for the same dose. Also as expected, increasing the ion energy increases the damage due to more energetic collision cascades being initiated. However, once the energy results in an ion penetration depth higher than the optical skin depth then Raman analysis is not able to provide the full picture of damage accumulation in the material.

Finally, as expected the Raman spectra obtained for ion irradiated graphite are analogous to those obtained for neutron irradiated specimens, even at relatively low energies. This confirms that, within the optical skin depth at least, the nature of the damage caused through ion-induced atomic displacements may, using the correct irradiation parameters, successfully mimic those induced through neutron bombardment occurring throughout the reactor lifetime.

4.6. References:

- [1] C. Kittel, 'Introduction to Solid State Physics', Wiley, New York, (1996).
- [2] B.S. Elman, M.S. Dresselhaus, G. Dresselhaus et al., *Phys. Rev. B*, **24** (1981) 1027.
- [3] J.W. Mayer, L. Eriksson, D. J.A., 'Ion Implantation in Semiconductors', Academic Press, (1970).

- [4] M.S. Dresselhaus, G. Dresselhaus, 'Light Scattering in Solids III', Springer-Verlag (1982), pp. 3.
- [5] A. Miyahara, T. Tanabe, *J. Nucl. Mat.*, **155-157** (1988) 49.
- [6] T. Tanabe, S. Muto, Y. Gotoh, K. Niwase, *J. Nucl. Mat.*, **175** (1990) 258.
- [7] T. Tanabe, S. Muto, K. Niwase, *Appl. Phys. Lett.*, **61** (1992) 1638.
- [8] B. Soder, J. Roth, W. Moller, *Phys. Rev. B*, **37** (1988) 815.
- [9] M. Miyake, W. Saki, T. Daimon, P. Son, et al., *J. Nucl. Mat.*, **187** (1992) 138.
- [10] P.Y. Yu, M. Cardona, 'Fundamentals of Semiconductors', Springer-Verlag, Berlin (1996).
- [11] F. Tuinstra, J. Koenig, Raman spectrum of graphite, *J. Chem. Phys.*, **53** (1970) 1126.
- [12] J.E. Smith Jr, M.H. Brodsky, B.L. Crowder, M.I. Nathan, *J. Non-Crystalline Solids*, **8-10** (1972) 179.
- [13] M.R. Ammar, J.-N. Rouzaud, C.-E. Vaudey, N. Toulhoat, N. Moncoffre, 'Structural Characterisation of Ion Implanted Nuclear Graphite', Nuclear Graphite Meeting, Lyon, France (2009).
- [14] R.J. Nemanich, S.A. Solin, *Solid State Commun.*, **23** (1977) 417.
- [15] R.J. Nemanich, S.A. Solin, D. Guerard, *Phys. Rev. B*, **16** (1977) 2965.
- [16] R.J. Nemanich, S.A. Solin, G. Lucovsky, *Solid State Commun.*, **23** (1977) 117.
- [17] L.J. Brillson, E. Burstein, A.A. Maradudin, T. Stark, Pergamon, New York, (1971).
- [18] S.A. Solin, A.K. Ramdas, *Phys. Rev. B*, **1** (1970) 1687.
- [19] S. Reich, C. Thomsen, *Phil. Trans. R. Soc. Lond. A*, **362** (2004) 2271.
- [20] D.L. Rousseau, R.P. Bauman, S.P.S. Porto, *J. Raman. Spectrosc.*, **10** (1981) 253.
- [21] E.B. Wilson, J.C. Decius, P.C. Cross, 'Molecular Vibrations', Dover, New York, (1980).
- [22] R.J. Nemanich, S.A. Solin, G. Lucovsky, in: M. Balkanski (Ed.) Proceedings of the International Conference on Lattice Dynamics, Paris,(1975), pp. 619.
- [23] R.J. Nemanich, S.A. Solin, R.M. Martin, *Phys. Rev. B*, **23** (1981) 6348.
- [24] A. Yoshimori, Y. Kitano, *J. Phys. Soc. Japan*, **2** (1956) 352.
- [25] J.A. Young, J.U. Koppel, *J. Chem. Phys.*, **42** (1965) 357.
- [26] R.J. Nemanich, S.A. Solin, *Phys. Rev. B*, **20** (1979) 392.
- [27] G. Dolling, B.N. Brockhouse, *Phys. Rev.*, **128** (1962) 1120.
- [28] R. Nicklow, N. Wakabayashi, H.G. Smith, *Phys. Rev. B*, **5** (1972) 4951.
- [29] B. Racine, A.C. Ferrari, N.A. Morrison, et al., *J. Appl. Phys.*, **90** (2001) 5002.
- [30] Y. Wang, D.C. Alsmeyer, R.L. McCreery, *Chem. Mater.*, **2** (1990) 557.
- [31] M. Nakamizo, R. Kammereck, Walker Jr, P.L, *Carbon*, **12** (1974) 259.

- [32] M.J. Matthews, M.A. Pimenta, G. Dresselhaus, et al., *Phys. Rev. B*, **59** (1999) 6585.
- [33] D.S. Knight, W.B. White, *J. Mater. Res.*, **4** (1989) 385.
- [34] R. Al-Jishi, G. Dresselhaus, *Phys. Rev. B*, **26** (1982) 4514.
- [35] R.P. Vidano, D.B. Fischbach, et al., *Solid State Commun.*, **39** (1981) 341.
- [36] A.V. Baranov, A.N. Bekhterev, et al., *Opt. Spektrosk.*, **62** (1987) 1036.
- [37] I. Pocsik, M. Hundhausen, M. Koos, L. Ley, *J. Non-Cryst. Solids*, **227-230** (1998) 1083.
- [38] H. Maeta, Y. Sato, *Solid State Commun.*, **23** (1977) 23.
- [39] R. Tsu, J.H. Gonzalez, I.G. Hernandez, *Solid State Commun.*, **27** (1978) 507.
- [40] A. Cuesta, P. Dhamelincourt, J. Laureyns, et al., *J. Mater. Chem.*, **8** (1998) 2875.
- [41] H. Wilhelm, M. Lelaurain, McRae, E, B. Humbert, *J. Appl. Phys.*, **84** (1998) 6552.
- [42] L.G. Cancado, K. Takai, T. Enoki, M. Endo, Y.A. Kim, et. al, *Appl. Phys. Lett.*, **88** (2006) 163106.
- [43] P. Lespade, R. Al-Jishi, M.S. Dresselhaus, *Carbon*, **20** (1982) 427.
- [44] E. Asari, I. Kamioka, K.G. Nakamura, M. Kitajima et al., *Phys. Rev. B*, **49** (1994) 1011.
- [45] K.G. Nakamura, M. Kitakima, *Appl. Phys. Lett*, **59** (1991) 1550.
- [46] K. Nakamura, M. Kitajima, *Phys. Rev. B*, **45** (1992) 78.
- [47] K.G. Nakamura, M. Kitakima, *Phys. Rev. B*, **45** (1992) 5672.
- [48] K.G. Nakamura, M. Kitakima, *Surface Science*, **283** (1993) 255.
- [49] A. Mabuchi, K. Tokumitsu, et al., *J. Electrochem. Soc.*, **142** (1995) 1041.
- [50] Y-J. Lee, *J. Nucl. Mat.*, **325** (2004) 174.
- [51] A. Theodosiou, A.F. Carley, S.H. Taylor, *J. Nucl. Mat.*, **403** (2010) 108.
- [52] K.G. Nakamura, M. Kitakima, *J. Nucl. Mat.*, **187** (1992) 294.
- [53] K. Niwase, K. Nakamura, T. Shikama, T. Tanabe, *J. Nucl. Mat.*, **170** (1990) 106.
- [54] J.F. Ziegler, J.P. Biersack, M.D. Ziegler, 'The Stopping and Range of Ions in Matter', Srim Co., USA (2008).
- [55] H. Ishida, H. Fukuda, G. Katagiri, A. Ishitani, *Appl. Spectros.*, **40** (1986) 322.
- [56] K. Nakamura, M. Fujitsuka, M. Kitajima, *Phys. Rev. B*, **41** (1990) 12260.
- [57] J.H.W. Simmons, 'Radiation Damage in Graphite', Pergamon Press, Oxford, (1965).
- [58] B.S. Elman, M.S. Dresselhaus, M. Shayegan, et al., *Phys. Rev. B*, **25** (1982) 4142.
- [59] A.C. Ferrari, *Solid State Commun.*, **143** (2007) 47.
- [60] C. Thomsen, S. Reich, *Phys. Rev. Lett.*, **85** (2000) 5214.
- [61] P. Lespade, A. Marchard, M. Couzi, F. Cruege, *Carbon*, **22** (1984) 375.
- [62] T. Shimada, T. Sugai, C. Fantini, M. Souza, et al., *Carbon*, **43** (2005) 1049.
- [63] J. Maultzsch, S. Reich, Thomsen, C, *Phys. Rev. B*, **70** (2004) 155403.

- [64] R. Saito, A. Jorio, G. Dresselhaus, et al., *Phys. Rev. Lett.*, **88** (2002) 27401.
- [65] R. Saito, A. Gruneis, Samsonidze, G.G, V.W. Brar, et al., *New J. Phys.*, **5** (2003) 157.
- [66] E.B. Barros, M.S. Dresselhaus et al., *Vibrational Spectroscopy*, **45** (2007) 122.
- [67] R.B. Wright, R. Varma, D.M. Gruen, *J. Nucl. Mat.*, **63** (1976) 415.

Chapter 5

Thermal annealing of Ion Irradiated Graphite

5.1 Introduction

Temperature is an important factor in the context of this work. It is crucial since the amount of radiation induced damage within a graphite system is dependant on the graphite temperature at that given time. Increasing sample temperature after irradiation will allow damage recovery to occur; this process, known as annealing, was used extensively in low temperature graphite moderated reactors to control the level of damage in the system. The temperature of graphite prior to irradiation is also known to affect considerably the damage accumulation within the system.

This chapter will focus on the affects of temperature on samples post irradiation and also on how the temperature of the sample during the irradiation affects the accumulation of damage. Raman spectroscopy, differential scanning calorimetry (DSC) and transmission electron microscopy (TEM) are utilised and previously published background and theory will also be discussed.

5.2. Experimental

The apparatus used to conduct the experiments are discussed in detail in Chapter 2. The controlled sample heating was achieved in a Carbolite[®] tube furnace programmed to heat to the desired temperature at the desired ramp rate. The furnace was equipped with an oil bubbler to ensure a constant flow of inert N₂ gas during operation. The heating ramp rate was 20 °C/min and the holding time at each temperature was 0.5 hrs, unless otherwise stated.

and will not be covered extensively here. Perhaps in the context of this research the most interesting defect is the intimate Frenkel pair defect which will be discussed later.

5.3.1. Stored (Wigner) Energy

One consequence of the production of many defects is the associated build up of potential energy, referred to as stored energy or Wigner energy. As discussed in Chapter 1 the creation of stored Wigner energy within a graphite matrix, as a result of fast neutron bombardment, is of concern due to the potential threats it can pose; particularly during decommissioning through rapid and uncontrollable temperature rises which have been calculated to theoretically reach temperatures as high as ~ 1500 °C [11]. Simply, the presence of unstable stored energy can be responsible for damage to graphite reactor cores [12].

An effective means of detecting the build up of stored energy is through standard calorimetry techniques [13-15]. One of the first measurements of Wigner energy release on neutron irradiated graphite was carried out in the 1950's on graphite irradiated at < 130 °C in the Oak Ridge graphite pile. These measurements recorded an energy release of 29 J/g upon heating from room temperature to 300 °C at 2 °C/min [16]. Other studies were carried out into the release of stored Wigner energy throughout the 1950s and particularly 1960s in graphite taken from Argonne [17], Hanford [18] and Chalk River [19]. Such work was deemed all the more important particularly after the 1957 Windscale fire, of which Wigner energy release was the indirect cause [12]. Further investigations were carried into stored energy release from neutron irradiated graphite by Bochirol, Bonjour and colleagues at Grenoble [20-22]. An extensive review of all this work and the theory behind the calorimetric investigation into stored energy release is given by Nightingale [23].

The linear-rise calorimeter described by Cottrell et al [24] allows a stored energy release spectrum to be generated for an irradiated sample. Simply, an irradiated sample is heated together with an identical unirradiated sample and the temperature of each sample is kept the same. The difference in electrical power used to maintain the sample temperatures equal is recorded and is equal to the rate of stored energy release. Thus a spectrum of the rate of energy release as a function of temperature against annealing temperature can be produced. Such a spectra is shown below, and shows significant energy release taken from CSF graphite irradiated at approximately 30 °C [25].

5.3. Overview/Background

In 1942, Hungarian physicist Eugene Wigner predicted that the carbon atoms present in the graphite moderator of a fission reactor could be displaced from their lattice sites [1]. Each fast neutron can produce thousands of displaced atoms and associated vacancies (Frenkel Pairs) leading to the variety of changes observed in the physical properties of irradiated graphite; such changes have been well studied [2-4] and the general change in properties seen in irradiated graphite is referred to as the Wigner effect.

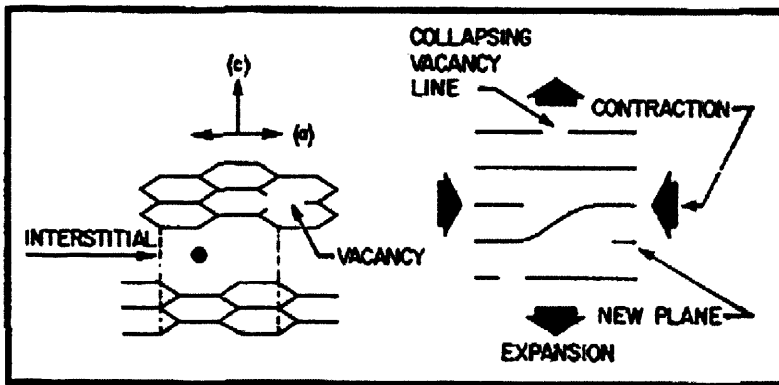


Fig. 5.1: Illustration of effects of irradiation of graphite. Such irradiation induced changes lead to changes in the physical properties such as increased elastic modulus, increased strength and decreased thermal conductivity [2].

In the early stages of irradiation, energy will be stored in simple defect types, involving a single Frenkel pair. However, as irradiation continues, various atomic scale processes will occur leading to more complex defect systems and effectively a ‘defect zoo’ [5], covering varying length scales within the graphite matrix. The ‘defect zoo’ will consist of various types of defect structures, each with different energies leading to different effects on the structural and electronic properties of the system. Defects may be interstitial atoms, interstitial clusters, mono-vacancies, or multi-vacancies. Multi-vacancies can occur when knock-on atoms are formed at sites close to single vacancies. Eventually more complex defect structures such as dislocation dipoles [6] and dislocation loops [7-8] may be formed as rapid diffusion of mobile interstitials causes successive knock-ons, close to the end of collapsed lines, to collapse to the basal planes. Such defects are one focus of study at the University of Sussex [9] where work on understanding defect behaviour in carbons also has some potential applications in the exciting field of carbon nanostructures [10]. An excellent review of the defects formed, their behaviour and physics is given by Telling and Heggie [5]

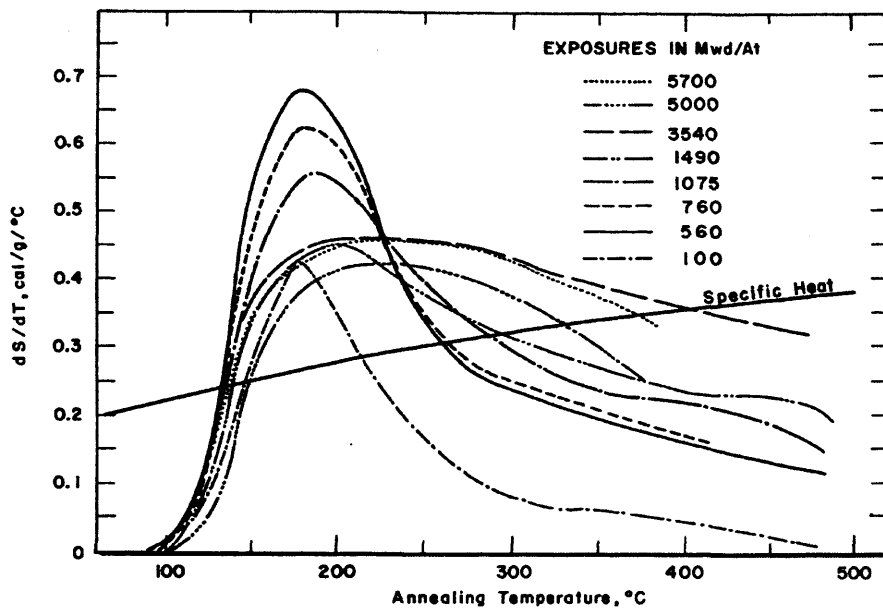


Fig. 5.2: DSC data showing the stored-energy release curves of CSF graphite irradiated near 30°C [25].

The spectra show clearly that a large energy release is observed around 200 °C, a feature often seen in neutron irradiated graphite [26] referred to as the Wigner energy release peak.

More recently, a study by Lexa and Kropf [27] involved DSC analysis of graphite irradiated in the inner thermal column of the ASTRA research reactor. Several samples of graphite exposed to varying degrees of radiation ($\sim 10^{17}$ to $\sim 10^{20}$ n/cm²) at temperatures below 100 °C, were found to exhibit varying amounts of Wigner energy release, from 25 to 572 J/g. Interestingly, at relatively high doses ($> 5.0 \times 10^{19}$ n/cm²) the peak at 200 °C disappeared, a phenomenon observed previously [28], and instead a much broader, continuous energy release is observed throughout the temperature range.

5.3.2. Energy Storage and Thermal Annealing

In irradiated graphite energy is stored amongst the various defect systems present. The total stored energy of the system, E_{ST} is known to equal the number of defects, N_j , of a given type, times their energy of formation, $E_{f,j}$ summed over all j defect types [5]:

$$E_{ST} = \sum_j N_j E_{f,j} \quad (\text{Eq. 5.1})$$

Upon heating, various energy release peaks can be observed, each relating to a defect of a given type gaining enough energy to overcome their particular energy barrier and move to a more stable, lower energy state; you could say to a less complex defect. In the case of the simple Frenkel pair defect, this energy release may be due to annihilation and hence complete removal of the defect altogether.

Many early studies allowed the energy stored within a interstitial-vacancy pair to be estimated [29-31]; however, presently, after many years of study, there is still mostly speculation with regards to the fundamental processes behind Wigner energy accumulation and release on the atomic scale. Early work carried out in the 1960s theoretically calculated the formation energy of a Frenkel defect to be 20.6 eV, which was made up of 10.7 eV, the formation energy calculated for a vacancy [32] and 9.9 eV, the formation energy calculated for an interstitial [33]. This value assumes that the interstitial atom does not form covalent bonds with its neighbouring atoms and was found to agree with the experimentally derived value of 18 ± 4 eV [34].

An in-depth studied was carried out in this area by Iwata and co-workers [34], who came to establish an interpretation of the recovery mechanisms summed up as follows:

1. Single interstitial atoms may migrate even at temperatures far below liquid nitrogen temperature and gather together to form loosely coupled clusters at slightly higher temperatures [34].
2. Interstitial C₂ carbon molecules are formed near 100 K, contributing to the reverse annealing in electrical resistivity [35].
3. C₂ molecules migrate at around 160 K forming larger clusters [36].
4. Larger sized clusters of C₂ molecules decompose to smaller constituents near 200 °C which in turn recombine with vacancies or are absorbed into larger clusters, causing the commonly observed Wigner energy release peak.

Later work carried out by Iwata on graphite samples taken from the JAERI JRR-2 reactor using DSC analysis [37] showed significant Wigner energy release . The graphite was exposed to a fast neutron fluence of 4.0×10^{21} n.m⁻² at a temperature of 80 °C. The majority of the energy was released when the sample temperature was between 150 – 300 °C. At a ramp rate of 20 °C/min, which is what was used in this study, the maxima of energy release

was approximately at 200 °C. Iwata observed that the total energy release involved three different energy peaks, combining to give a total energy release of 8 ± 1 J/g. The three peaks follow first order kinetics with average activation energies of 1.34 eV, 1.50 eV and 1.78 eV being calculated, each corresponding to a different rate determining step namely the decomposition of different interstitial molecules.

The table below is taken from the paper by Iwata [37] and outlines the steps considered to be involved in the annealing:

Table 5.1: Proposed mechanism of Wigner energy release in irradiated graphite. C_2 relates to interstitial carbon molecules, and V means vacancy. Annihilation of C_2 molecules with vacancies results in significant energy release [37].

Energy Released	Rate-determining reaction	Successive reactions
1.34 eV	$(C_2)_2 \longrightarrow C_2 + C_2$	$C_2 + 2V \longrightarrow$ annihilation $C_2 + (C_2)_2 \longrightarrow (C_2)_3$ $C_2 + (C_2)_3 \longrightarrow (C_2)_4$
1.50 eV	$(C_2)_3 \longrightarrow (C_2)_2 + C_2 \longrightarrow 3C_2$	$C_2 + 2V \longrightarrow$ annihilation $C_2 + (C_2)_3 \longrightarrow (C_2)_4$
1.78 eV	$(C_2)_4 \longrightarrow (C_2)_3 + C_2 \longrightarrow 4C_2$	$C_2 + 2V \longrightarrow$ annihilation

More recent studies, however, through the implementation of first-principle quantum mechanics, particularly density functional theory (DFT), have helped to shed new light on the annealing processes on the atomic scale, providing a deeper understanding of the processes behind Wigner energy release [38-39]. DFT can be used to calculate energies and forces on atoms from fundamental constants, atomic number of atoms and the Schrodinger equation [40-44]. In contrast to early research (discussed above), scientists now believe that the interstitial atoms may well bond with neighbouring atoms, and the huge diversity associated with such bonding means that there are many types of defect possible [45-50]. The affect of each defect on the properties of graphite depends on its complexity and stability; some defects may undergo very small rearrangements requiring less than 1 electronvolt

whereas others, such as the pinning of entire dislocations, will require much more energy to anneal out.

5.3.3. The Intimate Frenkel Pair.

Ewels et al [38] have reported the 200 °C Wigner release peak to be a result of the annihilation of an intimate Frenkel pair. This intimate Frenkel pair was calculated to have a barrier to recombination of 1.30 eV, a value close to the previously reported 1.38 eV [26], associated with the 200 °C peak. Employing a first principles approach, using the AIMPRO code the author was able to develop a structure for the intimate Frenkel pair, shown below:

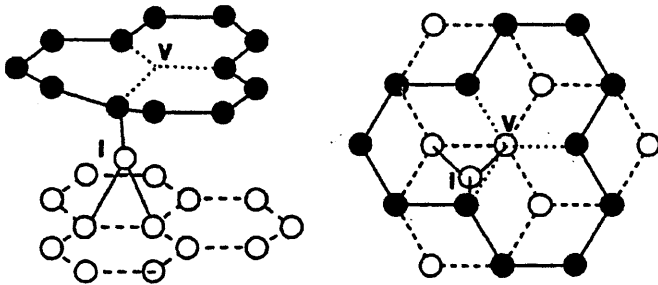


Fig. 5.3 : The metastable intimate Frenkel pair, I+V* defect, taken from the review by Telling and Heggie [5].

The I-V* complex consists of a C atom bonded to one of the three C atoms neighbouring the vacancy. It also forms two covalent bonds with C atoms from the graphene sheet below. The two other C atoms neighbouring the vacancy form a weakly reconstructed bond. The intimate I-V* complex arises from other Frenkel defects produced through irradiation, namely the separated Frenkel pair, which has an energy of 13.7 eV compared to perfect graphite. Depending on the nature of the interstitial atom and the bonding geometry, the separated Frenkel defect will either form a Stone-Wales defect [38] (not discussed here), or more commonly the intimate I-V* defect shown in Fig. 5.3. Once the activation is acquired (through annealing) the intimate I-V* defect system can relax into a ‘perfect’ graphite structure, releasing a further 10.1-10.8 eV, a significant energy release [38].

It also should be noted that a lesser known Wigner energy release peak is also observed at approx 1400 °C [51], corresponding to an energy barrier of 5.5 eV [5]. The deep trap responsible for this peak is not entirely certain; however it is likely that it corresponds to the breakdown of stable, complex prismatic loops that require significant temperatures in order to

be affected [52]. This peak is also of importance as it can potentially result in a release of heat, above the specific heat capacity, causing a dangerous and rapid heat rise during reactor operation.

The work carried out in this chapter involves the use of ion irradiation, under various experimental conditions, to try and simulate the affects of neutron irradiation in terms of introducing stored, Wigner-like energy into the system, with the aim of observing such energy release through modern calorimetric methods, such as differential scanning calorimetry (DSC). Again, using ions to simulate the effects of fast neutron bombardment is a valid concept, which can be carried out readily with standard laboratory equipment, making it convenient and relatively inexpensive [53]. This approach is very interesting; however currently there is a significant lack of publications involved in this particular work. If Wigner like energy could be introduced through ions in a cheap and simple manner then this would allow a much greater understanding of the potentially hazardous phenomenon of Wigner energy to be obtained rather rapidly, with obvious benefits to the nuclear community.

5.4. Results and Discussion

5.4.1. Room Temperature Irradiation

5.4.1.1. DSC Analysis

Modern studies into heat release from graphite samples involves the use of differential scanning calorimetry (see Chapter 2) to heat the samples, in this case under an inert atmosphere. Graphite discs were irradiated, at room temperature, with 5 keV He⁺, Ne⁺, Ar⁺ and Xe⁺ to a dose of $\sim 1.6 \times 10^{19}$ ions.m⁻². Each irradiated disc was placed in the sample pan and an identical, but unirradiated, graphite disc was placed in the reference pan. N₂ gas was flowed through the pans at a rate of 20 ml.min⁻¹ throughout the duration of the experiment, in order to minimise the potential for oxidation. The results are shown below in Fig. 5.4.

Results indicate that in all cases no stored energy release is observed, that is the spectra for the virgin sample and the ion irradiated samples are essentially the same. For each sample a second heating run was carried out which were almost identical to the first, again suggesting

that no heat was given off from the sample in the first run *i.e.* there was no observable heat release as a result of defect annihilation.

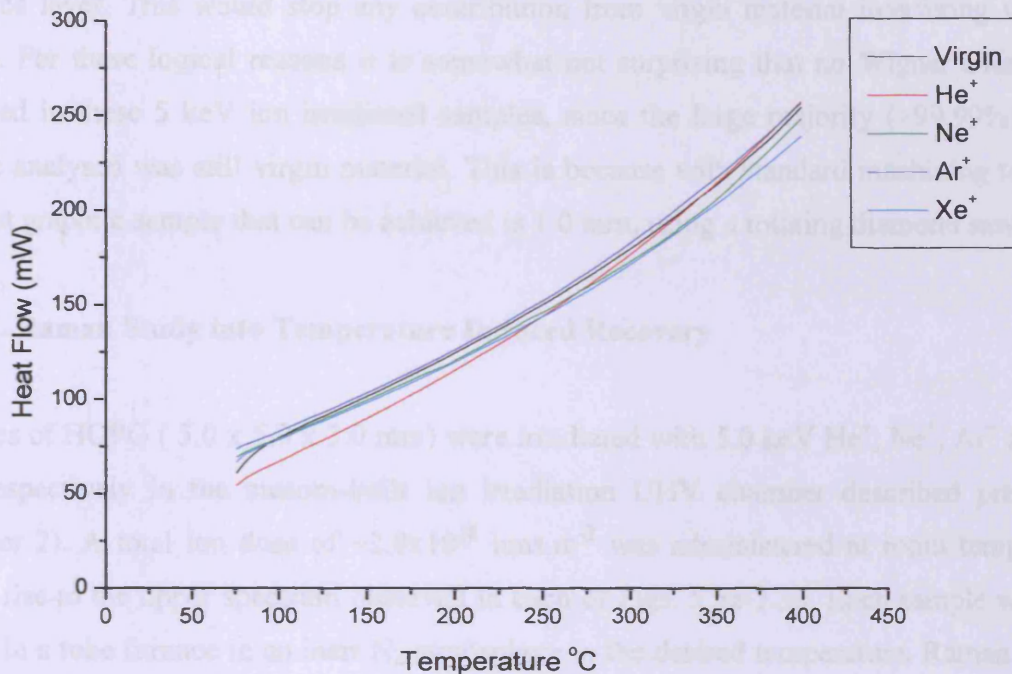


Fig. 5.4: DSC traces obtained from 5 keV inert-gas ion irradiation of nuclear grade graphite at a total fluence of $\sim 1.6 \times 10^{19}$ ions.m⁻² at 298 K. Below 75 °C the instrument is reaching equilibrium.

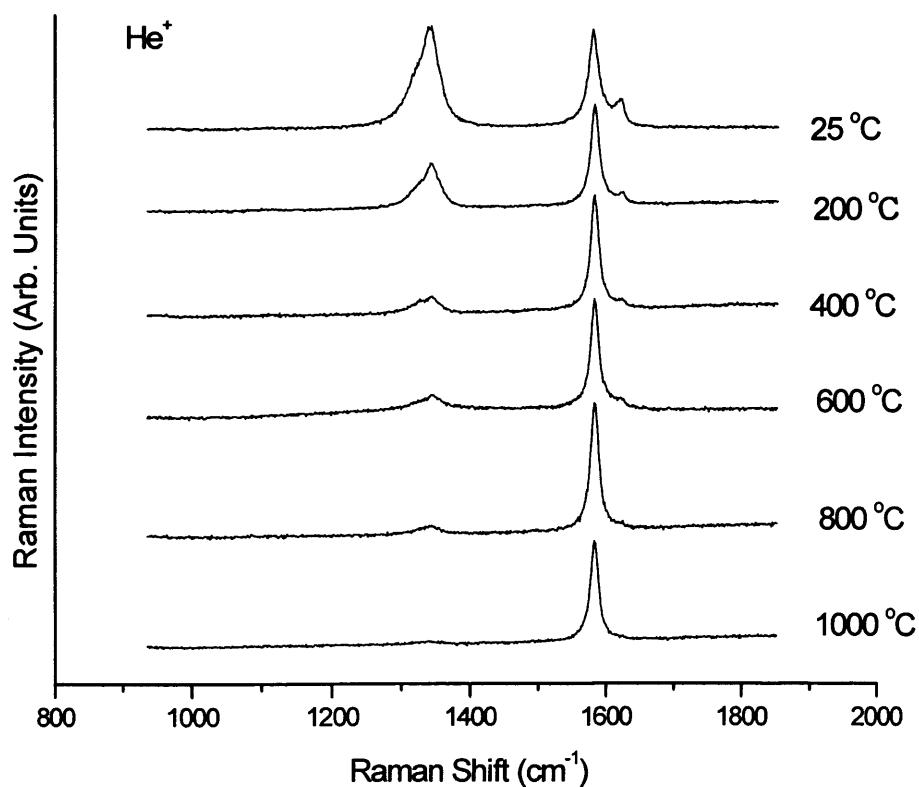
In some respects this is unexpected since we know that, from the theory discussed in Chapter 3, the collision mechanisms are essentially the same for charged ions and for neutrons. That is, graphite will become amorphised, due to the build-up atomic defects, after exposure to radiation regardless of the incident species [54-55]. Also an investigation carried out by Willis and co-workers [56] concluded that heavy-particle bombardment of graphite would indeed produce observable Wigner-like stored energy into graphite, in an analogous fashion to neutron bombardment.

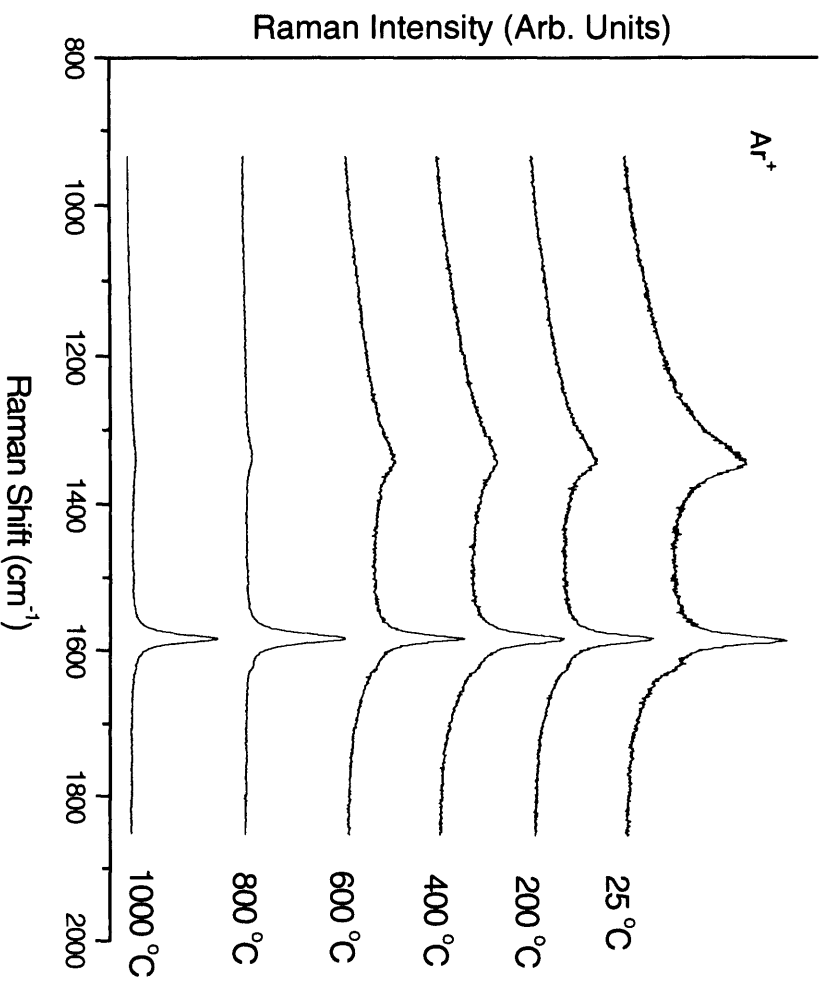
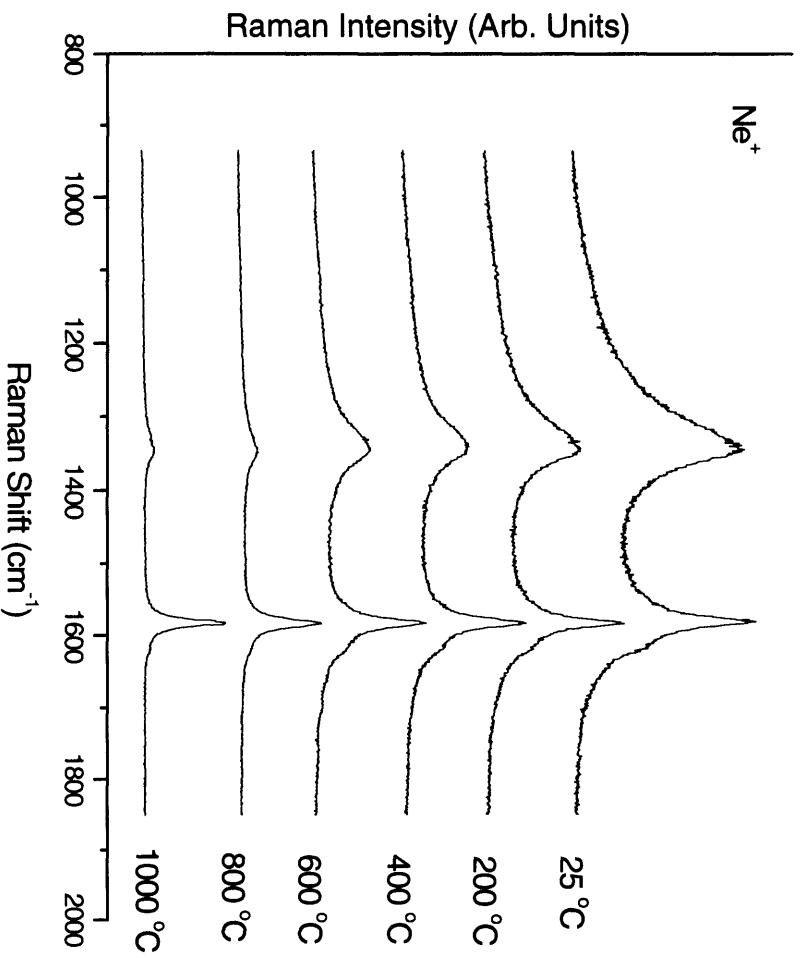
In the case of charged particle bombardment, however, the penetration depth and hence the depth of the resultant damage layer is considerably smaller than that caused by neutron bombardment. At these relatively low energies, even in the most penetrating case of He⁺, the damage layer will not extend far beyond 50 nm. Iwata has stated that despite being very informative the measurement of stored energy release is actually very difficult to observe and measure, in particular for charged particle irradiation [34]. The reason being that the irradiated cross-section of the sample is limited by the ion beam size, and so only a small

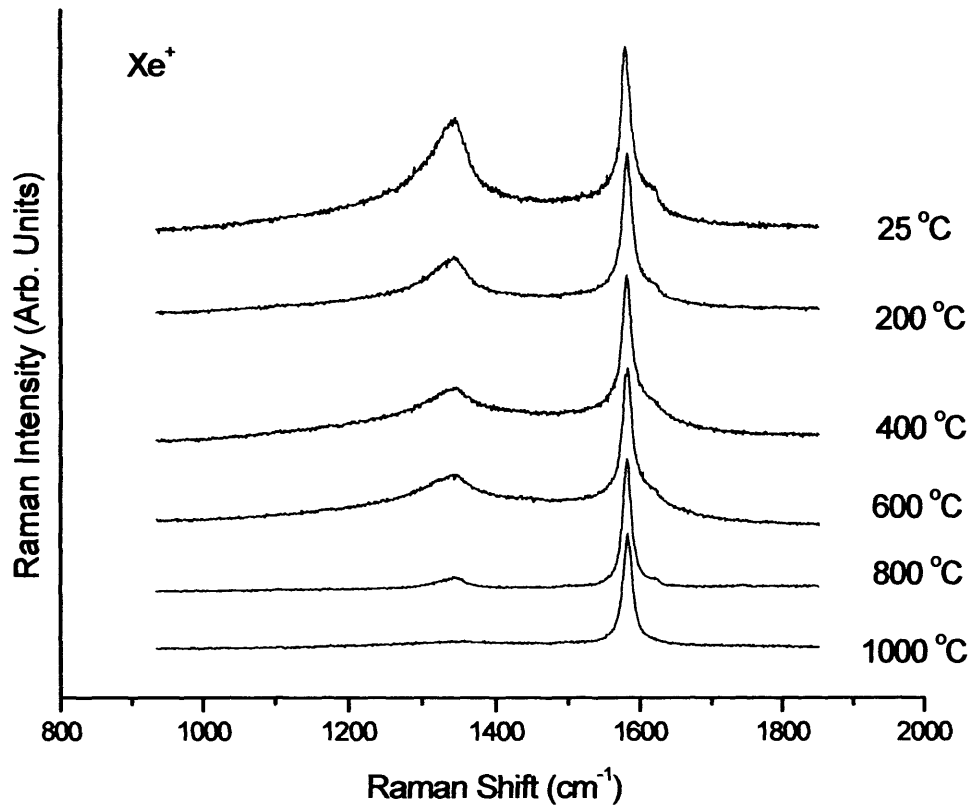
sample may be used; this ultimately leads to fewer defects being produced and consequently lower energy release. However, the thinness of the sample is also very important and ideally the sample should be thinner than the range of the charged particles and the extent of the damaged layer. This would stop any contribution from virgin material interfering with the results. For these logical reasons it is somewhat not surprising that no Wigner energy was observed in these 5 keV ion irradiated samples, since the large majority (>99.99%) of the sample analysed was still virgin material. This is because with standard machining tools the thinnest graphite sample that can be achieved is 1.0 mm, using a rotating diamond saw.

5.4.1.2. Raman Study into Temperature Induced Recovery

Samples of HOPG (5.0 x 5.0 x 3.0 mm) were irradiated with 5.0 keV He⁺, Ne⁺, Ar⁺ and Xe⁺ ions respectively in the custom-built ion irradiation UHV chamber described previously (Chapter 2). A total ion dose of $\sim 2.0 \times 10^{18}$ ions.m⁻² was administered at room temperature giving rise to the upper spectrum observed in each of Figs. 5.5a-5.5d. Each sample was then heated in a tube furnace in an inert N₂ atmosphere to the desired temperature. Raman spectra were taken at temperatures of 25, 200, 400, 600, 800 and 1000 °C.







Figs. 5.5a-5.5d: Raman spectra obtained for the annealing of 5.0 keV ion irradiated HOPG. Figs. 5a-5d correspond to He⁺, Ne⁺, Ar⁺ and Xe⁺ respectively.

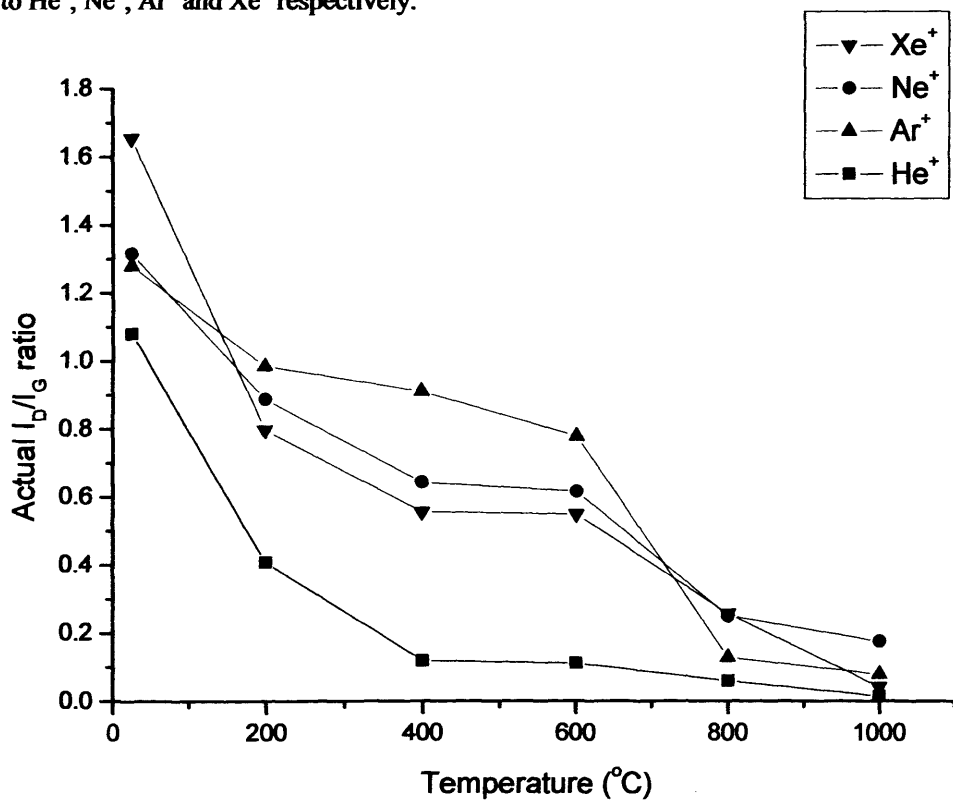


Fig. 5.6: A graph showing the decrease in the actual I_D/I_G ratio with increasing annealing temperature.

The Raman spectra obtained for each ion studied displays the expected pattern; that is a decrease in the I_D/I_G ratio with increasing temperature, a pattern observed previously in neutron irradiated nuclear graphite [57]. Fig. 5.6 is a comparison of the relative decrease in the actual I_D/I_G ratios with increasing annealing temperature. The actual ratios used do not correspond to those observed in Figs. 5.5a-5.5d but instead take into account the difference in the depth and size of the damage layer for each ion. That is, Raman information received from virgin material is not considered and hence gives a more realistic interpretation of the recovery processes involved within the damaged layer only. This has been discussed in detail in Chapter 4. It should be noted that the ion dose administered in Figs. 5.5a-5.5d is less than that received by the samples in Fig. 5.4 yet from the measured Raman data ion-induced damage can be clearly seen.

From Fig. 5.6 we can deduce that there is an effect of ion mass on the recovery process, the nature of the damage caused. It seems entirely logical that a heavier, larger ion such as Xe^+ will impart more destruction to the lattice system than a lighter ion such as He^+ . From this it follows that the nature of the defects will be different and that Xe^+ would lead to a more catastrophic breakdown of the lattice structure, whereas He^+ will cause more discrete packets of damage. Having said this, the annealing of the samples to 1000 °C results in very similar I_D/I_G ratios for all the ions studied, suggesting that such temperatures are high enough to recover even the more complex defect systems, quite remarkably, at these fluences at least.

In all cases there is a significant decrease in the I_D/I_G ratio upon heating the samples from 25 – 1000 °C, a recovery process that seems to occur in several steps, proceeding in the same direction to that of graphitisation in the manufacturing process [58]. The initial heating phase of 25 – 200 °C causes a significant drop in the observed I_D/I_G ratios. This is not surprising since there are a large number of relatively minor defect structures that require smaller activation energies with which to relax to their pre-irradiation positions. Niwase et al [59] observed similar results in 25.0 keV D^+ irradiated HOPG and suggested that the defects produced were mainly in-plane, discrete and primitive, resulting in their relatively low temperature of recovery.

Such unstable defects would likely be single vacancies or vacancy clusters, which may readily recombine with interstitials; these, when parallel to the basal plane, have a very small migration energy of < 0.1 eV [60].

temperature range $400 \leq T \leq 600$ °C it appears that there are no breakdown or annihilation of defects suggesting that the nature of the specific defects formed under these particular irradiation parameters are relatively stable over this temperature range.

At temperatures of 600 – 800 °C there is a further recovery of damage observed, perhaps suggesting a second recovery stage has been initiated as a result of the increased thermal energy into the system, with the more complex defect structures breaking down into smaller clusters resulting in the observed decrease in the I_D/I_G ratio. Interestingly, the rate of damage recovery in this temperature range is significantly higher for Ar^+ irradiation than for the other ions. Again, reasons for this are not entirely clear and perhaps further repeat experiments should be carried out in order to confirm this result. The only logical reason for this increased recovery rate would be down to the mass and size of Ar^+ being somehow more effective in generating damage clusters that are recovered at this stage; however as mentioned a further study would be needed in order to confirm and understand this.

In the final heating from 800 – 1000 °C a further drop in the I_D/I_G ratio is observed, resulting in a near 'perfect' graphite system. For all ions studied the I_D/I_G ratio at 1000 °C is very similar suggesting that at such high temperatures the majority of defects, regardless of the incident ion mass, are broken down and predominately annihilated. From Fig. 5.6 it is expected that even higher temperatures would eventually achieve a zero D band intensity, indicating a return to the pristine state; extrapolation of this graph indicates that the temperature needed may not be as high as perhaps expected. However, the reason for this is that in this case the ion doses administered were relatively low, and for greater ion fluence much higher temperatures would likely be required to achieve equivalent recovery due to the direct influence of radiation dose on defect complexity [5]. It has been reported in industry that even at temperatures as high as 2000 °C complete recovery is still not achieved [11].

5.4.1.3. Ion Implantation

An important factor that can cause damage to the graphite system is the implantation of the irradiated ion within the graphite lattice. It is conceivable that ions may easily come to rest within the material after losing all their kinetic energy, taking residence either between the graphene planes or even in-plane [61-62] in some cases, perhaps leading to significant disruption to the system on the atomic level. Such effects are expected to be larger with

heavier ions/ions with larger atomic radii. This is because they can take up more room and result in a greater amount of reordering. One method of observing any ion implantation is X-ray photoelectron spectroscopy (XPS) which is able to give elemental identification at the surface of the graphite. Since the energies used here are relatively small then a significant presence of the incident species would be expected in the XPS analysis. This is justified through SRIM 2008, where estimated penetration depths at 5.0 keV are 230, 30, 15 and 7 Angstroms for He^+ , Ne^+ , Ar^+ and Xe^+ respectively (Table 4.2. section 4.4.2). These values are the mean implantation depths and so there will of course be a proportion of ions present closer to the surface detectable through XPS.

In the case of He^+ irradiation, the ions would penetrate too far to be detected through XPS which is highly surface sensitive. However, the facility reported here is unable to detect the presence of He^+ within the sample, as the cross-section of the He^+ ions are too small and beyond the detection limit of the system. It is expected that because of the small size of the He^+ ions they would likely diffuse out of the graphite structure, far more easily than heavier ions of similar size and mass than the host carbon atoms would be able to.

5.4.1.4. XPS

The XPS spectra obtained from virgin PGA and virgin HOPG is shown below in Fig. 5.8

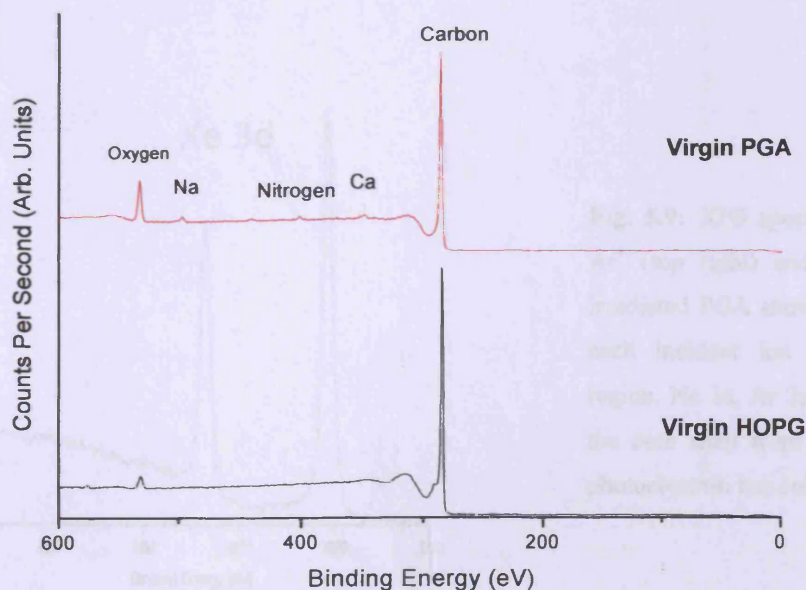


Fig. 5.8: XPS spectrum obtained for virgin PGA and virgin HOPG.

Obviously the largest peak is the carbon 1s peak appearing at 284.5 eV. Other notable surface elements are oxygen, as expected, which is more present in the polycrystalline PGA, due to the preferential desorption of oxygen on step edges [63]. Nitrogen is also detected in the PGA sample, along with other small impurities such as Na and Ca possibly present as a result of the manufacturing process or through the handling of the samples [64]. The HOPG is cleaved immediately before analysis, allowing investigation of a fresh surface.

After irradiation with Ne^+ , Ar^+ and Xe^+ ions, each of these species were found to be present within the graphite surface through XPS analysis:

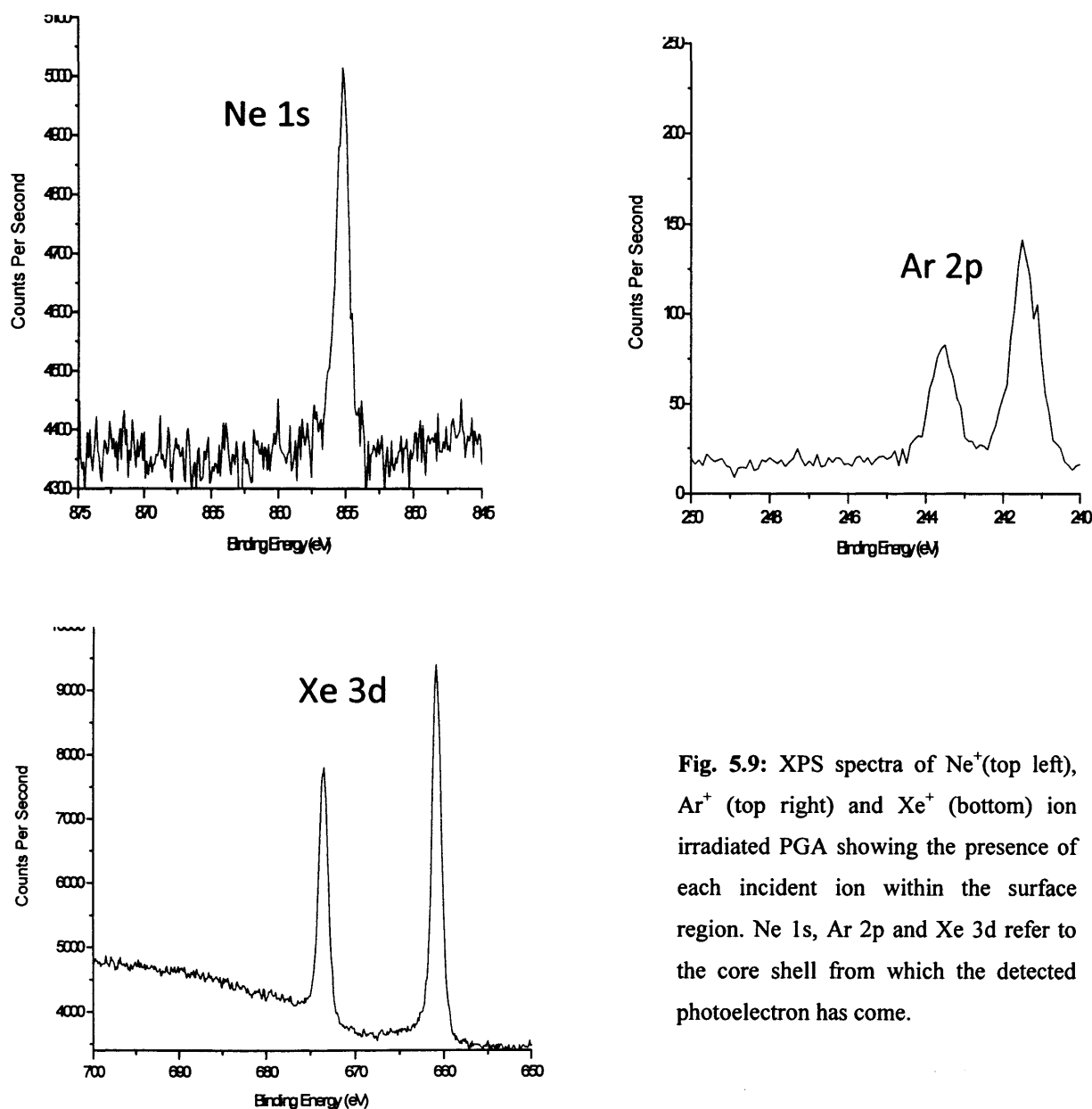


Fig. 5.9: XPS spectra of Ne^+ (top left), Ar^+ (top right) and Xe^+ (bottom) ion irradiated PGA showing the presence of each incident ion within the surface region. Ne 1s, Ar 2p and Xe 3d refer to the core shell from which the detected photoelectron has come.

The role of the implanted species is not really known however it must have an impact on the damage and the subsequent structure of the graphite lattice and also may play a role in hindering any recovery mechanisms. After annealing the samples the gas molecules are no longer observed through XPS, suggesting that they have been removed into the gaseous phase and likely caused further lattice disordering upon evaporation.

It is known that analysis of the Carbon 1s peak can provide information on the type of bonding present within the system, where broadening of the peak has been related to more sp^3 character bonding, which is indicative of a damaged graphite system [65-66].

Fig. 5.10 is a comparison of the C 1s photoemission peak for each of the graphite samples studied.

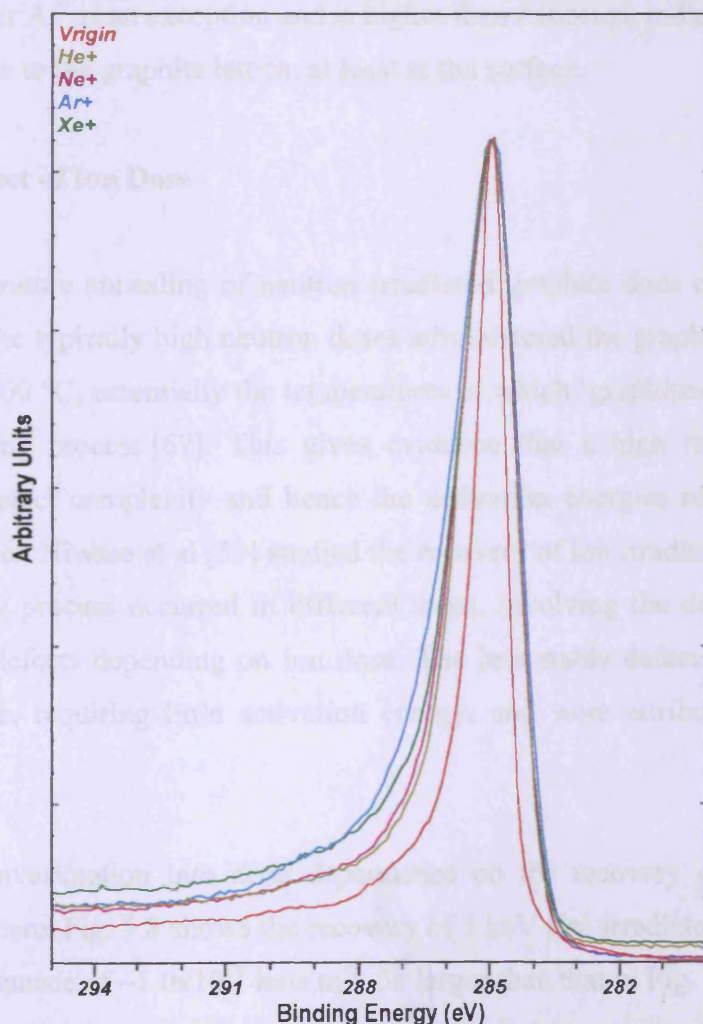


Fig. 5.10: XPS comparison of C 1s peaks for virgin and ion-irradiated nuclear grade graphite.

The resultant broadening is clear. The full width at half maximum (FWHM) of the peaks was calculated through the CasaXPS software package and the results tabulated in table 5.2.

Table 5.2: Calculated FWHM for the C 1s spectra of different graphites.

Sample	Measured FWHM (eV)
Virgin PGA	1.00
He+ irradiated PGA	1.57
Ne+ irradiated PGA	1.65
Ar+ irradiated PGA	1.98
Xe+ irradiated PGA	1.70
Xe+ irradiated HOPG	1.69

The data in the table shows a general increase in FWHM with increasing mass of the incident ion. However Ar⁺ is an exception and is higher than expected, indicating that Ar⁺ causes the most damage to the graphite lattice, at least at the surface.

5.4.1.5. Effect of Ion Dose

High temperature annealing of neutron irradiated graphite does encourage lattice recovery, but due to the typically high neutron doses administered the graphite is not fully recoverable until $T > 2000$ °C, essentially the temperatures at which ‘graphitisation’ starts to occur in the manufacturing process [67]. This gives evidence that a high radiation dose will lead to increased defect complexity and hence the activation energies required to induce recovery will be higher. Niwase et al [59] studied the recovery of ion irradiated graphite and found that the recovery process occurred in different steps, involving the dissolution of both unstable and stable defects depending on ion dose. The less stable defects relaxed at relatively low temperatures, requiring little activation energy, and were attributed to vacancy clustering processes.

A further investigation into dose dependence on the recovery of ion induced damage is carried out here. Fig. 5.8 shows the recovery of 5 keV He⁺ irradiated graphite, which received a total ion fluence of $\sim 1.0 \times 10^{19}$ ions.m⁻², 5x larger than that in Fig. 5.5a.

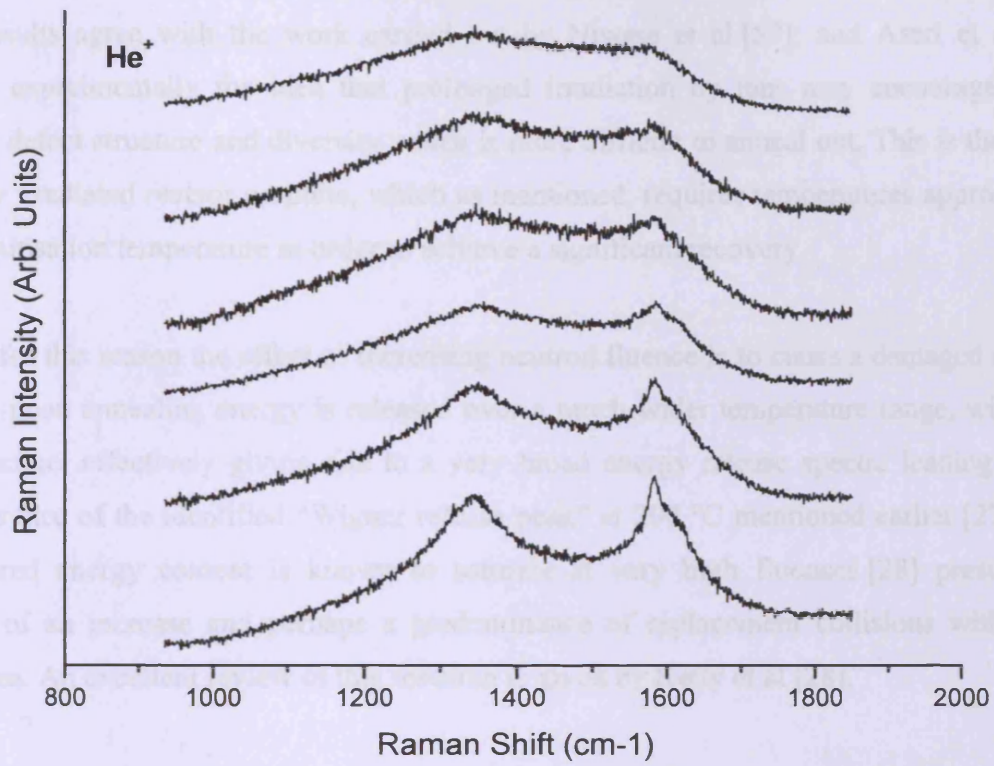


Fig. 5.11: A Raman study into 5.0 keV HOPG irradiated with He⁺ to a higher fluence of ~1.0x10¹⁹ ions.

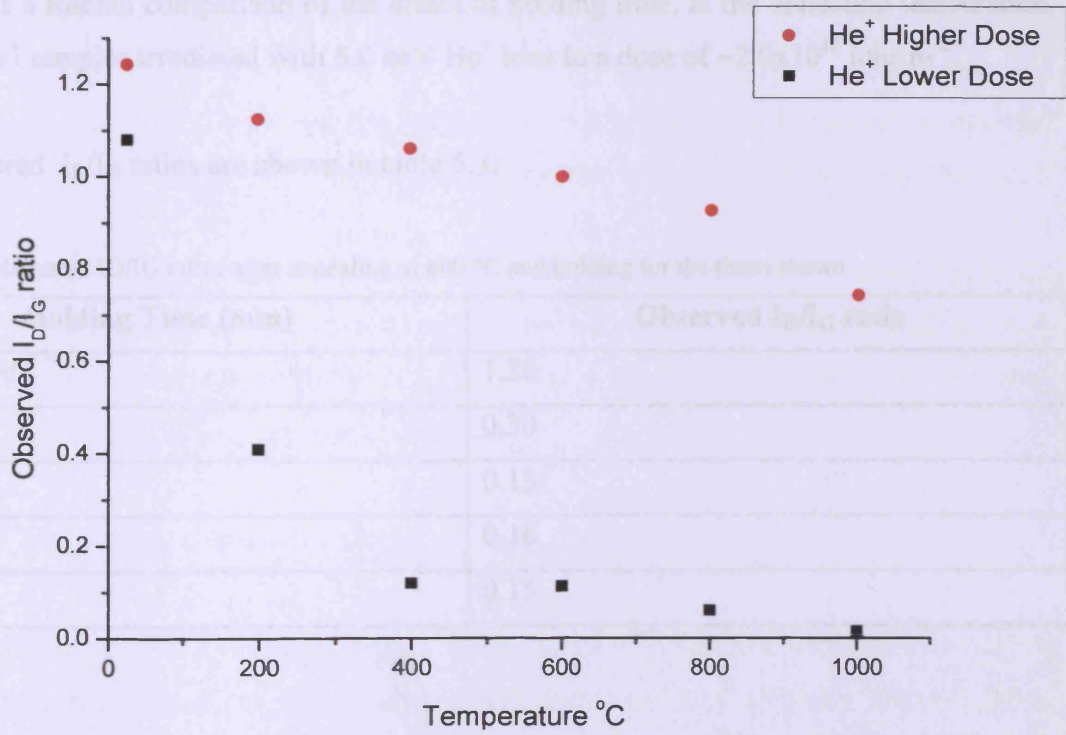


Fig. 5.12: Comparison of the rate of decrease of the I_D/I_G ratio with respect to temperature for two samples, one irradiated to a lower fluence of 2.0x10¹⁸ ions.m⁻² and one with a higher fluence of ~1.0x10¹⁹ ions.m⁻².

These results agree with the work carried out by Niwase et al [59]; and Asari et al [68] showing experimentally the idea that prolonged irradiation by ions may encourage more complex defect structure and diversity which is more difficult to anneal out. This is the same as highly irradiated reactor graphite, which as mentioned, requires temperatures approaching the graphitisation temperature in order to achieve a significant recovery.

Perhaps for this reason the effect of increasing neutron fluence is to cause a damaged system whereby upon annealing energy is released over a much wider temperature range, with less fine structure, effectively giving rise to a very broad energy release spectra leading to the disappearance of the identified “Wigner release peak” at 200 °C mentioned earlier [27]. The total stored energy content is known to saturate at very high fluences [28] presumably because of an increase and perhaps a predominance of replacement collisions within the target area. An excellent review of this research is given by Kelly et al [28].

5.4.1.6. Effect of Annealing Time

Fig. 5.13 is a Raman comparison of the effect of holding time, at the annealing temperature, for identical samples irradiated with 5.0 keV He⁺ ions to a dose of $\sim 2.0 \times 10^{18}$ ions.m⁻².

The measured I_D/I_G ratios are shown in table 5.3:

Table 5.3: Measured ID/IG ratios after annealing at 600 °C and holding for the times shown.

Holding Time (min)	Observed I _D /I _G ratio
Unannealed	1.20
0.1	0.30
1.0	0.15
10.0	0.16
100.0	0.15

The upper graph is the Raman spectrum taken directly after irradiation, whereas underneath are the Raman spectra taken after the sample was annealed, under an N₂ atmosphere, to

600 °C. The times shown indicate the length of time that the sample was maintained at 600 °C, before being cooled back down to room temperature.

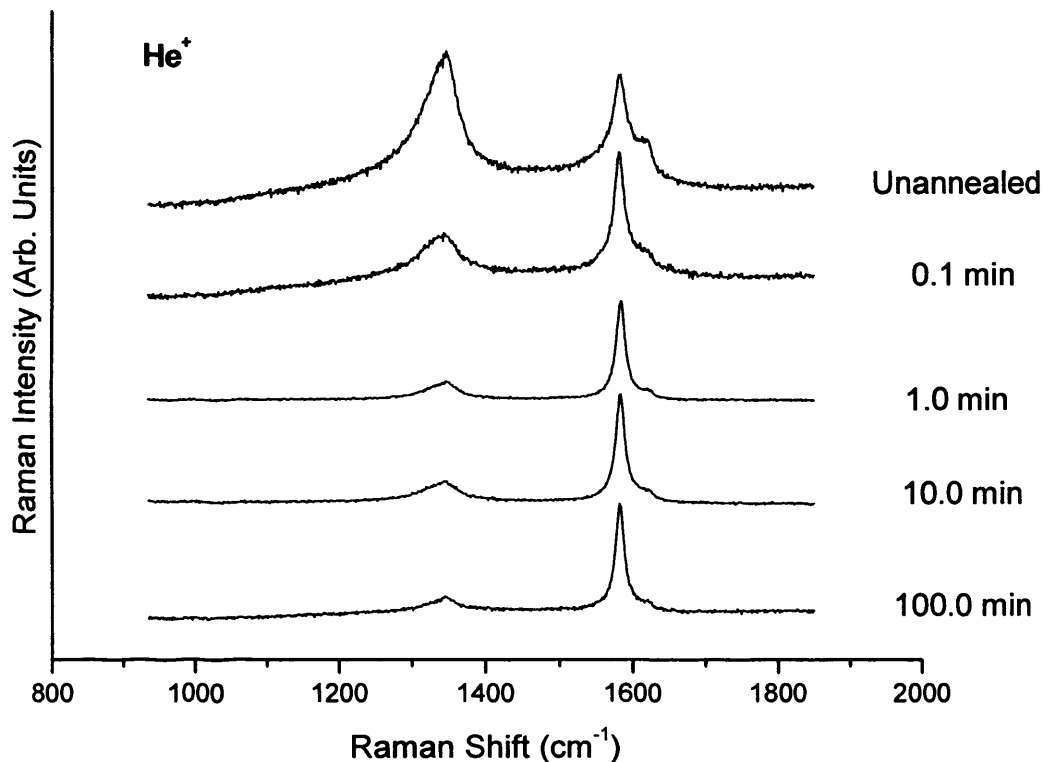


Fig. 5.13: Raman spectra of HOPG irradiated to a fluence of $\sim 2.0 \times 10^{18}$ ions.m⁻² with 5.0 keV He⁺ ions. Each spectra is taken after annealing at 600 °C. The times shown indicate the time spent holding at temperature.

Apart from the shortest holding time of 0.1 mins, the other spectra are very similar suggesting that the maximum amount of damage recovery occurs within the first minute at a temperature of 600 °C. The largest rate of recovery is observed within the first 6 seconds (0.1 min) indicating a very rapid kinetic process is involved.

5.4.2. Low Temperature Irradiations

In much the same way as increasing sample temperature can result in damage recovery, a low sample temperature prior to, and during, irradiation may lead to more damage being introduced. First measurements carried out by Austerman [69] were on neutron irradiated graphite at temperatures around -150 to -170 °C (*ca.* liquid nitrogen temperature). The results obtained were interesting and clearly showed that a considerable amount of damage was

retained at low temperatures. In one particular sample the energy release spectra observed contained an intense maxima at $-60\text{ }^{\circ}\text{C}$ with energy continually being released over the range -163 to $+2\text{ }^{\circ}\text{C}$ totalling to approximately one third of the total amount of energy released above $30\text{ }^{\circ}\text{C}$. These results suggest that defects may readily form at low temperatures which may rapidly anneal out at room temperature. Such defects can be imagined whereby they can only exist at sub-ambient temperatures; metastable Frenkel pairs which require only a very small amount of activation energy to overcome the barrier to recombination. At room temperature such defects could not occur or may occur but instantaneously annihilate. Parallel work by Austerman and Hove [35] on graphite irradiated at $-263\text{ }^{\circ}\text{C}$ (*ca.* liquid helium temperature) indicate that there is a temperature limit, whereby no appreciable increase in stored energy build-up may be expected at the even colder liquid helium temperatures.

Further sub-ambient irradiations were studied by Bonjour and Bochirol on three different graphites, varying in structure and crystallinity, irradiated at 77 K and 27 K [20]. Energy release peaks were observed at 75 , 110 and 135 K corresponding to activation energies of 0.09 , 0.13 and 0.17 eV respectively. No difference was observed between reactor grade and pyrolytic graphite, thus suggesting that initial levels of crystallinity of the graphite plays no role in the irradiation-induced stored energy accumulation. However, this is probably the case in this instance since the reactor grade graphite is far from amorphous, with crystallites of significant size. Early work by Ballinger [13] on samples of neutron irradiated carbon black and polymer carbon, both extreme samples of non-crystallinity, do show considerable differences in energy release spectra due to identically treated reactor grade graphite. The known release peak at $\sim 200\text{ }^{\circ}\text{C}$ begins to disappear as the crystallite size is reduced and at the same time the total amount of stored energy release also decreases with crystallite size. Such results suggest that microcrystalline graphites are indeed less susceptible to stored energy build-up, a difference only observed in samples vastly different in crystallinity. Austerman [69] suggests that such results are observed since during irradiation interstitials are trapped at crystal boundaries and at other defects present in non-crystalline carbons.

5.4.2.1. DSC Analysis

Fig. 5.14 below contains the DSC traces for ion irradiated PGA, irradiated at 5.0 keV at a total fluence of $\sim 1.6 \times 10^{19}\text{ ions.m}^{-2}$ at $\sim -173\text{ }^{\circ}\text{C}$ (100 K).

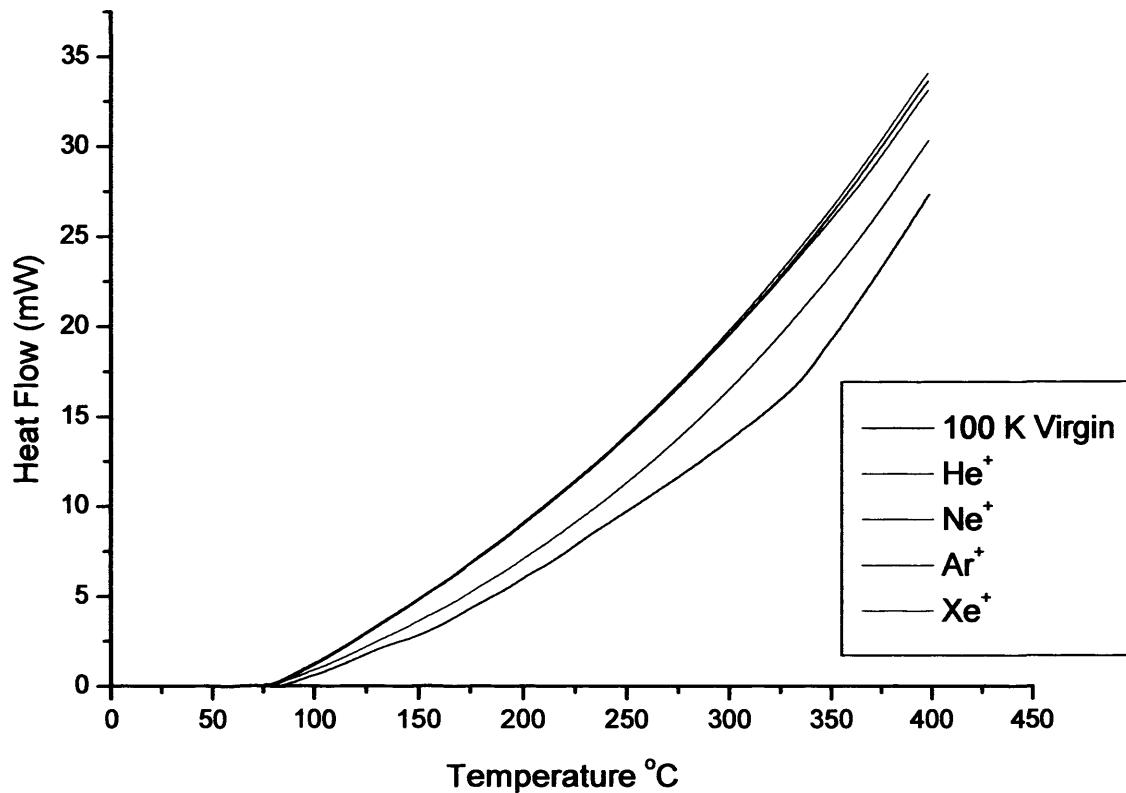


Fig. 5.14: DSC traces obtained from inert-gas ion irradiation of nuclear grade graphite at a total fluence of $\sim 1.6 \times 10^{19}$ ions.m⁻² at ~ 100 K. Below 75 °C the instrument is reaching equilibrium.

Despite the lower irradiation temperature used, the DSC traces were all very similar to the cooled virgin material after He⁺, Ne⁺, Ar⁺ and Xe⁺ irradiation. This confirms the hypothesis that at these relatively low energies the damage cascades are not powerful enough to install a detectable amount of Wigner-like energy into the system. Again, it is likely that indeed there is a form of ion-induced internal energy build-up but this is retained only in a very small fraction of the sample, whereas the overwhelming percentage of the sample is unaffected by the irradiation process. We know that cooling the sample prior to irradiation will enhance the effects of irradiation by locking in any defects produced, particularly metastable defects such as the intimate Frenkel pair, consequently lowering the rate of any self-annealing processes. However, even so, the ion energies used at Cardiff combined with the relatively low penetration depth achieved mean that no stored energy is observed in these cases.

5.4.2.2. Raman Analysis of Samples Irradiated at 100 K.

Figs. 5.15 and 5.16 below are the time-resolved Raman spectra obtained for the irradiation of HOPG at 100 K by 5.0 keV He⁺ and Xe⁺ ions respectively. The ion flux was $\sim 1.0 \times 10^{17}$ ions.m⁻².s⁻¹ and the irradiation times are displayed on the spectra.

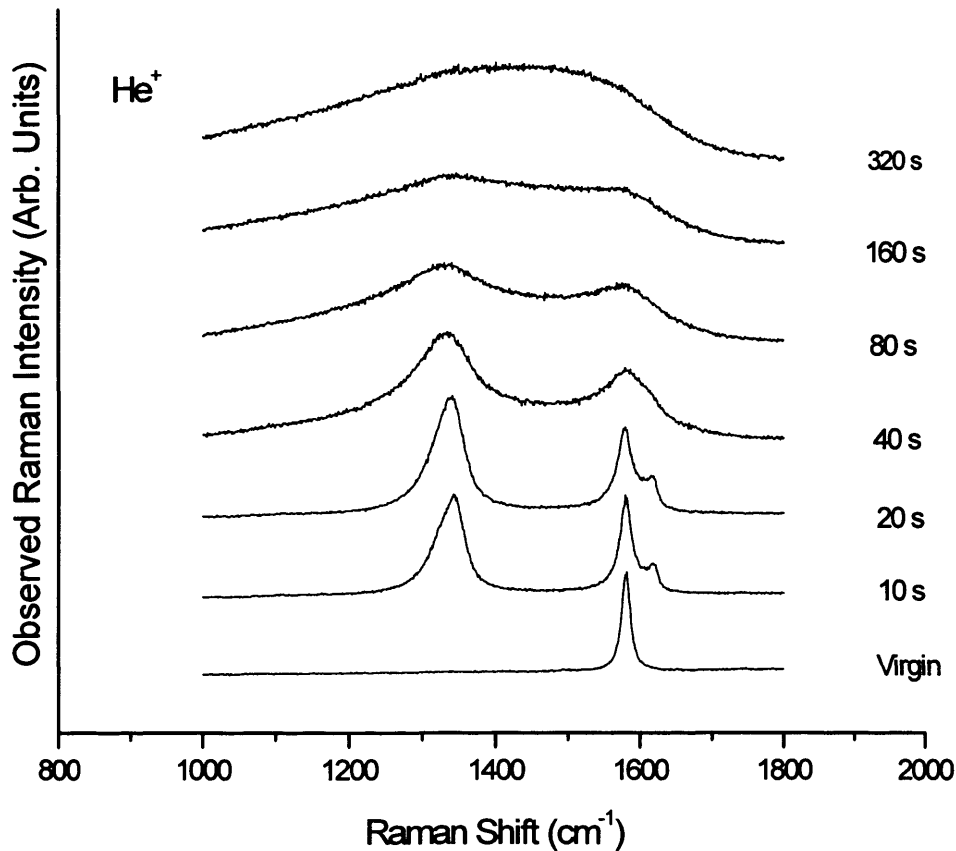


Fig. 5.15: Time-resolved Raman spectra obtained for the irradiation of HOPG at 100 K with 5 keV He⁺ ions at an ion flux of $\sim 1.0 \times 10^{17}$ ions.m⁻².s⁻¹.

The results show the same general trends seen at room temperature; however it is clear that, as expected, the irradiations carried out at *ca.* liquid nitrogen temperatures are considerably more effective in producing damage. This can be observed in Fig. 5.16 where the rate of increase of the actual I_D/I_G ratio in the Raman spectra for Xe⁺ irradiation is considerably higher at 100 K than at 298 K. In the case of He⁺ irradiated at 100 K an immediate increase in the I_D/I_G ratio is observed for an equivalent dose at room temperature, followed by a more rapid increase after 20 seconds irradiation.

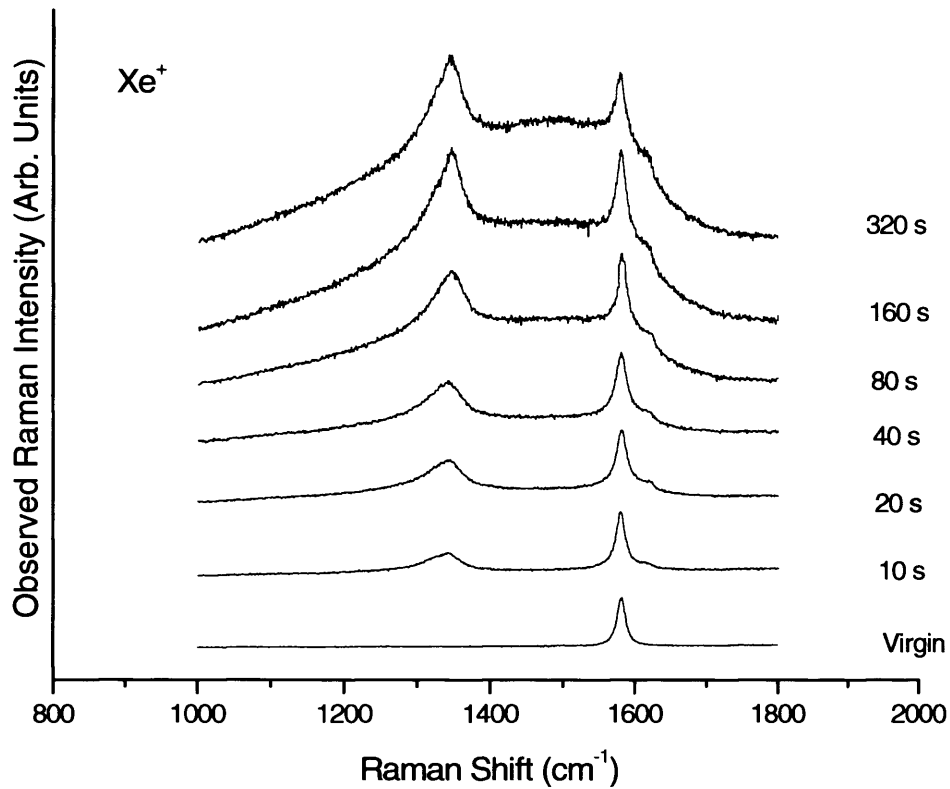


Fig. 5.16: Time-resolved Raman spectra obtained for the irradiation of HOPG at 100 K with 5 keV Xe^+ ions at an ion flux of $\sim 1.0 \times 10^{17} \text{ ions.m}^{-2}\text{s}^{-1}$.

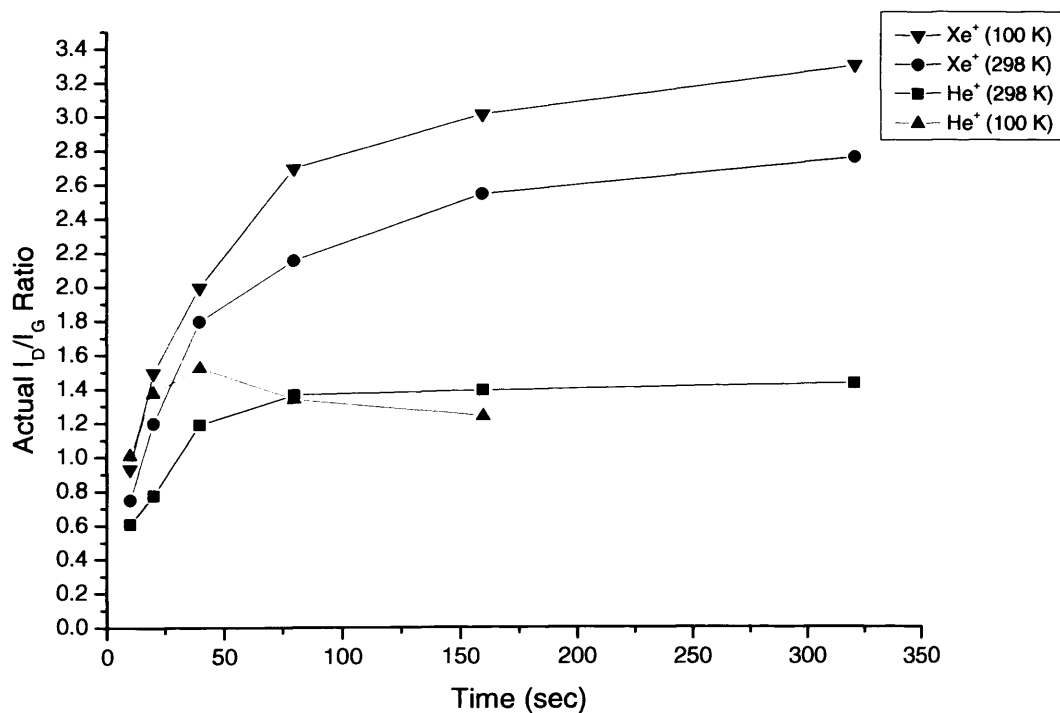


Fig. 5.17: The change in the actual I_D/I_G ratio with respect to irradiation time for 5.0 keV He^+ and Xe^+ irradiation. The effect of sample temperature prior to and during irradiation is clearly seen.

However, after an irradiation time of 40 seconds, the graph starts to change shape and the I_D/I_G ratio actually becomes lower. This signifies the breakdown of the T-K relation, which has been observed previously [70] and occurs when the damage to the system becomes quite large and the crystallites are < 2.5 nm [71].

From Fig. 5.15 it can be seen that the spectrum obtained does differ at higher doses; however, the I_D/I_G ratio may be the same or even lower at higher dose. At this point analysis of the I_D/I_G ratio becomes invalid and the spectra must be analysed using the peak width of the D band, which increases considerably from 40 seconds irradiation onwards. As Niwase pointed out, reduction of the crystallite size is not necessarily the origin of amorphisation and the increasing peak-width of the D band is a better means to distinguish amorphised samples after a critical dose; thus suggesting that the amorphisation proceeds through a change in the bonding nature from sp^2 to sp^3 carbon [72].

5.4.2.3. Highly Amorphised Graphite - The 1500 cm^{-1} Raman feature.

Another aspect to consider is the general broadening of the spectrum, and the presence and predominance of the previously observed peak at $\sim 1500\text{ cm}^{-1}$ [73-74]. Eventually a broad feature is observed, as shown in Fig. 5.12, indicating an amorphous system [75]. At this stage it becomes very difficult to obtain an accurate and meaningful I_D/I_G ratio, and hence there is a data point missing in Fig. 5.17. The broad band at $\sim 1500\text{ cm}^{-1}$ is indicative of a large decrease in crystallinity, and for the ion energies and doses used in this project, can only really be observed under prolonged He^+ irradiation or low-temperature irradiation for the heavier ions. The emergence of this band can be seen in Fig. 5.16, after 320 seconds irradiation with 5.0 keV Xe^+ ions at a sample temperature of ~ 100 K.

This feature has been observed previously in ion-irradiated graphite, but there has been no publication of such a feature with neutron irradiated material. Niwase et al [75] observed the feature in graphite irradiated with D^+ ions to a dose of 1.0×10^{22} ions. m^{-2} and attributed it to a C-D interaction and hence is assumed to be affected by ion implantation. In He^+ irradiation the band emerges rather suddenly from Fig. 5.15 it can be seen that somewhere between fluences of $\sim 1.6 \times 10^{19}$ ions. m^{-2} and 3.2×10^{19} ions. m^{-2} , relating to irradiation times of 160 and

320 seconds respectively, the Raman shape becomes such that it is impossible to accurately distinguish the D and G band positions and widths.

This feature was also observed in 5.0 keV Ne^+ , Ar^+ and Xe^+ irradiated graphite, but in these instances, due to the lower penetration depths, much higher fluences were required in order to achieve the complete amorphous spectra [74]. However, lowering the temperature of the sample during irradiation was also found to be sufficient in causing enough damage to the system to see the emergence of the broad feature.

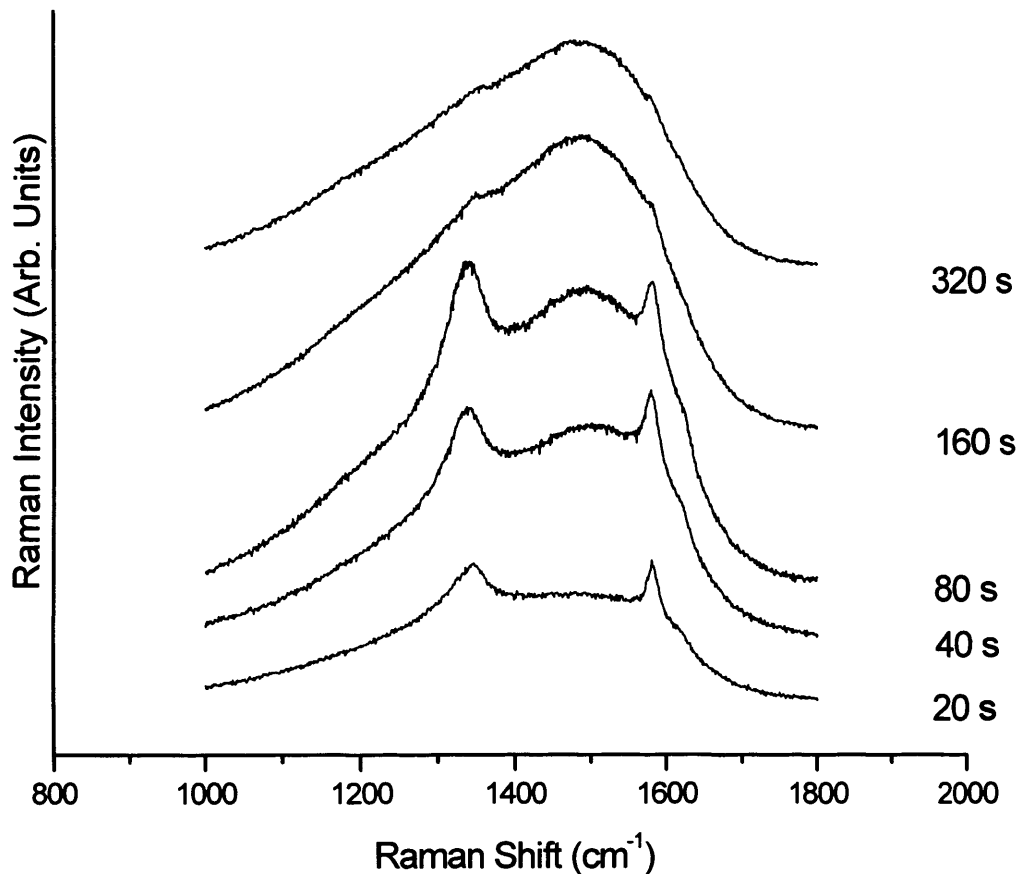


Fig. 5.18: Raman spectra obtained for 5.0 keV Ar^+ irradiated HOPG at 100 K and at an ion flux of $\sim 4.0 \times 10^{17}$ ions. m^{-2} . The duration of each irradiation is shown next to the spectra and times are cumulative. The emergence of the broad $\sim 1500\text{cm}^{-1}$ peak can be clearly seen.

Fig. 5.18 is for 5.0 keV Ar^+ irradiated graphite and the emergence of the additional band can be clearly seen, becoming more intense with increasing fluence, eventually generating the familiar broad 'hump' observed previously. Note that to obtain the spectra shown in Fig. 5.18 a considerably higher ion flux is required in order to achieve the necessary fluence over the same time period along with lowering the sample temperature to 100 K.

From what we know about the annealing process we can predict that once such a high level of amorphisation is achieved then recovering the lattice will be more difficult, requiring yet higher temperatures to tend to its pre-irradiated structure, and indeed this is the case. Although even at this high stage of amorphisation the graphitic system can start to be recovered, albeit somewhat slowly, by annealing as shown in Fig. 5.19 below, which is a case of highly damaged HOPG through 5.0 keV He^+ ions.

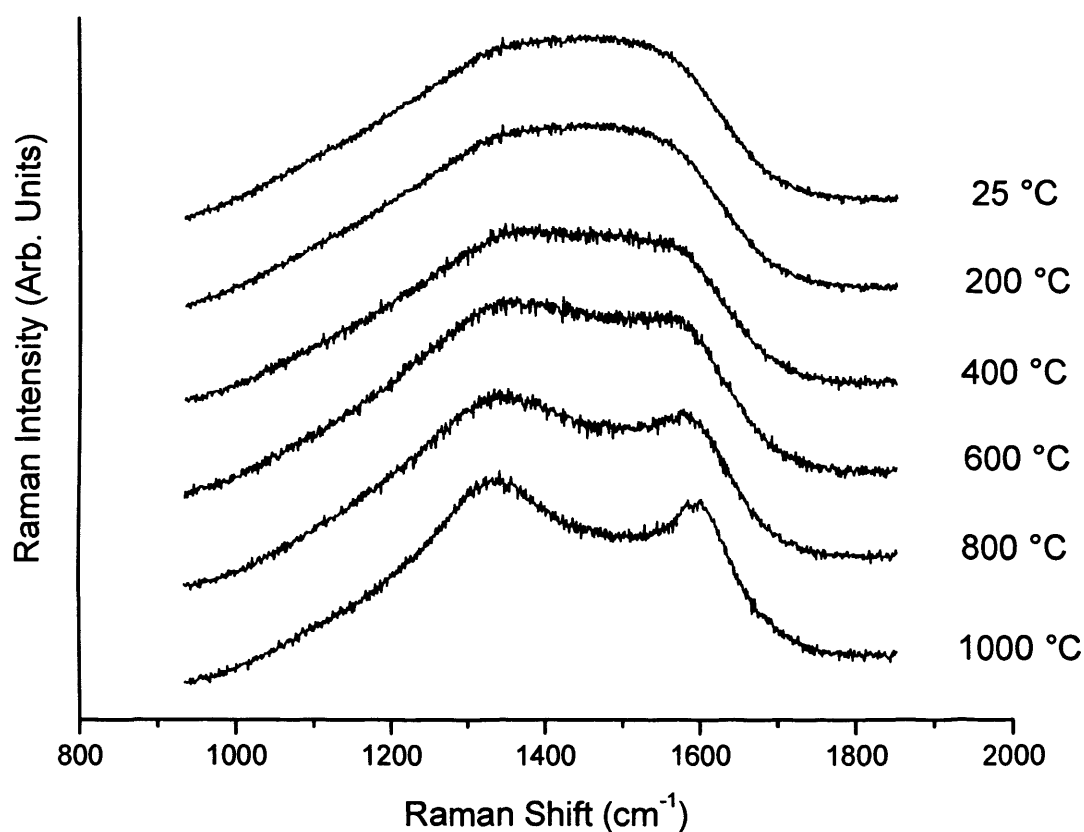


Fig. 5.19: Raman spectra of annealed 5.0 keV He^+ irradiated graphite, irradiated at 100 K with $\sim 3.2 \times 10^{19}$ ions.m⁻².

Initially the I_D/I_G ratios cannot be deduced, until an annealing temperature of approx 800 °C at which it starts to become possible to distinguish the two bands. At 1000 °C the spectra starts to look similar to other heavily ion irradiated samples observed previously, and there is a significant drop in any contribution from the 1500 cm⁻¹ feature.

Comparing this data with Fig. 5.12 it becomes apparent that, as expected, this more intense damage to the graphite system is even more difficult to recover than the high dose of He^+

irradiation received previously, and temperatures close to the graphitisation temperature would likely be required to achieve any significant recovery, indicating that this heavily damaged material is similar to the carbonaceous graphite-precursor material.

5.4.3. High Temperature Irradiation

Investigations carried out into irradiations at higher temperatures have shown that the rate of energy accumulation decreases with increasing temperature [28]. This is expected since at elevated temperatures the system will have enough energy to sustain self-annealing processes which will effectively allow any interstitial-vacancy pairs to recombine virtually instantaneously, resulting in a lower net damage accumulation. Early work at temperatures above 30 °C but below 200 °C showed the intensity of the 200 °C peak to decrease substantially with increasing temperature. Obviously for irradiations above 200 °C this peak does not exist, but even at irradiations at $T > 400$ °C some, relatively small, amounts of stored energy are observed [28].

For these reasons, DSC analysis of 5.0 keV ion irradiated graphite, at elevated temperatures, was not carried out since it would be highly unlikely that any energy release would be observed, particularly since none was observed at room temperature and below where there would be far fewer self-annealing processes occurring.

As for Raman analysis on samples irradiated at higher temperatures much work has been shown in the literature already. Experiments involving 5.0 keV inert-gas ion irradiation were not carried out due to experimental difficulties involved with heating the sample, but results would be expected to follow those previously published. That is for a given ion dose received by the sample the I_D/I_G ratio will decrease with increasing temperature [76-78]. Again, this is due to an increase in self-annealing processes hindering the development of damage into the system [79].

5.4.4. TEM Analysis

In order to understand fully radiation-induced damage in graphite it is important to be aware of the affect of radiation on the atomic scale. To do this an extensive investigation should be carried out utilising high-resolution TEM to try and observe the generation of defects, their

evolution with respect to increased radiation dose and also the mechanisms of recovery as a result of sample heating. Work has been carried out previously utilising TEM techniques to study the effects of ion irradiation on graphite [80-83]; however more studies need to be carried out in order to achieve a more comprehensive understanding.

Here a brief analysis is carried out on the effect of ion-irradiation on the microstructure of a nuclear grade graphite. Fig. 5.20 is a TEM image taken from a virgin sample of PGA. Samples were prepared through Focussed Ion-Beam (FIB) as discussed in chapter 2.



Fig. 5.20: A TEM image of virgin PGA showing the randomly orientated graphitic packets.

Fig. 5.20 shows clearly the basal planes present in the virgin PGA sample. The bands appear darker under the microscope and are randomly orientated amongst an amorphous matrix. The high-resolution dark-field image shown in Figs. 5.21 and 5.22 shows the basal planes in more detail and the angstrom-sized spaces between the basal planes can be clearly resolved. These results are rather similar to those obtained by Wen et al [84] on samples of Gilsocarbon, showing a rather similar structure as expected. The basal planes are far from ideal in structure and bending and buckling of the graphene layers is apparent.

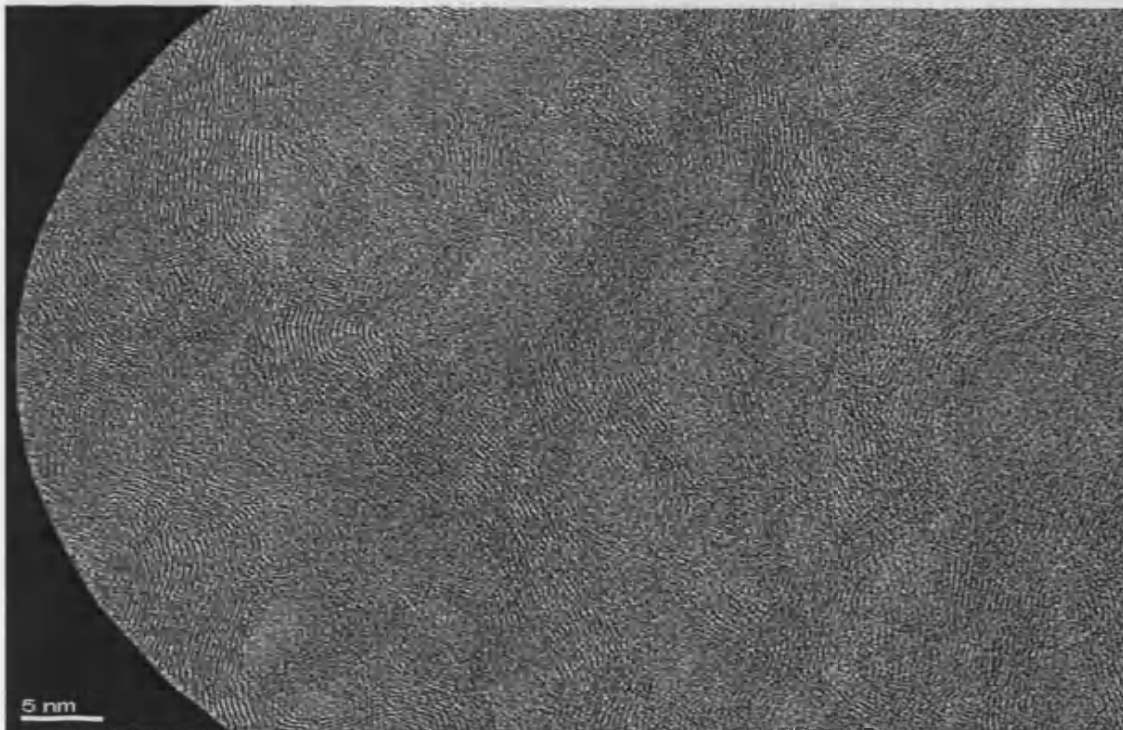


Fig. 5.21: A high-resolution dark field image of virgin PGA showing the randomly orientated graphite strands.

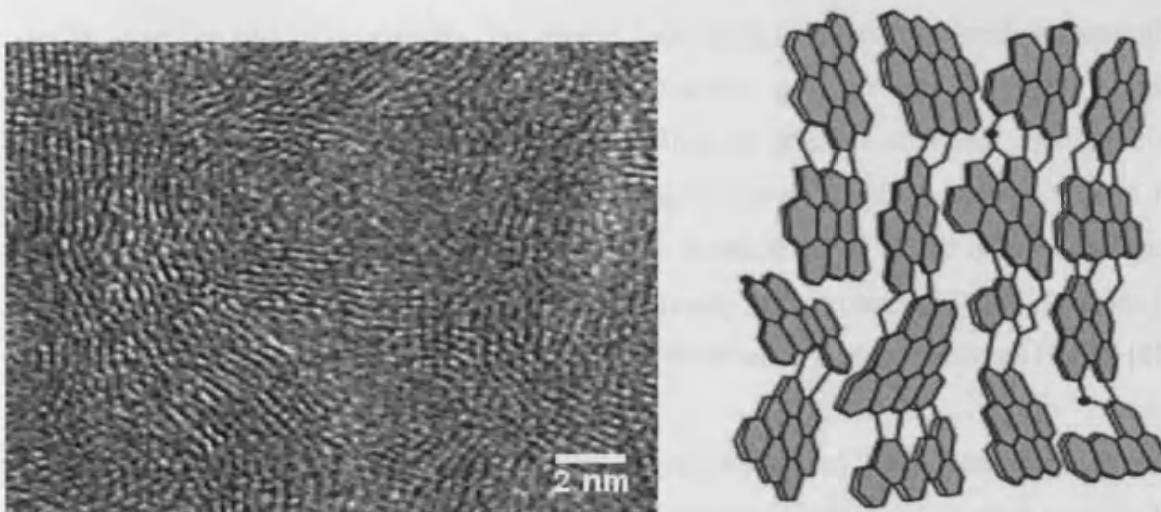


Fig. 5.22: (left) Enlarged section of Fig. 5.21 and the graphite fringes (right) an illustration to represent the inherent disorder and buckling present within the basal planes of PGA.

Ion-irradiation of the TEM specimen was carried out in order to induce damage into the system. Fig. 5.23 is an image taken after the sample was exposed to 5 keV He^+ irradiation to a fluence of 3.2×10^{19} ions. m^{-2} .

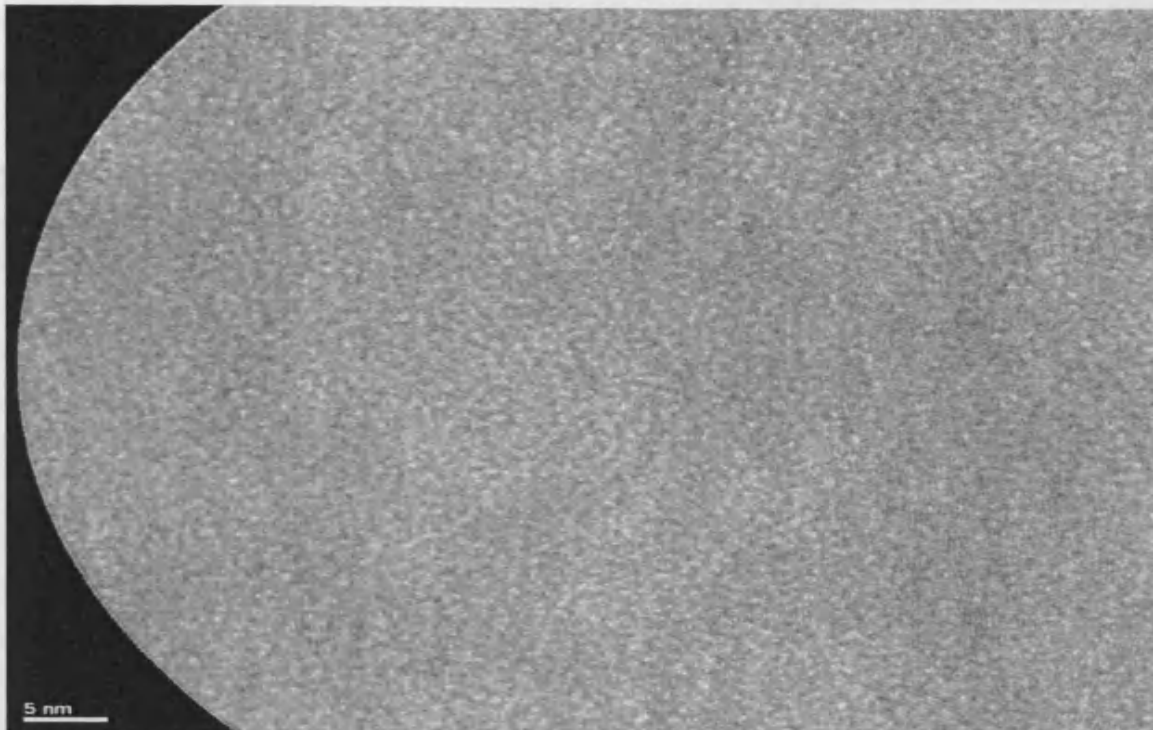


Fig. 5.23: High-resolution TEM image taken after 5 keV He^+ irradiation to a fluence of 3.2×10^{19} ions. m^{-2} .

After irradiation there is a distinct loss of structure and the graphitic bands can no longer be seen. Instead the image is generally featureless indicating a tendency towards an amorphous system. This was confirmed through electron diffraction to be the case. Similar conclusions are drawn by Muto et al [85] who studied thin films of graphite after He^+ irradiation with TEM. They found that a ridge network consisting of curled graphitic sheets starts to form causing a wrinkling of the graphite surface and a breakdown of lattice order. Also similar amorphisation of graphite has been observed previously with protons [86] and electrons [87]. The breakdown of long-range order has also been observed in highly irradiated HOPG [88].

Heating the ion-irradiated sample causes the expected recovery of the lattice which is also validated through the Raman analysis. Such a recovery has been observed on the atomic level previously in ion-irradiated HOPG samples [89] and similar images have been taken in the graphitisation of petroleum pitch [90]. In this particular case the radiation fluence received by the sample initially was reasonably high leading to a highly amorphous state. As a result annealing at 600 °C only leads to a partial recovery of the structure and from Fig. 5.24 it can be seen that the sample is still largely amorphous. These results agree with the Raman results presented in Fig. 5.19 and help to show that the recovery of a highly damaged system can be

difficult and quite high temperatures are needed for the graphitic structure to be clearly seen again.

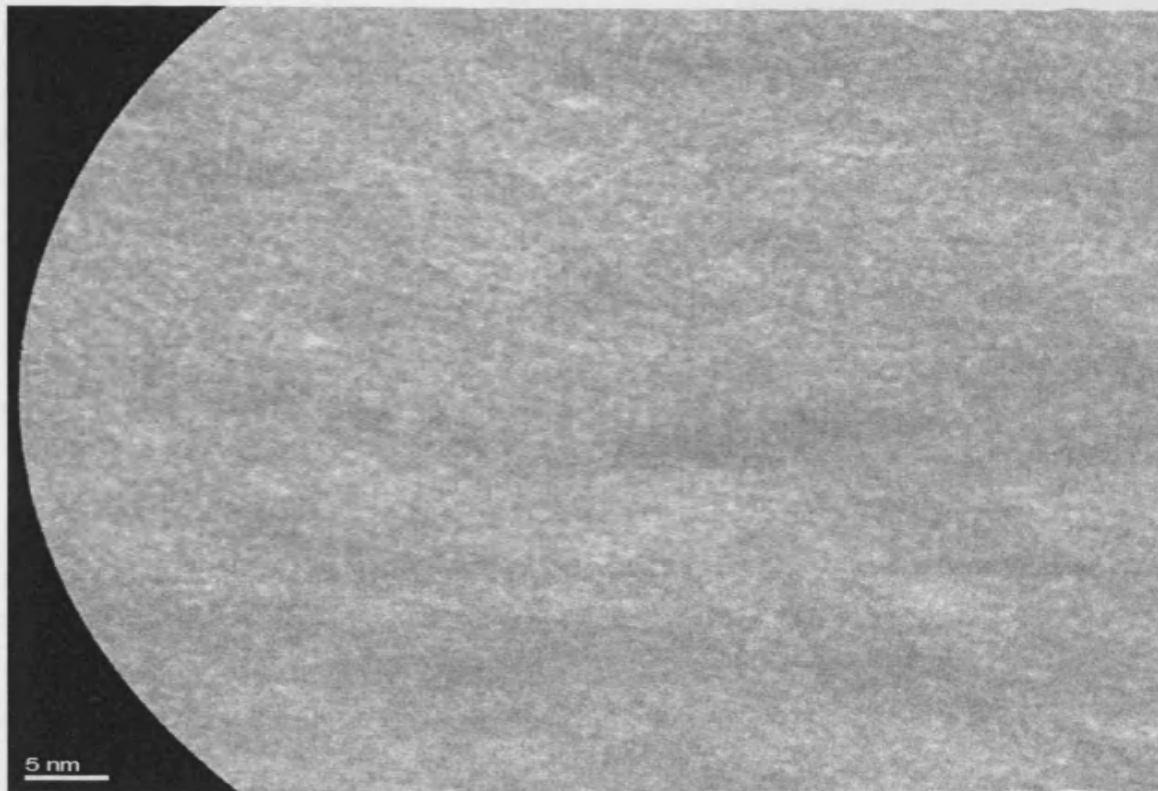


Fig. 5.24: High-resolution TEM image taken after the PGA sample was exposed to 5.0 keV He^+ irradiation to a fluence of 3.2×10^{19} ions. m^{-2} and subsequently annealed at 600 °C for 0.5 hours.

5.5. Conclusions

Raman analysis shows clearly the recovery effect of temperature on ion-irradiated graphite systems. Monitoring of the I_D/I_G ratio shows recovery to increase in various steps, each step likely to correspond to various type or types of defects, each with a different amount of energy required in order to be removed. The effect of temperature has been shown to depend on the initial radiation dose received, and more damaged systems require higher temperatures for an equivalent level of recovery. The effect of sample temperature prior to and during irradiation has also shown to be important, with the amount of damage increasing, for a given dose, as initial sample temperature decreases. At higher temperatures the opposite affect has been observed and reasons for this have been discussed.

DSC analysis has not shown any stored energy build-up for samples irradiated at 5 keV, even at temperatures as low as 100 K. Reasons for this are not entirely clear but is likely due to the low energies and subsequently low penetration depths involved.

TEM analysis has shown the recovery process occurring to some extent. The TEM investigation carried out here is only brief but it has shown that such work has the potential to provide the deeper understanding required to elucidate the damage and recovery mechanisms occurring in graphite on the atomic scale.

5.6. References

- [1] E.P. Wigner, *CP-387*, (1942) 4.
- [2] B.T. Kelly, 'Physics of Graphite', Applied Science Publishers, London, (1981).
- [3] J.H.W. Simmons, 'Radiation Damage in Graphite', Pergamon Press, Oxford, (1965).
- [4] T. Maruyama, T. Kaito, S. Onose, I. Shibahara, *J. Nucl. Mat.*, **225** (1995) 267.
- [5] R.H. Telling, M.I. Heggie, *Philosophical Magazine*, **87** (2007) 4796.
- [6] K. Niwase, *Phil. Mag. Lett.*, **82** (2002) 401.
- [7] A.I. Ryazanov, K. Yasuda, C. Kinoshita, *J. Nucl. Mat.*, **323** (2003) 372.
- [8] A.I. Ryazanov, A.V. Klapstov, A. Kohyama, *J. Nucl. Mat.*, **329-323** (2004) 486.
- [9] G. Haffenden, 'Thermodynamics and Spectroscopy of Defects in Graphite', University of Sussex Presentation (2007).
- [10] F. Banhart, *Rep. Prog. Phys.*, **62** (1999) 1181.
- [11] A.J. Wickham et al, 'Characterization, Treatment and Conditioning of Radioactive Graphite from Decommissioning of Nuclear Reactors', IAEA-TECDOC-1521, (2006).
- [12] L. Arnold, 'Windscale 1957: Anatomy of a Nuclear Accident', Palgrave Macmillan Publishers, London, (1995).
- [13] J.C. Ballinger, 'Twin crucible calorimeter for graphite stored energy study', USAEC Report HW-24692, Hanford Atomic Products Operation, (1952).
- [14] K. Koyama, 'A linear rise calorimeter for measuring stored energy in graphite', USAEC Report HW-63552, Hanford Atomic Products Operation, (1960).
- [15] R.W. Henson, J.H.W. Simmons, 'An adiabatic rise calorimeter for measuring stored energy in irradiated graphite', British Report AERE-M/R-2564, (1959).
- [16] T.J. Neubert, M. Burton, R.C. Hirt, A.R. VanDyken, et al, 'Neutron-induced decomposition of graphite', Argonne National Laboratory Report ANL-5472, (1956).

- [17] T.J. Neubert, R.B. Less, *Nuclear Sci. Eng.*, **2** (1957) 748.
- [18] G.P. Kerr, 'Summary of Sykes stored energy determinations', USAEC Report HW-17446, Hanford Atomic Products Operation, (1950).
- [19] R.W. Attree et al, 'The release of stored energy from N.R.X. reactor reflector graphite', Canadian Report CRC-541, (1953).
- [20] L. Bochirol, E. Bonjour, *Carbon*, **6** (1968) 661.
- [21] E. Bonjour, L. Bochirol, L. Weil, 'Radiation damage in reactor materials', IAEA, Vienna, (1963).
- [22] B. E. L. Bochirol, L. Weil, *Comptes Rendus*, **254** 456.
- [23] R.E. Nightingale, 'Stored Energy', in: R.E. Nightingale (Ed.) 'Nuclear Graphite', Academic Press, New York and London, pp. 325.
- [24] A.H. Cottrell, et al, 'Theory of Annealing Kinetics Applied to the Release of Stored Energy from Irradiated Graphite in Air-Cooled Reactors', Second United Nations International Conference on the Peaceful Uses of Atomic Energy, Geneva. (1959).
- [25] J.C. Bell, G.B. Greenough, 'Windscale Laboratories', Windscale Laboratories (1960).
- [26] E.W.J. Mitchell, M.R. Taylor, *Nature*, **208** (1965) 638.
- [27] D. Lexa, A.J. Kropf, *J. Nucl. Mat.*, **348** (2006) 122.
- [28] B.T. Kelly, B.J. Marsden, K. Hall, D.G. Martin, A. Harper, A. Blanchard, 'Irradiation damage in graphite due to fast neutrons in fission and fusion systems', IAEA-TECDOC-1154, (2000).
- [29] M.A. Kanter, G.R. Hennig, *Bull. Am. Phys. Soc.*, **1** (1956) 119.
- [30] M.A. Kanter, *Phys. Rev.*, **107** (1957) 655.
- [31] G.J. Dienes, *J. Appl. Phys.*, **23** (1952) 1194.
- [32] C.A. Coulson, M.A. Herraiez, M. Leal, E. Santos, S. Senent, *Proc. Roy. Soc.*, **A274** (1963) 461.
- [33] T. Iwata, F.E. Fujita, H. Suzuki, *J. Phys. Soc. Jap.*, **16** (1961) 197.
- [34] T. Iwata, T. Nihira, *Jap. J. Appl. Phys.*, **15** (1975) 575.
- [35] S.B. Austerman, J.E. Hove, *Phys. Rev.*, **100** (1955) 1214.
- [36] M. Pope, *J. Chem. Phys.*, **36** (1962) 1602.
- [37] T. Iwata, *J. Nucl. Mat.*, **133&134** (1985) 361.
- [38] C.P. Ewels, R.H. Telling, A.A. El-Barbary, M.I. Heggie, P.R. Briddon, *Phys. Rev. Lett.*, **91** (2003) 1.
- [39] R.H. Telling, C.P. Ewels, A.A. El-Barbary, M.I. Heggie, *Nature Mater.*, **2** (2003) 333.
- [40] M.C. Payne, M.P. Teter, D.C. Allan, e. al, *Rev. Mod. Phys.*, **64** (1992) 1045.

- [41] P. Hohenburg, W. Kohn, *Phys. Rev.*, **136** (1964) 864.
- [42] W. Kohn, L.J. Sham, *Phys. Rev.*, **140** (1965) 1133.
- [43] P.R. Briddon, R. Jones, *Phys. Status. Solidi B*, **217** (2000) 131.
- [44] M.D. Segall, P.L.D. Lindan, M.J. Probert, et al, *J. Phys: Cond. Matt.*, **14** (2002) 2717.
- [45] M.I. Heggie, 'Design and Control of Structure of Advanced Carbon Materials for Enhanced Performance', Kluwer Academic, Dordrecht, (2001).
- [46] P.O. Lehtinen, A.S. Foster, A. Ayuela, et al, *Phys. Rev. Lett.*, **91** (2003) 17202.
- [47] L. Li, S. Reich, J. Robertson, *Phys. Rev. B.*, **72** (2005) 184109.
- [48] M.I. Heggie, B.R. Eggen, C.P. Ewels, et al, *Electrochem. Soc. Proc.*, **98** (1997) 60.
- [49] C.H. Xu, C.L. Fu, Pedraza, D.F, *Phys. Rev. B.*, **48** (1993) 13273.
- [50] K. Nordlund, J. Keinonen, T. Mattila, *Phys. Rev. Lett.*, **77** (1996) 699.
- [51] J. Rappeneau, J.L. Taupin, J. Grehier, *Carbon*, **4** (1966) 115.
- [52] M.I. Heggie, 'Ruck, tuck and buckle - new ideas for irradiation damage', British Energy annual graphite meeting presentation, Manchester (2007).
- [53] C. Abromeit, *J. Nucl. Mat.*, **216** (1994) 78.
- [54] K. Niwase, M. Sugimoto, T. Tanabe, F.E. Fujita, *J. Nucl. Mater.*, **155-157** (1988) 303.
- [55] K. Niwase, K. Nakamura, T. Shikama, T. Tanabe, *J. Nucl. Mater.*, **170** (1990) 106.
- [56] A.H. Willis, J.M. Bagnat, R.C. De Beukelaer, *J. Appl. Phys.*, **32** (1961) 8.
- [57] K. Niwase, T. Tanabe, I. Tanaka, *J. Nucl. Mat.*, **191-194** (1992) 335.
- [58] T. Tanabe, K. Niwase, I. Tanaka, N. Tsukuda, E. Kuramoto, *J. Nucl. Mat.*, **191-194** (1992) 330.
- [59] K. Niwase, T. Tanabe, I. Tanaka, *J. Nucl. Mat.*, **191-194** (1992) 335.
- [60] P.A. Thrower, R.M. Mayer, *Phys. Status. Solidi.*, **47** (1978) 11.
- [61] R.A.P. Smith, G.C. Smith, P. Weightman, *Journal of Electron Spectroscopy and Related Phenomena*, **152** (2006) 152.
- [62] D. Marton, K.J. Boyd, T. Lytle, W. Rabalais, *Phys. Rev. B. Condensed Matter*, **48** (1993) 6757.
- [63] K. Wen, T.J. Marrow, B.J. Marsden, 'Simulation of Irradiated Graphite' Nuclear Graphite Research Group, The University of Manchester, School of Materials (2005).
- [64] Y.S. Virgil'ev, *Atomic Energy*, **84** (1998) 6.
- [65] L.A. Dollard, 'Chemistry of Carbon and Modified Carbon Surfaces', PhD Thesis, Cardiff University (1996).
- [66] J.A. Leiro, M.H. Heinonen, T. Laiho, I.G. Batirev, *J. Elec. Spec and Rel. Phen.*, **128** (2003) 205.

- [67] J. Lachter, R. Bragg, *Phys. Rev. B.*, **33** (1986) 8903.
- [68] E. Asari, M. Kitajima, K.G. Nakamura, *Phys. Rev. B.*, **47** (1993) 11143.
- [69] S.B. Austerman, 'Stored Energy Release in Graphite Irradiated at Low Temperatures', USAEC Report NAA-SR-1564, North American Aviation Inc (1956).
- [70] D.S. Knight, W.B. White, *J. Mater. Res.*, **4** (1989) 385.
- [71] E. Asari, *Carbon*, **38** (2000) 1857.
- [72] K. Niwase, K. Nakamura, I. Tanaka, Y. Miyamoto, T. Tanabe, *J. Nucl. Mat.*, **179-181** (1991) 214.
- [73] M. Iwaki, K. Takahashi, H. Watanabe, S. Sato, 'Structure and macroscopic properties of ion-implanted carbon materials', *RIKEN Review*, **12** (1996).
- [74] A. Theodosiou, A.F. Carley, S.H. Taylor, *J. Nucl. Mat.*, **403** (2010) 108.
- [75] K. Niwase, Y. Kakimoto, I. Tanaka, T. Tanabe, *Nuclear Instruments and Methods in Physics Research B*, **91** (1994) 78.
- [76] K. Niwase, T. Tanabe, M. Sugimoto, F.E. Fujita, *J. Nucl. Mat.*, **162-164** (1989) 856.
- [77] M. Yoshida, T. Tanabe, N. Ohno, Yoshimi, M, S. Takamura, *J. Nucl. Mat.*, **386-388** (2009) 841.
- [78] T. Hirai, T. Compan, Niwase, K, J. Linke, *J. Nucl. Mat.*, **373** (2008) 119.
- [79] K. Niwase, *Phys. Rev. B.*, **52** (1995) 15785.
- [80] G.J. Thomas, W. Bauer, P.L. Mattern, B. Granoff, *Advan. Chem. Ser.*, **158** (1976) 97.
- [81] K. Sone, T. Abe, K. Obara, R. Yamada, H. Ohtsuka, *J. Nucl. Mat.*, **71** (1977) 82.
- [82] S. Veprek, A. Portmann, A.P. Webb, H. Stuessi, *Radiat. Eff.*, **34** (1977) 183.
- [83] Y. Kazumata, *J. Nucl. Mat.*, **68** (1977) 257.
- [84] K.Y. Wen, J. Marrow, B.J. Marsden, *Journal of Physics: Conference Series*, **126** (2008) 12056.
- [85] S. Muto, T. Tanabe, M. Takeuchi, Y. Kobayashi, S. Furuno, K. Hojou, *J. Nucl. Mat.*, **271&272** (1999) 285.
- [86] A. Ishaq, L. Yan, J. Gong, D. Zhu, *Materials Letters*, **63** (2009) 1505.
- [87] S. Muto, T. Tanabe, *J. Nucl. Mat.*, **283-287** (2000) 917.
- [88] J. Koike, D.F. Pedraza, *J. Mater. Res.*, **9** (1994) 1899.
- [89] B. An, S. Fukuyama, K. Yokogawa, M. Yoshimura, *Jpn. J. Appl. Phys.*, **39** (2000) 3732.
- [90] H. Daniels, R. Brydson, B. Rand, A. Brown, *Philosophical Magazine*, **87** (2007) 4073.

Chapter 6

High Energy (≥ 100 keV) Ion Irradiation

6.1. Introduction

From what has been established so far, it can be said that increasing the incident ion energy will increase the ion penetration depth and hence the extent of the collision / damage cascade. Up to now the results have been discussed on graphite irradiated with ions of energies no greater than 10 keV. However, in order to better simulate the effects of fast neutron irradiation (which have a mean energy 2.0 MeV [1]) then perhaps it is more appropriate to use higher energy ions. This has been done externally at Surrey University, UK and at the Université de Lyon, France which have the necessary apparatus in which to carry out irradiations in the MeV energy regime.

It was hoped that the increased penetration depths would produce more bulk sample damage, and hence can be analysed effectively through DSC and XRD. The presence of stored Wigner energy in the samples after irradiation is more likely to be measured using DSC since it would be present in a much larger percentage of the total sample mass. As for XRD, which is a bulk technique, the increased depth of the damage will increase the chances of observing any ion-induced affects in the XRD pattern. Raman spectroscopy is also employed, where in all high energy irradiations the penetration depth of the ions exceed the 40 nm detection limit of the Raman laser.

6.2. Experimental

To carry out the high energy irradiations discussed in this chapter, an ion implanter and Van de Graff accelerator were used, both of which are discussed in Chapter 2. The graphite samples used were nuclear grade PGA graphite obtained from the University of Manchester.

For the carbon ion irradiations the ion implanter at Surrey Ion Beam Centre was used to irradiate with C^+ and C^{++} ions. The doubly charged ions are required in order to achieve the higher initial energies. In total seven samples were irradiated; the samples were 2 mm in diameter and 1mm thick and were placed in a 2 cm x 2cm piece of graphite, essentially a custom made sample holder (Fig. 6.1, left).

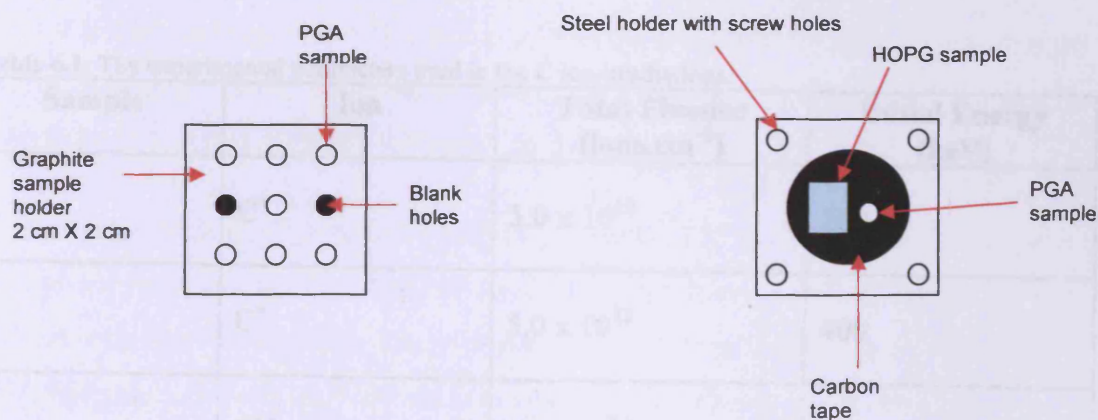


Fig. 6.1: a) (left) schematic of custom made graphite sample holder with 7 small graphite discs inside used at the Surrey Ion Beam centre. b) (right) Schematic of 2cm x 2cm steel holder used at Université de Lyon with a HOPG sample and a small graphite disc placed at the centre, both irradiated simultaneously by the ion beam.

For higher energies (> 1.0 MeV) the Van De Graff facility at the Université de Lyon was used. Samples were stuck down onto a metal holder which was screwed in place, in direct line of the ion beam. The beam covered a 1 cm^2 area in the centre of the holder (Fig. 6.1, right)

6.3. Results

6.3.1. Carbon Ion Irradiation

From the theory discussed in Chapter 3 the majority of the irradiation induced damage caused in graphite is a result of the primary knock-on atoms, and the extended collision cascades that develop as a result [2-5]. Each individual collision cascade must be initiated by a single carbon atom which, in the case of reactor graphite, was itself removed from its lattice position by a fast neutron. It therefore seems feasible that a good method of simulating neutron induced damage would be to irradiate with carbon ions in an attempt to simulate the primary knock-on atoms and thus try to cause similar damage cascades throughout the graphite matrix. The experiments carried out are summarised in Table 6.1.

Table 6.1: The experimental parameters used in the C ion irradiations.

Sample	Ion	Total Fluence (ions.cm ⁻²)	Initial Energy (keV)
A	C ⁺	5.0 x 10 ¹²	200
B	C ⁺	5.0 x 10 ¹²	400
C	C ⁺⁺	5.0 x 10 ¹²	800
D	C ⁺	5.0 x 10 ¹⁴	200
E	C ⁺⁺	5.0 x 10 ¹⁴	400
F	C ⁺⁺	5.0 x 10 ¹⁴	800
G	C ⁺	5.0 x 10 ¹⁶	400

All irradiations were carried out at room temperature. The ion energies used were picked in an attempt to match reasonably closely the energies of the primary-knock on

atoms, assuming its energy was passed on from a fast neutron with energy of 2.0 MeV. The experiments were designed in order to keep the fluence constant whilst increasing the energy and vice versa, allowing for an understanding of the affect of each parameter.

As discussed previously, the maximum energy transferred from a moving particle colliding with a stationary particle can be expressed by Eq. 6.1 [6]:

$$E_{\max} = \Lambda E \quad (\text{Eq. 6.1})$$

Where,

$$\Lambda = 4M_1M_2/(M_1+M_2)^2 \quad (\text{Eq. 6.2})$$

So, for a fast neutron ($M_1 = 1$ a.m.u.) of energy 2.0 MeV striking a carbon atom ($M_2 = 12$ a.m.u.) within the graphite lattice, the maximum energy passed on can be calculated to be approximately 0.57 MeV or 570 keV.

In practice, it is difficult to obtain energies of exactly 570 keV and also this is just an idea of the energies and is not exact, considering the neutron energy of 2.0 MeV is only an estimated mean value. The energies used of 200, 400 and 800 keV will give a sufficient range of energies with which to simulate the primary knock-on atom.

6.3.1.1. Ion Implantation

Using the SRIM 2008 software package it is possible to estimate the expected penetration depths of the carbon irradiated samples and to get an idea of the extent of the collision cascades [4]. Below is a screenshot taken for the simulation of 1000 C^+ ions incident on graphite, with initial energies of 200, 400 and 800 keV.

The implantation profile approximates a Gaussian distribution, and Fig. 6.3 clearly shows that the affect of increasing the initial ion energy is to increase the mean penetration depth, in an almost linear fashion.

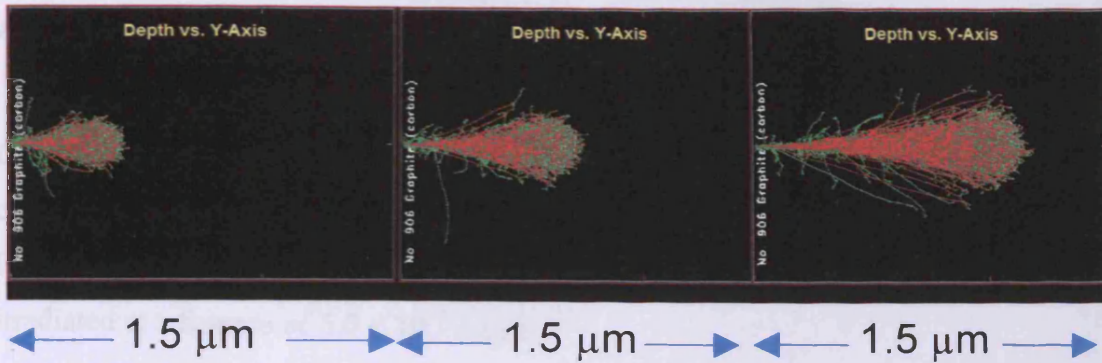


Fig. 6.2: A visual representation of the collision cascades generated from C ion irradiation of graphite at ion energies of 200 keV, 400 keV, and 800 keV (from left to right respectively) as simulated by SRIM 2008. Green represents displaced carbon atoms and red represents the ion path.

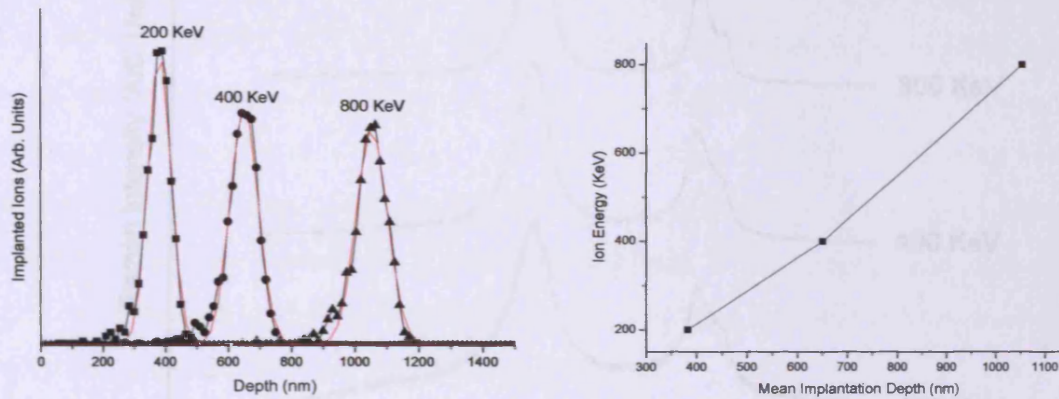


Fig. 6.3: **a left)** C ion implantation profiles. The energies stated refer to the initial C ion energy for that peak. The implantation profiles approximate well to a Gaussian distribution. **b right)** An almost linear relationship between ion energy and implantation depth.

Table 6.2 below is derived from the SRIM simulations and highlights the mean penetration depths, χ_0 , the range of ion implantation and the number of vacancies produced per carbon ion. Such information can provide a good understanding of the affect of ion energy on the irradiation processes.

Table 6.2: Ion penetration parameters as calculated by SRIM 2008.

Energy (keV)	χ_0 (nm)	Approx Implantation Range (nm)	Vacancies/ion
200	382.9	243 - 520	~ 324
400	651.5	475 - 827	~ 387
800	1054.5	842 - 1262	~ 428

6.3.1.2. Raman Analysis

Once irradiated the samples were analysed using Raman spectroscopy. Firstly comparison was made between graphite samples irradiated with C ions at the same fluence but at varying energies. Fig. 6.4 below is the spectra obtained for samples irradiated at a fluence of 5.0×10^{14} ions cm^{-2} .

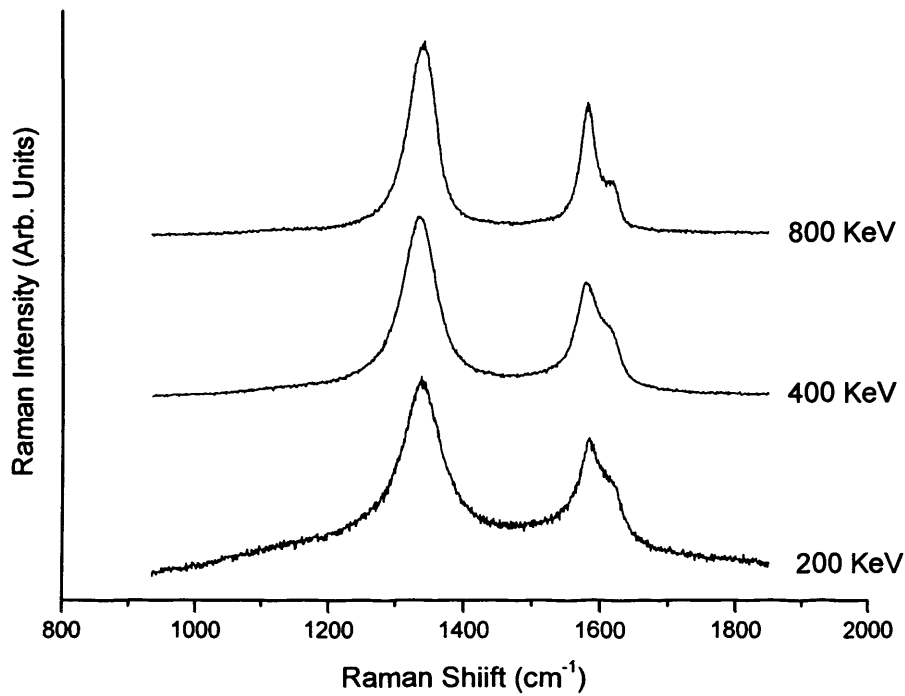


Fig. 6.4: Comparison of Raman spectra obtained for identical graphite samples irradiated with 200, 400 and 800 keV C ions to a fluence of 5.0×10^{14} ions. cm^{-2} .

In all cases irradiation shows a considerable I_D/I_G ratio, indicative of damage [7-10]. The measured ratios are displayed in table 6.3 along with virgin graphite material.

Table 6.3: I_D/I_G ratios for varying energies of C ion irradiation at a dose of 5.0×10^{14} ions. cm^{-2} .

Energy	I_D/I_G ratio
200	1.51
400	1.52
800	1.45
Virgin	0.49 (c.f. Fig. 4.1)

These values are all very similar and are considerably larger than the untreated virgin graphite material, displayed in Fig. 4.1. Interestingly the higher energy irradiation does not seem to indicate a more damaged system, in fact the opposite is true. The slightly lower I_D/I_G ratio, measured at 800 keV, accompanies a narrower band width than the lower energy spectra and also considerably less overlap of the D' and G bands, signs that have been ascribed previously to highly damaged systems [11]. The 800 keV spectrum also exhibits an almost flat baseline, again suggesting that advanced stages of irradiation damage have not yet been reached.

However, the Raman laser is only providing information from approximately the top 40 nm of the sample [12-13], which from Figs. 6.2 and 6.3 we know is far from the level of the majority of the ion induced damage in these higher energy cases. Therefore the Raman spectra observed can be explained by higher energy irradiations resulting in a deeper level of damage, with the maximum damage caused being further into the bulk. In the case of the sample irradiated at 800 keV it seems logical that the majority of the ions would pass the 40 nm threshold at high energy and as a result would not induce as many displacements as it would once it begins to lose energy and slow down at around 800 nm into the bulk (Fig. 6.3).

Even at 200 keV the incident ions surpass the 40 nm threshold at high energy, however with considerably less energy than at 400 and 800 keV. As a result the Raman spectra obtained gives the impression of a more damaged system since a higher proportion of ions will be able to cause the atomic displacements and subsequent damage events necessary for the observed Raman spectrum. However, this is unlikely to be the case in reality since the more energetic irradiation will produce a greater number of PKAs and hence more damage.

Further Raman analysis was carried out in order to compare samples irradiated at a constant energy but at increasing dose. Fig. 6.5 is a comparison of Raman spectra obtained from graphite irradiated at 400 keV at the doses stated.

As expected the Raman spectra indicate that as the total ion dose is increased then the damage to the system also increases. A dose of 5.0×10^{16} ions.cm⁻² seems to have caused significantly more damage than at 5.0×10^{12} ions.cm⁻², as indicated by the

significant peak broadening and the emergence of the broad feature at 1500 cm^{-1} [11].

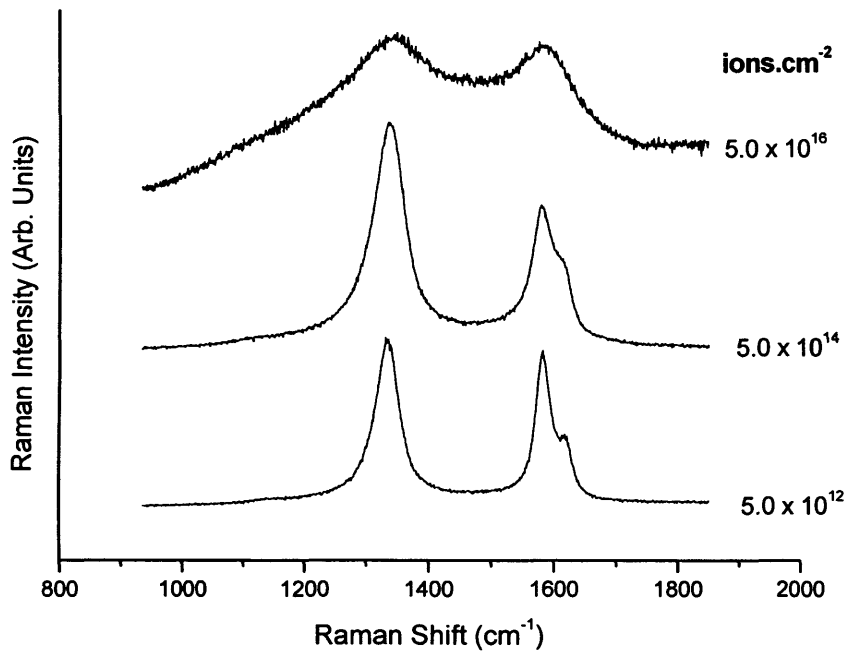


Fig. 6.5: A Raman comparison of graphite samples irradiated with 400 keV C ions at total ion doses of 5.0×10^{12} , 5.0×10^{14} and 5.0×10^{16} ions.cm⁻².

6.3.1.3. X-Ray Diffraction (XRD)

Nuclear grade graphites such as Gilsocarbon and PGA are polycrystalline materials and as such give rise to XRD spectra containing several features, some sharp and well defined and others broader and more rounded. XRD was used in early studies of graphite by Tuinstra and Koenig [14] who used it to determine the crystallite size, L_a , and hence were able to discover that Raman could also be used to calculate L_a accurately through the T-K relation (c.f. 4.3.6).

From the early work carried out by Zachariassen [15-16] in 1945, on graphite irradiated in the Hanford reactor, it is known that irradiation induced structural and dimensional changes can occur in nuclear grade graphites. An increase in the c spacing is observed along with a smaller decrease in the a spacing.

Space Group: D_{6h}^4

Unit Cell: $a = 2.4612 \pm 0.0001 \text{ \AA}$

$c = 6.7079 \pm 0.0007 \text{ \AA}$

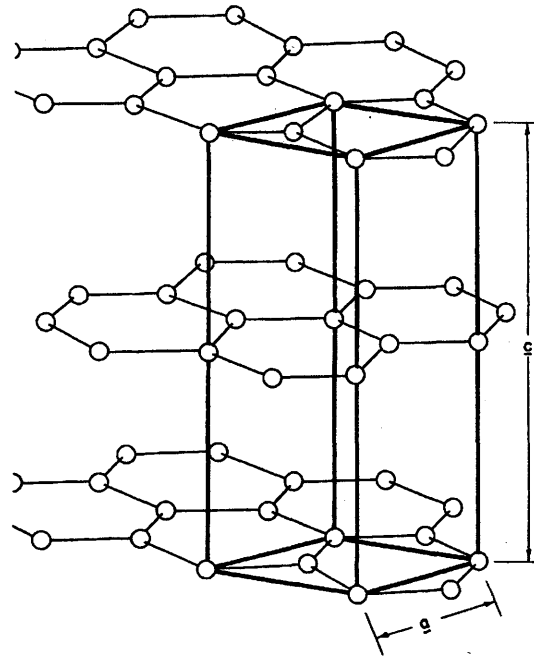


Fig. 6.6: Crystal structure of graphite as first proposed by J.D. Bernal [17].

Such changes are responsible for the macroscopic length change observed in moderator graphite and are also important in explaining the changes to some of the other properties [18].

The swelling in the c -axis can be explained by the formation of interstitial atoms/clusters residing in the area between planes. Fig. 6.7 is a schematic of such a scenario [19].

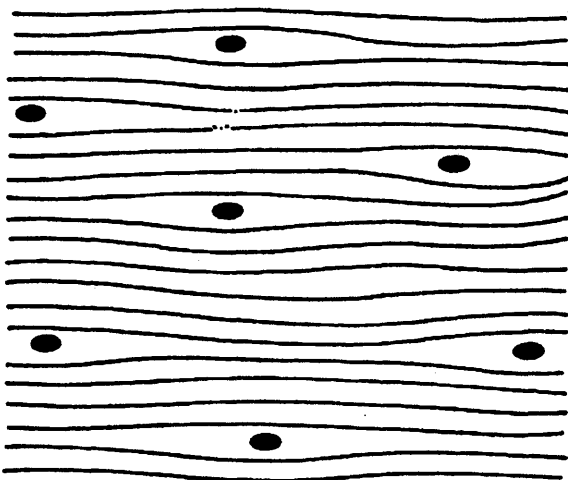


Fig. 6.7: A Schematic representation of radiation-damaged graphite showing interstitial groups on the associated local increase in layer spacing [19].

Such effects can be monitored through XRD which can detect bulk changes in structure very effectively [20]. Fig. 6.8 below is a comparison of poorly graphitised carbons, essentially the graphite precursors used in the manufacturing process, against a nuclear grade graphite, in this case Gilsocarbon.

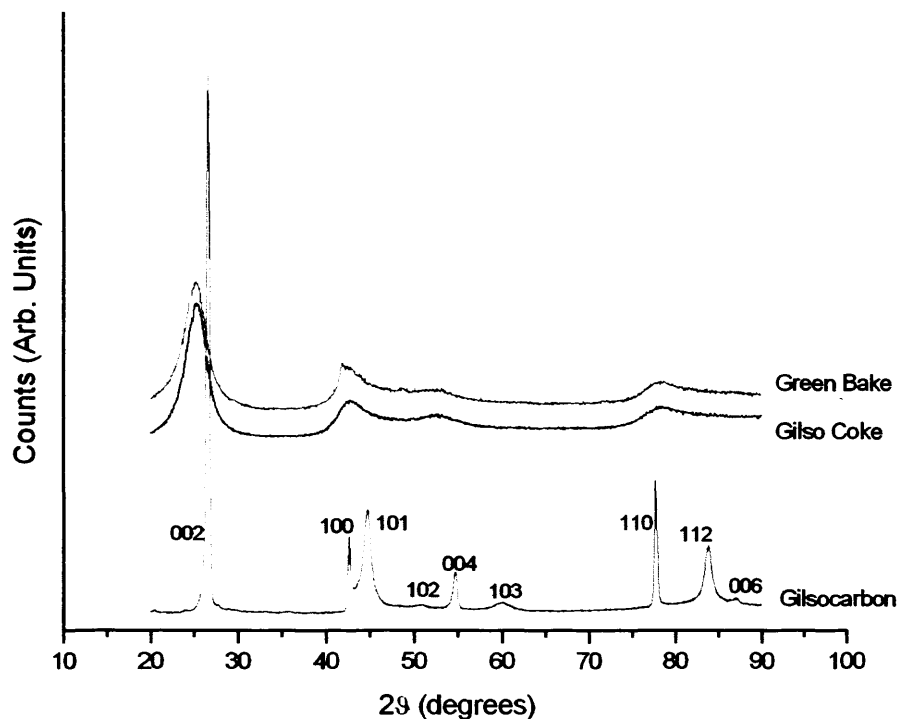


Fig. 6.8: XRD spectra of nuclear grade Gilsocarbon and the carbon precursors used in the manufacturing process (Courtesy of William Bodel). Stated next to each peak is the corresponding diffraction plane.

The patterns obtained for the poorly graphitised carbon is far different to that from the virgin graphite material. Generally there is a peak shift combined with a significant peak broadening and overall loss of features. Work carried out by Bacon and Warren [19] on neutron irradiated graphite confirms that the effect of neutron irradiation is to destroy any long range order and to cause the structure to tend to an amorphous state, not dissimilar to that of pre-graphitised or poorly graphitised carbon.

The first observable change, occurring at relatively low neutron doses, is a shift of the $\langle 006 \rangle$ and $\langle 004 \rangle$ lines to lower angles, due to an increase in c spacing [19]. Such doses exhibit no real broadening; however continued irradiation results in clear peak

broadening until the bands become much more diffuse and eventually disappear entirely.

A distinct sharp feature at $2\theta \sim 26.5^\circ$, ascribed to the $\langle 002 \rangle$ crystal plane, is observed in typical nuclear grade graphites [21]. It is indicative of crystallinity and is found in the XRD pattern of HOPG also [22]; it can be used to determine the crystallite size of the sample from its FWHM [23]. For this reason, at high doses it is beneficial to focus on this peak in order to gain quantitative information regarding the particle induced damage.

Townsend and Lund [21] discovered that the $\langle 002 \rangle$ peak of graphite irradiated in the Hanford reactor began to shift towards lower angles after a relatively short neutron exposure. As the dose increased the shift was found to increase and after a dose of $\sim 1.0 \times 10^{20} \text{ n.cm}^2$ (860 Mwd/At) a significant broadening was observed. At a higher dose of $\sim 2.0 \times 10^{20} \text{ n.cm}^2$ (1500 Mwd/At) a completely broad feature, peaking at $2\theta \sim 24.0^\circ$ was observed, again indicating an amorphous-like structure. A more recent study by Lexa and Kropf [24] of graphite irradiated in the ASTRA research reactor showed analogous results, with the $\langle 002 \rangle$ band tending to an amorphous pattern after a neutron dose of $1.5 \times 10^{19} \text{ n.cm}^{-2}$.

Therefore in order to establish if ion irradiation can cause similar damage to the graphite lattice, XRD can be employed. The changes observed previously (described above) and a tendency towards a poorly graphitised carbon pattern (Fig. 6.8 above) would suggest that similar damage processes were occurring.

However, since XRD is a bulk technique, the ion penetration depth, and the extent of the collision cascade becomes very important. That is, if the large majority of the sample is unaffected by the irradiation, and therefore is essentially virgin material, then the XRD trace obtained would be less likely to pick up any relevant changes in the spectra, induced by the irradiation. This can be seen in the XRD traces obtained in ion irradiated graphite at 5.0 keV (Fig. 6.9).

The results show all diffraction patterns to be virtually identical, thus indicating no observable change in c spacing due to ion bombardment. However, as explained, a

valid reason for this is the relatively low ion energies used, which for the He^+ case, which is the maximum, is only approximately 23 nm.

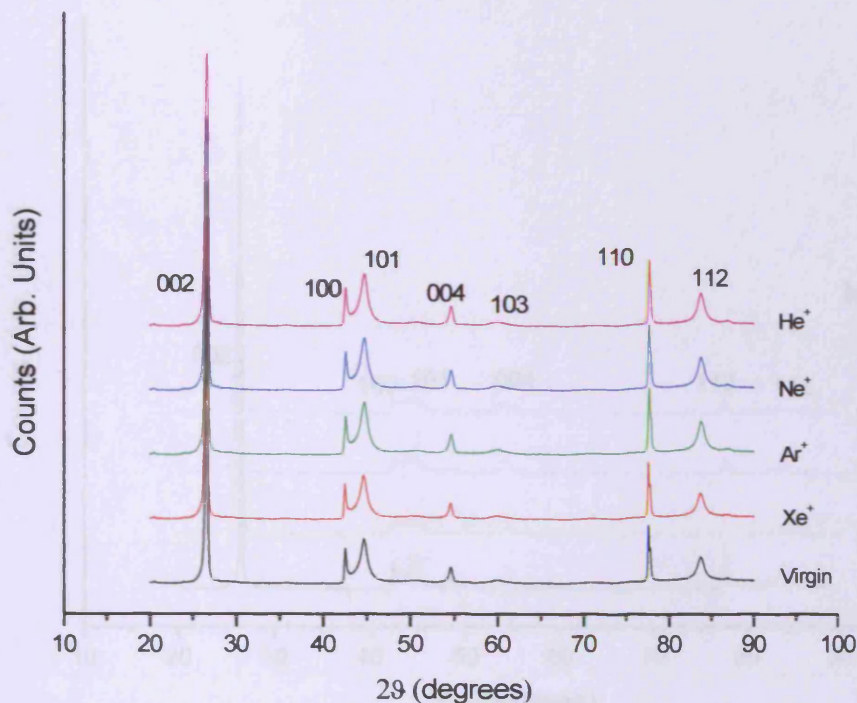


Fig. 6.9: XRD traces obtained for 5 keV He^+ , Ne^+ , Ar^+ and Xe^+ irradiated graphite.

Since the samples used were 1.0 mm thick, it is clear that only a very small percentage of the sample was affected by the irradiation. Since X-rays are able to pass through the bulk of the sample, it seems likely that any increase in lattice spacing or other structural affects within the surface of the sample are beyond the detection limits of XRD and are consequently drowned out by the much larger proportion of information coming from the unaffected bulk. To try and overcome this problem higher ion energies have been used, resulting in increased penetration. Additionally a low-angle version of XRD known as glancing-angle (or grazing-incidence) XRD can be used to obtain information only from the near-surface region (Fig. 2.10).

For the carbon ion irradiation experiments, outlined in Table 6.1, glancing-angle XRD spectra were obtained, at an angle of 2° relative to the surface of the sample.

This is the lowest angle achievable without large signal-noise becoming prominent in the spectra.

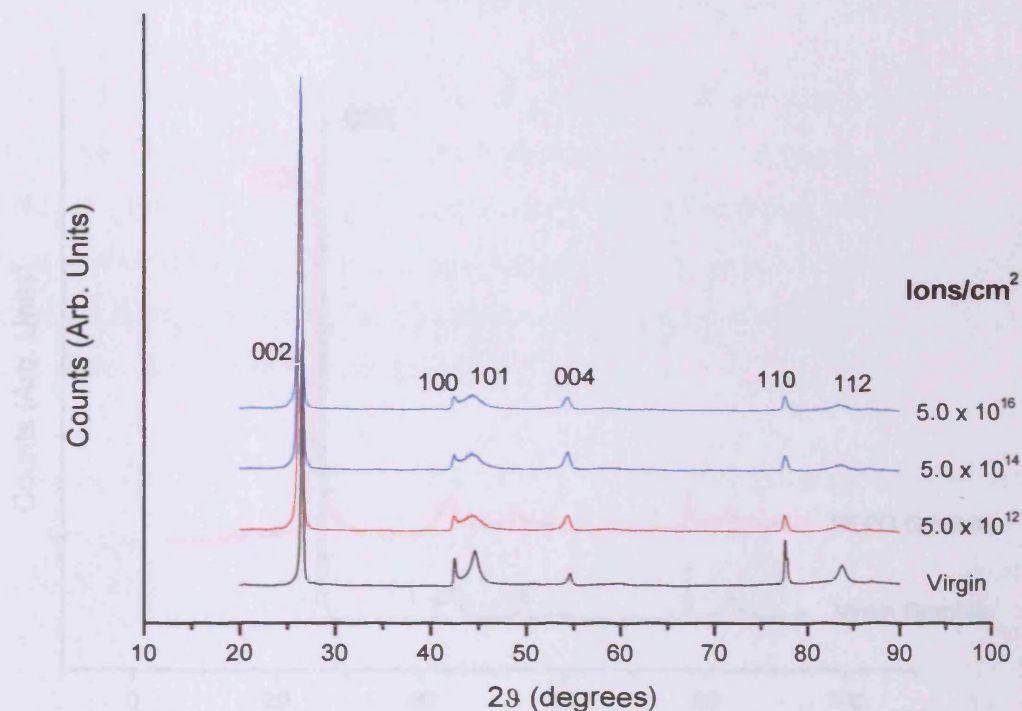


Fig. 6.10: Grazing-incidence XRD comparison of virgin graphite against C ion irradiated graphite at total ion doses of 5.0×10^{12} , 5.0×10^{14} and 5.0×10^{16} ions.cm⁻².

The XRD patterns obtained were virtually identical for all carbon ion irradiated samples. There seemed to be no observable change upon increasing the ion energy from 200 keV up to 800 keV or from increasing the dose from 5.0×10^{12} to 5.0×10^{16} ions.cm⁻², as shown in Fig. 6.9 above.

On comparison of the XRD spectra of virgin graphite with the ion irradiated material there again seems to be little change. The significant broadening and shift of the <002> peak that is indicative of lattice damage, is not present in the spectra, thus indicating that such damage processes have not occurred. Below is an XRD pattern taken of a similar nuclear grade graphite irradiated in the BEPO reactor, with a total neutron fluence of approximately 1.1×10^{21} n.cm⁻².

In Fig. 6.11 a clear broadening of the $\langle 002 \rangle$ peak can be clearly seen, along with a slight shift. The degree of both of these changes would increase as neutron dose increases and damage to the lattice intensifies.

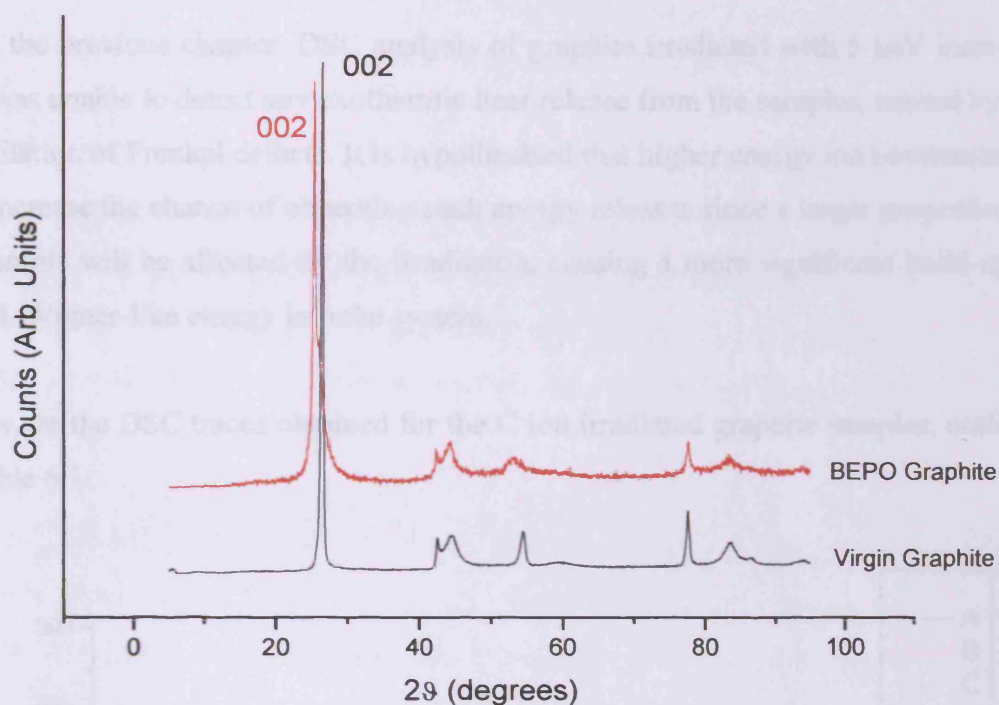


Fig. 6.11: An XRD comparison of virgin graphite and graphite irradiated in the BEPO experimental reactor.

The neutron dose received by this sample is far more than the equivalent ion dose received by the samples analysed in Figs. 6.9 and 6.10. This suggests that perhaps a much higher ion dose is required in order to see the expected changes (as observed above) and that there is a threshold at which the total radiation dose is enough to cause the lattice damage necessary to be picked up by the XRD technique. This would certainly be the case if ions and neutrons produced exactly the same damage cascades, but as discussed previously there are some differences in how they interact with matter and as a result these differences must be considered before coming to an accurate explanation.

From Fig. 6.9, there seems to be a broadening of the $\langle 101 \rangle$ peak in the ion-irradiated samples, with respect to the virgin sample. Additionally a drop in intensity of the

$\langle 110 \rangle$ peak is also apparent. Both these changes have been observed, amongst others, previously in neutron irradiated graphite by Bacon and Warren [19].

6.3.1.4. Differential Scanning Calorimetry (DSC)

From the previous chapter, DSC analysis of graphite irradiated with 5 keV inert-gas ions was unable to detect any exothermic heat release from the samples, caused by the annihilation of Frenkel defects. It is hypothesised that higher energy ion bombardment will increase the chance of observing such energy releases since a larger proportion of the sample will be affected by the irradiation, causing a more significant build-up of stored, Wigner-like energy into the system.

Below are the DSC traces obtained for the C ion irradiated graphite samples, outlined in Table 6.1:

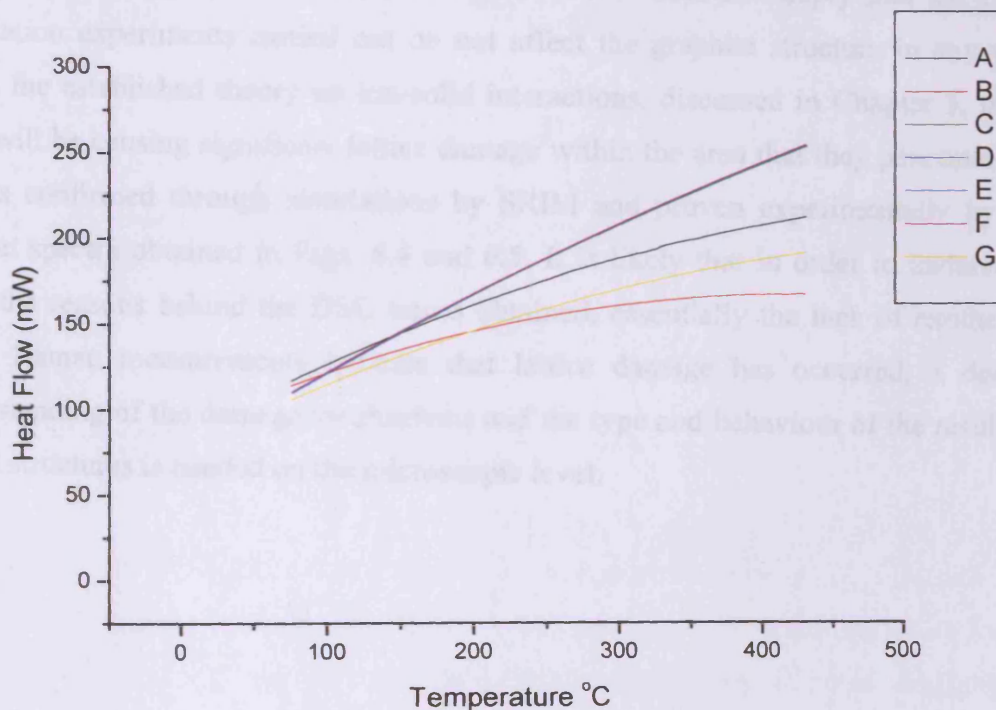


Fig. 6.12: DSC curves obtained for C ion irradiated specimens, outlined in Table 6.1. No energy releases are observed, and the slight changes in curvature observed are due to small differences in sample weight. Below 75 °C the instrument is reaching equilibrium.

The DSC data obtained shows no observable exothermic energy release upon heating over the temperature range 30 – 400 °C. This is unexpected and indicates that no internal, Wigner-like energy has been introduced into the graphite as a result of the irradiation. However, as discussed previously, it is perhaps the case that since the majority of the sample is effectively still virgin material any energy release coming from the small irradiated fraction is not being detected or is essentially overwhelmed by the undamaged bulk.

This is not the case in neutron irradiation whereby the whole of the sample is affected and thus there is no part of the sample that is left unaffected by the irradiation. It seems that even using the higher energies outlined in Table 6.1 the collision cascades for C ion irradiation do not reach far enough into the bulk of the sample to obtain desirable results.

However, it is important to note that this DSC data does not imply that the C ion irradiation experiments carried out do not affect the graphite structure in any way. From the established theory on ion-solid interactions, discussed in Chapter 3, the C ions will be causing significant lattice damage within the area that they penetrate and this is confirmed through simulations by SRIM and proven experimentally by the Raman spectra obtained in Figs. 6.4 and 6.5. It is likely that in order to understand fully the reasons behind the DSC traces obtained, essentially the lack of exotherms when Raman measurements indicate that lattice damage has occurred, a deeper understanding of the damage mechanisms and the type and behaviour of the resultant defect structures is needed on the microscopic level.

6.3.2. Irradiation at Higher Energies (> 1.0 MeV)

A study into the effects of yet higher ion energies was carried out in order to gather more knowledge on the damage processes and to try to improve the chances of observing stored, Wigner-like energy in these ion-irradiated samples.

Samples of and nuclear grade PGA graphite were irradiated with high energy He⁺ and Ar⁺ ions at the Institute of Nuclear Physics, at the Université de Lyon, using their Van de Graff accelerator. The irradiation conditions used for each sample are outlined in Table 6.3.

Table 6.3: Parameters of the irradiations carried out on the Van De Graff accelerator at Lyon. Ion penetration parameters are calculated by SRIM 2008. χ_0 is the mean penetration depth.

Sample	Ion	Total Fluence (ions/cm ²)	Initial Energy (keV)	χ_0 (nm)	Approx Implantation Range (nm)	Vacancies/ion
A	He ⁺⁺	5.0 x 10 ¹⁵	4000	13564	12246 - 14549	~ 103
B	He ⁺⁺	5.0 x 10 ¹⁵	7500	34781	33001 - 35997	~ 118
C	Ar ⁺⁺⁺	5.0 x 10 ¹⁴	4000	2116	1609 - 2620	~ 2980
D	Ar ⁺⁺⁺	5.0 x 10 ¹⁴	8000	3262	2786 - 3797	~ 3300

Using a Van de Graff accelerator, higher ion energies could be easily achieved and higher fluences than on the ion implanter. To achieve the acceleration necessary to get up to the desired energy the ions must be double or triply charged, however this does not affect the interaction with the sample, since the ions are stripped of their electrons very quickly anyway as they travel through the graphite matrix [4,25-26].

6.3.2.1. Ion Implantation

As before a SRIM calculation was carried out for each experiment in order to determine the penetration depth of the ions and the extent of the collision cascades involved.

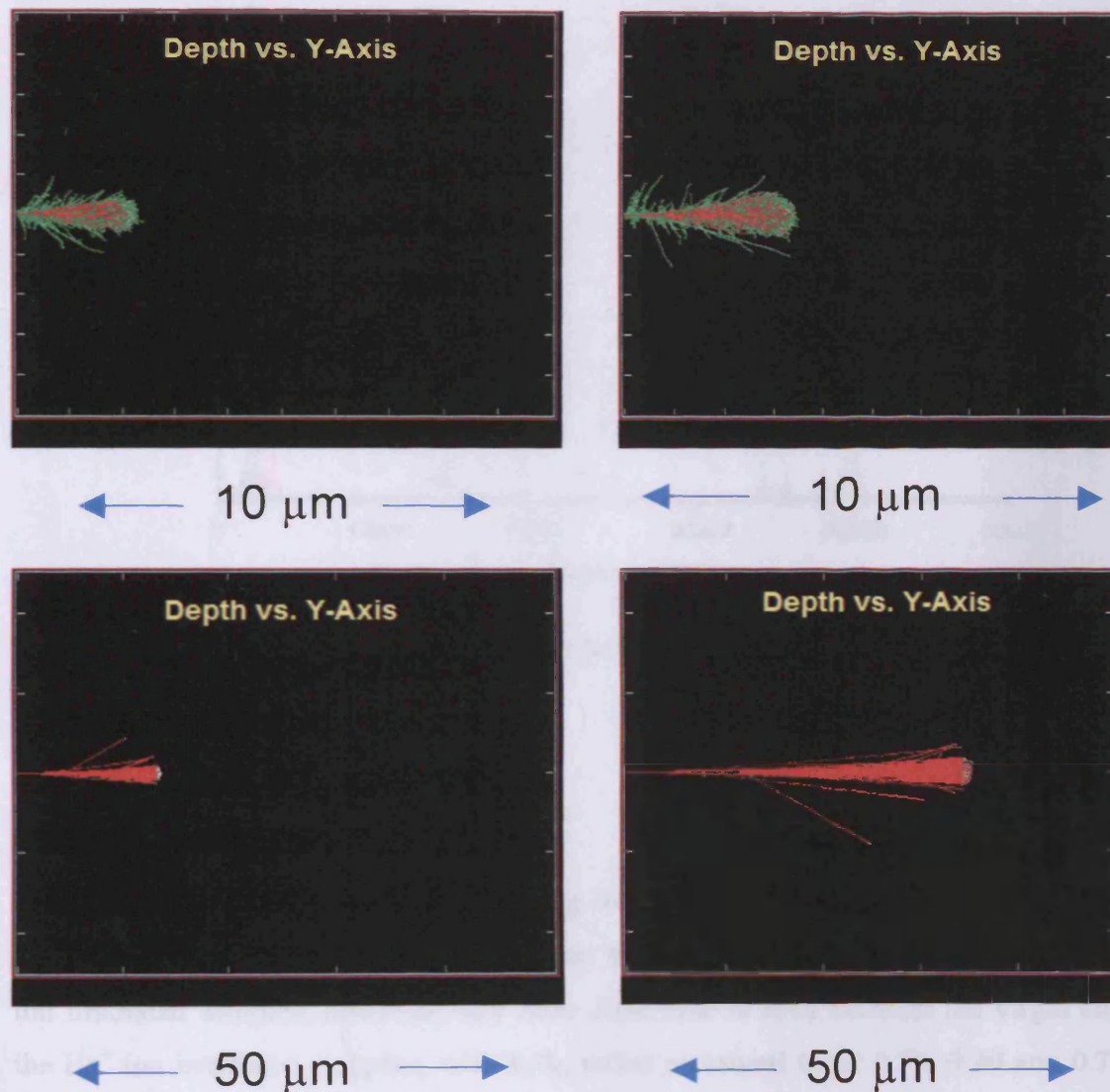


Fig. 6.13: A visual representation of the distribution of high energy ions as they penetrate a graphite surface, simulated using SRIM 2008. The images refer to 4.0 MeV Ar⁺ (top left), 8.0 MeV Ar⁺ (top right), 4.0 MeV He⁺ (bottom left) and 7.5 MeV He⁺ (bottom right). Green represents displaced carbon atoms and red represents the ion path. Note in the case of He⁺ irradiation full damage cascades could not be calculated easily due to the difficulties involved with simulating high energy light ions [4].

The implantation profiles for the high energy irradiations are shown below, with the mean implantation depth being much higher than observed previously, of the order of micrometers.

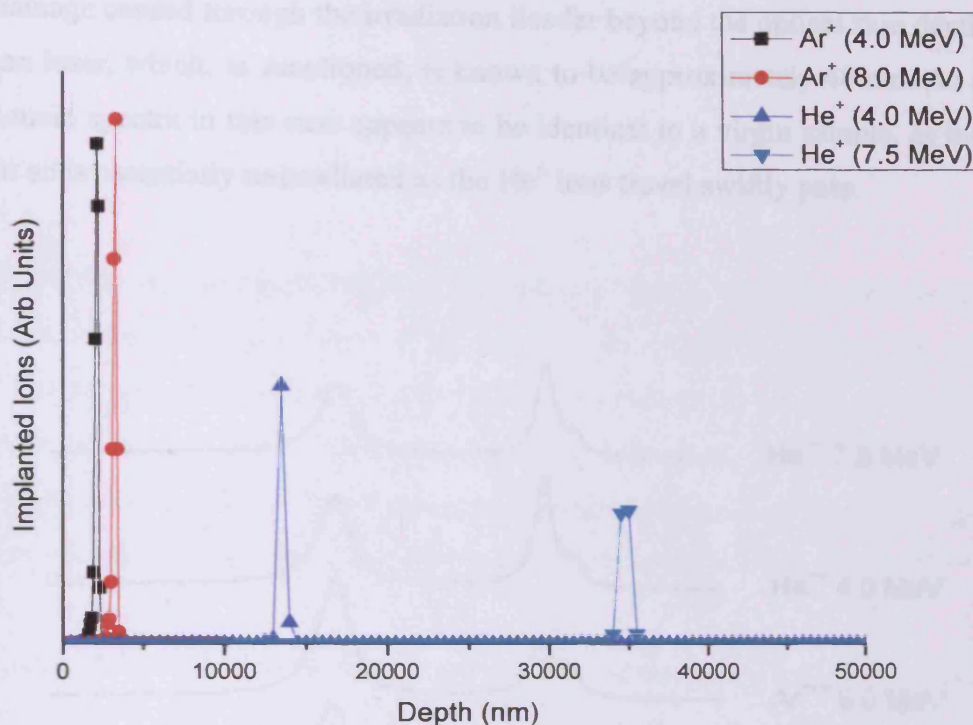


Fig. 6.14: Ion implantation profile for high energy Ar and He ion irradiation, achieved using the VdG accelerator at Lyon.

6.3.2.2. Raman Analysis

The Raman spectra obtained for the highest energy He and Ar irradiations is shown in Fig. 6.15. A considerable difference is seen between the virgin graphite and the Ar⁺ ion irradiated samples, however very little difference is seen between the virgin and the He⁺ ion irradiated samples, with I_D/I_G ratios measured to be 0.79, 0.80 and 0.77 for the virgin, 4.0 MeV and 7.5 MeV irradiated samples respectively. The latter issue is expected, particularly from the SRIM simulations (Fig. 6.13 and Table 6.3) as the He ions pass swiftly through the surface of the graphite and penetrate relatively deep into the bulk, at a mean distance of 13.6 and 34.8 μm for 4.0 and 7.5 MeV ions respectively. Due to this the ions do not interact with the host atoms close to the surface, and only begin to collide with atoms mostly towards the end of their

trajectory when they are travelling at slower speeds [27-30]. This can be seen from the vacancies/ion calculations outlined in Table 6.4, which, when compared to the Ar^+ case are much lower, with the vast majority expected to be relatively deep into the bulk. Therefore, the Raman spectra obtained for the He^+ case can be explained by this in that the damage caused through the irradiation lies far beyond the optical skin depth of the Raman laser, which, as mentioned, is known to be approximately 40 nm. As a result the Raman spectra in this case appears to be identical to a virgin sample, as the top 40 nm or so is essentially unirradiated as the He^+ ions travel swiftly pass.

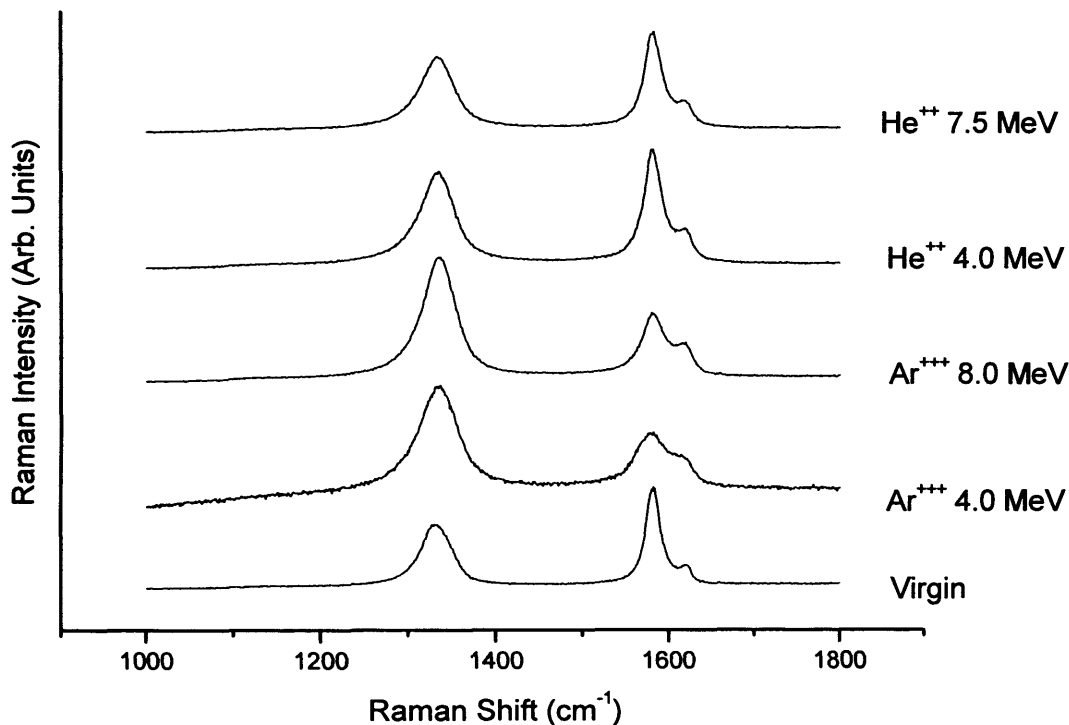


Fig. 6.15: Comparison of Raman spectra of the graphite samples after irradiation with the high energy ions outlined in Table 6.3.

For the Ar^+ ion irradiated samples, the spectra exhibit a clear increase in I_D/I_G ratios compared to the virgin material, being 1.92 and 1.95 for 4.0 MeV and 8.0 MeV ion irradiation respectively. As is the case with the He^+ ion irradiation discussed above, the high energy Ar^+ ions travel much further than the optical skin depth of the Raman laser; however, in contrast to the He^+ ion case there is an observed damage increase within this depth. The reason for this is probably the large difference in atomic radii and mass between the two ions. The larger Ar^+ ions are able to destroy most of the

graphite lattice as they pass through the sample, before coming to rest. Ar^+ is also considerably larger than C meaning that they will be able to move and disrupt the lattice more easily, rather than moving past at high velocity in the same manner as lighter projectiles such as He^+ ions, protons and neutrons are able to. Essentially these spectra illustrate the differences between the damage caused by ions predominately slowed down through nuclear stopping and those slowed through electronic stopping.

6.3.2.3. XRD measurements

The even higher penetration depths reached by using the Van de Graff accelerator for the ion irradiation means that a larger proportion of the sample is affected by the irradiation. The sample thickness is 1.0 mm (1000 μm) and in the case of 7.5 MeV He^+ ion irradiation the mean penetration depth is expected to be approximately 34.8 μm , which is roughly 3.5 % of the total sample volume. This is still not a large proportion but is considerably larger than that in the 5 keV experiments.

The XRD traces obtained for samples A-D are almost identical to those obtained for the C ion irradiated samples, shown in Fig. 6.10. The same subtle differences are observed between the irradiated specimens and the virgin material; however no significant broadening or shift, particularly of the $\langle 002 \rangle$ band is observed.

The glancing-angle XRD spectra obtained for samples A-D is shown in Fig. 6.16. These results are somewhat unexpected. For the case of Ar^{+++} irradiation the XRD results seem to contradict the Raman data obtained. Since the Raman analysis indicates that lattice damage is caused within the optical skin depth of 40 nm then it follows that even more damage must be caused further into the sample as the ions start to slow down. Therefore one would expect a considerable level of damage at around 2-3 μm into the sample, extending even further due to the knock-on cascades. However, as explained previously the glancing-angle XRD is limited to an incident angle of 2° and even at this low angle of approach the depth at which the X-Rays are diffracted is approximately 90 μm . Therefore it seems plausible that perhaps in this instance the vast majority of the information obtained is coming again from undamaged graphite and as a result is giving very similar traces to the virgin material.

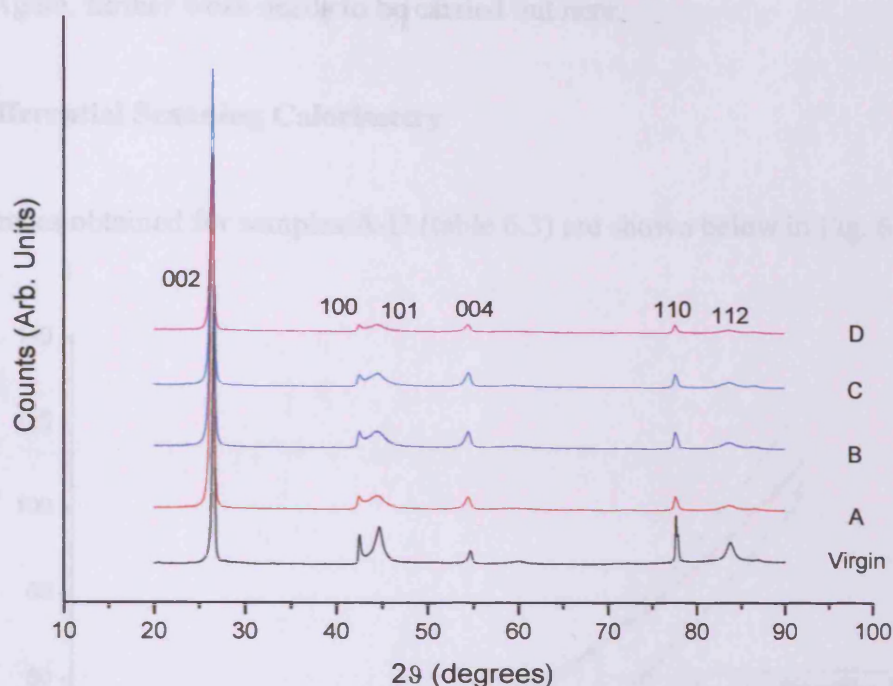


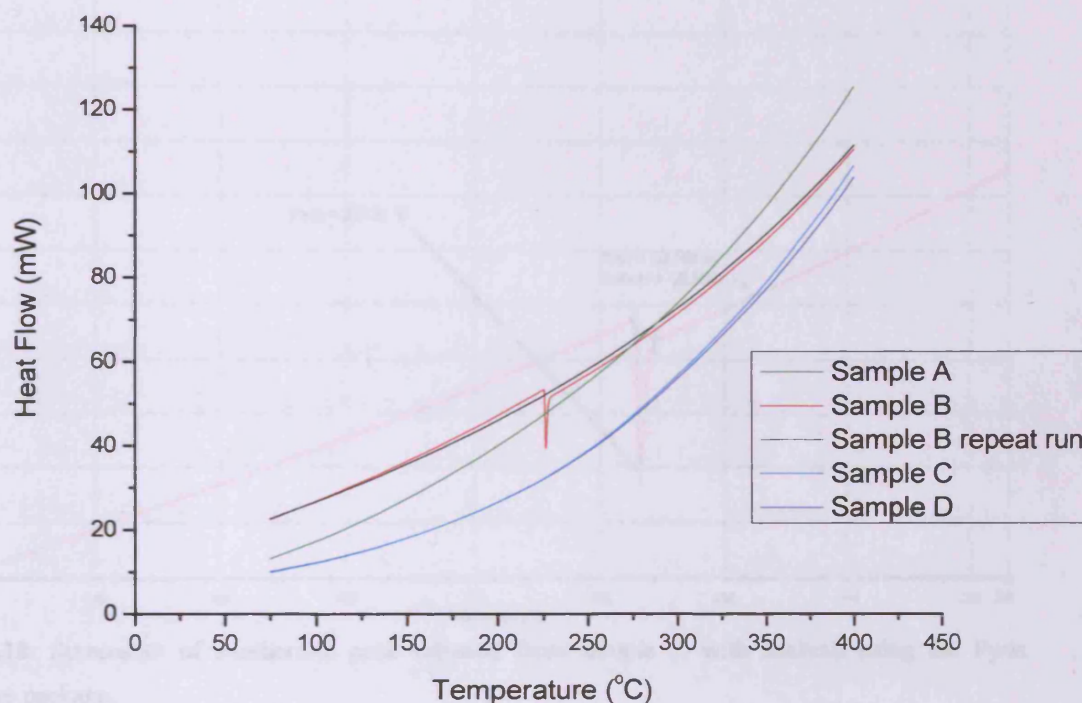
Fig. 6.16: XRD comparison of virgin graphite against high energy ion irradiated graphite, irradiated using the Van de Graff accelerator, under the parameters outlined in Table 6.4.

In the case of He^{++} irradiation the penetration depth is considerably further (Table 6.4) reaching approximately $35 \mu\text{m}$ for 7.5 MeV energy. However, the XRD patterns obtained are virtually identical to the rest of the samples analysed, indicating no observable difference even after a much increased penetration depth. This is more difficult to explain since now a much larger portion of the sampling depth is affected by the irradiation and any irradiation induced broadening or shifting of the peaks should be easily detected by this method. The fact that this is not the case is difficult to explain but suggests that glancing-angle XRD is not an appropriate technique by which to study ion-irradiated graphite, unless perhaps either higher ion energies (and hence higher penetration depths) are used or that the incident angle of the X-ray beam can be reduced even further. However, it may indicate that ion irradiation differs from neutron irradiation in that the same type of structural disorder necessary to deliver a change in XRD pattern is not being produced. Perhaps ions somehow lead to less interstitials residing in between the planes consequently giving rise to less c axis expansion and therefore less shifting of the XRD peaks. However, on the contrary, the XPS data indicates that after irradiation the ions will reside within the graphite bulk,

presumably between the layers, thus suggesting an even bigger expansion in the c direction. Again, further work needs to be carried out here.

6.3.2.4. Differential Scanning Calorimetry

The DSC traces obtained for samples A-D (table 6.3) are shown below in Fig. 6.17.



6.17: DSC traces obtained for samples A-D outlined in Table 6.3. Below 75 °C the instrument is reaching equilibrium.

The data obtained in the DSC analysis samples 1-4 is interesting in that an exothermic peak is observed in one of the samples, but curiously not in the others. The exotherm is present in sample 2, which was irradiated with 7.5 MeV He^{++} ions at a dose of 5.0×10^{15} ions.cm², and is centred at 226 °C. The same sample is then run again in the DSC and the repeat run is also shown in Fig. 6.17; this run displays no exothermic releases. This is an expected result indicative of defect-induced stored energy release since once the defects are annealed out the first time then the lattice will be reformed to its pre-irradiated state and hence no more energy release should be observed during the second heating cycle. This trace also proves that the exotherm is not just an artefact of the sample.

Using the Pyris software package the area under the peak can be measured resulting in a value for the enthalpy change i.e. the amount of energy given off by the sample. A close-up of the peak is shown below in the screenshot taken from the Pyris software.

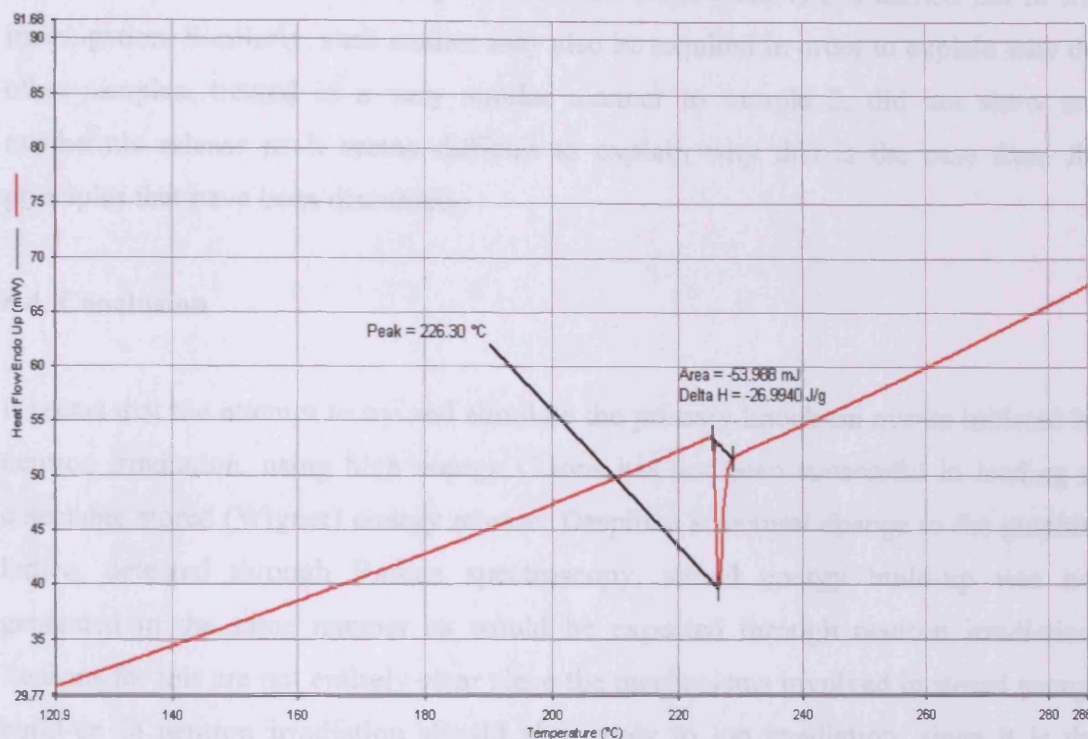


Fig. 6.18: Screenshot of exothermic peak released from sample 2, with analysis using the Pyris software package.

Integration of the peak gives a ΔH value of -27 Jg^{-1} , which results in an overall energy release for the sample (weight = 40 mg) of 1.01 J or $6.7 \times 10^{18} \text{ eV}$. This can be seen as a rather high energy release and would suggest that a significant reorganising of the lattice, and annealing of defects is occurring upon heating of the specimen. From the many studies carried out [31-35] and those particularly discussed in Chapter 5, typical energy ranges for many of the atomic scale processes such as vacancy migration, interstitial annihilation etc. are in the range of tens of eV or lower, thus suggesting that the exothermic energy release peak observed here is the result of a vast number of these processes occurring at once. This conclusion seems feasible since ions are large enough to cause significant lattice disruption, including the production of many interstitial-vacancy pairs and other irradiation-induced phenomena that may be annealed out once enough heat, in this case $\sim 226 \text{ }^\circ\text{C}$, has been added to the system.

However it is important to note that the exact atomic scale processes and mechanisms responsible for this exothermic release can only be speculated about at this stage; to know exactly the origin of this heat release a further study would be required likely utilising advanced modelling techniques and some high-resolution-TEM work to try and 'see' the processes occurring in real-time. Such work is not carried out in this investigation. Similarly, such studies may also be required in order to explain why the other samples, treated in a very similar manner to sample 2, did not show any exothermic release as it seems difficult to explain why this is the case from the principles that have been discussed.

6.4. Conclusion

It seems that the attempt to try and simulate the primary knock-on events initiated by neutron irradiation, using high energy C ions has not been successful in leading to detectable stored (Wigner) energy release. Despite a structural change to the graphite lattice, detected through Raman spectroscopy, stored energy build-up was not generated in the same manner as would be expected through neutron irradiation. Reasons for this are not entirely clear since the mechanisms involved in stored energy build-up in neutron irradiation should also apply to ion irradiation, since it is the primary knock-on atoms that produce most of the defects and not the incident particle. It seems sensible that a simulating the primary knock on atom by irradiating with C^+ of appropriate energy should yield very similar defects to neutron irradiated graphite. Perhaps higher ion doses would be needed since neutron irradiated specimens that show significant stored energy release are exposed to neutron doses several orders of magnitude higher. However, despite this an exothermic release was observed in 7.5 MeV He^{++} irradiated samples, which was at a relatively low dose of 5.0×10^{15} ions.cm². In this case the He^{++} ions are able to penetrate deep into the bulk of the sample used and hence have a much larger collision cascade. This could explain why heat release was observed in this sample and not in the other samples, suggesting that perhaps the detection of any exotherms is limited by the extent of the collision cascade throughout the sample.

The work also carried out in this chapter also showed that XRD and even glancing-angle XRD are not suitable for detecting any changes to the graphite lattice caused as

a result of ion irradiation, at least for the energies and fluences used in this study. XRD may only be useful if either higher ion energies could be utilised or lower incidence angle of the X-rays can be achieved resulting in less data picked up from the unaffected virgin areas of the sample. However it is clear that more work needs to be done to understand exactly why observing a significant change in XRD patterns before and after ion irradiation is proving so difficult when we know that the ions are clearly damaging the graphite structure.

6.5. References

- [1] B.E. Watt, *Phys. Rev.*, **31** (1952) 65.
- [2] G.J. Dienes, *Annu. Rev. Nucl. Sci.*, **2** (1953) 187.
- [3] D.R. De Halas, 'Theory of Radiation Effects in Graphite', in: R.E. Nightingale (Ed.) 'Nuclear Graphite', Academic Press: New York and London, (1962).
- [4] J.F. Ziegler, J.P. Biersack, M.D. Ziegler, 'The Stopping and Range of Ions in Matter', Srim Co., USA (2008).
- [5] J.C. Slater, *J. Appl. Phys.*, **22** (1951) 237.
- [6] Thompson, J.J, *Phil. Mag.*, **6-23** (1912) 449.
- [7] K. Niwase, M. Sugimoto, et al., *J. Nucl. Mat.*, **155-157** (1988) 303.
- [8] K. Niwase, K. Nakamura, T. Shikama, T. Tanabe, *J. Nucl. Mat.*, **170** (1990) 106.
- [9] S. Reich, C. Thomsen, *Phil. Trans. R. Soc. Lond. A*, **362** (2004) 2271.
- [10] K. Niwase, K. Nakamura, I. Tanaka, Y. Miyamoto, T. Tanabe, *J. Nucl. Mat.*, **179-181** (1991).
- [11] A. Theodosiou, A.F. Carley, S.H. Taylor, *J. Nucl. Mat.*, **403** (2010) 108.
- [12] K.G. Nakamura, M. Kitakima, *Phys. Rev. B*, **45** (1992) 5672.
- [13] K.G. Nakamura, M. Kitakima, *Surface Science*, **283** (1993) 255.
- [14] F. Tuinstra, J. Koenig, *J. Chem., Phys.*, **53** (1970) 1126.
- [15] W.H. Zachariasen, 'X-Ray Diffraction Studies of Irradiated Graphite', USAEC Report CP-3010, University of Chicago (1945).
- [16] W.H. Zachariasen, 'X-Ray Evidence for Structural Change in Irradiated Graphite', USAEC Report MUC-FWHZ-126, University of Chicago (1945).
- [17] J.D. Bernal, *Proc. Roy. Soc.*, **A106** (1924) 749.

- [18] R.E. Nightingale, H.H. Yoshikawa, E.M. Woodruff, 'Radiation-induced Structural and Dimensional Changes', in: R.E. Nightingale (Ed.) 'Nuclear Graphite', Academic Press, New York and London (1962).
- [19] G.E. Bacon, B.E. Warren, *Acta Cryst.*, **9** (1956) 1029.
- [20] B.D. Cullity, 'Elements of X-Ray Diffraction', Addison-Wesley, (1978).
- [21] J.R. Townsend, C.A. Lund, 'X-Ray Diffraction Peak Shapes from Irradiated Graphites', USAEC Report HW-25019, Hanford Works (1952).
- [22] E. Bourelle, Y. Tanabe, E. Yasuda, S. Kimura, *Carbon*, **39**.
- [23] E.P. Warekois, X-Ray Diffraction Studies of Irradiated Graphites, (Interim Report No. 12), USAEC Report HW-20435, Hanford Works, in,(1951).
- [24] D. Lexa, A.J. Kropf, *J. Nucl. Mat.*, **348**.
- [25] Y. Miyamoto, *Appl. Phys. Lett.*, **91** (2007) 113120.
- [26] H. Paul, *Ion interaction with matter*, in,(2009).
- [27] G.H. Kinchin, R.S. Pease, The Displacement of Atoms in Solids by Radiation, *Rep. Prog. Phys.*, **18** (1955).
- [28] G. Carter, J. Colligon, *Ion Bombardment of Solids*, Heinemann, (1968).
- [29] R.S. Averback, *J. Nucl. Mat.*, **108 & 109** (1982).
- [30] M. Nastasi, J.W. Mayer, J.K. Hirvonen, *Ion-Solid Interactions: Fundamentals and Applications*, Cambridge University Press, (1996).
- [31] T. Iwata, F.E. Fujita, H. Suzuki, *J. Phys. Soc. Jap.*, **16** (1961) 197.
- [32] T. Iwata, T. Nihira, *Jap. J. Appl. Phys.*, **15** (1975) 575.
- [33] T. Iwata, *J. Nucl. Mat.*, **133&134** (1985) 361.
- [34] F. Seitz, *Disc. Faraday. Soc.*, **5** (1949) 271.
- [35] R.H. Telling, M.I. Heggie, Radiation defects in graphite, *Philosophical Magazine*, **87** (2007) 1.

Chapter 7

Conclusions

7.1. Overview

An in-depth scientific study has been carried out on the effects of ion irradiation on graphitic structures, with the aim to understand the damage processes that occur. The work carried out in this project has been presented at international conferences and to a range of people from the nuclear industry. It is hoped that the results obtained are of benefit to those in the nuclear industry aiming to elucidate the fundamental processes behind the Wigner effects observed in nuclear graphite and consequently may help to aid the large graphite decommissioning task that lays ahead, particularly in the UK.

As discussed in detail in Chapter 2, ion irradiations were carried out using standard UHV equipment. Subsequent analysis involved the use of experimental techniques such as Raman spectroscopy, XRD, DSC, XPS, and TEM alongside the SRIM 2008 Monte Carlo simulation software. The results obtained have been discussed in detail in each chapter; this chapter aims to summarise the main points.

7.2. Summary of Results

7.2.1. Raman – (Chapter 4)

Raman spectroscopy has shown to be an effective tool in detecting the damage induced through ion irradiation, and has been the primary method of analysis in this

project. Previously published work has shown that the ratio of the D and G bands, observed in the first order Raman spectrum of graphite, can provide qualitative information on the damage induced. The results of the ion irradiation experiments carried out here are in agreement with the published work and show, as expected, that as the amount of ion irradiation increases then so does the damage to the system. Importantly, these results are analogous to neutron irradiation, and from the Raman data received it seems that both ions and neutrons cause similar defects within the graphite lattice.

However the Raman information obtained is taken only from a depth of approximately 40 nm, meaning that any results interpreted only apply to this volume. A fundamental difference between neutrons and ions is that neutrons are much smaller and consequently penetrate far deeper into the bulk for a given energy; this demonstrates that a Raman analysis of neutron irradiated samples does not provide information on bulk damage, which is likely to be considerable for high neutron fluences. For ions this is not the case. Using the SRIM 2008 software penetration depths can be calculated for all ions used in the irradiation experiments carried out. For energies of 5 keV or less the penetration depths are all in the range of nanometres, indicating that such irradiations are unable to cause any damage beyond this depth. Using higher ion energies increases the penetration depth and as a result will cause damage to the bulk graphite, however in this instance Raman spectroscopy would not be very beneficial as the ions, and hence the damage, would surpass the optical skin depth of 40 nm (Chapter 6).

7.22. XPS – (Chapter 5)

Analysis of ion irradiated samples through XPS has shown that a proportion of the incident ions remain embedded within the graphite lattice after irradiation. This is likely to disrupt the organisation of the host atoms as they are forced to reorganise. This is an area where ion irradiation differs from neutron irradiation. Analysis of the C 1s band in the XPS spectra shows a broadening after irradiation consistent with a change in bonding from sp^2 to sp^3 , a change, linked with amorphisation. However it is difficult to try and establish the effect of the implanted ion and its role in defect formation and subsequent amorphisation of the irradiated graphite. Further work

would be required in order to understand these affects in more detail, likely incorporating the use of computer modelling systems.

7.2.3. XRD – (Chapter 6)

Neutron irradiated graphite samples have shown a broadening and shift of the $\langle 002 \rangle$ diffraction peak, the extent of which is dependant on neutron fluence. However, XRD experiments on ion irradiated samples have not shown such broadening which is attributed to a break down of long-range order and a more amorphous system. Higher ion energies were employed to increase the penetration depth and cause more bulk damage detectable through XRD. However, despite such high energies no broadening affects were observed. Reasons for this are not clear and it is possible that maybe not enough of the sample is affected though the ion irradiation or that higher ion fluences are required. Even the use of glancing-angle XRD, capable of studying the top 100 microns of the sample did not yield any results that could be assigned to ion induced damage.

7.2.4. Annealing – (Chapter 5)

Heating neutron irradiated graphite provides enough energy to the system to cause the annihilation of particular defects, gradually leading to the removal of damage and a return towards the pristine state. This annealing has been widely used in the industry in the past in order to alleviate the neutron-induced effects, particularly the build up of stored energy. The work carried out here shows that in the same way as neutron induced damage can be removed, ion induced damage can also be healed by increasing the sample temperature. This has been observed through Raman analysis (Figs. 5.5a – 5.5d and Fig. 5.11) and TEM (Fig. 5.24). These results are again as expected since the damage processes and the nature of the defects caused are thought to be largely the same.

The temperature of the sample prior to irradiation also affects the rate of damage accumulation in a very similar way for both ions and neutrons. Cooling the sample to below room temperature leads to increased damage for an equivalent dose.

7.2.5. DSC - Wigner Energy Detection (Chapters 5 and 6)

Perhaps the main objective of this project was to try and improve the understanding of Wigner energy build-up and release in neutron irradiated graphite. Using ions to simulate neutrons and induce Wigner energy accumulation would be a cheap, easy and convenient way of doing this and improving understanding and hence safety with regards to the decommissioning of such graphites.

Using ions to generate detectable amounts of Wigner energy proved very difficult. At 5 keV ion irradiation no exothermic releases were detected through DSC, suggesting that perhaps not enough of the total sample volume was affected by the irradiation to accumulate enough Wigner energy. In chapter 6 even higher ion energies were used resulting in the majority of the sample bulk being affected by the collision cascades, but still in the majority of samples no energy release was observed.

Curiously, even when irradiating with high energy carbon ions, which would simulate the primary knock-on atoms generated through neutron bombardment, no stored energy was observed.

However, in one sample irradiated with high energy, 7.5 MeV, He^{++} ions an exothermic energy release was observed. The temperature of release was very similar to that observed in Wigner release from neutron irradiated material though the amount of energy given off seemed relatively high. Perhaps this could be explained by the larger collision cross-section of the He nucleus as opposed to a neutron, causing more collision cascades and hence ultimately more damage into the graphite system than a neutron would. However, repeating similar experiments using similar ions and initial energies resulted in no heat release. Why one particular sample displayed a Wigner-like energy release as expected but the other did not is not entirely certain and a more detailed investigation and further repeats of these experiments would need to be carried out. Time constraints did not allow for that work to be carried out here.

7.2.6. TEM

After successfully preparing thin graphite samples through focussed ion beam, PGA graphite was observed under the microscope. Images clearly showed randomly orientated packets of graphitic structure situated amongst an amorphous matrix (Fig. 5.20) with higher resolution images (Fig. 5.21) allowing the graphene planes to be resolved.

After ion irradiation the images show an amorphous state, with no graphitic packets present. This occurs after 5 keV He⁺ irradiation to a fluence of 3.2×10^{19} ions.m⁻². We know such results are similar to those observed in neutron irradiated graphite and again tells us that ions are able to damage the graphite structure effectively and that such damage can be recovered, at least partially (Fig. 5.23) in much the same way as neutron damage is recovered.

7.3. Summary

The use of ion bombardment on graphite systems is an effective method of introducing damage into the graphite lattice, a type of damage that is largely comparable to neutron induced damage, inflicted during the time in a reactor core. The mechanisms behind the damage production are essentially the same for both ions and neutrons and hence such damage is also recoverable in much the same way.

However, certain questions remain unanswered, most of all regarding the generation of stored Wigner-like energy. Such energy is produced all too easily in many low-temperature graphite moderated reactors; however, using ion irradiation to input a similar potential energy into the system was not an easy task and could not be achieved in a reproducible manner. This, along with the XRD patterns that seemed relatively unchanged before and after a variety of ion irradiations, suggests that perhaps the damage mechanisms are somehow different and that the defects introduced into graphite may be more unstable for ion irradiation than they are for neutron irradiation.

Overall this project has provided an interesting and useful insight into the effects of ion irradiation on nuclear grade graphites, and is hopefully of interest to many people involved in the nuclear industry. However, the potential problem caused by a build up of large amounts of Wigner energy is still of concern and more work should be done in understanding this aspect of radiation damage if the potential risks are to be fully understood.

7.4. Future Work

Future work should focus on defect formation and the exact nature of the defects induced through both ion and neutron irradiation. It seems that more work needs to be done on understanding the fundamental damage processes occurring on the atomic scale and the recovery associated with each defect type. To do this experimentally, high-resolution TEM should be used allowing for defects to be actually observed, with such work complementing the computer modelling that is going on in this field. An exciting method of monitoring defect formation would be in real time using an in-situ irradiation/microscope facility. Such a facility exists in the UK at the University of Salford and is an in-situ ion-irradiation/TEM microscope. Such a system may provide the necessary insight into achieving the required understanding of radiation damage in graphite.

